Effect of impurities with variable valency on the transport phenomena in a quantum well

I. I. Lyapilin

Institute of Metal Physics, Ural Branch of the Russian Academy of Sciences, 620219 Ekaterinburg, Russia
(Submitted April 9, 1996; resubmitted October 5, 1996)
Fiz. Tekh. Poluprovodn. **31**, 769–773 (April 1997)

Transport phenomena in a quantum well containing a multivalent impurity are investigated on the basis of a model of strong Coulomb correlations. It is shown that as the iron content in the quantum well increases, the Coulomb correlations grow and produce ordering in the impurity system. As a result, the scattering of $2d$ electrons by them should weaken, and this should result in a substantial increase in the mobility of $2d$ electrons. [S1063-7826(97)00207-X]

1. INTRODUCTION

Dilute magnetic semiconductors (DMS) in which the magnetic ion is iron — $A_{1-x}Fe_xB$ — have attracted considerable interest in recent years. Many experiments performed thus far have shown that most physical properties of DMS are determined by the position of the Fe^{2+} states relative to the conduction band bottom.[1] The Fe^{2+} ions are neutral donors, whose levels lie in the conduction band 210 meV from the bottom. At a low iron content, all Fe^{2+} ions autoionize, transforming into Fe^{3+} ions. This process continues until the Fermi energy reaches the donor level. As the iron content increases further, only some donors are ionized. In this case, a mixed system of $3d^5$ and $3d^6$ states of Fe is realized in the DMS. Our analysis of the mobility of the conduction electrons and thermomagnetic phenomena showed that for a sufficiently high iron content in DMS the Coulomb repulsion between the charged Fe^{3+} donors results in a strong correlation in their arrangement. This is manifested primarily in the dependence of the conduction-electron relaxation time τ on the energy ε.[2] This behavior of $\tau(\varepsilon)$ near the Fermi energy decisively affects the density dependence of thermal magnetic effects, resulting in a change in the signs of the Nernst–Ettingshausen effects[3] and the nonmonotonic dependence of the mobility on the content of iron atoms in the DMS.[2] Moreover, as was shown in Ref. 4, a new inelastic mechanism of conduction electron scattering, which is associated with charge exchange of the Fe^{2+} and Fe^{3+} iron ions in a scattering event, is realized in a system with mixed valence.

The possibility of the realization of a quantum well (QW), which contains two-dimensional charge carriers and impurities with variable valence, was first studied in Ref. 5. An example of such a structure is $Hg_{1-y}Cd_ySe/Hg_{1-x}Fe_xSe/Hg_{1-y}Cd_ySe$ with the appropriate choice of the composition parameter y. Such structures can be obtained experimentally by molecular-beam epitaxy. For example, growth of two-dimensional systems based on HgSe:Fe was reported in Ref. 6. Analysis of the experimental data showed that in such two-dimensional systems the Coulomb correlations in the system of impurities with mixed valence are very strong.

Here we shall examine, on the basis of the model in Ref. 2 the transport phenomena in a QW containing impurity Fe. We shall study the dependence of the conduction electron density on the width of the QW and the doping level. We shall examine the effect of mixed-valence impurities on the momentum relaxation of $2d$ electrons.

2. EQUATION OF ELECTRICAL NEUTRALITY; STABILIZATION OF THE CONDUCTION ELECTRON DENSITY

We shall study a QW of width W_z, which, for simplicity, we assume to be infinitely deep. In this case the wave functions of the two-dimensional electrons have the standard form

$$\Psi_\nu(\mathbf{R}_j,z_j)=\Psi_{\mathbf{k}L}(\mathbf{R}_j,z_j)=\frac{1}{(L_xL_y)^{1/2}}\exp(i\mathbf{k}\mathbf{R}_j)\,\phi_L(z_j). \tag{1}$$

Here $\phi_L(z)$ is the envelope of the wave function

$$\phi_L(z_j)=(2W_z)^{1/2}\sin(Lz/W_z+L\pi/2);$$
$$z\in[-W_z/2;W_z/2],$$
$$\mathbf{R}=(x,y);\quad \nu=k,L\quad L=1,2,3, \tag{2}$$

where L characterizes the number of the quantum-well level which can be realized in the QW.

We assume that the dispersion relation for the $2d$ conduction electrons is quadratic and isotropic

$$\varepsilon_\nu=\varepsilon_{kL}=\frac{\hbar^2k^2}{2m}+E_L,\quad E_L=E_0L^2,\quad E_0=\frac{\pi^2\hbar^2}{2mW_z^2}, \tag{3}$$

where E_L is the energy of the quantum-well level, and m is the effective mass of the electron. (Taking into account the finite depth of the quantum well, just as the nonparabolicity of the conduction band, does not result in any qualitative changes in the calculations.)

To analyze the changes in the transport coefficients as a function of the iron impurity density, it is necessary to determine the Fermi energy from the electric-neutrality equation. Since the $2d$ conduction electron density in our situation is determined by the donor density (Fe^{3+}) in the QW, it is obvious that the electric-neutrality equation has the form

$$N_e=W_zN(Fe^{3+})=W_z[N(Fe)-N(Fe^{2+})], \tag{4}$$

where the conduction electron density is

 1063-7826/97/070651-04$10.00

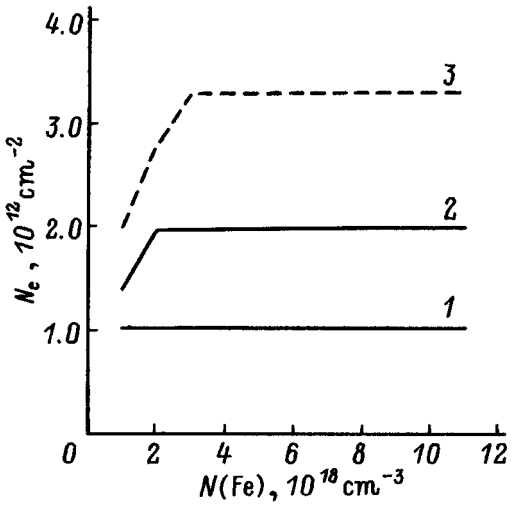

FIG. 1. $2d$-electron density versus the iron content in QWs of different widths W, Å: *1* — 50, *2* — 70, *3* — 90.

$$N_e=\frac{1}{L_xL_y}\int_0^\infty \rho(\varepsilon)f(\varepsilon)d\varepsilon. \tag{5}$$

Here $\rho(\varepsilon)$ is the density of states in the conduction band and $f(\varepsilon)$ is the Fermi distribution function. To calculate the density of the electron-occupied (neutral) donors

$$N(\mathrm{Fe}^{2+})=\int_0^\infty \rho_{\mathrm{Fe}}(\varepsilon)f(\varepsilon)d\varepsilon, \tag{6}$$

it is necessary to know the density of states $\rho_{\mathrm{Fe}}(\varepsilon)$. The ground state of the iron donors can be assumed to be[7]

$$\rho_{\mathrm{Fe}}(\varepsilon)=N_{\mathrm{Fe}}\delta(\varepsilon-\varepsilon_{\mathrm{Fe}}). \tag{7}$$

For sufficiently high densities N_{Fe} in the QW the expression (7) is a rough approximation, since it disregards the natural and density-induced broadening of the level. However, it should be noted that, in practice, calculations employing a constant value of $\rho_{\mathrm{Fe}}(\varepsilon)$ in the range of the finite width yield the same results as the expression (7).

The Fermi energy E_F and the conduction electron density N_e curves calculated from the electric-neutrality equation (Fig. 1), just as in the case of bulk crystals, show that the Fermi level and conduction electron density stabilize near the resonance donor level. However, in contrast to bulk crystals, where E_F and N_e stabilize at iron ion density $N(\mathrm{Fe})=4.5\times10^{18}$ cm^{-3}, the situation is entirely different in two-dimensional structures. Stabilization occurs when the Fermi level reaches the donor level of iron, but the conduction electron density at which this will occur depends strongly on the width of the QW, i.e., on the position of the quantum-well level (or levels) relative to the resonance donor level of iron. If one quantum-well energy level is realized in the QW, then the conduction electron density at which the Fermi level stabilizes is determined by the expression

$$N_e=[E_d-E_0]\frac{m}{\pi\hbar^2}. \tag{8}$$

Since the spatial correlations in the system of ions Fe^{3+} increase with the density of neutral centers Fe^{2+}, i.e., with increasing free locations for redistribution of electrons in a sysetm with mixed valence. It is obvious that the QW width should also have a strong effect on the degree of correlation and hence on the momentum relaxation of the $2d$ electrons.

3. ELECTRON RELAXATION TIME WITH ALLOWANCE FOR CORRELATIONS

We shall treat the system of iron ions Fe^{3+}–Fe^{2+} in a QW as a binary alloy consisting of charged Fe^{3+} and neutral Fe^{2+} centers. We restrict the discussion below to the scattering of electrons only by ion pairs Fe^{3+}–Fe^{3+}, whose distributions are correlated. This case is of greatest interest.

The degree of spatial correlations in the system of charged iron ions is determined by the structure factor $S(\mathbf{q})$, which depends on the iron density and temperature. The structure factor can be expressed in terms of the pair correlation function $g(r)$ for the Fe^{3+} ions as[3]

$$S(q)=1+4\pi N(\mathrm{Fe}^{3+})\int_0^\infty [g(r)-1]\frac{r\sin(qr)}{q}dr. \tag{9}$$

To determine the structure factor in the region of strong Coulomb correlations, it is necessary to solve a nonlinear integral equation for the pair correlation function $g(r)$. This problem has been solved in the Percus–Yevick approximation for a model system of hard spheres.[8] The calculations of the thermodynamic and transport characteristics of strongly correlated systems, such as liquid metals and alloys, performed in this approximation, agree well with the Monte Carlo results. An analysis of the concentration dependence of the mobility showed[2] that a complete analogy exists between the correlation properties of ions in a liquid and the correlation properties of charged donors in HgSe:Fe. The structure and properties of the liquids are determined mainly by the repulsive part of the ion-ion interaction potential,[7] which can be approximated, to good accuracy, by a hard-sphere potential.

Expressing the structure factor $S(q)$ in terms of the Fourier transform of the direct correlation function $C(q)$, we have

$$S(q)=\{1-N(\mathrm{Fe}^{3+})C(q)\}^{-1}, \tag{10}$$

where

$$C(q)=\frac{4\pi d^3}{u^3}\left\{\left[\alpha+2\beta+4\gamma-\frac{24\gamma}{u^2}\right]\sin u+\left[\frac{2}{u}(\beta-6\gamma)-(\alpha+\beta+\gamma)u-\frac{24\gamma}{u^3}\cos u\right.\right.$$
$$\left.\left.+\frac{24\gamma}{u^3}-\frac{2\beta}{u}\right\},\quad u=dq, \tag{11}$$

and

$$\alpha=\frac{(1+2\eta)^2}{(1-\eta)^4},\quad \beta=\frac{6\eta(1+0.5\eta)}{(1-\eta)^4},\quad \gamma=0.5\alpha\eta. \tag{12}$$

Here η is the packing parameter, which determines the degree of correlation in the arrangement of the hard spheres

$$\eta = \pi d^3 N(\mathrm{Fe}^{3+})/6. \tag{13}$$

At $T=0$ the packing parameter is determined by an equation which is valid for the case of strong correlation of the Fe^{3+} ions:[2]

$$\eta[N(\mathrm{Fe}^{3+})] = \eta_L\left[1-\exp\left[\frac{\eta N(\mathrm{Fe})}{\eta_L N(\mathrm{Fe}^{3+})}\right]\right]. \tag{14}$$

For a strongly correlated liquid $\eta_L = 0.45$. The inequality $\eta \ll 1$ will correspond to a weakly correlated gas, and in the limit $\eta \to 0$ the scattering centers are completely disordered and $S(q)=1$.

To calculate the conduction electron relaxation rate τ^{-1} for conduction electrons scattered by charged correlated centers, it is convenient to employ the Kubo–Mori formalism[9], which yields

$$\tau^{-1} = (\mathbf{J},\mathbf{J}^+)_0^{-1}(\mathbf{J}_V\mathbf{J}_V^+)^{\omega=0}. \tag{15}$$

Here $\mathbf{J}$ are the two-dimensional charge-flow operators of the $2d$ electrons

$$\mathbf{J} = \sum_k e(\hbar k/m)a_{\mathbf{k}}^+ a_{\mathbf{k}}, \quad \mathbf{J}_V = \frac{1}{i\hbar}[J, H_{eV}], \tag{16}$$

where H_{eV} is the interaction Hamiltonian of $2d$ electrons with three-dimensional impurities

$$H_{eV} = \sum_{\mathbf{k},\mathbf{k}'} u(\mathbf{k}'/\mathbf{k})a_{\mathbf{k}}^+ a_{\mathbf{k}},$$

$$u(\mathbf{k}'/\mathbf{k}) = \sum_{\mathbf{q}} G_{\mathbf{q}}\langle \mathbf{k}'|e^{i\mathbf{q}\mathbf{r}}|\mathbf{k}\rangle \rho_{-\mathbf{q}}. \tag{17}$$

Here $G_{\mathbf{q}}$ is the Fourier transform of the scattering potential $U(\mathbf{r})$, (A,B) are correlation functions

$$(A,B(t))^{\omega} = \int_{-\infty}^{0} dt e^{t(\varepsilon - i\omega)}(A,B(t)), \quad \varepsilon \to +0,$$

$$(A,B(t)) = \int_0^1 d\lambda \langle (A, B(t+i\hbar\beta\lambda))\rangle_0, \quad \beta^{-1} = T; \tag{18}$$

and T is the temperature expressed in energy units. The index 0 in the correlation function means that the correlation function is calculated in the zeroth approximation in the interaction with the scatterers. Calculating the commutator and the correlation functions, we represent the expression for the relaxation rate in the form

$$\tau^{-1} = \frac{\hbar}{(L_x,L_y)}\frac{N(\mathrm{Fe}^{3+})}{mN_e T}\sum_{\mathbf{q}} q_x^2 S(q) G_q^2 \sum_{\nu\nu'} |\langle \nu'|e^{i\mathbf{q}\mathbf{r}}|\nu\rangle|^2 \times f(\varepsilon_{\mathbf{k}})[1-f(\varepsilon_{\mathbf{k}})]\delta(\varepsilon_{\mathbf{k}'}-\varepsilon_{\mathbf{k}}), \tag{19}$$

where the matrix element in the expression (19) is given by

$$\langle \nu'|e^{i\mathbf{q}\mathbf{r}}|\nu\rangle = \langle \mathbf{k}'|e^{iq_\perp r_\perp}|\mathbf{k}\rangle\langle L'|e^{iq_z z}|L\rangle; \quad q_\perp = (q_x, q_y).$$

Next, according to Ref. 10,

$$A_L = \sum_{q_z} |\langle L'|e^{iq_z z}|L\rangle|^2 = L_z\int_{-\infty}^{\infty}\varphi^4 L(z)dz = 3/2. \tag{20}$$

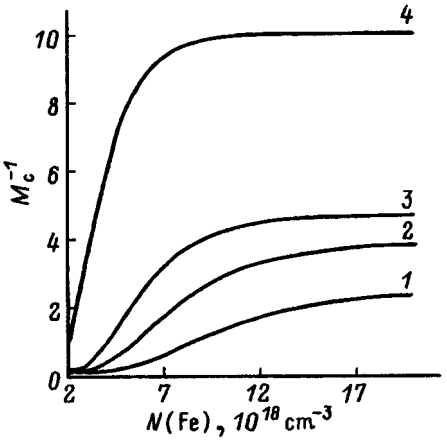

FIG. 2. M_c^{-1} ($\mu \sim M^{-1}$) versus the iron content in QWs of different width W, Å: *1* — 90, *2* — 70, *3* — 65, *4* — 50.

We now switch in Eq. (19) from summation over q and k to integration, and taking into account the fact that in our situation the electron gas is strongly degenerate, after simple calculations we obtain

$$\tau^{-1} = \frac{8\pi N(\mathrm{Fe}^{3+})W_z m e^4}{\hbar^3 k_F b^2 \chi^2} M_c,$$

$$M_c = \int_0^1 dx \frac{x^2 S(2k_F x)}{\left(x^2 + \dfrac{Q_s}{2k_F}\right)^2 [1-x^2]^{1/2}};$$

$$Q_s = \frac{1}{br_s}, \quad b = 1 + \frac{5W_z}{4\pi^2 r_s}. \tag{21}$$

Here $\tau_s = a_B/2$ is the screening length (a_B is the Bohr radius), and χ is the permittivity of the medium.

This expression makes it possible to analyze the role and the effect of Coulomb correlations in a system of charged centers on momentum relaxation and therefore on the mobility of two-dimensional charge carriers.

The results of a numerical analysis of the quantity $M_c \sim \mu^{-1}$ are shown in Fig. 2. As follows from these calculations, the effect of Coulomb correlations in a system of charged donors is stronger in narrower QWs. This effect is attributable to the fact that in wider QWs the quantum-well energy level lies closer to the donor level of iron. For this reason, the Fermi level determined by the $2d$-electron density reaches its maximum value earlier ($E_d = E_F$) as the density of iron atoms in the QW increases. The distribution of charged donors in this case is random. A further increase of the iron atom content, where neutral iron atoms Fe^{2+} appear in the impure system, gives rise to the correlation interaction-induced effects in the system of impurities, which lead to the appearance of ordered charged impurity centers. The appearance of such ordering results in a substantial weakening of the scattering in the system of charged iron ions. It is natural to assume that this effect should result in a higher mobility of $2d$ electrons in the QW. The mobility will increase until the ordered centers in the impurity system reach their maximum value, which is determined by the order parameter. The packing parameter η reaches the maxi-

mum value $\eta = 0.45$ in the limit $N(\mathrm{Fe}) \gg N\ [(\mathrm{Fe}^{3+})]$. In this case a system of Fe^{3+} ions with a high iron content near low temperatures becomes similar to a liquid. The scattering of $2d$ electrons by the correlated system of impurities will then no longer depend on the iron content in the QW, and the mobility should reach its maximum value.

Finally, it is definitely of interest to examine the energy dependence of the relaxation time near the Fermi level. Knowledge of such dependences is helpful for studying thermomagnetic effects in our systems. Indeed, thermomagnetic effects are very sensitive to a change in the electron scattering mechanism. The dominant scattering mechanism under the given conditions can be determined according to the sign of the effect (for example, the sign of the Nernst–Ettingshausen effect).[11]

Calculations of the dependence of the relaxation time for systems with different iron content and therefore with different degree of ordering in a system of charged impurity centers showed that the Coulomb correlations strongly influence the energy dependence of the relaxation time. In the region of weak Coulomb correlations, the time derivative of the energy relaxation is positive and changes sign at the transition into the region of strong correlations. This behavior of the relaxation time near the Fermi energy should also influence the density dependence of the thermomagnetic coefficients. We hope to study this effect in greater detail in subsequent studies.

Analysis of the relaxation time of two-dimensional electrons in QWs containing impurities with a variable valence has shown that the presence of strong Coulomb correlations in a system of mixed-valence impurities, just as in bulk crystals, should result in a substantial weaking of electron scattering by them. This effect results in higher conduction electron mobility in the QW. The energy dependence of the relaxation time at low temperatures in the region of strong Coulomb correlations should manifest itself in unusual dependences of the thermomagnetic coefficients on the content of iron atoms in the QW.

This work was supported by INTAS under Grant No. 93-3657.

[1] C. Skierbisszewski, Z. Wilamowski, and J. Kossut, Semicond. Sci. Technol. **8**, S 22, (1993).
[2] I. G. Kullev, I. I. Lyapilin, and I. M. Tsidil'kovskiĭ, Zh. Éksp. Teor. Fiz. **102**, 1652 (1992) [Sov. Phys. JETP **75**, 893 (1992)].
[3] I. G. Kullev, I. I. Lyapilin, A. T. Lonchakov, and I. M. Tsidil'kovskiĭ, Zh. Éksp. Teor. Fiz. **103**, 1447 (1993) [JETP **76**, 707 (1994)].
[4] I. G. Kullev, I. I. Lyapilin, A. T. Lunchakov, and I. M. Tsidil'kovskiĭ, Zh. Éksp. Teor. Fiz. **106**, 1205 (1994) [JETP **79**, 653 (1994)].
[5] M. von Ortenberg, O. Portugal, W. Dobrowolski, A. Mycielski, R. Galazka, and F. Herlach, J. Phys. C: Sol. State Phys. **21**, 5392 (1988).
[6] Th. Widmer, D. Shikora, G. Hendorfer, S. Luther, W. Jantsch, K. Lischka, and M. V. Ortenberg, in *II–VI Compounds and Semimagnetic Semiconductors, 14th International Workshop on Semimagnetic Semiconductors*, Linz, Austria, 1994, p. 395.
[7] F. S. Pool, J. Kossut, U. Debska, and R. Reifenberger, Phys. Rev. B **35**, 3900 (1987–I).
[8] J. M. Ziman, *Models of Dusorder: The Theoretical Physics of Homogeneously Disordered Systems*, Cambridge University Press, N. Y., 1979 [Russian transl., Mir, Moscow, 1982].
[9] R. Kubo, J. Miyake, and H. Haschitsume, Solid State Phys. **17**, 269 (1965).
[10] K. Vijay, L. Arora, G. Fawry, and N. Awad, Phys. Rev. B **23**, 5570 (1981).
[11] I. M. Tsidil'kovskiĭ, *Thermomagnetic Phenomena in Semiconductors*, Academic Press, N. Y., 1962 [Russian orig., Nauka, Moscow, 1960].

Translated by M. E. Alferieff

Charge-carrier lifetime in $Hg_{1-x}Cd_xTe$ ($x=0.22$) structures grown by molecular-beam epitaxy

A. V. Voĭtsekhovskiĭ, Yu. A. Denisov, and A. P. Kokhanenko

Siberian Physicotechnical Institute, 634050 Tomsk, Russia

V. S. Varavin, S. A. Dvoretskiĭ, V. T. Liberman, N. N. Mikhailov, and Yu. G. Sidorov

Institute of Semiconductor Physics, Siberian Branch of the Russian Academy of Sciences, 630090 Novosibirsk, Russia

(Submitted July 1, 1996; accepted for publication October 25, 1996)
Fiz. Tekh. Poluprovodn. **31**, 774–776 (July 1997)

Measurements of the charge carrier lifetime in epitaxial structures based on narrow-gap $Hg_{1-x}Cd_xTe$ ($x=0.22$), grown by molecular-beam epitaxy with pulsed excitation using radiation at different wavelengths, are reported. It is shown that in *p*-type epitaxial films the lifetime is determined by the Auger recombination mechanism at temperatures corresponding to the impurity conductivity, and for *n*-type epitaxial films recombination via local centers is characteristic. © *1997 American Institute of Physics.* [S1063-7826(97)00307-4]

The material $Hg_{1-x}Cd_xTe$ grown by molecular-beam epitaxy (MBE) is characterized by a high degree of uniformity of the properties within large enough dimensions of the substrate. In addition, it is possible to realize desired doping and composition profiles. This makes it possible to use this material to produce multielement semiconductor radiation detectors for signal processing directly in the focal region.[1–3] The most important parameter of the photosensitive material is the charge-carrier lifetime, which ultimately determines its photoelectric and fluctuation characteristics.

It should be noted that there are now only few papers in which the results of measurements of the charge-carrier lifetime in MBE $Hg_{1-x}Cd_xTe$ films are reported.[4–6] For this reason, it is of interest to perform measurements of the photocarrier lifetime in epitaxial material and analyze the possible recombination mechanisms in the temperature range corresponding to extrinsic conductivity of the semiconductor compound. In this paper we report the results of an experimental study of the recombination properties of epitaxial *p*- and *n*-type $Hg_{1-x}Cd_xTe$ ($x=0.22$).

Epitaxial layers of $Hg_{1-x}Cd_xTe$ were grown by MBE at a temperature of 190 °C.[7] The substrates consisted of CdTe and GaAs plates with (112) and (103) orientation and CdTe and CdZnTe buffer layers. To obtain ρ-type films, the material was annealed[8] and the composition was determined with an automated ellipsometer during film growth.[9] To decrease recombination on the surface of the film and near the interface with the substrate, variable-gap structures with the corresponding composition profile over the thickness were grown. A composition corresponding to $x=0.3$ was realized in the surface (wide-gap) layer, a composition $x=0.21-0.22$ (narrow-gap layer) was realized in the central part of thickness 5–11 μm, and a less than 1- μm-thick (variable-gap) layer with $x=0.5$ was grown near the buffer layer. The density and mobility of the charge carriers in the films were measured at $T=80$ K by the van-der-Pauw method. The photocarrier lifetime was measured from the kinetics of the photoconductivity signal which accompanied the generation of nonequilibrium charge carriers by optical radiation pulses.[10] Radiation with $\lambda=10.6$ μm was used to generate photocarriers in the volume of the film and radiation with $\lambda=0.9$ and 1.5 μm was used to generate photocarriers in the surface layer.

The typical temperature dependence of the photocarrier lifetime τ in the temperature range T corresponding to the extrinsic conductivity for a *n*-type sample (sample 4) is shown in Fig. 1. It should be noted that the temperature dependences of the lifetime and photoresponse signal (see the inset in Fig. 1) are similar for excitation with 10.6 and 0.9- μm radiation. A small characteristic feature is observed in the temperature range 120–150 K, where the function $\tau(T)$ for $\lambda=0.9$ μm increases more slowly than the function for $\lambda=10.6$ μm, apparently because of the surface recombination that accompanies the short-wavelength excitation. At the same time, the temperature dependence of the photoresponse signal with increasing temperature characteristically decreases, and the curve shifts by a small amount in the direction of high temperatures as the $\lambda=10.6$-μm radiation is replaced by $\lambda=0.9$-μm radiation. For *p*-type samples (samples 2), the temperature dependences of the charge-carrier lifetime and the photoresponse signal in the case of 10.6 and 0.9-μm excitation are shown in Fig. 2. We see that the presence of two components is characteristic of the temperature dependence of the lifetime $\tau(T)$ in the case $\lambda=10.6$ μm: fast and slow components. The fast component varies from 10 to 160 ns in the temperature range 80–170 K and, correspondingly, the slow component varies from 1 to 10 μs. For $\lambda=0.9$ μm the function $\tau(T)$ is characterized by the presence of a ''plateau'' at low temperatures. The substantial difference in the form of the temperature dependence of the photoresponse for the cases studied is interesting. For $\lambda=0.9$ μm the curve of the photoresponse versus temperature has a maximum in the region 90–100 K. A similar photoresponse kinetics is also observed for *n*-type samples (sample 3), but in this case for excitation with $\lambda=0.9$ μm. Just as in the preceding case, here there are two components in $\tau(T)$ and an extremum at $T=120$ K. We note that, as a

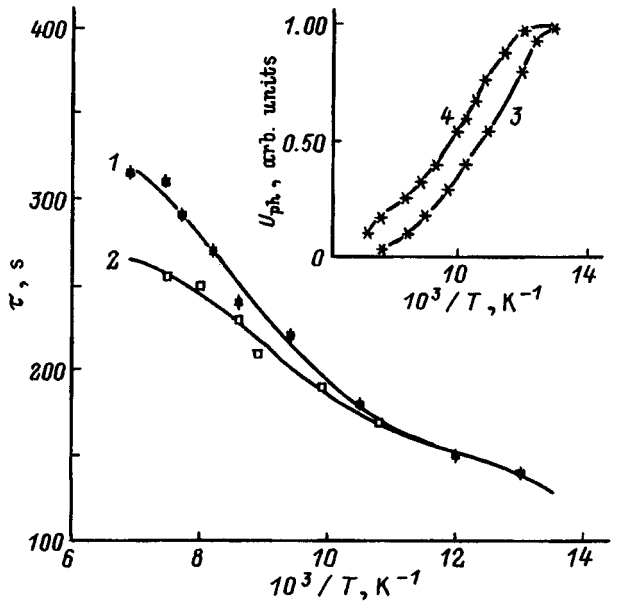

FIG. 1. Temperature dependences of the charge carrier lifetime τ (*1*, *2*) and the photoresponse signal $U_{\rm ph}$ (*3*, *4*) for an epitaxial film (sample 4). The curves were measured during radiation-induced excitation with $\lambda = 10.6$ μm (1, 3) and $\lambda = 0.9$ μm (*2*, *4*).

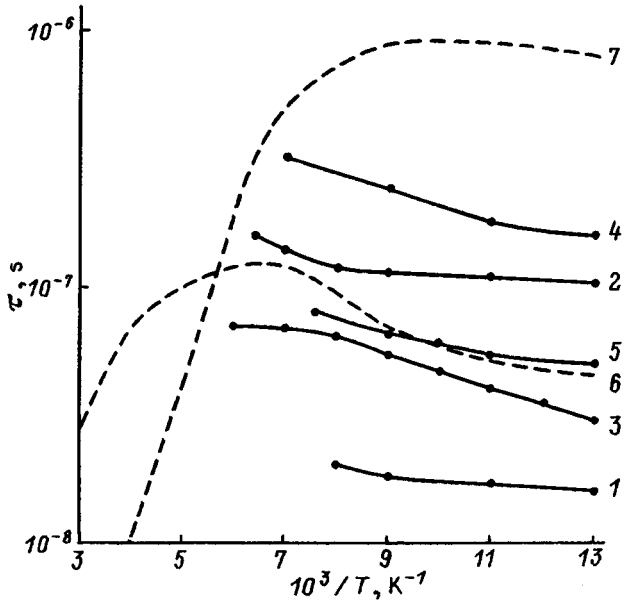

FIG. 3. Temperature dependences of the charge carrier lifetime for the experimental epitaxial films: experimental (*1–5*) and computed (*6*, *7*). The numbers on the curves correspond to the numbers of the samples with the following parameters: *1* — $x = 0.208, p = 2.2\times10^{15}$ cm^{-3}; *2* — $x = 0.224$, $p = 6.5\times10^{15}$ cm^{-3}; *3* — $x = 0.223$, $n = 1.2\times10^{15}$ cm^{-3}; *4* — $x = 0.210$, $n = 6.2\times10^{15}$ cm^{-3}; *5* — $x = 0.225$, $p = 1.2\times10^{15}$ cm^{-3}. Post-growth anneal regime — temperature T_a/time t_a: *2* — 200 °C/100 h; *5* — 200 °C/120 h. *6*, *7* — see explanation in the text.

rule, for three samples in which the temperature dependence of the resistance with an extremum is observed, the temperature dependence of the photoresponse is typically similar. This should have been expected, since the temperature dependences of the photoresponse signal are determined not only by the dependence $\tau(T)$, but also by the temperature dependence of the conductivity of the sample (photoresponse $\sim\Delta\sigma/\sigma_0$, where σ_0 is the dark conductivity, $\Delta\sigma = \eta P\tau/h\nu$ is the change in the conductivity under the action of the radiation, η is the quantum efficiency, P is the power of the incident radiation, and $h\nu$ is the photon energy). The variation of the photoresponse as a function of temperature is influenced by the dependence $\eta(\lambda)$, since the maximum absorption wavelength decreases with increasing temperature and band gap E_g and, correspondingly, the absorption coefficient decreases by 10.6 μm. The absorption at $\lambda = 0.9$ μm occurs in the surface layer of the film, since the absorption coefficient is large in this case. This can explain the different behavior of the photoresponse curves for the cases of excitation with $\lambda = 10.6$ and 0.9 μm with temperature dependences $\tau(T)$ of similar form.

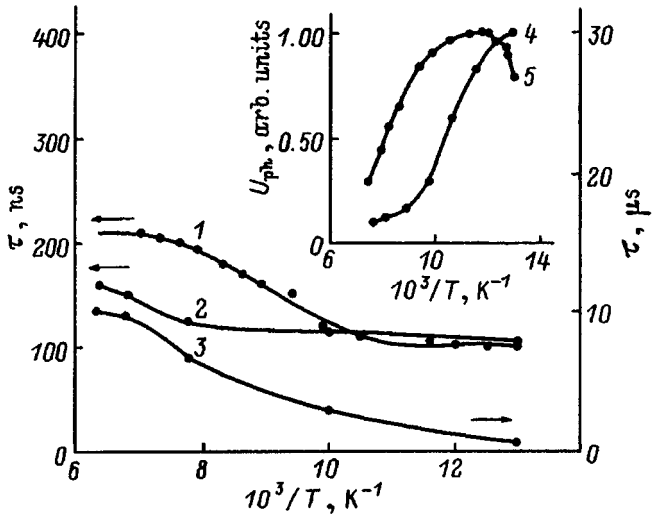

FIG. 2. Temperature dependences of the charge-carrier lifetime τ (*1–3*) and photoresponse signal $U_{\rm ph}$ (*4*, *5*) for *p*-type epitaxial films (sample 2) measured during radiation-induced excitation with $\lambda = 10.6$ μm (*2–4*) and $\lambda = 0.9$ μm (*1*, *5*). *2* — Fast, *3* — slow components.

To interpret the recombination mechanisms, we turn to Fig. 3, which shows the experimental temperature dependences of the charge-carrier lifetime of the experimental samples with $\lambda = 10.6$ μm, corresponding to volume excitation of photocarriers. This figure also shows the computed curves $\tau(T)$ for Auger recombination mechanisms in *n*- and *p*-type $Hg_{1-x}Cd_xTe$ with $x = 0.2$ (curves *7* and *6*, respectively) with charge carrier densities $n = 1\times10^5$ and $p = 1\times10^{16}$ cm^{-3}, respectively. We see that for *p*-type samples (samples 2 and 5) the most likely recombination mechanism in the range of temperatures corresponding to extrinsic conductivity is the Auger recombination accompanying hole collisions with a hole making a transition from the heavy-hole band into the light-hole band.[11] For *n*-type samples (samples 3 and 4), as the calculations show, the interband recombination mechanism of the Auger type or radiative mechanisms make a very small contribution.[11,12] The most likely mechanism is recombination via local centers. The presence of two components for the lifetime could be due, for *p*-type samples, to the contribution of mechanisms associated with recombination centers, together with interband mechanisms, to the recombination process. At the

same time, for *n*-type samples the presence of two components in the lifetime can be explained by the presence of recombination centers with a sharp asymmetry of the electron and hole trapping cross sections.

A substantial difference of the results obtained from the data in Ref. 5 is the fact that in the *p*-type experimental samples the interband Auger mechanism of charge-carrier recombination is realized in the temperature range corresponding to extrinsic conductivity. This is apparently due to the post-growth thermal treatment of the *n*-type epitaxial films, in which recombination was observed via centers with radiation near the center of the band gap, just as in Refs. 5 and 6. The decrease in the defect density in the films after annealing makes it possible to obtain lifetimes limited by interband Auger recombination. This fact is supported by the temperature dependence $\tau(T)$ for the *p* -type sample 1, prepared with no annealing, for which lower (compared with the values computed for Auger recombination) charge carrier lifetimes are characteristic.

[1] A. V. Voĭtskhovskiĭ and V. N. Davydov, *Photoelectric MIS Structures Based on Narrow-Gap Semiconductors* [in Russian], Radio i svyaz', Tomsk, 1990, p. 382.

[2] V. A. Kemarskiĭ and N. A. Kul'chitskiĭ, in *Review Information* [in Russian], No. 5207, Part 2, p. 3 (1990).

[3] A. V. Voĭtsekhovskiĭ, I. I. Izhnin, N. A. Kul'chitskiĭ, and V. A. Kemarskiĭ, in *Electronics Abroad* [in Russian], Central Scientific-Research Institute ''Élektronika,'' Moscow, 1992, No. 12, p. 3.

[4] V. C. Lopes, A. G. Syllaics, and N. C. Chen, Semicond. Sci. Technol. **8**, 824 (1993).

[5] M. E. de Souza, M. Boukerche, and J. P. Faurie, J. Appl. Phys. **68**, 5195 (1990).

[6] S. N. Shin, J. M. Arias, M. Zandian, J. G. Pasko, and R. E. De Wames, Appl. Phys. Lett. **59**, 2718 (1991).

[7] V. S. Varavin, Yu. G. Sidorov, V. G. Remesnik, S. I. Chikichev, and I. E. Nis, Fiz. Tekh. Poluprovodn. **28**, 577 (1994) [Semiconductors **28**, 348 (1994)].

[8] K. N. Svitashev, S. A. Dvoretsky, Yu. G. Sidorov, V. A. Shvets, A. S. Mardezhov, I. E. Nis, V. S. Varavin, V. I. Liberman, and V. G. Remesnik, Cryst. Res. Technol. **29**, 931 (1994).

[9] V. N. Ovsyuk, V. V. Vasil'ev, T. I. Zakhar'rash, V. G. Remesnik, S. V. Studenikin, N. Kh. Suslyakov, N. Kh. Talipov, Yu. G. Sidorov, S. A. Dvoretskiĭ, N. N. Mikhaĭlov, V. I. Liberman, and V. S. Varavin, Fiz. Tekh. Poluprovodn. **2**, 193 (1996) [Semiconductors **2**, 109 (1996)].

[10] A. V. Voitsekhovskiĭ and Yu. V. Lilenko, Phys. Status Solidi A **67**, 381 (1981).

[11] A. V. Voĭtsekhovskiĭ, Izv. Vyssh. Uchebn. Zaved., Fiz. **37**, 99 (1994).

[12] A. V. Voĭtsekhovskiĭ and Yu. V. Lilenko, VINITI, No. 5200-81 Dep., p. 36 (1981).

Translated by M. E. Alferieff

Frenkel'–Poole effect for boron impurity in silicon in strong warming electric fields

A. M. Kozlov and V. V. Ryl'kov

Institute of Radio Engineering and Electronics, Russian Academy of Sciences, 141120 Fryazino, Russia
(Submitted May 23, 1996; accepted for publication October 25, 1996)
Fiz. Tekh. Poluprovodn. **31**, 777–780 (July 1997)

A method based on measurement of the thermally stimulated conductivity of a weakly compensated semiconductor, which is doped with a deep impurity and which contains an impurity component that is shallower than the main component, has been developed for investigating the Frenkel'–Poole effect. The results of an investigation of the thermally stimulated conductivity of Si:Ga samples with gallium density $N_A=(2-3)\times10^{18}$ cm^{-3} and low accompanying impurity content ($\leqslant10^{13}$ cm^{-3}) are reported. The conductivity was measured after extrinsic photoexcitation of samples heated at a rate $\beta=0.6$ K/s in the temperature range $T=4.2-24$ K in electric fields $E=20-1000$ V/cm. It is shown that the maximum on the curves of the thermally stimulated conductivity is due to the thermally stimulated emptying of the boron impurity and shifts to lower values of T as E increases. The decrease of the ionization energy of impurity B in an electric field, which turns out to be somewhat weaker than the field according to the Frenkel'–Poole model for singly charged Coulomb centers, is found from the shift of the maximum. © *1997 American Institute of Physics.* [S1063-7826(97)00407-9]

Study of the Frenkel'–Poole effect in doped semiconductors is impeded, as we know, by heating of the charge carriers in an electric field and by impact ionization of the impurities. For this reason, this effect is usually studied on the basis of the change in the conductivity in pulsed electric fields, and it has been observed repeatedly in the case of ionization of deep impurities,[1–4] whereas for shallow impurities it has been observed only recently.[5] In addition, the measurements in Ref. 5 were performed under conditions of a strong fluctuation potential, when the heating of the charge carriers is weakened and the change in the ionization energy of the shallow impurity is determined not only by the external electric field but also by the random fields generated by the charged centers. In this paper we demonstrate that the Frenkel'–Poole effect can be investigated by measuring the thermally stimulated conductivity (TSC) of a weakly compensated semiconductor which is doped with a deep impurity[6] and which contains a shallow accompanying impurity. The approach is based on the fact that the impurity breakdown field is determined by the parameters of the dopant, while the TSC in the region of prebreakdown fields is sensitive only to the presence of the impurity. We shall show that under certain impact ionization conditions the impurity can be disregarded up to impurity breakdown fields. The change in the position of the maximum of the curve of the TSC as a function of temperature with increasing electric field is determined entirely by the Frenkel'–Poole effect.

For definiteness, we shall study the TSC for the example of a weakly compensated p-type semiconductor with doping level N_A and shallow acceptor impurity density $N_a \ll N_A$. Just as in the preceding work,[6] we assume that the accompanying impurity density N_a is less than the density N_d of the compensating donors. In this case, at a sufficiently low temperature, when the dark hole density $p_d \ll N_d$, all of the impurity as well as some of the dopant will be ionized, and the total density of ionized centers is $N_a^- + N_A^- = N_d$. Under photoexcitation of the semiconductor from the extrinsic absorption region, the filling of the accompanying impurity in warming electric fields will be controlled by photohole capture by ionized atoms of the impurity and impact ionization of neutral impurity centers. From the equality of the rates of these processes

$$\alpha_a^- N_a^- p = \alpha_{aI} N_{aS}^0 p \tag{1}$$

we find the density of filled impurity atoms under stationary conditions

$$N_{aS}^0 = N_a/(1+\alpha_{aI}/\alpha_a^-). \tag{2}$$

Here α_a^- is the hole capture coefficient of an ionized impurity center, p is the hole density with photoexcitation, and α_{aI} is the impact ionization coefficient of neutral impurity atoms.

One can see from the relations (1) and (2) that in warming electric fields the degree of filling of the impurity does not depend on the photoexcitation level. Comparing the rates of impact and optical ionization of neutral impurity centers, it is not difficult to show that this behavior is realized as soon as $\alpha_{aI} = \alpha_a^- K$, where K is the degree of compensation. In other words, in a weakly compensated semiconductor ($K \ll 1$) the expression (2) is valid in fields in which α_{aI} is still appreciably less than α_a^-.

After the photoexcitation is switched off, the conductivity relaxation in the sample, as a result of thermal and impact ionization of neutral impurity centers, is described by the kinetic equations

$$dp/dt = -p(\alpha_A^- N_A^- + \alpha_a^- N_a^-) + \gamma_T N_a^0 + p\alpha_{aI} N_a^0 + p\alpha_{AI} N_A^0, \tag{3}$$

$$dN_a^0/dt = p\alpha_a^- N_a^- - \gamma_T N_a^0 - p\alpha_{aI} N_a^0, \tag{4}$$

where α_A^- is the hole capture coefficient of ionized dopant atoms,

$$\gamma_T = N_\nu \alpha_a^- \exp(-\varepsilon_a/kT)$$

is the thermal generation coefficient, N_ν is the effective density of states in the valence band, k is Boltzmann's constant, α_{AI} is the impact ionization coefficient of neutral dopant centers, and ε_a is the impurity activation energy.

In fields less than the impurity breakdown field of the semiconductor, $\alpha_A^- N_A^- \gg \alpha_{AI} N_A^0$.[7] Furthermore, for $N_a \ll N_d$ the hole trapping in impurity levels can be ignored:

$$\alpha_A^- N_A^- \gg \alpha_a^- N_a^- .$$

Here we have taken into account the fact that at low temperatures the charge carrier trapping coefficients for attractive centers of the same type are approximately the same,[8] and

$$N_A^- \simeq N_d \gg N_a^- .$$

Under these conditions the expressions (3) and (4) simplify and for a linear heating law $T = T_0 + \beta t$ (T_0 is the initial temperature of the sample at which photoexcitation was performed, and β is the rate of heating) we obtain

$$p(T) = -\tau \beta dN_a^0/dT, \tag{5}$$

$$dN_a^0/dT = -\beta^{-1} \gamma_T N_a^0/(1 - \alpha_{aI} N_a^0 \tau), \tag{6}$$

where $\tau \sim 1/(N_d \alpha_A^-)$ is the hole lifetime. It follows from Eq. (6) that impact ionization effects can be ignored if $\alpha_{aI} N_a^0 \tau \ll 1$. Taking into account the relation (2), the maximum value of this quantity is

$$(\alpha_{aI} N_a^0 \tau)_{\max} = \alpha_{aI} N_{aS}^0 \tau < (N_a/N_d)(\alpha_a^-/\alpha_A^-),$$

i.e. for $N_a \ll N_d$ the effect of impact ionization on the TSC is negligible. In this case $p(T)$ has a maximum at a temperature T_m which is determined by the standard relation[9]

$$\frac{kT_m^2 \alpha_a^- N_\nu}{\beta \varepsilon_a} = \exp\left(\frac{\varepsilon_a}{kT_m}\right). \tag{7}$$

Therefore, for $N_a \ll N_d$ the change in the position of the maximum of the TSC curve in an electric field E is determined directly by the dependence of ε_a on E.

The experimental studies of the Frenkel'–Poole effect were performed on Si:Ga samples obtained by the zone melting method, with a doping level of $(2-3)\times 10^{16}$ cm^{-3} and residual impurity density less than or of the order of 10^{13} cm^{-3}. Previous studies of the TSC in these samples[6] showed that they can contain small quantities ($\simeq 10^{12}$ cm^{-3}) of boron accompanying impurity. Furthermore, samples with linear recombination kinetics, corresponding to the case $N_a \ll N_d$, were found by analyzing the increasing and decreasing branches of the TSC curve.[6]

The conductivity of the samples was measured after photoexcitation by IR semiconductor laser radiation ($\lambda = 5$ μm) with heating at a rate $\beta = 0.6$ K/s in the temperature range $T = 4.2-2.4$ K. The details of the measurement procedure are describe in Ref. 6. The maximum electric fields in the experiments ($\simeq 1000$ V/cm) did not exceed the impurity breakdown field ($\simeq 1500$ V/cm). We note that impurity breakdown of the Si:B samples with a close doping level and degree of compensation occurs in fields[10] $E \leqslant 300$ V/cm, i.e., at much lower average hole energies, taking into account the fact that the hole mobility in Si:B and Si:Ga are nearly identical under the same doping conditions.[11,12]

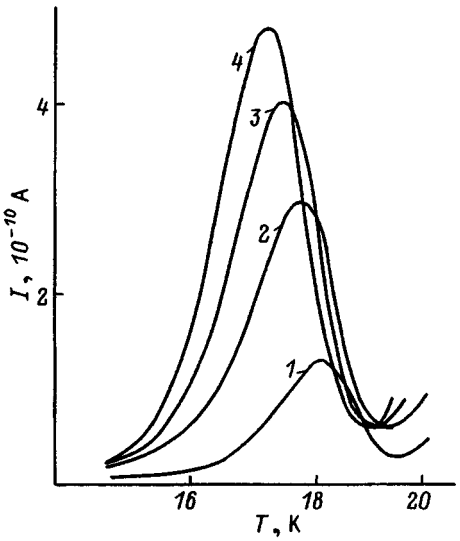

FIG. 1. Curves of the thermally stimulated current I for a sample with accompanying impurity density $N_a \ll N_d$ in different electric fields E, E/cm: *1* — 270, *2* — 540, *3* — 810, *4* — 1080.

The typical curves of the thermally stimulated current for a sample with Ga density $N_A \simeq 2.6\times 10^{16}$ cm^{-3} and boron density $N_a \simeq 1.5\times 10^{12}$ cm^{-3} (a method for determining N_a using this sample is presented in Ref. 6) in different electric fields are presented in Fig. 1. The observed shift of the curves in the direction of low temperatures indicates, according to Eq. (7), that the active energy of the boron impurity decreases with increasing electric field. One can also see that the maximum temperature shift $\Delta T_m = 0.9$K ($E = 1080$ V/cm) is small compared with the value $\Delta T_m = 18.07$ K at $E = 270$ V/cm. For this reason, to obtain the field dependence $\varepsilon_a(E)$, it is reasonable to employ an expansion of (7) in the small parameter $\Delta T_m/T_m$:

$$\varepsilon_a = \varepsilon_{a0} - \varepsilon_{a0} \frac{2T_{m0}k + \varepsilon_{a0}}{T_{m0}k + \varepsilon_{a0}} \left(\frac{T_{m0} - T_m}{T_{m0}} + \frac{T_{m0}k}{\varepsilon_{a0}} \ln \frac{\alpha_{a0}^-}{\alpha_a^-} \right). \tag{8}$$

The index 0 in Eq. (8) corresponds to the values of ε_a, T_m, and α_a^- in the initial field $E_0 = 270$ V/cm. The value of ε_{a0} can be determined from the half-width of the TSC curve, after which α_{a0}^- can be found[6] by using Eq. (7). At $E = 270$ V/cm for the present sample $\varepsilon_{a0} = 41.33$ meV and $\alpha_{a0}^- = 1.74\times 10^{16}$ cm$^{-3}\cdot$s^{-1} (Ref. 6). In Ref. 6 it was also shown that the change in α_a^-, which determines the hole thermal generation coefficient from neutral impurity centers [see Eqs. (3) and (4)], is due to delocalization in the electric field of highly excited impurity states. According to Ref. 12,

$$\alpha_{a0}^-/\alpha_a^- = (E/E_0)^{1/2}. \tag{9}$$

The computational results for ε_a as a function of $(E)^{1/2}$, using expressions (8) and (9), are presented in Fig. 2 (represented by the dots on curve *1*). A least-squares fit to a linear dependence gives

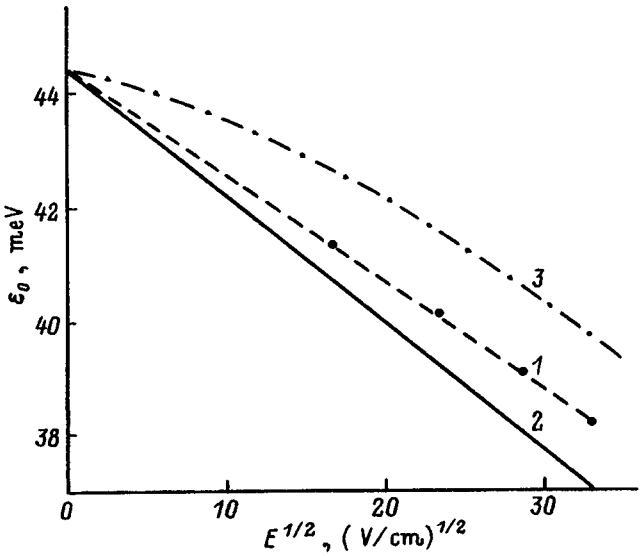

FIG. 2. Experimental (*1*) and computed (*2, 3*) curves of the activation energy ε_a versus $E^{1/2}$. The curves were obtained using Eqs. (11) (*2*) and (7) (*3*) from Ref. 13. The dashed curve represents the dependence of ε_a on $E^{1/2}$ obtained by a least-squares fit of the experimental dependence.

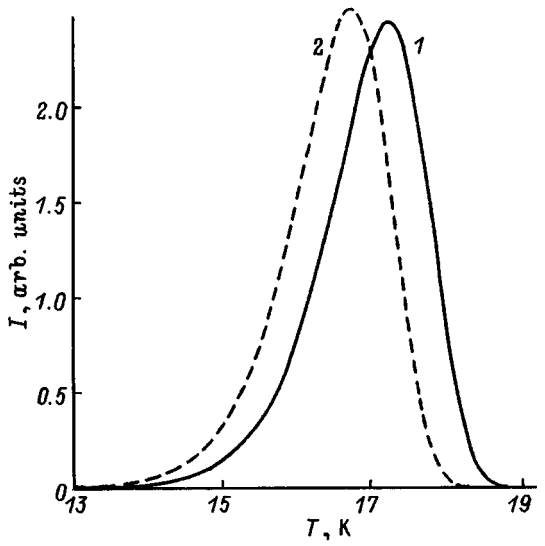

FIG. 3. Computed curves of the thermally stimulated conductivity in an electric field $E=1080$ V/cm for values of ε_a: *1* — Experimental, *2* — theoretical.

$$\varepsilon_a(E)=44.42-0.186(E)^{1/2}, \tag{10}$$

where ε_a is in meV, and E is in V/cm. According to Eq. (10), the activation energy in a zero field is $\varepsilon_a=44.42$ meV, which agrees very well with the data from optical measurements $\varepsilon_a=44.39$ (Ref. 14) and shows that the method developed is correct. On the other hand, the slope of the experimental curve is appreciably smaller (by 15%) than the slope of the theoretical curve (shown by the solid line in Fig. 2), which follows from the classical Frenkel'–Poole model for singly-charged Coulomb centers:[12]

$$\varepsilon_a(E)=\varepsilon_a(0)-2(e^3E/\varkappa)^{1/2}, \tag{11}$$

where $\varkappa$ is the permittivity. For Si $\varkappa=11.7$, which gives

$$\Delta\varepsilon=2(e^3E/\varkappa)^{1/2}=0.222E^{1/2}.$$

We note that the observed difference cannot be explained by impact ionization of boron, since it would account for a stronger temperature shift of the TSC curves and therefore to an observation of a sharper decrease of ε_a with increasing E.

Figure 3 also shows the computed TSC curves for experimental and theoretical values of ε_a in the field $E=1080$ V/cm. The shift of the maxima of the curves along the temperature axis is of the order of 0.5 K and is much greater in our case than the sensitivity of the TSU-1 thermometer to the relative change in temperature ($\Delta T\simeq 0.05$ K).

The weakening of the dependence $\varepsilon_a(E)$ is most likely attributable to the fact that the one-dimensional Frenkel'–Poole model disregards angular effects.[13] The decrease in ε_a with increasing **E** in the three-dimensional case can be estimated from the increase in the hole thermal emission rate γ_T in an electric field, using, for example, expression (7) from Ref. 13 for γ_T:

$$\Delta\varepsilon\simeq kT_m\ln(\gamma_T/\gamma_{T0}),$$

where γ_{T0} is the thermal emission rate in a zero electric field. The curve of ε_a versus $E^{1/2}$ obtained in this manner is shown in Fig. 2 (curve *3*). It is interesting to note that in this case the slope of the curve increases with E, but in strong fields it changes very little and is virtually identical to the slope of the experimental curve. In the interval of fields $E=900-1600$ V/cm the slope of the curve *3* changes in the range 0.181–0.187 meV $(\text{V/cm})^{-1/2}$, while the experimental value is 0.186 meV$(\text{V/cm})^{1/2}$.

We thank B. A. Aronzon and A. S. Vedeneev for a discussion and remarks. This work was supported by the Fund of the International Association INTAS under Grant 93-1403 and the Russian Fund for Fundamental Research under Grant 96-02-18429-a.

[1] T. E. Hartman, J. C. Blair, and R. Bauer, J. Appl. Phys. **37**, 2468 (1966).
[2] A. G. Dmitriev, D. N. Nasledov, and B. V. Tsarenkov, Fiz. Tekh. Poluprovodn. **6**, 345 (1972) [Sov. Phys. Semicond. **6**, 293 (1972)].
[3] G. A. N. Connel and D. L. Camphausen, Philos. Mag. **26**, 541 (1972).
[4] S. D. Ganichev, J. Diener, L. M. Yassievich, and W. Preitl, Europhys. Lett. **29**, 315 (1995).
[5] N. G. Zhdanov, M. S. Kagan, E. G. Landsberg, L. V. Levkin, and V. V. Petrishchev, JETP Lett. **62**, 119 (1995).
[6] J. Leotin and V. V. Ryl'kov, Fiz. Tekh. Poluprovodn. **30**, 1525 (1996) [Semiconductors **30**, 802 (1996)].
[7] É. É. Godik, *Author's Abstract of Doctoral Dissertation*, Moscow, 1980.
[8] V. M. Abakumov, V. I. Perel', and I. N. Yassievich, Fiz. Tekh. Poluprovodn. **12**, 3 (1978) [Sov. Phys. Semicond. **12**, 1 (1978)].
[9] R. Chen and Y. Kirsh, *Analysis of Thermally Stimulated Processes*, Pergamon Press, N. Y., 1981.
[10] Yu. A. Gurvich, A. R. Mel'nikov, A. N. Shestakov, and E. M. Gershenzon, JETP Lett. **61**, 730 (1995).
[11] R. A. Smith, *Semiconductors*, Cambridge University Press, N. Y., 1978, 2nd edition [Russian trans., Mir, Moscow, 1982).
[12] V. N. Abakumov, P. M. Kreshchuk, and I. N. Yassievich, Fiz. Tekh. Poluprovodn. **12**, 264 (1978) [Sov. Phys. Semicond. **12**, 152 (1978)].
[13] P. A. Martin, B. G. Streetman, and K. Hess, J. Appl. Phys. **52**, 7209 (1981).
[14] T. M. Lifshitz, Prib. Tekh. Éksp., No. 1, 10 (1993).

Translated by M. E. Alferieff

Measurement of the diffusion length of minority charge carriers using real Schottky barriers

N. L. Dmitruk, O. Yu. Borkovskaya, and S. V. Mamykin

Institute of Semiconductor Physics, Ukrainian National Academy of Sciences, 252650 Kiev, Ukraine
(Submitted August 7, 1996; accepted for publication October 25, 1996)
Fiz. Tekh. Poluprovodn. **31**, 781–785 (July 1997)

The characteristic features of the field dependence of the short-circuit photocurrent of real Schottky barriers based on strongly doped semiconductors under conditions of an oscillatory dependence of the light absorption coefficient α on the field intensity in the space-charge region and the photon energy ($h\nu > E_g$) are analyzed. An analytical expression is obtained for the dependence of the photocurrent on the thickness W of the space-charge region when the condition $\alpha W \ll 1$ is satisfied. An improved method is proposed for determining the diffusion length of minority charge carriers by analyzing the dependence $I_p(W)$ in the spectral region satisfying the conditions of applicability of the expressions obtained. Some improvements are also made in the method for distinguishing the capacitance of the space-charge region from the high-frequency capacitance of a real Schottky barrier. The method is tested on structures Au–GaAs with $N_d = 4.5\times 10^{16} - 1\times 10^{18}$ cm^{-3}. The method of determining L is checked independently on the basis of a theoretical descripion of the spectral dependence of the quantum efficiency of the structure. [S1063-7826(97)00507-3]

The diffusion length L (lifetime $\tau = L^2/D$) of minority charge carriers is a very important parameter of a semiconductor. It is most sensitive to the structural-impurity perfection of the material, and it determines the sensitivity of photodetectors and the efficiency of solar cells. At the same time, for most semiconductor materials, where $L \lesssim 1$ μm, it is difficult to determine reliably, since the methods of relaxation of the photoconductivity (τ-meter) and current induced by an electronic probe (EPIC) are virtually ineffective. Under such conditions, when the diffusion length is short and comparable to the Debye screening length and the width of the surface (near-boundary) space-charge region (SCR), there is available a method based on the dependence of the short-circuit photocurrent of a Schottky-diode-type structure on the capacitance of the SCR under a reverse bias.[1–4] The advantages of this method are experimental simplicity and accuracy inaccessible in other methods, especially in the case of submicron diffusion lengths. At the same time, the possibility of applying the method to real Schottky barriers, containing an intermediate layer between the metal and the semiconductor and surface electronic states (SECs), requires additional investigation, especially in the case of strongly doped material. Under conditions of strong doping of a semiconductor, a substantial electric field $E \gtrsim 10^5$ V/cm forms in the SCR under a reverse bias, and as a result of electroabsorption, it leads to a nonmonotonic, oscillatory spectral and field dependence of the light absorption coefficient α of the semiconductor.[5] This in turn has the result that the intercept on the $1/C$ axis depends on the wavelength of the incident light.[6] For this reason, to determine the diffusion length of minority carriers correctly, it is necessary to have a spectrum of intercepts measured in the spectral region satisfying the conditions of applicability of the method and to make an analysis which takes into account the effect of the field on the absorption coefficient. Moreover, the presence of an intermediate layer between the metal and the semiconductor and the SEC in ''real'' Schottky barriers influences the magnitude of the measured capacitance and the redistribution of voltage between the intermediate layer and the SCR in the semiconductor. For this reason, to determine correctly the dependence of the capacitance C_{SCR} of the SCR on the bias voltage U, it is necessary to make an additional analysis of the high-frequency capacitance versus voltage (CVC) and the static current versus voltage (IVC) characteristics of the contact. In this paper we propose an improved method for determining the diffusion length L of the minority current carriers in real Schottky barriers, and we analyze the measured spectral and field dependences of the short-circuit photocurrent, the CVC, and the IVC, using computer data analysis.

1. ANALYSIS OF THE HIGH-FREQUENCY CAPACITANCE VERSUS VOLTAGE CHARACTERISTICS

In real Schottky barriers C_{SCR} is related with the rf capacitance C of the contact as

$$\frac{1}{C} = \frac{1}{C_0} + \frac{1}{C_{SCR}(U_{SCR})}, \tag{1}$$

where

$$C_{SCR} = \left(\frac{q\varepsilon_0\varepsilon_s N_d s^2}{2}\right)^{1/2} (U_0 - U_{SCR})^{-1/2}$$

$$= \frac{1}{B}(U_0 - U_{SCR})^{-1/2},$$

s is the area of the diode, and the effective of the capacitance C_0 of the intermediate layer increases with the thickness of this layer and with the doping level of the semiconductor.

When deep levels are present in the SCR, the capacitance of the region becomes frequency-dependent and, as shown in Ref. 7, the rf capacitance, for which the charge in

 1063-7826/97/070661-05$10.00

the deep levels cannot follow the test voltage signal, must be measured in order to measure the width W of the SCR. The relation between the rf capacitance C and the low-frequency capacitance C_{SCR} can also be represented in the form of Eq. (1), where $1/C_0$ does not depend on U, but has a different meaning. The method proposed in Ref. 7 for determining $1/C_0$ from the intercept on the $1/C$ axis of the straight line which the dependence $1/C(U^{1/2})$ reaches for large values of $U^{1/2}$ does not rule out an effect of $1/C_0$ in the entire range of $U^{1/2}$. In the case of strongly doped material the range of U is bounded by the breakdown voltage; this increases the error in determining $1/C_0$. Under the condition $N_d=$ const and $1/C_0 \neq f(U)$, using the derivative of $1/C$ with respect to U_{SCR}, we obtain

$$\frac{d1/C}{dU_{SCR}}=\frac{1}{2}B(U_0-U_{SCR})^{-1/2}, \tag{2}$$

where

$$U_0=U_d-\frac{kT}{q}-\Delta U_0,$$

where $N_d=N_{ds}+N_{dd}$ is the total density of shallow N_{ds} and deep N_{dd} donors,

$$U_d=\left[\phi_b-\left(\frac{E_c-E_f}{q}\right)\right]$$

is the diffusion potential for an unbiased diode,

$$\Delta U_0=\frac{N_{dd}}{N_{ds}+N_{dd}}\left(\frac{E_f-E_{dd}}{q}\right),$$

ϕ_b is the height of the barrier in the contact, and E_c, E_f, and E_{dd} are the conduction band bottom energy, the Fermi energy in the volume of the semiconductor, and the energy of the deep donor, respectively.

Hence

$$U_{SCR}=U_0-\frac{B^2}{4}\left(\frac{dU_{SCR}}{d1/C}\right)^2.$$

In other words, B and hence N_d can be determined from the slope of the curve of U_{SCR} versus $[dU_{SCR}/(d1/C)]^2$, and U_0 is determined from the intercept on the abscissa. The constant component $1/C_0$ of the capacitance can then be defined as

$$\frac{1}{C_0}=\frac{1}{N}\sum_{i=1}^{N}\left(\frac{1}{C}-B(U_0-U_{SCR_i})^{1/2}\right),$$

which makes it possible to calculate correctly the capacitance of the SCR from Eq. (1), i.e., its extent $W=\varepsilon_s\varepsilon_0 s/C_{SCR}$.

The function $U_{SCR}(U)$ is determined from the reverse current-voltage characteristic, with allowance for the analysis of the function $I_R(U)$ in order to determine the current-flow mechanism. In the case of structures where the main mechanism of the reverse current is thermionic emission

$$I_R=DA^*sT^2e^{-\frac{q(\phi_{b0}-\Delta\phi_0(U_{SCR})-U_i)}{kT}}, \tag{3}$$

where D is the transmittance of the barrier with an intermediate layer, A^* is Richardson's constant, U_i is the bias voltage drop across the intermediate layer, $U=U_i+U_{SCR}$, and $\Delta\phi_0$ is the decrease in the barrier height as a result of the mirror reflection forces and the field-emission forces. For a sufficiently thick intermediate layer and a small bias voltage range, the dependence of $\Delta\phi_b$ on the bias can be ignored compared with U_i, setting

$$I_R=DA^*sT^2e^{-\frac{q(\phi_b-U_i)}{kT}}, \tag{4}$$

where ϕ_b is the barrier height determined from the straight I-V characteristic.

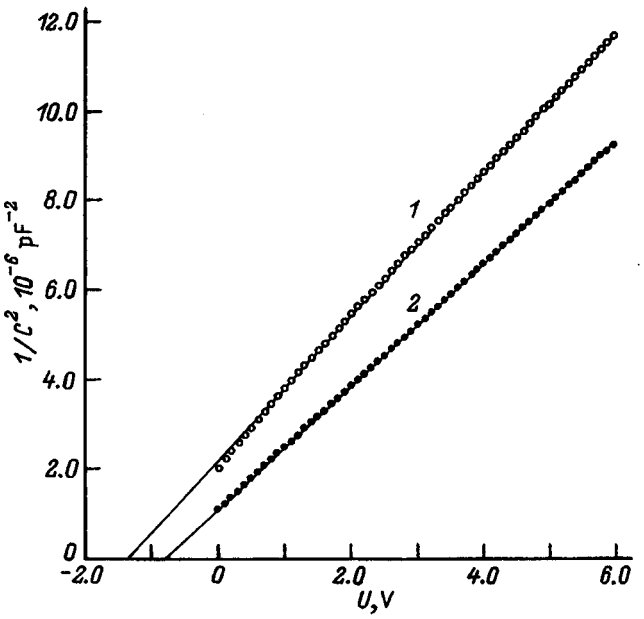

FIG. 1. Capacitance versus voltage curve of a barrier structure with majority carrier density 4.5×10^{16} cm^{-3} (1) and the capacitance of the SCR, recalculated taking into account the intermediate layer and deep levels, versus U_{SCR} (2) in the coordinates $1/C^2-U$.

2. EXPERIMENT

The rf capacitance of a diode is measured with illumination at a frequency of 1 MHz. This eliminates the direct participation of deep levels in the formation of the capacitance. The short-circuit photocurrent is measured with ac current at a light modulation with frequency $\sim$100 Hz.

As test samples we used Schottky diodes, prepared by the method of vacuum deposition of a semitransparent gold film on a single-crystalline n-type GaAs (doping level $N_d=10^{16}$–10^{18} cm^{-3}) substrate heated to 100–150 °C. The typical capacitance-voltage characteristic is shown in Fig. 1 (curve *1*) for a sample with $N_d=4.5\times10^{16}$ cm^{-3}. As one can see, it is slightly nonlinear and has a large intercept on the voltage axis $U_0=1.4$ V. This could be due to the presence of an intermediate layer of oxides at the metal–semiconductor interface and the contribution of deep levels to the SCR. Taking into account these two factors by the method proposed above completely rectifies this dependence (straight line 2) and makes it possible to determine the true barrier height at the Au–n-GaAs boundary: $\phi_b=0.82$ eV. This value agrees, to a high degree of accuracy, with the value determined from the straight current-voltage characteristic.

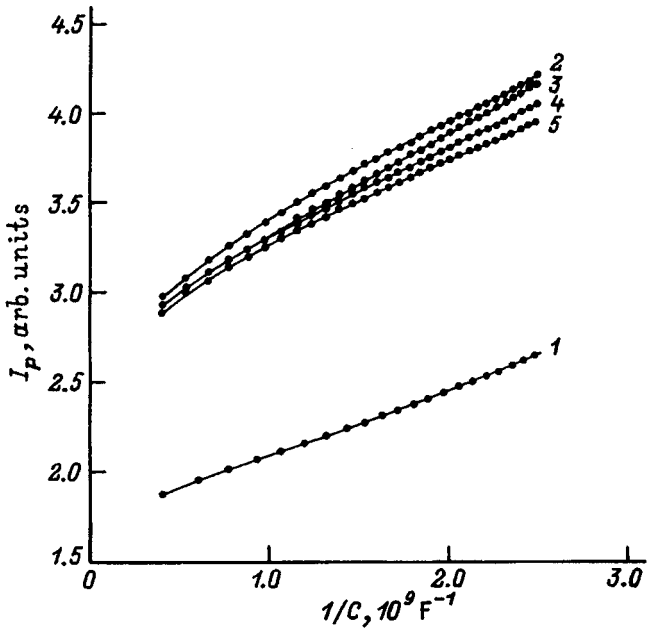

FIG. 2. Short-circuit photocurrent versus the reciprocal of the capacitance of a Au–*n*-GaAs barrier with $N_d=4.5\times10^{16}$ cm^{-3} for different wavelengths of the incident light, nm: *1* — 856, *2* — 828, *3* — 800, *4* — 775, *5* — 752.

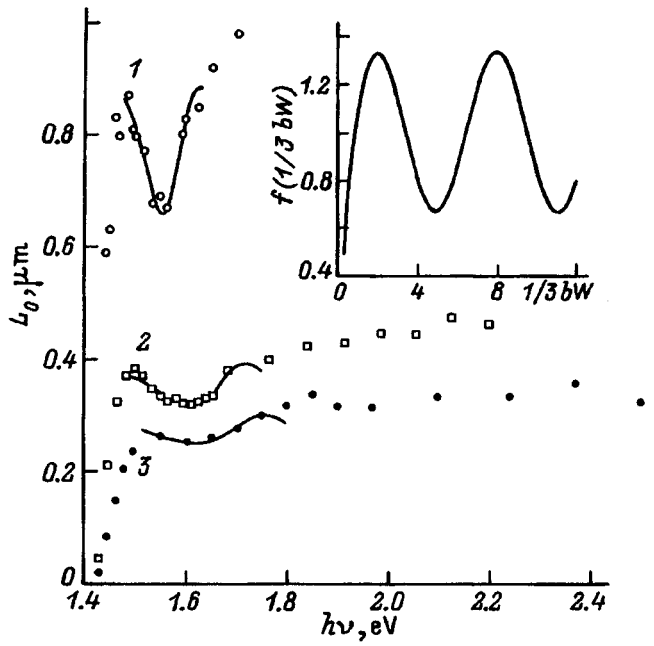

FIG. 3. Experimental and computed [according to expressions (8) and (9)] spectral dependences of the intercept L_0 for Au–*n*-GaAs samples with doping level N_d, cm^{-3}: *1* — 4.5×10^{16}, *2* — 3.48×10^{17}, *3* — 1.08×10^{18}. Parameters of the computed curves, $\varkappa$: *1* — 1/45, *2* — 1/64, *3* — 1/90; E_g, eV: *1* — 1.43, *2* — 1.41, *3* — 1.37; μ: *1* — 0.06, *2* — 0.068, *3* — 0.068; L, μm: *1* — 0.77, *2* — 0.35, *3* — 0.27. Inset: Form of the correction function $f(1/3bW)$.

A series of curves of the short-circuit photocurrent versus the capacitance of a reverse-biased barrier for the same structure with different incident-photon energies is shown in Fig. 2. We see that for sufficiently large values of $1/C$ the curves are linear, but the intercepts I_0 on the abscissa are different. The dependences of the intercept on the wavelength for materials with different doping levels are shown in Fig. 3. They are nonmonotonic. The character of this dependence indicates that the electric field strongly influences the absorption coefficient and makes it necessary to take into account this fact in determining the diffusion length L of the minority carriers. It should be noted that the condition $W\alpha\ll1$ was satisfied for these dependences, and all the better with increasing doping level of the samples. For this reason, the intercept spectrum $I_0(\lambda)$ for the most strongly doped *n*-type GaAs with $N_d=1.08\times10^{18}$ cm^{-3} is the longest. For a material with $N_d<10^{16}$ cm^{-3} the condition of weak absorption in the SCR $W\alpha\ll1$ holds only at the absorption edge itself, so that the dependence $I_0(\lambda)$ becomes completely meaningless.

The photocurrent of the Schottky barrier under the condition $W\alpha\ll1$ can be written in the form

$$I_p\sim K^*\left(\alpha_0 L+\int_0^W \alpha(x)dx\right), \tag{5}$$

where K^* can be regarded as being independent of the field (the width of the SCR),[3] especially in the case of strongly doped material. In fields $>10^4$ V/cm the absorption coefficient is no longer constant and, as shown in Ref. 6, for incident photon energy $h\nu$ sufficiently greater than the band gap E_g it can be approximately expressed by the formula

$$\alpha(x)=\alpha_0\left[1-\frac{hqE(x)}{8\pi(2\mu^{1/2}(h\nu-E_g)^{3/2}}\times\cos\left(\frac{8\pi(2\mu)^{1/2}(h\nu-E_g)^{3/2}}{3hqE(x)}\right)\right], \tag{6}$$

where α_0 is the light absorption coefficient in a weak field, and μ is the effective mass of the electron. The dependence of the field $E(x)$ in the space charge region with a constant doping level has the form $E(x)=(qN_d/\varepsilon_s\varepsilon_0)(W-x)$. Substituting $E(x)$ and $\alpha(x)$ into the expression for the photocurrent and integrating by parts, we obtain an analytic expression for the photocurrent of a Schottky barrier in the form of an infinite series:

$$I_p=K^*\alpha_0\left(L+W\left[1-\frac{1}{6}\left(\frac{\cos(y)}{y}-\sin(y)-y\,\mathrm{Ci}(y)\right)\right]\right), \tag{7}$$

where

$$y=1/(3bW);\quad b=\frac{q^2N_dh}{\varepsilon_0\varepsilon_s8\pi(2\mu)^{1/2}(h\nu-E_g)^{3/2}},$$

Ci is the cosine integral,

$$\mathrm{Ci}(y)=0.5772+\ln(y)-\int_0^y\frac{\cos(y)}{y}dy,$$

where the last integral is tabulated. The expression in brackets as a function of y is shown in the inset in Fig. 3. In the general form

$$I_p=K^*\alpha_0(L+W[1-f(y)]). \tag{8}$$

Comparing the experimental spectral dependences of the intercept I_0 with the dependences calculated from Eq. (8) for diodes with a different degree of doping shows that there is a reasonably good agreement in the region of the first minimum when

$$f(y)=1-\varkappa\left(\frac{\cos(y)}{y}-\sin(y)-y\,\mathrm{Ci}(y)\right), \tag{9}$$

where the coefficient $\varkappa$ and the values of E_g or and/or μ depend on the doping level in the semiconductor and are determined by fitting. The parameters of the computed curves, presented in Fig. 3, are given in the caption of the figure. The value of $E_g$tends to decrease as the doping level increases; this can be explained by the action of the Franz–Keldysh effect as a result of the increase in the surface field with increasing doping of the semiconductor. The decrease in $\varkappa$ (decrease in the effect of the field on I_0) with increasing N_d is apparently mainly due to the scattering of current carriers by ionized impurities, resulting, according to Ref. 8, in a ''broadening'' of the electro-optic functions, decrease in the amplitude and increase in the width of the electroabsorption peaks. For $N_d>10^{18}$ cm^{-3}, effects arising due to the random fields of clusters of charged impurities, band degeneracy, optical nonuniformity of the SCR in the case where a thin inversion layer is present beneath the contact, intensification of the effect of the scattering of current carriers by surface defects (interface),[9] which likewise changes the character of the field dependence of α, are also possible. The diffusion length L of the minority charge carriers can be determined by fitting the computed curve given by Eqs. (8) and (9) to the experimental curve.

A proof of the fact that the value of L determined in this manner is the true diffusion length of minority charge carriers was obtained by an independent method by fitting the photocurrent spectrum calculated according to the general formula (12) of Ref. 10 to the measured spectrum. Accordingly, the measured photocurrent spectrum normalized to an incident photon was converted into the quantum efficiency spectrum, taking into account the transmission of the Au film on GaAs in accordance with Ref. 11. The thickness and optical parameters of the Au film were determined from ellipsometric measurements and the transmission spectrum of an Au film on a quartz plate–step. It was determined that to describe the transmission spectrum of Au films obtained by vacuum sputtering on a heated substrate (quartz), the optical parameters of Au from Ref. 12 can be used starting with film thicknesses of $\sim$200 Å. According to Ref. 10, the short-circuit photocurrent spectrum, calculated with the correct boundary conditions and taking into account electroabsorption in the SCR, is given by the formula

$$\frac{I_p}{qI}=\frac{1}{1+S/V_p}\left(\frac{1-\dfrac{\exp\left[-\int_0^W\alpha(x)dx\right]}{1+\alpha_0 L}+I_2}{1+L_1+\dfrac{D/L}{S+V_p}e^{-\psi(0)}}\right)$$
$$-\frac{\alpha_0}{\alpha_0-\dfrac{qE(0)}{kT}}\left(1-\frac{qE(0)}{kTV_n/D_n}\right)^{-1}, \tag{10}$$

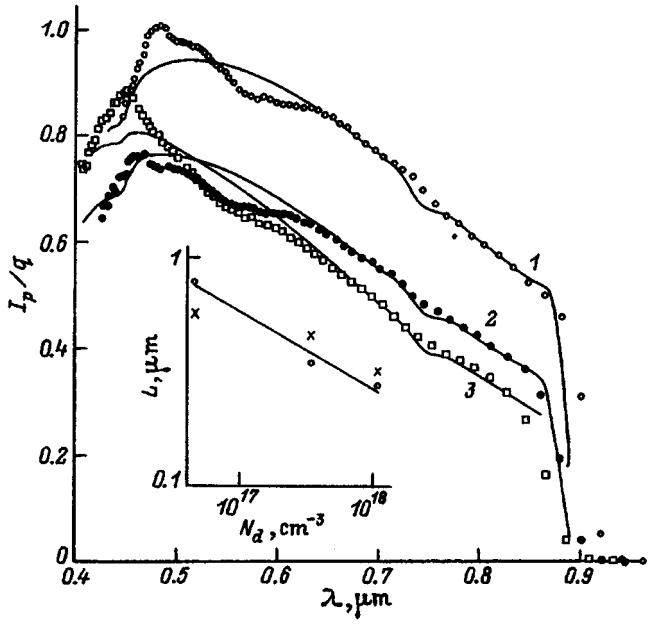

FIG. 4. Experimental (dots) and theoretically computed spectral dependences of the ratio of the short-circuit photocurrent to the number of photons passing through GaAs for Au–GaAs structures with N_d, cm^{-3}: *1* — 4.5×10^{16}, *2* — 3.48×10^{17}, *3* — 1.08×10^{18}. Parameters of the computed curves, L, μm: *1* — 0.57, *2* — 0.46, *3* — 0.32; S/V_p: *1* — 0.01, *2* — 0.18, *3* — 0.12; V_n/D_n, cm^{-1}: *1* — 2×10^6, *2* — 7.8×10^6, *3* — 1.3×10^7. Inset: Hole diffusion length versus donor impurity density. L was determined by the following methods: $I_p(1/C)$ — circles, $I_p(h\nu)$ — crosses.

where

$$I_1=\frac{1}{L}\int_0^W e^{-\psi(x)}dx,$$

$$I_2=\frac{1}{L}\int_0^W (1-e^{-\alpha(x)x})e^{-\psi(x)}dx,$$

$E(0)$ is the field at the semiconductor–intermediate layer boundary, $\psi(x)$ is the potential in the SCR, S is the boundary recombination rate, D and D_n are the diffusion coefficients, and V_p and V_n are the velocities of the transport of holes and electrons from the semiconductor into the metal. We note that the second term in expression (10) describes the decrease in the photocurrent as a result of the direct transport of the majority current carriers into the metal. It is important for low barrier heights at the boundary, and in the presence of reverse biases in a strongly doped material it can be disregarded in almost the entire spectral range $\lambda>0.5$ μm. We have therefore assumed it approximately to be $\alpha(x)\approx a_0$. The first term describes well the long-wavelength part of the spectrum, which is most sensitive to the diffusion length L. The values of L, S/V_p, and V_n/D_n can be determined from the agreement of the theoretical and experimental photocurrent spectrum, using them as adjustable parameters. Figure 4 shows the experimental and computed quantum-efficiency spectra for the same structures as in Fig. 3. The adjustable parameters are presented in the caption, and the dependence of L, determined by the two methods, on the dopant density is shown in the inset. We see that the values of L agree within $\pm10\%$. The error of the second method (based on the

spectrum I_p) is much larger, since this method requires knowledge of the spectral dependence of the optical parameters (n,k) of the metal and (n,k,α) of the semiconductor, which themselves can depend on the thickness of the metal film, the surface treatment, and the doping level of the semiconductor. Data for n,k, and $\alpha(h\nu)$, given in Ref. 13 for GaAs, were used in the calculation. In the investigated range of N_d for single-crystal *n*-type GaAs, the dependence $L(N_d)$ is a power law with exponent $\sim -1/3$.

In summary, the well-known method of determining the diffusion length of minority charge carriers, improved for real Schottky barriers taking into account the correct boundary conditions at the interface and the Franz–Keldysh effect in the SCR, reflects to a high degree of accuracy the real values of the diffusion lengths in semiconductor materials and makes it possible to describe in a self-consistent manner the spectral and field dependences of the photosensitive structures with a Schottky barrier.

[1] V. A. Tyagaĭ, Fiz. Tverd. Tela (Leningrad) **6**, 1260 (1964) [Sov. Phys. Solid State **6**, 1156 (1964)].

[2] N. L. Dmitruk and A. K. Tereshchenko, Élektron. Tekhn., Ser. 2, Poluprovodnikovye Pribory, No. 4, 68 (1972).

[3] O. Yu. Borkovskaya, N. L. Dmitruk, M. Dubovinski, R. V. Konakova, O. N. Mishchuk, Yu. A. Tkhorik, P. Kardosh, and F. Shtofanik, Eleltrotechn. Čas. **40**, 877 (1989).

[4] N. L. Dmitruk, O. Yu. Borkavskaya, O. N. Mishchuk, and Ya. Charyev, Élektron. Tekhn., Ser. 2, Poluprovodnikovye Pribory, No. 1, 210 (1991).

[5] J. Callaway, Phys. Rev., **134**, A998 (1964).

[6] J. Darantes-Davila, A. Lastras-Martinez, and P. M. Raccah, Appl. Phys. Lett. **38**, 442 (1981).

[7] N. L. Dmitruk, A. K. Tereshchenko, O. I. Maeva, V. I. Lyashenko, and A. M. Raskevich, Fiz. Tekh. Poluprovodn. **7**, 671 (1973) [Sov. Phys. Semicond. **7**, 469 (1973)].

[8] N. Nottka and B. O. Seraphin, Phys. Rev. A **139**, A560 (1965).

[9] V. A. Tyagaĭ and O. V. Snitko, *Electroreflection of Light in Semiconductors* [in Russian], Naukova dumka, Kiev, 1980.

[10] O. Yu. Borkovskaya, N. L. Dmitruk, and A. N. Zyuganov, **4**, 82 (1983).

[11] N. L. Dmitruk, O. V. Fursenko, and O. Yu. Borkovskaya, Optoelektron. i Poluprovodn. Tekhn., No. 27, 115 (1994).

[12] P. B. Johnson and R. W. Christi, Phys. Rev. B **6**, 4370 (1972).

[13] D. E. Aspnes and A. A. Studna, Phys. Rev. B **27**, 985 (1983).

Translated by M. E. Alferieff

Effect of successive implantation of $Ag^+(Cu^+)$ and Xe^+ ions on the recombination properties of $Cd_xHg_{1-x}Te$ crystals

M. I. Ibragimova, N. S. Baryshev, V. Yu. Petukhov, and I. B. Khaĭbullin

Kazan' Physicotechnical Institute, Russian Academy of Sciences, 420029 Kazan', Russia
(Submitted August 7, 1996; accepted for publication October 25, 1996)
Fiz. Tekh. Poluprovodn. **31**, 786–789 (July 1997)

The effect of successive double implantation of $Ag^+(Cu^+)$ and Xe^+ ions on the recombination properties of $Cd_xHg_{1-x}Te$ ($0.2<x<0.3$) crystals has been investigated. It is shown that after implantation of ions of one chemical element, followed by diffusion thermal annealing at temperatures below 150–200 K, recombination through local levels lying 30 ± 5 meV below the conduction band bottom dominates. Successive double implantation of $Ag^+(Cu^+)$ and Xe^+ ions followed by diffusion thermal annealing changes the course of the temperature dependence of the lifetime of the nonequilibrium charge carriers. It was determined that for $Cd_xHg_{1-x}Te$ crystals with $x=0.20-0.25$ in the temperature interval 700–200 K the lifetime of the nonequilibrium charge carriers is low ($\tau<0.15$ μs) and does not depend on the temperature. For $Cd_xHg_{1-x}Te$ crystals with $x\simeq0.3$ recombination of nonequilibrium charge carriers occurs through two types of levels: in the temperature range 140–200 K — deep levels $E_{t1}\simeq E_c-51$ meV and at lower temperatures (77–140 K) — through shallower levels $E_{t2}\simeq E_c-(16\pm2)$ meV. © *1997 American Institute of Physics.* [S1063-7826(97)00707-2]

1. INTRODUCTION

The narrow-gap semiconductor compound $Cd_xHg_{1-x}Te$ is the basic material used in the fabrication of infrared-radiation detectors. From the scientific standpoint, it is of great interest to investigate the lifetime of nonequilibrium charge carriers in this material, since this parameter determines the characteristics of photodetectors. A great deal of experimental data on the recombination processes and on the clarification of the nature of Shockley–Read centers arising mainly in crystals subjected to special doping (see Refs. 1–5) have now been accumulated. Ion implantation has been very successful for forming high-quality p–n junctions on substrates with different types of conductivity.[6–9] Moreover, in Refs. 10 and 11 it was shown that the electrical parameters of $Cd_xHg_{1-x}Te$ can be controlled by measured implantation of group-I and -III ions, which makes it possible to obtain n- and p-type bulk material with a prescribed charge-carrier density. Investigations of the recombination properties of these crystals with $x=0.204-0.3$ established that under conditions when conductivity-type inversion $n\rightarrow p$ occurs, at temperatures below 150–200 K recombination through local levels lying 25 ± 10 meV below the conduction band bottom dominates.[12] The recombination centers arising in the process are apparently associated with the formation of vacancy complexes of the type $V_{Hg}V_{Te}$. At the same time, it should be noted that implantation of inert-gas ions, specifically Xe^+, in $Cd_xHg_{1-x}Te$ followed by thermal annealing does not change the electrical properties, while the lifetime of the nonequilibrium charge carriers (at 77 K) decreases by several factors up to two orders of magnitude.[13] To determine the specific nature of the ion implantation and subsequent diffusion annealing in narrow-gap semiconductors, it is of interest to investigate the effect of double successive implantation on the electric and photoelectric properties of $Cd_xHg_{1-x}Te$. In the present work we investigated the recombination properties of $Cd_xHg_{1-x}Te$ ($x=0.2-0.3$) crystals in which group-I and Xe^+ ions were successively implanted and the crystals were then subjected to diffusion annealing after each irradiation.

2. EXPERIMENT

Bulk n-type single crystals of the solid solution $Cd_xHg_{1-x}Te$, grown by different methods, with cadmium telluride content $x=0.2-0.3$ were used as the initial material. Implantation in freshly etched samples was conducted in two stages: first, Cu^+ or Ag^+ ions with energy 40 or 30 keV, respectively, and doses in the range $2.0\times10^{14}-2.0\times10^{15}$ cm^{-2} were implanted, after which 30-keV Xe^+ ions with a dose of 1.25×10^{16} or 2.5×10^{16} cm^{-2} were implanted. In some control experiments the implantation was performed in the reverse order. In all implantation experiments the ion current density j was held below $0.7\mu A/cm^2$ to prevent strong heating of the sample. After each irradiation a diffusion thermal annealing (DTA) was performed in sealed quartz cells in saturated mercury vapor at a temperature 573 ± 10 K for a period of 10–12 days. Such annealing is necessary for diffusion redistribution of the embedded impurity over the entire thickness of the sample and for annealing of radiation defects. The electric and photoelectric parameters of the samples were measured after each implantation operation followed by diffusion annealing.

The Hall coefficient R_H and the resistivity (conductivity σ) were measured by the van der Pauw method at 77 and 300 K in magnetic fields of 500 and 15 000 Oe. The lifetime of the nonequilibrium charge carriers (NCCs) τ in the temperature range 77–300 K was determined by the method of photoconductivity relaxation with pulsed excitation by GaAs-diode radiation with wavelength $\lambda=0.91$ μm.

 1063-7826/97/070666-03$10.00

TABLE I. Parameters of samples at 77 K before and after $Cu^+(Ag^+)$ and Xe^+ implantation followed by DTA.

Sample No.	x	Before implantation: Type of conductivity	Before implantation: $1/eR_H$, 10^{15} cm^{-3}	Before implantation: $\lvert R_H\rvert\sigma$, 10^4 cm^2/(V·s)	Before implantation: τ, μs	Implantation conditions: Ion	Implantation conditions: Dose, 10^{15} cm^{-2}	After implantation+DTA: Type of conductivity	After implantation+DTA: $1/eR_H$, 10^{15} cm^{-3}	After implantation+DTA: $\lvert R_H\rvert\sigma$, 10^4 cm^2/(V·s)	After implantation+DTA: τ, μs
C1	0.23	*n*	−0.38	5.5	–	Ag^+	1.8	*p*	8.4	0.062	0.1
					0.1	Xe^+	25.0	*p*	8.5	0.060	0.1
C2	0.24	*n*	−4.64	6.1	–	Xe^+	12.5	*n*	−4.7	6.0	–
					–	Ag^+	1.25	*p*	2.5	0.013	0.14
C3	0.3	*n*	−1.23	5.4	–	Ag^+	0.62	*p*	2.1	0.029	0.29
					0.29	Xe^+	25.0	*p*	2.15	0.029	0.2
M1	0.25	*n*	−1.49	1.05	–	Cu^+	0.94	*p*	6.86	0.031	0.13
					0.13	Xe^+	12.5	*p*	6.85	0.035	0.13
M2	0.208	*n*	−2.1	1.07	–	Cu^+	1.9	*p*	8.8	0.043	0.1
					0.1	Xe^+	12.5	*p*	8.7	0.043	0.1
M3	0.3	*n*	−1.23	5.4	–	Cu^+	0.25	*p*	1.2	0.053	0.6
					0.6	Xe^+	25.0	*p*	1.3	0.053	0.25
K1	0.24	*p*	1.15	0.018	7.0	Xe^+	37.4	*p*	1.1	0.018	0.1

3. RESULTS AND DISCUSSION

The data from electric and photoelectric measurements at 77 K for $Cd_xHg_{1-x}Te$ ($x=0.2-0.3$) crystals before implantation and after each stage of implantation followed by annealing are given in Table I. As one can see from the table, ion implantation $Cd_xHg_{1-x}Te \leftarrow Cu^+$ inverts the conductivity type $n \rightarrow p$ and increases the photosensitivity of the material. Bombardment of $Cd_xHg_{1-x}Te$ crystals with Xe^+ ions only (see data for the samples K1 and S2) has no effect on the electrical parameters, but it does drastically decrease the NCC lifetime.

The measurements of the temperature dependences of the NCC lifetime in $Cd_xHg_{1-x}Te$ after double implantation followed by diffusion annealing showed that it is convenient to divide the results into two groups, depending on the composition of the solid solutions: $x=0.20-0.25$ and $x\simeq 0.3$. Using sample M1 (curve *1*) as an example, Fig. 1 shows a typical temperature dependence of the lifetime in $Cd_xHg_{1-x}Te$ crystals with $x\leqslant 0.25$ after irradiation with group-I ions and subsequent DTA. The course of the temperature dependence of τ attests to the fact that after implantation of group-I ions in $Cd_xHg_{1-x}Te$ recombination through local levels in the band gap is observed in the impurity region. A calculation in the single-level Shockley–Read model showed that recombination in sample M1 occurs through the level $E_{t1}=E_c-26$ meV (see data in Table II). The temperature dependence of the lifetime of nonequilibrium charge carriers for $Cd_xHg_{1-x}Te$ crystals, subjected to implantation with Xe^+ ions combined with subsequent DTA, is shown using sample K1 (curve *2*) as an example. It should be noted (see Ref. 13) that the temperature variation of τ in the initial K1 crystal was explained satisfactorily by interband processes, while as a result of implantation of Xe^+ ions, the dependence $\tau(1/T)$ acquired a form characteristic of recombination of NCCs on Shockley–Read centers with a level $E_t=E_c-30$ meV (see Table II). Curve *3* in Fig. 1 illustrates the variation of the temperature dependence of τ in $Cd_xHg_{1-x}Te$ samples subjected to double successive implantation with group-I ions and Xe^+ combined with subsequent DTA. As one can see from the experimental data, after the successive double implantation in $Cd_xHg_{1-x}Te$, the temperature variation of $\tau(1/T)$ cannot be satisfactorily described in the one-level Shockley–Read model. In a wide temperature interval (77–200 K) the short NCC lifetime is temperature-independent. It was also determined that the order of double irradiation of $Cd_xHg_{1-x}Te$ with $x\leqslant 0.25$ (group-I ions and then Xe^+ ions or vice versa) has no effect on the value of τ: For sample M1 (Cu^+ ions and then Xe^+ ions) $\tau=0.13$ μs and for sample S2 (Xe^+ ions and then Ag^+ ions) $\tau=0.14$ μs at $T=77-200$ K. Therefore, our investigations established that successive double irradiation of $Cd_xHg_{1-x}Te$ crystals (with $x\leqslant 0.25$) with group-I and Xe^+ ions results in the formation of a strong channel for recombination and stabilization of the NCC lifetime in the temperature region corresponding to the extrinsic conductivity.

Figure 2 shows the temperature dependences of τ for two samples of $Cd_xHg_{1-x}Te$ ($x=0.3$), irradiated first with Cu^+ ions (sample M3, curve *1*) or Ag^+ ions (sample S3, curve *2*), after which Xe^+ ions were implanted (curves *3*

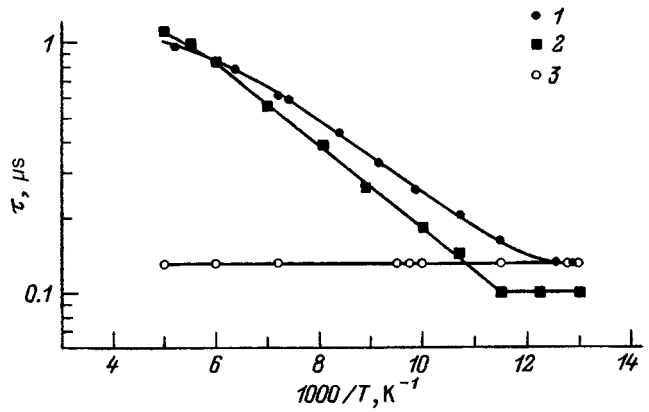

FIG. 1. Temperature dependences of the lifetime of nonequilibrium charge carriers for $Cd_xHg_{1-x}Te$ samples with $x\leqslant 0.25$: *1* — Sample M1, implantation of Cu^+ ions; *2* — sample K1, implantation of Xe^+ ions; *3* — sample M1, successive implantation of Cu^+ and Xe^+ ions.

TABLE II. Parameters of recombination centers.

Sample No.	Ion	x	Dose, 10^{15} cm^{-3}	$1/eR_H$, 10^{15} cm^{-3}	E_c-E_{t1}, meV	τ_p, 10^{-6} s	τ_n, 10^{-6} s	E_c-E_{t2}, meV	τ_{p2}, 10^{-6} s
M1	Cu^+	0.25	0.94	6.86	26	2.0	0.1		
M3	Cu^+	0.3	0.25	1.2	28	0.17	0.6		
	Xe^+		25.0	1.3	51	0.52	0.26	18	0.055
C3	Ag^+	0.3	0.62	2.1	35	0.48	0.29		
	Xe^+		25.0	2.15	51	1.26	0.21	14	0.064
K1	Xe^+	0.24	37.4	1.1	30	0.1			

Note: τ_n is the lifetime of nonequilibrium electrons; $\tau_{\rho 1}$ and $\tau_{\rho 2}$ are the lifetimes of nonequilibrium holes relative to the recombination through E_{t1} and E_{t2} levels.

and *4*, respectively). The temperature variation τ for $Cd_xHg_{1-x}Te$ irradiated with electrically active group-I impurity ions shows that, just as for samples with $x=0.25$, recombination occurs through one local level in the band gap. The calculations presented in Table II gave the values $E_{t1}=E_c-28$ meV and $E_{t1}=E_c-35$ meV for $Cd_xHg_{1-x}Te$ irradiated with Cu^+ and Ag^+ ions, respectively. Subsequent implantation of Xe^+ ions in these samples has the effect that the temperature dependences $\tau(1/T)$ can no longer be described by recombination through one local Shockley–Read center. As an example, Fig. 2 shows (dashed lines) the computational results for the case $E_{t1}=E_c-51$ meV. In contrast with crystals with low values of x, for this group of samples the NCC lifetime increases monotonically with temperature. The temperature dependence of τ in a $Cd_xHg_{1-x}Te$ $\times(x=0.3)$ sample subjected to double successive implantation was described assuming two NCC recombination levels. The computational results presented in Table II show that in the region 140–200 K recombination occurs through a deep level $E_{t1}\simeq E_c-51$ meV, and as the temperature increases (77–140 K), recombination through the shallower levels $E_{t2}=E_c-18$ meV and E_c-14 meV dominates in samples initially irradiated with Cu^+ ions (sample M3) and Ag^+ ions (sample S3), respectively.

Our results on the effect of double successive implantation on the recombination properties of $Cd_xHg_{1-x}Te$ crystals can be explained as follows. As follows from the data in Ref. 12, ion implantation in $Cd_xHg_{1-x}Te$ crystals combined with prolonged DTA leads to the formation of radiation defects, which are probably constituents of the complexes of the type $V_{Hg}V_{Te}$. It was determined that the charged state of such complexes depends on x: neutral for $x\simeq 0.3$ and positive $(+1)$ for $x\leqslant 0.25$. The differences which we observed in the temperature dependences of the NCC lifetime in $Cd_xHg_{1-x}Te$ crystals subjected to successive double implantation, depending on x are most likely determined by the character of the initially existing complexes. Moreover, in the solid solutions $Cd_xHg_{1-x}Te$ with low values of x $\times(x<0.25)$ the complexes form more easily and their density is higher than in crystals with high values of x at the same implantation doses. Therefore, it can be assumed that in $Cd_xHg_{1-x}Te$, after successive double implantation, new complexes based on initially existing ones are formed, and in samples with $x\leqslant 0.25$, i.e., in a crystals with a narrower gap [at 77 K $E_g=0.197$ eV (Ref. 14)] their density is high and they make the main contribution to the recombination processes, which is what stabilizes the NCC lifetime with low values of τ in a wide temperature interval.

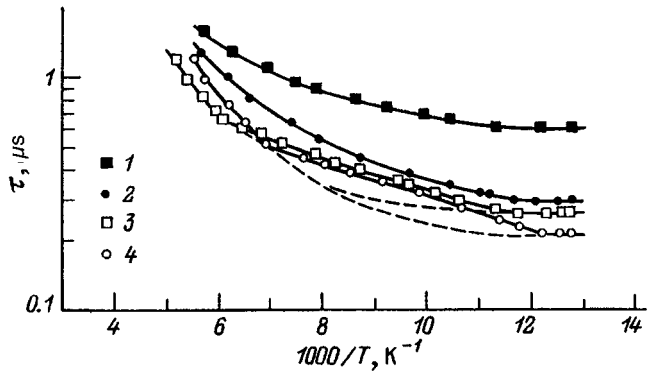

FIG. 2. Temperature dependences of the lifetime of nonequilibrium charge carriers for $Cd_xHg_{1-x}Te$ samples with $x=0.3$: *1* — Sample M3, implantation of Cu^+ ions; *2* — sample S3, implantation of Ag^+ ions; *3* — sample M3, successive implantation of Cu^+ and Xe^+ ions; *4* — S3 sample, successive implantation of Ag^+ and Xe^+ ions.

[1] R. G. Pratt, J. Hewett, P. Capper, C. L. Jones, and M. J. Quelch, J. Appl. Phys. **54**, 5152 (1983).
[2] R. G. Pratt, J. Hewett, P. Capper, C. L. Jones, and N. Judd, J. Appl. Phys. **60**, 2377 (1986).
[3] D. E. Lacklison and P. Capper, Semicond. Sci. Technol. **2**, 33 (1987).
[4] P. S. Wijewarnasuriya, M. D. Lange, S. Sivanathan, and J. P. Faurie, J. Appl. Phys. **75**, 1005 (1994).
[5] N. S. Baryshev, B. L. Gel'mont, and M. I. Ibragimova, Fiz. Tekh. Poluprovodn. **24**, 209 (1990) [Sov. Phys. Semicond. **24**, 127 (1990)].
[6] G. L. Destefanis, J. Vac. Sci. Technol. A **3**, 171 (1985).
[7] L. O. Bubulac, W. E. Tennant, D. S. Lo, D. D. Edwall, J. C. Robinson, J. C. Chen, and G. Bostrup, J. Vac. Sci. Technol. A **5**, 3166 (1987).
[8] J. Baars, H. Seelewind, Ch. Fritzshe, U. Kaiser, and J. Ziegler, J. Cryst. Growth **86**, 762 (1988).
[9] L. O. Bubulac, D. D. Edwall, D. McConnell, R. E. De Wames, E. R. Blazejewski, and E. R. Gertner, Semicond. Sci. Technol. **5**, N 3S, S45 (1990).
[10] M. I. Ibragimova, N. S. Baryshev, I. B. Khaĭbullin, F.I. Akhmedova, and A. P. Fadeeva, Fiz. Tekh. Poluprovodn. **23**, 1249 (1989) [Sov. Phys. Semicond. **23**, 779 (1989)].
[11] F. I. Akhmedova, N. S. Baryshev, M. I. Ibragimova, and I. B. Khaĭbullin, Fiz. Tekh. Poluprovodn. **21**, 575 (1987) [Sov. Phys. Semicond. **21**, 353 (1987)].
[12] M. I. Ibragimova, N. S. Baryshev, V. A. Zhikharev, and I. B. Khaĭbullin, Fiz. Tekh. Poluprovodn. **29**, 1755 (1995) [Semiconductors **29**, 917 (1995)].
[13] N. S. Baryshev, M. I. Ibragimova, and I. B. Khaĭbullin, Fiz. Tekh. Poluprovodn. **24**, 363 (1990) [Sov. Phys. Semicond. **24**, 224 (1990)].
[14] W. Dexter, Phys. Rev. **181**, 1181 (1969).

Translated by M. E. Alferieff

Characteristic features of Raman scattering of light in silicon doped with high krypton doses

M. F. Galyautdinov, N. V. Kurbatova, S. A. Moiseev, and E. I. Shtyrkov

Kazan' Physicotechnical Institute at the Kazan Science Center of the Russian Academy of Sciences, 4220029 Kazan', Russia

(Submitted August 30, 1996; accepted for publication October 25, 1996)
Fiz. Tekh. Poluprovodn. **31**, 790–793 (July 1997)

A high-frequency 20-cm^{-1} shift in the Raman spectrum of silicon implanted with krypton ions has been observed experimentally. The dynamics of the transformation of the microscopic structure of the surface layer of silicon was investigated on the basis of Raman scattering data obtained for different regimes of Kr^+ implantation and laser annealing. The experimental data obtained by us are explained well by the presence of local mechanical stresses ($\sim$40 kbar) due to the presence of heavy inert Kr atoms at the lattice sites. © *1997 American Institute of Physics.* [S1063-7826(97)00807-7]

A number of interesting effects appear when heavy elements are introduced into silicon: Chemical activity of inert heavy gases,[1] low-temperature recrystallization stage together with gas release[2] and displacement of hydrogen impurity,[3] and formation of a porous structure[4] which in turn intensifies Raman scattering and luminescence.[5] For reasons of new practical applications, the physical nature of these effects is drawing a great deal of interest.

We have investigated by the method of Raman scattering the transformation of the microscopic structure of the crystal lattice of silicon and its dynamic properties with different implantation regimes and laser annealing (LA).

1. EXPERIMENTAL PROCEDURE

First, a single-crystal plate of KDB-1 (111) silicon was bombarded at room temperature with krypton ions Kr^+ with energy $E=40$ keV and current density of the ion beam in the range 2–5 μA/cm^2. High ion-implantation doses in the range $D=6\times10^{14}-2.4\times10^{17}$ cm^{-2} were used for the effects studied. Next, the experimental samples were annealed with a ruby laser ($\lambda=694.3$ nm) with pulse duration $\tau\sim50$ ns; the energy density in a 5-mm-diameter spot varied in the range $W=0.2-1.5$ J/cm^2.

The Raman spectra were obtained in the ''reflection'' geometry on a DFS-62 spectrometer for different conditions of treatment of silicon at room temperature. Raman scattering was excited by the $\lambda=510.6$-nm line of a copper-vapor laser, operating in a quasicontinuous mode with frequency 11 kHz and a pulse duration of 20 ns. The power density of a laser pulse at the sample did not exceed 10^3 W/cm^2. The spectral slit width was equal to 2 cm^{-1}. The Raman scattering signals were recorded in the photon counting mode with synchronization of the laser pulses.

2. EXPERIMENTAL RESULTS AND DISCUSSION

The Raman spectrum obtained made it possible to follow the transformation of the structure of a $\sim$100-nm-thick surface layer and localization of Kr atoms in the Si matrix with increasing implantation dose and increasing laser irradiation energy. The Raman scattering spectrum for the initial implanted samples corresponds mainly to the amorphous state of the surface layer of Si. However, a weak doublet band with frequencies 512 and 517 cm^{-1} (Fig. 1a), which indicates the appearance of a microcrystalline phase,[6] is observed even for an implantation dose of $D=6\times10^{15}$ cm^{-2}. As the LA energy density is increased, this band becomes narrower in the direction of the crystal peak at 518 cm^{-1} (Fig. 1 b–1d). The appearance of a doublet band in the Raman scattering spectrum is explained by an initial low-temperature stage of recrystallization of the disordered layer. Heating of the sample to $\sim$400 °C at this implantation dose can be attributed to the high ion current (>3 μ A/cm^2). It has been determined[2] that the effect of low-temperature annealing is characteristic of such implantation doses of krypton in silicon.

An unexpected occurrence was the appearance of a new narrow line at 538 cm^{-1} in the spectrum together with the crystal peak at 518 cm^{-1} (Fig. 1b–1d). It is significant that the position of this peak and its half-width do not depend on the implantation and LA regimes, while the intensity of the peak increases substantially, compared with the intensity of the crystal peak at 518 cm^{-1}, as the LA energy density increases. For all implantation doses investigated the maximum intensity of the low-frequency peak at 538 cm^{-1} is observed with LA energy density $W\cong0.5$ J/ cm^2. This characteristic dependence is presented in Fig. 2 for the implantation dose $D=6\times10^{15}$ cm^{-2}. As the LA energy density is increased further to $W\cong1$ J/cm^2, the intensity of the crystal peak at 518 cm^{-1} saturates while the intensity of the peak at 538 cm^{-1} drops sharply (almost by an order of magnitude). Under these conditions a regime of epitaxial recrystallization of the disordered layer is realized; this is also indicated by the ellipsometric investigation of the complex index of refraction for such implantation and LA regimes.[4]

The existing theories of the dynamics of nonideal crystal lattices for a light substitution impurity explain well the appearance of local oscillations of the initial perfect crystal above the photon frequency. As a rule, a heavy impurity leads to the appearance of quasilocalized resonance oscillations, whose frequencies fall in the region of the allowed photon frequencies of the initial crystal.[7] In our opinion, the

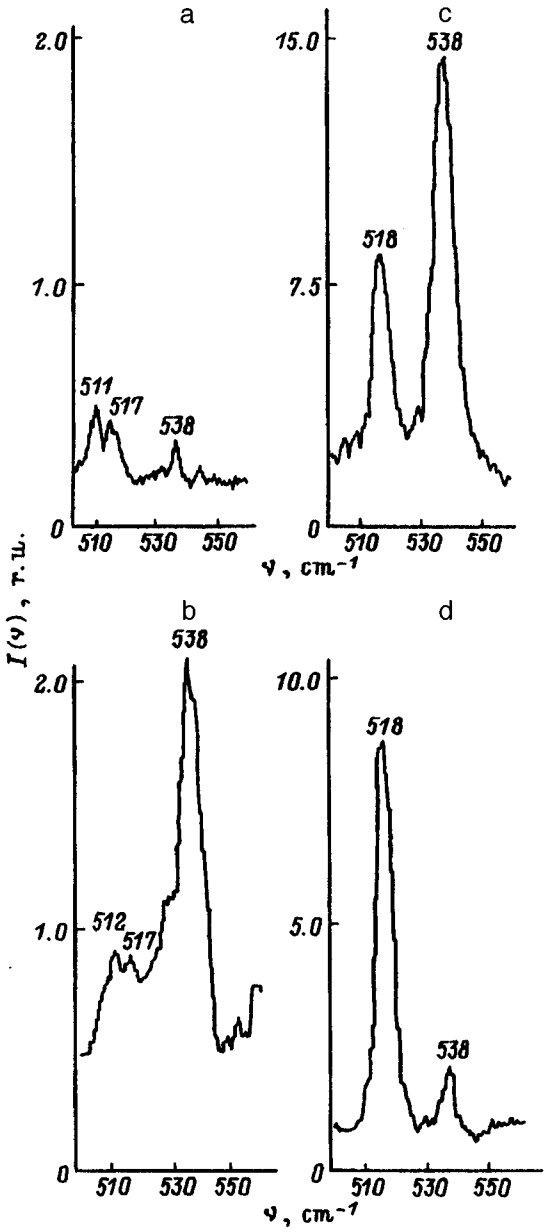

FIG. 1. Transformation of the Raman spectrum in silicon doped with Kr^+ ions ($E=40$ keV, $D=6\times10^{15}$ cm^{-2}) under the action of laser irradiation ($\lambda=694.3$ nm, $\tau\sim50$ ns) with energy density W (J/cm^2): a — 0, b — 0.34, c — 0.53, d — 0.96.

high-frequency peak at 538 cm^{-1} should be attributed to the appearance of a local mode due to krypton atoms at the sites of the silicon crystal lattice. The constancy of the magnitude of the high-frequency shift and the absence of an additional broadening of this peak, as compared with the half-width of the 518-cm^{-1} peak show unequivocally that this signal is due to the additional high-frequency vibration of the crystal lattice. Such a high-frequency vibration can be attributed to the presence of a strong deformation potential due to the localization of heavy inert krypton atoms at the silicon-lattice sites and, correspondingly, to a change in the elastic coupling constants of the Si atoms. Accordingly, a local change occurs in the frequency of the characteristic vibrations of the lattice atoms.

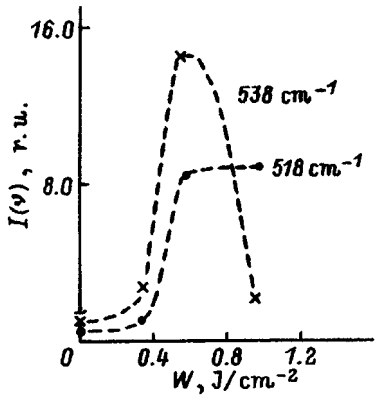

FIG. 2. Intensity of the 518- and 538-cm^{-1} lines in the Raman spectrum of silicon doped with Kr^+ ions ($E=40$ keV, $D=6\times10^{15}$ cm^{-2}) versus the laser irradiation energy density.

In the case of the implantation of a heavy but electrically active indium impurity in silicon, an additional high-frequency peak was not observed in the Raman spectrum in the range investigated (Fig. 3). In all likelihood, the localization of the In atoms at the Si lattice sites does not produce a strong deformation of the electronic subsystem of the Si atoms and, correspondingly, does not change appreciably the force constants binding the atoms of the substrates, because the covalent bond with the implanted impurity is preserved.

A small (~3 cm^{-1}) increase in the frequency of the characteristic vibrations of single-crystalline silicon has been observed in several studies. This was attributed to the presence of in mechanical stresses that appear because of the differences in the lattice constants of the epitaxial silicon film and the substrate[8] or as a result of local laser annealing of the amorphous layer[6] or a local perturbation by the substitution dopant.[9] In our opinion, the observed high-frequency shift $\Delta\nu=20$ cm^{-1} could be due to strong local mechanical stresses in the crystal lattice. We shall employ the Grüneisen approximate model to estimate these

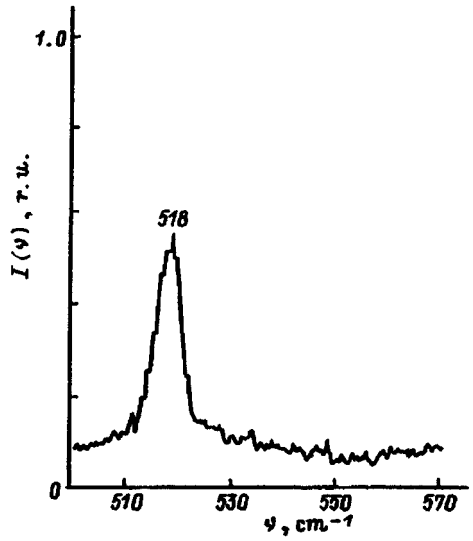

FIG. 3. Raman spectrum of silicon doped with In^+ ions ($E=30$ keV, $D=9.6\times10^{15}$ cm^{-2}) after laser annealing.

stresses.[10] In this phenomenological model the relative change $\Delta\nu/\nu_i$ of the corresponding vibrational frequency of the lattice is related to the volume compression $\Delta V/V$ of the sample through the Grüneisen mode parameter γ_i for modes with index i in a crystal subjected to pressure P:

$$\Delta\nu_i/\nu_i = -\gamma_i(\Delta V/V) = \gamma_i\beta P, \quad (1)$$

where β is the isothermal compressibility,[9] $\beta_{Si}=1.012\times10^{-11}$ m^2/N. For the optical mode E_{2g}, the Grüneisen parameter is[10] $\gamma_i=0.98$. An estimate of the local pressure according to the formula (1) with $\Delta\nu=20$ cm^{-1} and $\nu=518$ cm^{-1} gives the value $P\cong40$ kbar. Therefore, localization of heavy krypton atoms at crystal-lattice sites in silicon can give rise to substantial stresses that result in a compression of the lattice.

It is well known that stresses appearing in the Si matrix can also strongly influence the recrystallization kinetics during laser annealing.[11] In our case this is indicated by the behavior of the intensity of the 518-cm^{-1} and 538-cm^{-1} peaks as a function of the LA energy density. The appearance of these signals even with a low energy density ($W=0.4$ J/cm^2) is unequivocally due to the recrystallization of the disordered layer of Si (Fig. 1). The intensity of the peak at 538 cm^{-1} corresponds to the fraction of localized Kr atoms in the crystal lattice. Recrystallization is accompanied by a simultaneous sharp displacement of the Kr impurity toward the surface. The extra krypton atoms which did not occupy a substitution position at sites of the Si crystal lattice accumulate in the form of gas bubbles. This is indicated by the data from ellipsometric investigations and the porosity of the structure observed with a scanning force microscope.[12] For LA energy density $W>0.5$ J/cm^2 a sharp drop of the signals at 538 cm^{-1} and slow growth of the intensity of the peak at 518 cm^{-1} are observed. The increase in the intensity of the 518-cm^{-1} line saturates at $W\simeq1$ J/cm^2, and in the process the magnitude of the signal at 538 cm^{-1} drops approximately by a factor of 13. We attribute these changes to the low-temperature stage of recrystallization, which is accompanied by a rapid release of Kr gas.[2] According to Ref. 2, the residual Kr content in the Si matrix as a result of complete recrystallization for an implantation dose $D=2.2\times10^{15}$ cm^{-2} equals 6%, which agrees with our estimates based on an analysis of the decrease of the signal at 538 cm^{-1}.

In closing, we note that although the nature and mechanism of low-temperature recrystallization with gas release have not been inadequately studied, it can be assumed, on the basis of the experimental data obtained by us, that recrystallization is stimulated by local stresses. This conclusion is supported by the experimentally verified results on the stimulating effect of hydrostatic pressure on crystallization of amorphous silicon,[13] where it was shown that the crystallization rate increases by a factor of 5 under a pressure of 32 kbar at a temperature of 520 °C.

This work was supported by the Russian Fund for Fundamental Research under Grant No. 96-02-18245.

[1] V. D. Tkachev, A. V. Mudryi, and N. S. Minaev, Phys. Status Solidi A **81**, 313 (1984).
[2] C. Jech and R. Kelly, J. Phys. Chem. Sol. **30**, 465 (1969).
[3] A. D. Lozovskiĭ and A. M. Panesh, Izv. Akad. Nauk, Ser. Fiz. **58**, No. 5, 209 (1994).
[4] M. F. Galyautdinov, É. Yu. Karas', N. V. Kurbatova, and E. I. Shtyrkkov, Opt. Spektrosk. **73**, 344 (1992) [Opt. Spectrosc. (USSR) **73**, 200 (1992)].
[5] A. V. Andrianov, L. V. Belyakov, D. N. Goryachev, D. I. Kovalev, O. M. Sreseli, I. D. Yaroshetskiĭ, and B. Ya. Averbukh, Fiz. Tekh. Poluprovodn. **28**, 2210 (1994) [Semiconductors **28**, 1213 (1994)].
[6] L. P. Avakyants, G. D. Ivlev, and E. D. Obraztsova, Fiz. Tekh. Poluprovodn. **34**, 3334 (1992) [Sov. Phys. Semicond. **34**, 1784 (1992)].
[7] A. A. Maradudin, *Theoretical and Experimental Aspects of the Effects of Point Defects and Disorder on the Vibrations of Crystals*, Academic Press Inc., N. Y., 1966 [Russian transl., Mir, Moscow, 1968].
[8] V. S. Gorelik, R. N. Khashimov, and M. M. Sushinskiĭ, Poverkhnost'. Fizika, Khimiya, Mekhanika **6**, 77 (1985).
[9] M. Chandrasekhar, H. R. Chandrasekhar, M. Grimsdich, and M. Cardona, Phys. Rev. B **22**, 4825 (1980).
[10] M. Cardona and G. Gunterodt [Eds.], *Light Scattering in Solids IV*, Springer-Verlag, N. Y., 1984. [Russian transl., Mir, Moscow, 1986].
[11] L. N. Aleksandrov, Pis'ma Zh. Tekh. Fiz. **11**(5), 286 (1985) [Tech. Phys. Lett. **11**, 115 (1985)].
[12] M. F. Galyautdinov, N. V. Kurbatova, É. Yu. Buĭnova *et al.*, in *Abstracts of Reports at the Conference on the ''Structure and Properties of Crystalline and Amorphous Materials''* [in Russian], Nizhniĭ Novgorod, 1996, p. 86.
[13] Guo-Quan, E. Nugren, and M. J. Aziz, J. Appl. Phys. **70**, 5323 (1991).

Translated by M. E. Alferieff

Simulation of heat and mass transfer during growth of silicon carbide single crystals

B. A. Kirillov, A. S. Bakin, and Yu. M. Tairov

Department of Microelectronics, St. Petersburg State Electrical Engineering University, 197376 St. Petersburg, Russia

S. N. Solnyshkin

Department of Higher Mathematics, St. Petersburg State Electrical Engineering University, 197376 St. Petersburg, Russia

(Submitted October 7, 1996; accepted for publication October 25, 1996)
Fiz. Tekh. Poluprovodn. **31**, 794–799 (July 1997)

Interest in silicon carbide as a semiconductor suitable for fabricating devices operating under extreme conditions has increased sharply in recent years. The main problem now lies in the mass production of silicon carbide single crystals with a low defect density and high cross-sectional uniformity of the properties. This study involves a numerical simulation of heat and mass transfer processes during growth of SiC single crystals by the sublimation method. The results obtained make it possible to trace the effect of the growth conditions on the temperature distribution and the distribution of the main components in the vapor phase, as well as the radial profile of the rate of growth of a single crystal for different stages of growth process. © *1997 American Institute of Physics.* [S1063-7826(97)00907-1]

1. INTRODUCTION

Silicon carbide is a semiconductor material with unique properties. It can be used to fabricate devices operating at high temperatures and also high-power and radiation-resistant devices. The main problem now lies in the mass production of silicon carbide single crystals with a low defect density and high cross-sectional uniformity of properties.

Investigators have concentrated their efforts on studying the processes occurring in a reactor during crystal growth.[1–3] Nonetheless, these processes have still not been adequately studied because of the impossibility of using modern research tools due to the very high working temperatures in the growth zone. For this reason, attempts have recently been made to simulate on a computer the heat and mass transfer processes with allowance for the chemical reactions occurring in the growth cell.[4]

The setups employed in different laboratories for growing SiC single crystals differ with respect to the configuration of the reactors and the growth cells, as well as with respect to the growth conditions. This study is devoted to numerical simulation of the heat and mass transfer processes occurring in a reactor under the conditions employed for growing SiC single crystals in the Laboratory of Wide-Gap Semiconductors at the St. Petersburg Electrical Engineering University (SPEEU). The objective of this work is to determine the laws governing these processes at different stages of the technological process of growing SiC single crystals by constructing a mathematical model of these processes and performing a computational experiment.

2. FORMULATION OF THE PROBLEM

The main and most important aspects of studying the laws governing heat and mass transfer processes occurring during growth of SiC single crystals include the following:

— determination of the temperature distribution in the growth cell in order to optimize the conditions of growth of SiC single crystals in order to decrease the defect density and to study the effect of the convection of the gas mixture on the distribution of the main gaseous components responsible for crystallization and, hence, on the rate of growth and the shape of the growth front of the SiC ingot;

— determination of the effect of a change in the conditions of crystallization of SiC during the technological process; the conditions of crystallization of silicon carbide change due to graphitization and sintering of the initial charge; and

— allowance for the contribution of the chemical reactions which occur at the graphite wall of the reactor and which result in the formation of gaseous components that participate in the precipitation of silicon carbide.

Let us examine the convection of a multicomponent gas mixture in a two-dimensional cylindrical cavity of radius R (Fig. 1). The growth cavity is filled with an inert gas (argon) under pressure P_{Ar}. The source of vapor is pulverized SiC powder (2) poured into a graphite vessel 3 so that the distance from the surface of the fill to the seed 1 equals H. The vessel is closed at the top by a cover 4, to which the seed is secured. The graphite vessel is placed into a resistance furnace so that the fill is located in a region of higher temperature than the temperature T_1 of the the cover with the seed. The temperature gradient fixed in this manner produces conditions for growing SiC single crystals in the process of sublimation of the fill and subsequent transport of reagents to the seed and precipitation of the reagents. When the temperature gradient is directed downward in this system, free convection striving to mix the gas components so as to establish a constant temperature can appear.

Since the gas in the reactor is transparent to the thermal radiation from the graphite walls, radiation transfer can be ignored. Thus we shall seek the temperature distribution due

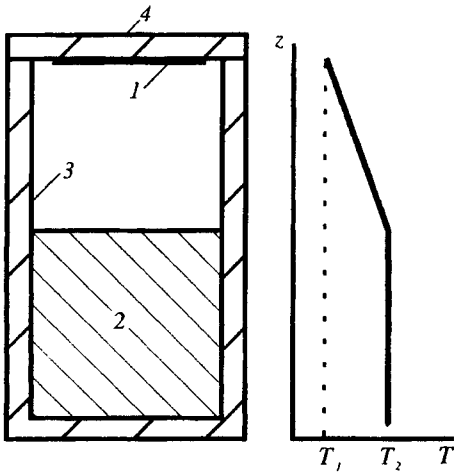

FIG. 1. Schematic diagram of the reactor for growing SiC single crystals and the distribution of the on-axis temperature gradient.

to the mechanisms of heat conduction and convection. We shall study the mass transfer, taking into account the diffusion and convection.

We shall describe the convective motion in a multicomponent gas mixture in a cylindrically symmetric reactor by the system of Navier–Stokes equations together with the equations describing the transport of each component. The initial system has the following form in the variables $\Psi-\omega$, where Ψ is the stream function, and ω is the vorticity:

$$\frac{\partial T}{\partial t}+\frac{1}{r}\frac{\partial}{\partial r}(r\nu_r T)+\frac{\partial}{\partial z}(\nu_z T)$$
$$=\frac{1}{r}\frac{\partial}{\partial r}\left[r\chi(T)\frac{\partial T}{\partial r}\right]+\frac{\partial}{\partial z}\left[\chi(T)\frac{\partial T}{\partial z}\right],$$
$$\frac{\partial c^{(i)}}{\partial t}+\frac{1}{r}\frac{\partial}{\partial r}(\nu_r c^{(i)})+\frac{\partial}{\partial z}(\nu_z c^{(i)})$$
$$=\frac{1}{r}\frac{\partial}{\partial r}\left[r\varphi^{(i)}(T)\frac{\partial c^{(i)}}{\partial r}\right]+\frac{\partial}{\partial z}\left[\varphi^{(i)}(T)\frac{\partial c^{(i)}}{\partial z}\right],$$
$$\frac{\partial\omega}{\partial t}+\frac{\partial}{\partial r}(\nu_r\omega)+\frac{\partial}{\partial z}(v_z\omega)=\frac{\partial}{\partial r}\left\{\frac{1}{r}\frac{\partial}{\partial r}[r\nu(T)\omega]\right\}$$
$$+\frac{\partial^2}{\partial z^2}[\nu(T)\omega]-G\frac{\partial T}{\partial r}-\sum_{i=1}^{N}G^{(i)}\frac{\partial c^{(i)}}{\partial r},$$
$$\frac{\partial}{\partial r}\left(\frac{1}{r}\frac{\partial\Psi}{\partial r}\right)+\frac{1}{r}\frac{\partial^2\Psi}{\partial z^2}=-\omega,\quad i=1,\ldots,N-1, \tag{1}$$

where

$$\nu_r=-\frac{1}{r}\frac{\partial\Psi}{\partial z},\quad \nu_z=\frac{1}{r}\frac{\partial\Psi}{\partial r},\quad \omega=\frac{\partial\nu_r}{\partial z}-\frac{\partial\nu_z}{\partial r},$$
$$G=\beta_T g, G^{(i)}=\beta_c^{(i)}g,$$

$V=(\nu_r,\nu_z)$ is the flow velocity; T is the temperature; $c^{(i)}$ is the molar concentration of the ith component; $\nu(T)$ is the kinematic viscosity; $\chi(T)$ is the thermal diffusivity; $\varphi^{(i)}$ is the diffusion coefficient of the ith component in the mixture; β_T is the thermal expansion coefficient of the material; $\beta_c^{(i)}$ is the concentration expansion coefficient of the ith component; and g is the acceleration of gravity.

The computational region for the system of equations (1) covers half of the axial cross section of the growth cell (from the axis to the side wall). For this region the interior boundary-value problem, whose solution must satisfy the following boundary conditions, is studied:

1) At the solid walls:

$$\Psi|_b=\left.\frac{\partial\Psi}{\partial n}\right|_b=\text{const},\quad T|_b=T(\xi),\varphi^{(i)}(T)\left.\frac{\partial c^{(i)}}{\partial n}\right|_b=q^{(i)}(\xi),$$

where ξ is the instantaneous coordinate;

2) on the symmetry axis:

$$\Psi|_{r=0}=0,\quad \omega|_{r=0}=0,\quad \left.\frac{\partial T}{\partial r}\right|_{r=0}=0,\quad \left.\frac{\partial^2 c^{(i)}}{\partial r^2}\right|_{r=0}=0.$$

The boundary conditions for the vorticity ω at the solid walls are determined in the finite-difference form [see Eq. (3)].

3. NUMERICAL SOLUTION METHOD AND DISCUSSION OF THE RESULTS

The system (1) is solved numerically using a constant time step τ and the computational region is covered with a grid which is uniform along z and r axes:

$$\Omega_h=\{z_i,\ 0\leqslant 1\ \dim Z;\quad r_j,\ 0\leqslant j\leqslant\ \dim R\},$$

for which $h_i=z_{i+1}-z_i$ is the constant step along z, $h_j=r_{j+1}-r_j$ is the constant step along r; $\dim Z+1$ is the number of points on the generatrix of the side wall of the reactor, and $\dim R+1$ is the number of points along r at the base of the reactor. All variables are assumed to be determined at the grid nodes. The initial system of equations (1) is approximated at the wall Ω_h by a longitudinal–transverse scheme in the operator form:

$$\frac{\overline{T}-T}{\tau/2}=L_r\left[\frac{1}{r},r\chi(T),\ 1\right]\overline{T}-k_r\left(\frac{1}{r},r\nu_r\right)\overline{T}$$
$$+L_z[1,\chi(T),\ 1]T-k_z(1,\nu_z)T,$$
$$\frac{\hat{T}-\overline{T}}{\tau/2}=L_r\left[\frac{1}{r},r\chi(T),\ 1\right]\overline{T}-k_r\left(\frac{1}{r},r\nu_r\right)\overline{T}$$
$$+L_z[1,\chi(T),\ 1]\hat{T}-k_z(1,\nu_z)\hat{T},$$
$$\frac{\overline{c^{(i)}}-c^{(i)}}{\tau/2}=L_r\left[\frac{1}{r},r\varphi^{(i)}(T),\ 1\right]\overline{c^{(i)}}-k_r\left(\frac{1}{r},r\nu_r\right)\overline{c^{(i)}}$$
$$+L_z[1,r\varphi^{(i)},\ 1]c^{(i)}-k_z(1,\nu_z)c^{(i)},$$
$$\frac{\hat{c}^{(i)}-\overline{c^{(i)}}}{\tau/2}=L_r\left[\frac{1}{r},r\varphi^{(i)}(T),\ 1\right]\overline{c^{(i)}}-k_r\left(\frac{1}{r},r\nu_r\right)\overline{c^{(i)}}$$
$$+L_z[1,r\varphi^{(i)},\ 1]\hat{c}^{(i)}-k_z(1,\nu_z)\hat{c}^{(i)},$$
$$\frac{\overline{\omega}-\omega}{\tau/2}=L_r\left[1,\frac{1}{r},r\nu(T)\right]\overline{\omega}-k_r(1,\nu_r)\overline{\omega}$$

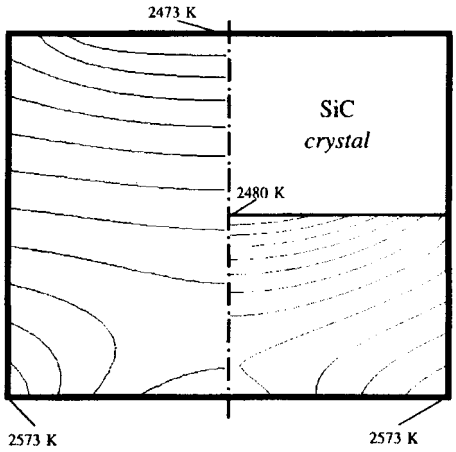

FIG. 2. Temperature distribution in the gas volume of the growth cell at the initial (left side) and intermediate (right side) stages of growth. The step between the isotherms equals 8.3 K.

$$+L_z[1,1,\nu(T)]\omega-k_z(1,\nu_z)\omega-G_T-\sum_{i=1}^{N}G_c^{(i)},$$

$$\frac{\hat{\omega}-\overline{\omega}}{\tau/2}=L_r\left[1,\frac{1}{r},r\nu(T)\right]\overline{\omega}-k_r(1,\nu_r)\overline{\omega}+L_z[1,1,\nu(T)]\hat{\omega}-k_z(1,\nu_z)\hat{\omega}-G_T-\sum_{i=1}^{N}G_c^{(i)},$$

$$\frac{\overline{\Psi}-\Psi^s}{\tau/2}=L_r\left(1,\frac{1}{r},1\right)\overline{\Psi}+L_z\left(\frac{1}{r},1,1\right)\Psi^s+\hat{\omega}r,$$

$$\frac{\Psi^{s+1}-\overline{\Psi}}{\tau/2}=L_r\left(1,\frac{1}{r},1\right)\overline{\Psi}+L_z\left(\frac{1}{r},1,1\right)\Psi^{s+1}+\hat{\omega}r. \tag{2}$$

Here T, $c^{(i)}$, and ω are, respectively, the temperature, concentration of the ith component, and vorticity at the nth layer; $\overline{T}$, $\overline{c^{(i)}}$, and $\overline{\omega}$ are the same quantities at the $(n+1/2)$th layer; and $\hat{T}$, $\hat{c}^{(i)}$, and $\hat{\omega}$ are the same quantities at the $(n+1)$st layer; s is the number of the iteration of Ψ; L_r, L_z, k_r, and k_z are operators:

$$L_x(a,b,d)u=a\frac{\partial}{\partial x}\left[b\frac{\partial}{\partial x}(du)\right],\quad k_x(a,b)u=a\frac{\partial}{\partial x}(bu).$$

The temperature was fixed at the inner walls of the graphite vessel and at the surface of the fill (see Fig. 1). The characteristic features of the crucible construction in a real setup for growing SiC single crystals were taken into account by prescribing different temperature boundary conditions. Furthermore, in simulating the heat and mass transfer processes in a gas volume at different stages of growth, when the growing crystal fills part of the initial volume of the growth cell, we solved the Fourier equation for determining the temperature of the growth front.

In prescribing the boundary conditions for the concentrations of the main components in the gas mixture, we took into account the temperature dependences of the partial pressures of these components. The dissociation of the polycrystalline fill and the precipitation of the silicon carbide single crystal are described by the reactions[5]

$$(SiC)_{solid}\rightarrow Si_{gas}+C_{solid},\qquad k_{p1}=p(Si),$$

$$2(SiC)_{solid}\rightarrow(SiC_2)_{gas}+Si_{gas},\quad k_{p2}=p(Si)p(SiC_2)$$

$$(SiC)_{solid}+Si_{gas}\rightarrow(Si_2C)_{gas},\quad k_{p3}=p(Si_2C)/p(Si),$$

$$(SiC)_{solid}\rightarrow(SiC)_{gas},\qquad k_{p4}=p(SiC),$$

where k_{pi} is the equilibrium constant for the ith reaction and $p(j)$ is the partial pressure of the jth component. The boundary conditions for the concentrations also take into account the chemical reactions which occur on the side wall of the graphite vessel and which lead to the additional formation of the carbon-containing components SiC_2, Si_2C, and SiC:[1]

$$C_{solid}+2Si_{gas}=(Si_2C)_{gas}\quad k_{p5}=p(Si_2C)/p^2(Si),$$

$$2C_{solid}+Si_{gas}=(SiC_2)_{gas},\quad k_{p6}=p(SiC_2)/p(Si),$$

$$C_{solid}+Si_{gas}=(SiC)gas,\quad k_{p7}=p(SiC)/p(Si).$$

Since different data for the temperature dependences of the partial pressures of the indicated gaseous components are available in the literature,[6,7] the calculations were performed for all known data. In addition, the change occuring in the growth conditions during the technological process of SiC single crystal growth as a result of a decrease in the gas volume in the growth cell as well as graphitization of the polycrystalline fill was taken into account.

The boundary conditions for the vorticity are calculated at each time layer. At the solid walls they are obtained by realizing attachment conditions, which signify that all velocity components vanish in an arbitrary coordinate system; i.e., any partial derivative of the stream function vanishes at a solid wall with an arbitrary angle of inclination. Therefore, we have for ω at the solid walls

$$\omega_{i,\dim R}=\frac{\Psi_{i,\dim R-2}+7\Psi_{i,\dim R}-8\Psi_{i,\dim R-1}}{2r_jh_j^2},$$

$$\omega_{0j}=\frac{\Psi_{2,j}+7\Psi_{0,j}-8\Psi_{1,j}}{2r_jh_i^2}, \tag{3}$$

$$\omega_{\dim Z,j}=\frac{\Psi_{\dim Z-2,j}+7\Psi_{\dim Z,j}=8\Psi_{\dim Z-1,j}}{2r_jh_i^2}.$$

The system (2) is solved by successive sweeps. The algorithm for solving this mathematical problem is described in detail in Ref. 8.

The rate of growth of the SiC single crystal was determined on the basis of an assumption that the limiting stage of the growth process is mass transfer of carbon-containing components:[9]

$$V_{growth}=M_{SiC}j_C/\rho_{SiC}, \tag{4}$$

where M_{SiC} is the molar mass of silicon carbide, and ρ_{SiC} is the density of single-crystalline SiC. The total flux of carbon-containing gaseous components is described by Fick's first law

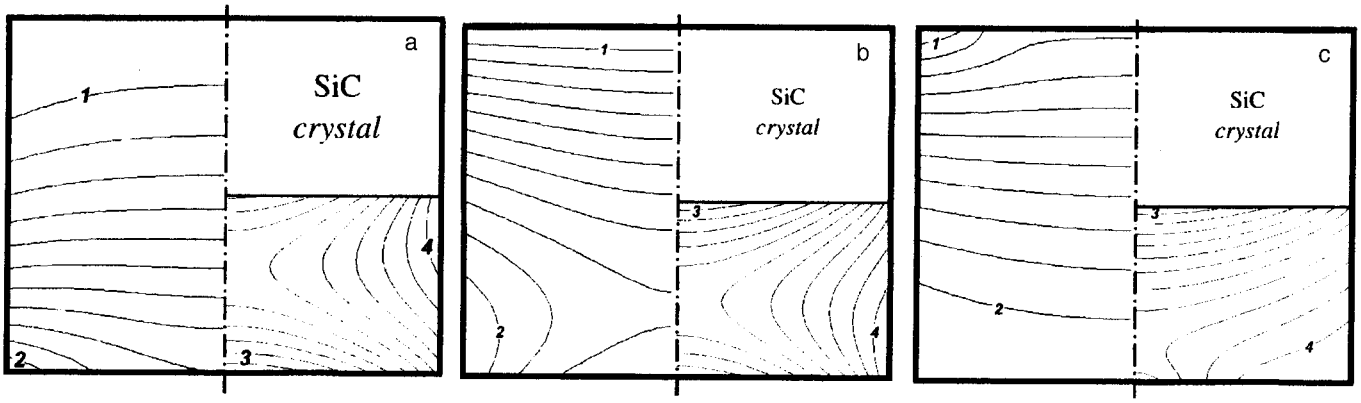

FIG. 3. Distribution of the main gaseous components in the growth cell at the initial (left side) and intermediate (right side) stages of growth. The values of the molar concentrations C for each component at both stages of growth and also the step ΔC between the isoconcentration lines are given in Table I.

$$j_C = -\left(\varphi_{Si_2C-Ar} \frac{dc^{Si_2C}}{dz} + 2\varphi_{SiC_2-Ar} \frac{dc^{SiC_2}}{dz} + \varphi_{SiC-Ar} \frac{dc^{SiC}}{dz} \right). \quad (5)$$

In the relation (5) φ_{i-Ar} is the binary diffusion coefficient of the ith component in argon [we assume $p(Ar) \gg p(Si)$, $p(Si_2C)$, $p(SiC_2)$, $p(SiC)$]; $dc^{(i)}/dz$ is the gardient of the concentration of the ith component at the growth surface. The diffusion coefficients φ_{i-Ar} were calculated on the basis of the data in Ref. 10 and the concentration gradients are obtained by solving the equations of convective and diffusion mass transfer in the system (1) for each component.

For quasiclosed systems, in which free convection can appear, the dimensionless similarity criteria are introduced in order to describe the hydrodynamics:[11]

a) Prandtl's criterion: $Pr = \nu/\chi = \nu\rho c_p/\varkappa$;

b) Rayleigh's criterion: $Ra = g\beta_T \delta T H^3/\nu\chi = g\beta_T \delta T H^3 \rho c_p/\nu\varkappa$, where ν is the kinematic viscosity, χ is the thermal diffusivity, ρ is the density, c_p is the specific heat, $\varkappa$ is the thermal conductivity, β_T is the temperature expansion coefficient of argon, g is the acceleration of gravity, and, δT and H are the characteristic temperature drop and size of the growth cell, respectively. The values of the indicated constants and parameters for argon were obtained by extrapolating the data given in Ref. 12 to high temperatures and by estimating on the basis of thermodynamic laws.

The heat and mass transfer processes were modeled for different conditions of growth of SiC crystals: argon pressure $P_{Ar} = 10^{-3}-1$ atm, growth temperature $T = 2400-2700$ K, and on-axis temperature gradient grad$T = 20-30$ K/cm. The dimensions of the computational region covered by the grid Ω_h are $R = 1.5-2$ cm and $H = 1-3$ cm. The computational experiments performed showed that for the indicated conditions of growth and the configuration of the reactor employed in a real setup, convection has a very little effect on the heat and mass transfer. The effect of convection becomes appreciable at pressures $P_{Ar} \geqslant 1.5$ atm.

Examples of the computational results at the initial and intermediate stages of growth for a growth cell with radius $R = 1.5$ cm and initial distance from the surface of the fill to the seed $H = 3$ cm at argon pressure $P_{Ar} = 0.5$ atm are presented in Figs. 2–4 and in Table I. The Rayleigh number is $Ra = 92$ and $Ra = 8$ for the initial and intermediate stages of growth, respectively; the Prandtl number varies very little during the growth process and equals $Pr = 0.93$.

The variation in the temperature distribution during the growth process is shown in Fig. 2. As a result of the high thermal conductivity of single-crystalline silicon carbide, there is a very small temperature difference between the growth front of the crystal and the temperature of the graphite walls of the reactor. This increases the on-axis temperature gradient in the gas medium of the cell.

As is well known, a change in the growth conditions is manifested in the graphitization of the polycrystalline fill. This causes a redistribution of the gaseous components during growth (see Fig. 3). We see that the on-axis component of the gradient of the SiC_2 concentrations is at first directed upward (see Fig. 3c, on the left, and Table I), in contrast to Si and Si_2C. Therefore, the growth velocity profile V_{growth} (Fig. 4, curve *1*) and ultimately the shape of the crystal growth front are affected mainly by the Si_2C distribution. During growth, the direction of the SiC_2 flux reverses (the gradient is oriented downward — see Fig. 3c, on the right,

TABLE I. Molar concentration C on the isoconcentration lines 1–4 and the step ΔC between the neighboring isoconcentration lines in Figs. 3a–3c.

Growth stage	Number of the isoconcentration line	Si (Fig. 3a) C	Si (Fig. 3a) ΔC	Si_2C (Fig. 3b) C	Si_2C (Fig. 3b) ΔC	SiC^2 (Fig. 3c) C	SiC^2 (Fig. 3c) ΔC
I	*1*	2.5×10^{-7}	2.4×10^{-7}	6.0×10^{-8}	5.8×10^{-8}	8.9×10^{-8}	8.0×10^{-11}
	2	2.6×10^{-6}		6.4×10^{-7}		8.8×10^{-11}	
II	*3*	6.0×10^{-9}	5.0×10^{-10}	1.1×10^{-9}	1.1×10^{-10}	1.8×10^{-9}	2.4×10^{-10}
	4	1.1×10^{-8}		2.2×10^{-9}		4.3×10^{-9}	

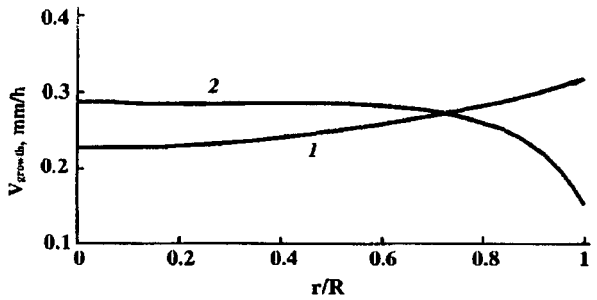

FIG. 4. Radial profile of the growth velocity V_{growth} of a SiC single crystal at the initial (*1*) and intermediate (*2*) stages of growth.

and Table I); the contribution of this component is found to be substantial, and the profile of the growth velocity (form of the growth front) becomes convex (Fig. 4, curve *2*). The experimental results confirm this change in the form of the growth front.

A change in the distribution of the components in the gas phase produces a change in the evaporation–condensation conditions, a change in the equilibrium concentrations, a difference in the intrinsic point defects (as a result of the difference in deviations from the stoichiometric composition) distributed along the length and radius of the crystal, and mechanical stresses in the crystal lattice. In practice, these processes are intensified by fluctuations of the technological conditions. Unfortunately, at present there are no results available from investigations of the distribution of intrinsic point defects and their correlation with growth conditions in the SiC single crystals obtained.

Despite the simplifications employed in the calculations, the results obtained agree satisfactorily with the experimental results. At present, calculations for a more complicated configuration of the growth cell and simulation of the mechanical stresses in the volume of the crystal are being conducted on the basis of these results.

[1] Yu. M. Tairov and V. F. Tsvetkov, J. Cryst. Growth, **52**, 146 (1981).
[2] Yu. M. Tairov and V. F. Tsvetkov, in *Crystal Growth and Characterization of Polytype Structures*, edited by P. Krishna, Pergamon Press, N. Y., 1983, Vol. 7. p. 111.
[3] Yu. M. Tairov and V. F. Tsvetkov, in *Growth and Defect Structures* (series on *Crystals: Growth, Properties, and Applications*) edited by H. C. Freyhardt, Springer-Verlag, N. Y., 1984, Vol. 10, p. 1.
[4] D. Hofmann, M. Heinze, A. Winnacker, F. Durst, and L. Kadinski *et al.*, J. Cryst. Growth **146**, 214 (1995).
[5] F. Raĭkhel', Yu. M. Tairov, M. G. Travadzhyan, and V. F. Tsvetkov, Izv. Akad. Nauk SSSR, Neorg. Mater. **16**, 1011 (1980).
[6] J. Drowart and G. De Maria, *Silicon Carbide — A High Temperature Semiconductor*, Pergamon Press, N. Y., 1960, p. 16.
[7] Yu. M. Tairov and V. F. Tsvetkov, Izv. Akad. Nauk SSSR, Neorg. Mater. **13**, 1606 (1976).
[8] B. P. Gerasimov, A. V. Lesunovskiĭ, V. V. Mitin, T. A. Borisova, and D. Ya. Rovenskiĭ in *Numerical Methods* [in Russian], Nauka, Moscow, 1989, p. 112.
[9] Yu. M. Tairov, V. A. Taranets, and V. F. Tsvetkov, Izv. Akad. Nauk SSSR, Neorg. Mater. **15**, 9 (1979).
[10] S. K. Lilov, Yu. M. Tairov, and V. F. Tsvetkov, J. Cryst. Growth **46**, 269 (1979).
[11] L. D. Landau and E. M. Lifshitz, *Fluid Mechanics*, Pergamon Press, N. Y. [Russian orig., Nauka, Moscow, 1988].
[12] *Gas Encyclopaedia*, Elsevier, 1976.

Translated by M. E. Alferieff

Polarization photosensitivity of silicon solar cells with an antireflection coating consisting of a mixture of indium and tin oxides

V. M. Botnaryuk, A. V. Koval', A. V. Simashkevich, and D. A. Sherban

State University of Moldovia, Kishinev, Moldovia

V. Yu. Rud'

State Technical University, 195251 St. Petersburg, Russia

Yu. V. Rud'

A. F. Ioffe Physicotechnical Institute, Russia Academy of Sciences, 194021 St. Petersburg, Russia
(Submitted August 15, 1996; accepted for publication October 29, 1996)
Fiz. Tekh. Poluprovodn. **31**, 800–805 (July 1997)

The photoelectric properties of ITO/*n*-Si solar cells with ITO-side oblique incidence of linearly polarized light on the solar cells have been studied. Polarization photosensitivity and an increase in the relative quantum efficiency of photoconversion as a result of a decrease in reflection losses were found. The induced photopleochroism coefficient P_I increases with the angle of incidence θ as $P_I \sim \theta^2$. The polarization photosensitivity of solar cells was studied as a function of the photon energy between the band gaps of the two contiguous materials. The results show that the solar cells studied can be used as selective polarimetric photosensors. © *1997 American Institute of Physics.* [S1063-7826(97)01007-7]

Transparent conducting oxides are widely used as a wide-gap semiconductor window, which simultaneously acts as an antireflection coating with a low surface layer resistance. As a whole, this gives a substantial increase in the efficiency of solar cells (SCs).[1–3] Specifically, solar cells with $\approx 43\%$ higher efficiency than cells without an antireflection film consisting of a mixture of indium and tin oxides [$10\%SnO_2 + 90\%In_2O_3$ (ITO) $E_G \simeq 3.6$ eV] have been developed on the basis of the heterosystem ITO/$p-n$-Si.[1,4,5] The polarization photosensitivity of solar cells has still not been investigated.[1] In the present article we report the results of an experimental study of the photoelectric processes in ITO/*n*-Si structures in linearly polarized radiation (LPR); this study suggests that solar cells can be used in polarization photoelectronics as well as in polarization photoelectric spectroscopy — for diagnostics of the antireflection properties of coatings in ready-made components.

1. The solar cells were produced using a *n*-type KEF-4.5 silicon plate oriented in the (111) crystallographic plane. The ITO films were deposited on *n*-Si plates preheated to temperatures $T_s \approx 400-500$ °C. The deposition was performed by the method of pulverization of alcohol solutions[6] of indium and tin chlorides 9 parts ($InCl_3 : 3H_2O$) + 1 part ($SnCl_3 : 5H_2O$) in an oxygen atmosphere. The ITO layers with geometric thickness $d \approx 0.5$ μm were deposited under the indicated conditions in a time $\tau \approx 40-60$ s. The films obtained were electrically uniform. The free electron density and the Hall mobility in the ITO films obtained were equal to $\simeq 10^{21}$ cm^{-3} and $\simeq 30$ cm^2/(V·s) at $T = 300$ K, respectively. The films possessed a uniform dark-lilac color and high adhesion to the chemically polished surface of the *n*-type Si plates. The films exhibited high optical transmission $\approx 95\%$ in the wavelength range from 0.25 up to 1 μm. After deposition the ITO film was equipped with an indium contact grid, and the free silicon surface of the plate was coated with an Al layer. The area of the finished solar cells was equal to ≈ 1 cm^{-2}.

To determine the polarization parameters of the photosensitivity the solar cells were secured on a STF-1 Fedorov table, which made it possible to vary continuously the angle of incidence θ of the radiation on the receiving surface and the azimuthal angle φ between the electric vector **E** of the light wave and the plane of incidence of the radiation (PIR) to within $\pm 30'$. The ratio of the areas of the photoreceiving surface and the light beam was chosen in such a way that the flux of the linearly polarized radiation would not fall outside the limits of the ITO film right up to the maximum angles $\theta \approx 85°$. To make sure that the photosensitivity of the solar cells could be measured with maximum values of θ, measures were taken to eliminate the vignetting of the illuminated ITO surface. The photosensitivity of the solar cells in LPR was measured in the regime of a short-circuit photocurrent, which was proportional to the flux density of the incident radiation, making it possible to determine the relative photoconversion quantum efficiency η as the ratio of the photocurrent to the number of incident photons.

2. The solar cells obtained by us had good rectifying properties. The typical stationary current-voltage characteristic of one such structure is shown in Fig. 1 (curve *1*). The transmission direction in the SC corresponded to a negative polarity of the external bias voltage on the ITO film. The direct I–V characteristic in the bias range $U > 0.2$ V can be approximated as $U = U_{\text{cut off}} + R_{\text{res}} i$. The cutoff voltage is reproduced well in the SCs obtained and reaches $U_{\text{cut off}} \approx 0.1$ V, which probably corresponds to the contact potential difference of the isotopic ITO/*n*-Si heterocontact. The residual resistance $R_{\text{res}} \approx 4-5$ kΩ at $T = 300$ K, and the reverse currents with $U \approx 0.5$ V usually did not exceed 2×10^{-5}A. Sharp breakdown occurs at voltages $U \approx 2-2.5$ V. When the SCs were illuminated from the ITO side, the photosensitivity

 1063-7826/97/070677-04$10.00

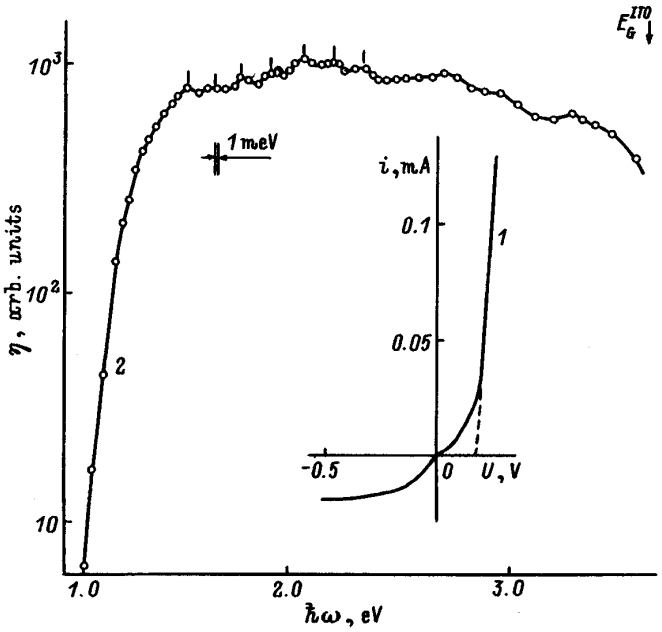

FIG. 1. Stationary current–voltage characteristic (1) and the spectral dependence of the relative quantum efficiency of photoconversion of a ITO/*n*-Si solar cell ($T=300$ K; illumination with unpolarized radiation in a direction along the normal from the ITO side of the film).

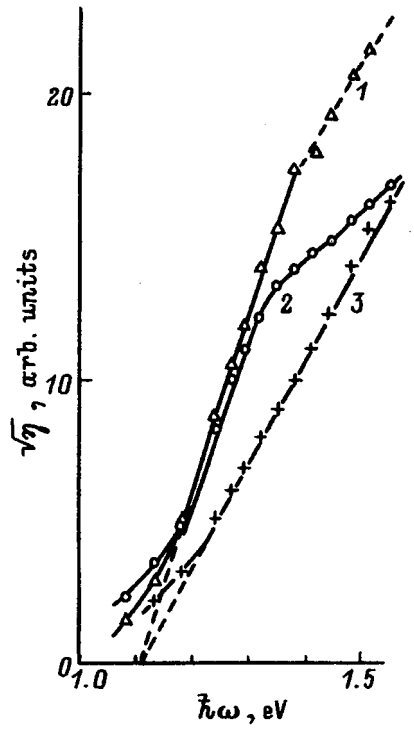

FIG. 2. Spectral dependence of the relative quantum efficiency of photoconversion in the coordinates $\sqrt{\eta}-t\omega$ for an ITO/*n*-Si solar cell ($T=300$ K; *1* — unpolarized radiation, $\theta=0°$; *2* — **E** ∥ PIR, $\theta=70°$; *3* — **E**⊥ PIR, $\theta=70°$).

was high and reached ≈80−90 mA/w. Under AM 1.5 illumination conditions the efficiency of the solar cells obtained was equal to 10–11%.

The spectral dependence of the relative quantum efficiency η of photoconversion for one typical SC is shown in Fig. 1 (curve *2*). Under illumination in a direction normal to the ITO plane the photosensitivity spectrum is a wide-band spectrum. The total width of the spectral band of photosensitivity at half-height is $\delta_{1/2}\approx 2.0$ eV, making it possible to cover a wide spectral region from 1.4 to 3.4 eV. Therefore, the contact between *n*-Si and the ITO antireflection film exhibits a window effect, which is characteristic of ideal heterostructures. The long-wavelength limit of the SC is determined by indirect interband transitions in the narrow-band gap component of the heterostructure. We see from Fig. 2 (curve *2*) that in the coordinates $\sqrt{\eta}-\hbar\omega$ the long-wavelength edge of photosensitivity rectifies and under the extrapolation $\sqrt{\eta}\to 0$ is characterized by the intercept on the photon energy axis at $\hbar\omega=1.1$ eV, which equals the band gap in silicon.[7]

A system of equidistant peaks, whose maxima are separated by ≈0.13 eV, appeared clearly in the spectral curves $\eta(\hbar\omega)$ for all solar cells in the case of natural radiation incident on the ITO film in a direction normal to the plane. If this system of bands is attributed to interference in the ITO layer with refractive index[1] $n=1.8$, then we obtain a thickness $d=2.2$ μm, which is clearly greater than the thickness of the ITO film. Therefore, it can be assumed that the observed system of bands cannot be attributed to the interference of radiation in the ITO film, and additional investigations of the solar cells must be performed in order to clarify its nature.

3. When the structures are illuminated with LPR in a direction normal to the plane of the ITO film ($\theta=0°$), the photocurrent is independent of the position of **E** relative to the principal crystallographic axes of the Si plates. This is determined by the isotropic character of the photoactive absorption in ITO and Si. As a result, the photopleochroism coefficient

$$P_I=\left(\frac{i^p-i^s}{i^p+i^s}\right)100\%$$

where i^p and i^s are, respectively, the photocurrents with **E** ∥ PIR and **E**⊥ PIR, is equal to zero in the entire region of photosensitivity of the SC. For this reason, there are grounds for believing that these solar cells do not possess natural photopleochroism (Fig. 3).[8] Switching to measurements of the photosensitivity of SCs in a geometry with oblique incidence of LPR on the receiving plane of the cells, i.e., $\theta>0°$, differences appear in the values of the photocurrents i^p and i^s. As a result, the photopleochroism coefficient becomes different from zero and increases continuously with increasing angle of incidence as a square law $P_I\sim\theta^2$. Indeed, as one can see from Figs. 3a and 3b, the function $P_I(\theta)$ ''leaves'' zero at $\theta=0°$, which shows that there is no natural photopleochroism.[8] In the case $\theta>0°$ the photopleochroism which appears is classified, according to Ref. 8, as induced, and in the coordinates $\sqrt{P_I}-\hbar\omega$ these curves are straight lines (Fig. 3a and 3b, curves *4*), in agreement with the analysis in Ref. 9.

It also follows from the data in Figs. 3a and 3b that the coefficient P_I exhibits an explicit dependence on the energy of the LPR photons in the region of photosensitivity of the

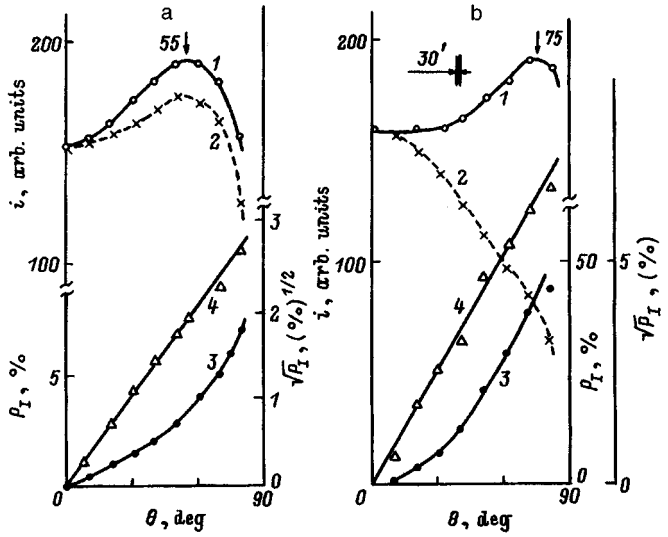

FIG. 3. Short-circuit photocurrents (*1*, *2*) and induced photopleochroism coefficient (*3*, *4*) of an ITO/*n*-Si solar cell ($T=300$ K; $\hbar\omega$, eV: a) 1.60, b) 1.27).

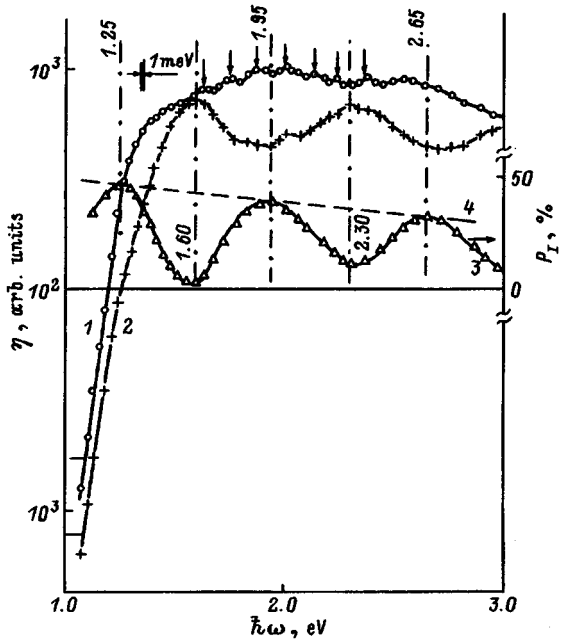

FIG. 4. Spectral curves of the relative quantum efficiency (*1*, *2*) and induced photopleochroism coefficient (*3rs*, *4*) of an ITO/*n*-Si solar cell ($T=300$ K; $\theta=70°$, *1* — $\mathbf{E}\parallel$ PIR, *2* — $\mathbf{E}\perp$ PIR).

SCs. This result is at variance with the theoretical analysis performed without regard for the antireflection effect and for numerous experimental results obtained under conditions at which this effect can be disregarded.[8–12]

It is also evident from the curves in Figs. 3a and 3b for the photocurrents i^p and i^s versus the angle of incidence of the LPR that for one of the polarizations these dependences agree qualitatively with the dependence expected from the Fresnel relations describing the passage of a light wave through the boundary between two media.[13] Such dependences are shown in Fig. 3b (curves *1* and *2*). It follows from them that for a light wave polarized in the plane of incidence the photocurrent i^p increases with the angle of incidence and passes through a maximum near $\theta\approx 75°$. This increase is $i^p_{75°}/i^p_{0°}\approx 1.2$, which corresponds to a decrease in reflection losses. For the other polarization $\mathbf{E}\perp$ PIR (Fig. 3, curve *2*), on the other hand, the photocurrent i^s decreases with increasing angle of incidence in the entire range of variation of θ, and this corresponds to an increase in reflection losses.

For other photon energies (Fig. 3a, curves *1* and *2*) the photocurrents i^p and i^s have the same angular dependence, they are close in magnitude for the same values of θ, and they reveal a maximum at nearly the same angle, $\theta\approx 55°$. Therefore, as the energy of the incident radiation photons varies, we see regions in which for both polarizations of the LPR the photocurrents increase with increasing angle θ; this indicates a decrease in the reflection losses not only for the wave $\mathbf{E}\parallel$ PIR, but also for $\mathbf{E}\perp$ PIR, which does not follow from the Fresnel relations.[13,14] In our opinion, such a behavior in the polarization dependence of the photocurrent versus the angle of incidence of the LPR can be attributed to the antireflection effect of the ITO film. As follows from Fig. 1 (curve *2*), this effect was not sharply manifested in the spectral dependence of the η in the case where unpolarized light was used. However, on switching to LPR, there appear in the spectral dependences of i^p and i^s photocurrent maxima and minima which were ''hidden'' in the case of the natural radiation by the summation of the contribution from light with the complete set of polarizations.

Figure 4 shows the typical spectra of the quantum efficiency of photoconversion for two polarizations of the LPR incident on the surface of a ITO film at angle $\theta\approx 75°$, when the effect of polarization on the photoactive absorption is now quite large in accordance with the relation $P_I\sim\theta^2$. The long-wavelength edge of the photoactive absorption splits in this case, $i^p>i^s$ in accordance with the Fresnel relations.[13] It is evident from Fig. 2 (curves *2* and *3*) that for both polarizations the long-wavelength photosensitivity of the SC follows the square-root dependence $\sqrt{i^p, i^s}\sim\hbar\omega$, which is characteristic of indirect interband transitions, and that extrapolation of these dependences to zero gives the same value of the intercept on the energy axis, which coincides with the case of natural radiation (Fig. 2, curve *1*), and which is equal to the band gap in silicon.[7] This fact agrees with the nature of the anisotropy of the photoactive absorption induced by oblique incidence of LPR[8] and arising as a result of the polarization dependence of the passage of radiation of different polarizations through the air/ITO interface and reflecting the degeneracy of the states in the upper valence band of silicon in the absence of directed perturbations.

In the region of the maximum photosensitivity of the SCs (Fig. 4, curves *1* and *2*), the photocurrents i^p and i^s for different polarizations vary in phase opposition. For example, the maxima in the spectral curve $i^p(\hbar\omega)$ at 1.95 and 2.65 eV correspond to minima in the curve $i^s(\hbar\omega)$ and, conversely, the maxima in the spectrum $i^s(\hbar\omega)$ at 1.60 and 2.30 eV correspond to the minima in the spectrum $i^s(\hbar\omega)$. We call attention to the fact that near the photon energies 1.60 and 2.30 eV the spectral curves converge to one another, while at energies 1.95 and 2.65 eV, on the other hand, a

maximum divergence is observed between $i^s(\hbar\omega)$ and $i^p(\hbar\omega)$.

We see that the spectrum $\eta(\hbar\omega)$, which is observed under illumination with unpolarized light and in which the characteristic features manifested in LPR (Fig. 4, curves *1* and *2*) are ''closed'' and therefore not manifested, can be obtained by adding the polarization dependences $i^s(\hbar\omega)$ and $i^p(\hbar\omega)$, which corresponds to a transition from LPR to natural radiation. Here it is relevant to note that the system of seven equidistant maxima (Fig. 1, curve *2*) that appears in natural radiation also remained in LPR but only in the polarization $\mathbf{E} \parallel$ PIR.

If the minima manifested in LPR at 1.95 and 2.65 eV or maxima at 1.60 and 2.30 eV in the dependences $\eta^p(\hbar\omega)$ and $\eta^s(\hbar\omega)$ are attributed to interference of radiation in the ITO film, then estimates of the film thickness give the value $d \approx 0.47$ μm, which is virtually identical to the measured thickness of the ITO.

The most distinct effect of polarization on the photoactive absorption in ITO/Si structures was reflected in the spectral dependence of the induced photopleochroism coefficient (Fig. 4, curve *3*). The oscillatory character of the photopleochroism is clearly seen in it. The minima of the photopleochroism correspond to regions of convergence in the spectral dependences $\eta^p(\hbar\omega)$ and $\eta^s(\hbar\omega)$, while the maxima of P_I correspond to maxima in the curves $\eta^p(\hbar\omega)$ and minima in $\eta^s(\hbar\omega)$. Therefore, there are grounds for concluding that the spectral dependence of the induced photopleochroism can be used to monitor the magnitude and spectral position of the antireflection effect. It is obvious that the effect is maximum in the minima of the spectral dependence of induced photopleochroism as $P_I \to 0$. Since the photocurrents $i^p = i^s$ when $P_I = 0$, it can be assumed that we have antireflection in this case for waves of both polarizations. At the same time, we also have antireflection at the maxima of the dependences $P_I(\hbar\omega)$. However, since in this case $i^p > i^s$, it can be asserted that antireflection is attained only for a wave with $\mathbf{E} \parallel$ PIR, while for $\mathbf{E} \perp$ PIR polarization reflection predominates, which accounts for the decrease of i^s relative to i^p.

If the values of the induced photopleochroism at the maxima of the dependence $P_i(\hbar\omega)$ are connected by a straight line (Fig. 4, curve *4*), then the photon-energy dependence of P_I is weak, as theoretical analysis of the induced photopleochroism predicts.[9] Then the existing ''dips'' in the experimental dependence $P_I(\hbar\omega)$ (curve *3*) relative to the dependence extrapolated according to its maximum values (curve *4*) then clearly show a region of antireflection action of the ITO film. The maximum values P_I^m make it possible, in accordance with Ref. 9, to estimate the refractive index of the material of the entrance window of the SC as $n \approx 1.8-2$, which corresponds to ITO. The drop observed in P_I^m with increasing photon energy (Fig. 4, curve *4*) apparently indicates that n decreases slightly along the thickness of the film in the direction toward the outer plane of ITO.

In closing, we note that the maximum azimuthal current photosensitivity in our SCs at angles of incidence $\theta \approx 70°$ reaches 80 mA/(W·deg) at $T = 300$ K. Therefore, such solar cells can be used as selective polarimetric sensors, and the polarization measurements of the photosensitivity of a SC can themselves be used in nondestructive diagnostics of ready-made structures and in the technology of fabricating antireflection coatings.

This work was supported by the Committee of the European Society under contract INTAS N 94-3998.

[1] M. M. Koltun, *Optics and Metrology of Solar Radiation* [in Russian], Nauka, Moscow, 1985, p. 280.
[2] Yu. N. Malevskiĭ and M. M. Koltun [Eds.], *Solar Power* [Russian trans., Mir, Moscow, 1979, p. 375].
[3] O. P. Agnikhatri and B. K. Gupta, *Selective Surfaces in Solar Setups* [Russian trans., Mir, Moscow, 1984, p. 312].
[4] A. I. Malik, V. A. Baranyuk, and V. A. Manasson, Geliotekhnika, No. 1, 3 (1980).
[5] N. Mardesich, in *Rec. 15th IEEE Photovolt. Spec. Conf.*, Kissimee, 1981, IEEE, N. Y., 1981, p. 446.
[6] N. V. Suĭkovskaya, *Chemical Methods of Obtaining Thin Transparent Films* [in Russian], Khimiya, Leningrad, 1971, p. 198.
[7] P. I. Baranskiĭ, V. P. Klochkov, and I. V. Potykevich, *Handbook of Semiconductor Electronics* [in Russian], Naukova dumka, Kiev, 1975, p. 240.
[8] Yu. V. Rud', Izv. Vyssh. Uchebn. Zaved., Fiz. **29**, No. 8, 67 (1986).
[9] G. A. Medvedkin and Yu. V. Rud', Phys. Status Solidi A **67**, 333 (1981).
[10] N. N. Konstantinova, M. A. Magomedov, V. Yu. Rud', and Yu. V. Rud', Fiz. Tekh. Poluprovodn. **26**, 1861 (1992) [Sov. Phys. Semicond. **26**, 1043 (1992)].
[11] S. G. Konnikov, V. Yu. Rud', Yu. V. Rud', D. Melebaev, A. Berkeliev, M. Serginov, and S. Tilevov, Jap. J. Appl. Phys. **32-3**, 515 (1993).
[12] V. Yu. Rud', *Author's Abstract of Candidate's Dissertation*, Physicotechnical Institute, Russian Academy of Sciences, St. Petersburg, 1995, p. 17.
[13] G. S. Landsberg, *Optics* [in Russian], Moscow, 1976, p. 927.
[14] R. Azzam and M. Bashara, *Ellipsometry and Polarized Light* [in Russian], Moscow, 1981, p. 584.

Translated by M. E. Alferieff

Photosensitivity of thin-film ZnO/CdS/Cu(In, Ga)Se_2 solar cells

T. Walter

Institut für Physikalische Elektronik, Universitat Stuttgart D-70569 Stuttgart, Germany

V. Yu. Rud'

State Technical University, 195251 St. Petersburg, Russia

Yu. V. Rud' and H. W. Schock

A. F. Ioffe Physicotechnical Institute, Russian Academy of Sciences, 194021 St. Petersburg, Russia
(Submitted August 15, 1996; accepted for publication October 29, 1996)
Fiz. Tekh. Poluprovodn. **31**, 806–810 (July 1997)

The photoelectric properties of thin-film ZnO/CdS/Cu(In,Ga)Se_2 solar cells were studied by polarization photoactive absorption spectroscopy. It was shown that the thin-film solar cells have a high efficiency relative to the intensity of unpolarized radiation in the photon energy range from 1.2 to 2.5 eV. The induced photopleochroism coefficient P_I increases with the angle of incidence of the incident radiation as $P_I \sim \theta^2$ and at 70° it reaches 17–20% with photon energy 1.3 eV. Oscillations of the photopleochroism were also observed. These results are discussed taking into account the antireflection effect. The results obtained by us make it possible to use such solar cells as wide-band photosensors for linearly polarized radiation and for monitoring the production of high-efficiency, thin-film solar cells based on ternary semiconductors. [S1063-7826(97)01107-1]

I–II–VI_2 ternary compounds have already found application in the production of high-effciency photovoltaic solar cells, since their electrical and optical properties are optimal for devices of this kind. Polycrystalline $CuIn_xGa_{1-x}Se_2$ (CIGSe) thin films make it possible to obtain solar photoconversion efficiency of up to 17%.[1–4] Further optimization of the production of thin-film solar cells (TSCs) of this type and an increase in the photoconversion efficiency will require a more thorough study of the relationship between the photoelectric parameters and the technological conditions under which the films based on I–III–VI_2 compounds are formed.[1,5] In this paper we report the results of comprehensive experimental study of the photoelectric properties of ZnO/CdS/CIGSe TSCs by the methods of polarization photoactive absorption spectroscopy.[6]

1. In the study we used ZnO/CdS/CIGSe thin-film solar cells fabricated at the Institute of Physical Electronics (IPE, Germany). Films of the solid solution were produced by vacuum thermal sputtering of the components from individual sources. The composition of the films corresponded to the ratio In/(Ga + In) = 0.25 and was chosen on the basis of the requirements which must be met in order to obtain the maximum photoconversion efficiency.[1] The films were deposited on metallized molybdenum glass. The molybdenum ensured an ohmic contact to the CIGSe film. The photosensitive structure was produced by depositing on the CIGSe surface a $\simeq 0.5$-μm-thick film which was not specially doped cadmium sulfide. Next, a $\simeq 1$-μm-thick ZnO film was deposited on the CdS surface; this film provided high optical transmission and allowed for collection of charge carriers. The technological process of production of TSCs was completed by deposition of a current-extracting metal grid on the ZnO surface. Under AM–1.5 illumination conditions (100 mW/cm^2) the photoconversion efficiency in the TSCs obtained with an active surface area of up to 2 cm^2 was equal to 12–15%.

The TSCs ordinarily contained six separate heterostructures on a single glass substrate. The heterostructures could then be switched in the required manner, taking into account the ratio of their photoelectric parameters.

2. Figure 1 shows a typical stationary current-voltage characteristic (IVC) of one such structure. The transmission direction in the TSC corresponds to a negative external bias voltage on ZnO; this corresponds to the energy diagram of the heterostructure.[3] One can see from Fig. 1 (curve 1) that for $U_d > 0.4$ V the direct current grows exponentially as

$$I = I_0(\exp eU_d/\beta kT - 1).$$

The typical value of β for the TSCs is $\beta = 2.0-2.2$. A high value of β is also known in other types of solar cells based on $CuInSe_2$ (CISe) and is ordinarily attributed to the recombination of photogenerated pairs in the space-charge region.[3,4] The deviation observed for $U_d > 0.7$ V from an exponential law is due to the effect of the serial resistance of the TSC on the straight IVC. In the region $U_d > 0.7$ V, as one can see from Fig. 1, the relation between the current and the voltage is linear

$$U = U_0 + R_0 \cdot I,$$

where the cutoff voltage U_0 in different structures is in the range 0.6–0.7 V, and the residual resistance is in the range $R_0 = 6-16\ \Omega$ at $T = 300$ K. The reverse current in the TSC grows in proportion to the voltage up to $\simeq 5$ V; this reflects the fact that the leakage currents make the determining contribution to charge-carrier transport in reverse-biased structures. As an illustration, the values of some parameters for six TSCs, arranged on a common glass substrate, are presented in Table I. One can see from the table that, together

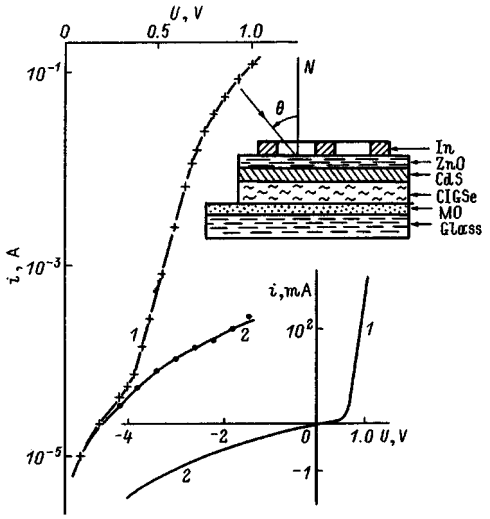

FIG. 1. Stationary current-voltage characteristic of a *n*-ZnO/*n*-CdS/*p*-CIGSeTSC. *1* — Direct bias, *2* — reverse bias. $T=300$ K. Inset: Construction and scheme of illumination of the TSC.

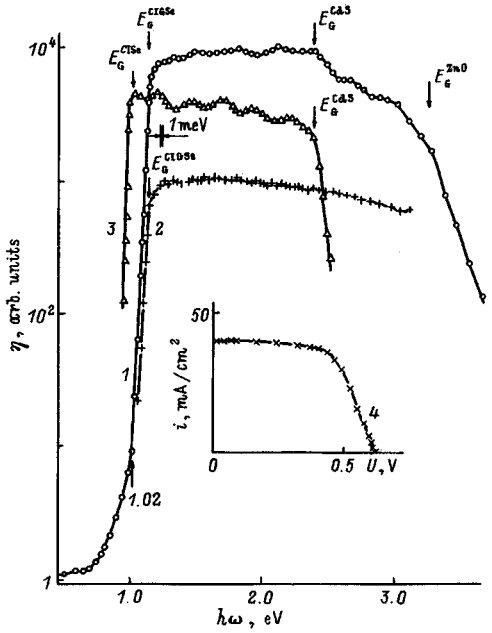

FIG. 2. Spectral dependences of the relative quantum efficiency η of photoconversion for ZnO/CdS/CISe/Mo (*1*), In/CIGSe/Mo (*2*), and CdS/CISe (*3*) structures and the load characteristic of a ZnO/CdS/CIGSe TSC (*4*) at $T=300$ K (illumination from the wide-gap film or indium side in the case of the surface-barrier structure); unpolarized radiation: to prevent superposition, the curves are shifted relative to one another along the ordinate.

with R_0, a large spread is observed in the values of the reverse current I_R for $U_R=1$ V. The most reproducible parameter for the TSCs obtained in a single technological process is probably the cutoff voltage, which equals the saturation photovoltage U_∞ on the same structures and which can be compared with the contact potential difference Φ. The relatively good reproducibility of Φ in these cells shows that the doping level of the layers and the compositions of the solid solution in the TSCs being compared are quite close.

3. When the TSC is illuminated, a photovoltaic effect appears; here the sign of the photovoltage corresponds to the negative polarity of the voltage on ZnO. Figure 2 (curve *4*) shows a typical load characteristic of one of the best TSCs, characterized by a filling factor of 0.83. The values of the open-circuit photovoltage U_i and the short-circuit current I_s under AM-1.5 illumination conditions are also presented in Table I. In the best cells i_s reaches 40 mA/cm^2, which is a record high value for the TSC construction under study. The observed variance in i_s for the TSCs formed on a common substrate shows that the technology must be improved so as to decrease the variance in the parameters of individual cells. As a result of the observed variance of the TSC parameters, the photoconversion efficiency decreases with increasing active area of the TSC.

Figure 2 shows the spectral dependences of the relative quantum efficiency η of photoconversion, calculated as the ratio of the short-circuit photocurrent i_s to the number of incident photons, for several types of photovoltaic cells at $T=300$ K under conditions such that the cells are illuminated by unpolarized light in a direction normal to the photoreceiving surface. We see that in the ZnO/CdS/CIGSe TSCs photosensitivity is observed in a wide spectral region from 0.5 to 3.5 eV. The long-wavelength exponential edge of η is described by a steep slope $S=45-60$ eV^{-1} for different TSCs (see Table I). The energy position of the long-wavelength edge of η in a CIGSe-based TSC is displaced relative to the similar edge of η for a CdS/CISe structure obtained by depositing a $\simeq 2$-μm-thick CdS film on a thick ($\simeq 0.5$ mm) *p*-CISe substrate obtained by crystallization of a stoichiometric melt. This shift is due to the substitution of In atoms for Ga atoms,[5] while the close slope of the long-wavelength edge for ZnO/CdS/CIGSe and CdS/CISe structures indicates that the energy spectrum of the solid solution CIGSe, just as the completely ordered compound CISe, is characterized by direct interband transitions. This result agrees with Ref. 5.

TABLE I. Photoelectric properties of a ZnO/CdS/CIGSe TSC at $T=300$ K.

Cell No.	U_0, V	R_0, Θ	i_R, mA ($U=1$V)	S, eV^{-1}	$\delta_{1/2}$, eV	U_∞ V	i_s, mA/cm^2 ($L\simeq 100$ mW/cm^2)	U_i, V ($L\simeq 100$ mW/cm^2)
1	0.6	16	0.2	55	1.5	0.60	30	0.60
2	0.6	16	0.7	48	1.6	0.62	35	0.62
3	0.7	7.1	0.1	58	1.6	0.65	40	0.68
4	0.6	6.7	50	42	1.5	0.61	28	0.58
5	0.6	11.4	7	48	1.6	0.62	32	0.60
6	0.7	14.5	0.5	52	1.6	0.70	33	0.70

The sharp short-wavelength boundary of photosensitivity for CdS/CISe structures (Fig. 2, curve *3*) is caused by the interband transitions in CdS and extension of the layer of photogenerated pairs from the active region of the TSC over distances greater than the diffusion length of holes in CdS. A similar, with respect to spectral position and physical nature, short-wavelength dropoff of η near the band gap in CdS, as one can see from Fig. 2 (curve *1*), also appears in a ZnO/CdS/CIGSe TSC. However, because of the much thinner CdS layer, in the latter case the drop in η is much weaker.

To determine the role of CdS and ZnO films in the short-wavelength photosensitivity of TSCs based on polycrystalline CIGSe films, we also obtained surface-barrier In/CIGSe structures. The typical spectral dependence of η for one such structure is shown in Fig. 2 (curve *2*). The long-wavelength edge of η in these structures has the same spectral position and slope as those characteristic of ZnO/CdS/CIGSe TSCs; this serves as additional evidence indicating that this edge is related to direct interband electronic transitions in the energy spectrum of CIGSe. As the photon energy increases to 3 eV, the photosensitivity of In/CIGSe structures does not show a pronounced short-wavelength drop; this shows that the efficiency of collection of photogenerated pairs by a surface-barrier junction is high. Switching to TSC (Fig. 2, curve *1*), it should be noted that the drop in η arising for $\hbar\omega > E_G^{\mathrm{CdS}}$, even for small CdS thicknesses, is due to the influence of radiation absorption in the narrow-gap CdS film, and for $\hbar\omega > E_G^{\mathrm{CdS}}$ in the ZnO film as well.

The spectral contour $i(\hbar\omega)$ for separate TSCs formed on a common glass substrate turned out to be quite reproducible. The total width of their spectral characteristic $\eta(\hbar\omega)$ at half-height is $\delta_{1/2} = 1.5-1.6$ eV for different TSCs (see Table I) and it characterizes them as wide-band phototransducers of natural radiation.

It should also be noted that a system of equidistant peaks is consistently observed in the spectral dependence $\eta(\hbar\omega)$ of the TSCs. In the best structures (Fig. 2, curve *1*), seven peaks can be distinguished in the spectrum of η. If their appearance is attributed to the interference of radiation in the ZnO film, then an estimate gives a thickness equal to the measured value. The manifestation of the interference features in the photosensitivity of the TSC is evidence of the rather high structural perfection of their constituent polycrystalline films.

The wide-band character of the photosensitivity spectra remains after the transition to the surface-barrier structures based on CIGSe films which are analogous to TSCs, but the system of maxima characteristic of TSCs is absent (Fig. 2, curves *1* and *2*). These features show that both types of energy barriers (In/CIGSe and CdS/CIGSe) are efficient enough to suppress the recombination losses at the *p*-CIGSe surface, and the interference peaks in η (Fig. 2, curve *1*) can be attributed to optical processes in the ZnO films.

According to Fig. 2 (curve *3*), in the case of CdS/CISe structures a system of six equidistant peaks is clearly seen in the entire range of maximum photosensitivity; this system agrees with the interference of the incident radiation in the CdS film.

4. In the case of illumination of the thin-film ZnO/CdS/CIGSe structures with linearly polarized radiation (LPR) in a direction normal to the ZnO surface, the short-circuit photocurrent is independent of the position of the polarization plane **E** of the radiation. It can be concluded, therefore, that the natural photopleochroism P_N is absent in heterostructures fabricated using the anisotropic materials (CIGSe, CdS, and ZnO[7–10]). This situation can be attributed to the polycrystalline structure of the films or to texturing, when the tetragonal and hexagonal axes are predominantly oriented in a direction normal to the ZnO surface.

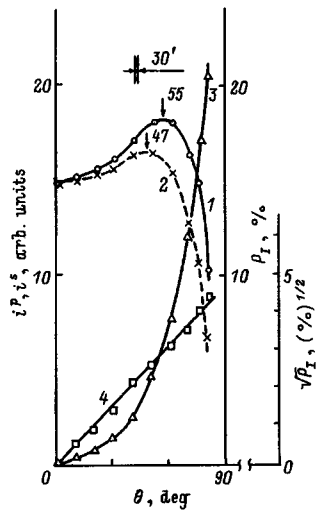

FIG. 3. Short-circuit photocurrents i^p (*1*) and i^s (*2*) and the induced photopleochroism coefficient (*3, 4*) as a function of the angle of incidence of LPR on the receiving surface of a ZnO/CdS/CIGSe TSC at $T = 300$ K ($\hbar\omega = 1.33$ eV).

As soon as the angle of incidence Θ of the LPR is different from 0°, the short-circuit photocurrent manifested in the entire photosensitivity range from 0.5 to 3.5 eV in all tested TSCs begins to exhibit a dependence on the orientation of the electric field vector **E** of the light wave relative to the plane of incidence (PI) of the radiation on the receiving ZnO surface. The periodic dependence of the photocurrent on the azimuthal angle φ between **E** and PI with $\Theta = \text{const}$ was consistent in the entire range of photosensitivity of the TSC with the law

$$i_\varphi = i^p \cos^2\varphi + i^s \sin^2\varphi,$$

where the photocurrents i^p and i^s correspond to the polarizations $\mathbf{E} \parallel$ PI and $\mathbf{E} \perp$ PI, respectively.

The typical dependences of the photocurrents i^p and i^s on the angle of incidence of the LPR for one TSC are shown in Fig. 3 (curves *1* and *2*). We see that for $\Theta = 0°$ the values of i^p and i^s are the same, and that they differ only for $\Theta > 0°$. The angular dependences obtained for TSCs show a new feature with respect to the results of investigations of the induced photopleochroism.[11–15] Indeed, as one can see from Fig. 3 (curves *1* and *2*), the photocurrents i^p and i^s exhibit a similar behavior. At first, they increase with Θ, reach a maximum value for definite angles of incidence for each polarization, and only then start to drop rapidly. According to the Fresnel relations, such a behavior of the amplitude transmission coefficients of the air–conductor interface should be

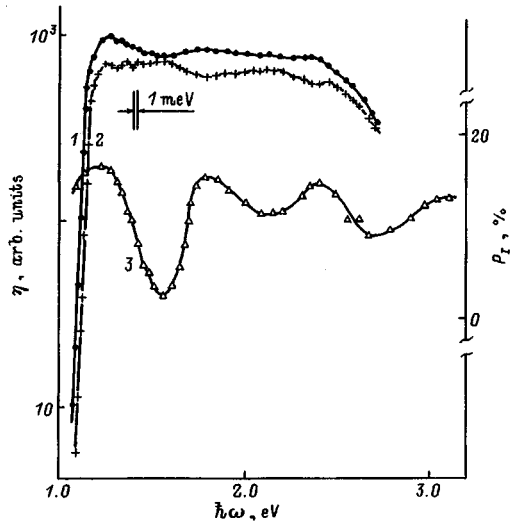

FIG. 4. Spectral dependences of the relative quantum efficiency of photoconversion η^p (*1*), η^s (*2*), and the induced photopleochroism coefficient (*3*) of a ZnO/CdS/CIGSe/Mo TSC ($\Theta = 70°$).

observed only for i^p, while the photocurrent i^s should drop monotonically with increasing $\Theta > 0°$.[16,17] Previous investigations for the case of a perfect photoreceiving plane of the structures agree with the model of Refs. 11–15. The degradation of the quality of the semiconductor surface usually had the effect that both dependences $i^p(\Theta)$ and $i^s(\Theta)$ became similar, exhibiting a monotonic drop with increasing $\Theta > 0°$.[18]

However, in the case of highly efficient TSCs with a mirror ZnO surface, for both polarizations the photocurrent starts to increase with the angle of incidence, as shown in Fig. 3 (curves *1* and *2*). This can occur as a result of an elimination of reflection losses not only for the *p*-wave but also for the *s*-wave; i.e., antireflection appears for radiation with both polarizations. Since this effect did not appear in previous investigations, the optical processes were checked using the Fresnel relation.[15,16]

As one can see from Fig. 2 (curves *3* and *4*), the coefficient of induced photopleochroism due to oblique incidence of LPR, defined as

$$P_I = (i^p - i^s)/(i^p + i^s),$$

increases gradually according to a quadratic law $P_I \sim \Theta^2$ with increasing angle of incidence in the entire region of photosensitivity of the TSC. This result is in agreement with Ref. 15.

It should be noted that the characteristic feature of i^p and $i^s(\Theta)$ studied here could find applications for monitoring the antireflection effect in TSCs. It is obvious that total antireflection corresponds to the condition where the polarization difference of the photocurrents $\Delta i = i^p - i^s$ and, correspondingly, the induced photopleochroism coefficient approach zero.

5. For the TSCs obtained by us, a typical example of the spectral dependences of the photocurrents i^p and i^s for one of the fixed angles of incidence $\Theta = 70°$ is shown in Fig. 4. We see that for oblique incidence of LPR on the receiving ZnO surface of a TSC, the wide-band character of the photovoltaic effect is observed for both polarizations of the radiation; here the relation $i^p > i^s$ holds in the entire range of photosensitivity. As a result, the polarization difference Δi is positive. Similar regularities are observed in the experimental range of angles of incidence $0° < \Theta < 90°$. As Θ is increased, the spectral curves Δi approach $i^p(\hbar\omega)$.

In accordance with Ref. 15, the induced photopleochroism coefficient is determined by the refractive index n and also by the angle of incidence. For this reason the photopleochroism in ZnO/CdS/CIGSe TSCs is weaker than in CdS/CISe.[19] An estimate of the index of refraction on the basis of the maximum value $P_I = 17-20\%$ for TSCs with $\hbar\omega = 1.3$ eV and $\Theta = 70°$ gives $n = 1.5-1.7$, which, because of the antireflection, is slightly less than the standard value $n = 2.0$ for ZnO.[20] This situation could be attributed to the fact that interference was completely disregarded in Ref. 15.

The spectral dependence of the induced photopleochroism coefficient in TSC (Fig. 4, curve *3*) exhibits sharp oscillations which accompany the interference effects. We see that the photon-energy dependence of the photopleochroism coefficient is much stronger and therefore appears to be much more pronounced than for the photocurrents (Fig. 4, curves *1* and *2*). If in the absence of interference the induced photopleochroism is nonselective and remains virtually constant in the entire range of photosensitivity,[12,13] then as soon as conditions for interference appear, sharp oscillations arise in the spectral dependence of the photopleochroism.

In summary, the polarization photoactive absorption spectroscopy applied to thin film ZnO/CdS/CIGSe solar cells showed that (a) they can be used in a new capacity for these devices — wide-band photoanalyzers of LPR — and (b) the photopleochroism is sensitive to the optical quality of the wide-gap heterostructure window. The antireflection required to achieve a high photoconversion efficiency in TSCs suppresses the induced photopleochroism; this could find application in the development of a technology for fabricating highly efficiency solar cells.

This work is supported under INTAS Grant No. 95-3998.

[1] L. Stolt, J. Hedstrom, J. Kessler, M. Ruckh, K. O. Velthevs, and H. W. Schock, Appl. Phys. Lett. **62**, 597 (1993).
[2] N. Kohara, T. Negami, M. Nishitani, and T. Wada, Jpn. J. Appl. Phys. **34**, L 1141 (1995).
[3] Ch. Goradia and M. Ghalla-Goradia, Solar. Cells. **16**, 611 (1986).
[4] R. R. Potter, Solar. Cells. **16**, 521 (1986).
[5] T. Yamaguchi, M. Suzuki, Y. Yamamoto, Y. Demizu, T. Tanaka, and A. Yoshida, Cryst. Res. Technol. **31**, 481 (1996).
[6] Yu. V. Rud', Jpn. J. Appl. Phys. **32–3**, 512 (1986).
[7] A. A. Abdurakhimov and Yu. V. Rud', Fiz. Tekh. Poluprovodn. **16**, 959 (1982) [Sov. Phys. Semicond. **16**, 618 (1982)].
[8] A. A. Abdurakhimov, B. Kh. Baĭramov, A. Geĭnrik, and Yu. V. Rud', Fiz. Tverd. Tela (Leningrad) **24**, 2495 (1982) [Sov. Phys. Solid State **24**, 1418 (1982)].
[9] I. V. Bodnar, A. A. Vaĭpolin, I. K. Polushina, V. Yu. Rud', and Yu. V. Rud', Fiz. Tekh. Poluprovodn. **28**, 1763 (1994) [Semiconductors **28**, 978 (1994)].
[10] I. V. Bodnar, A. A. Vaĭpolin, V. Yu. Rud', and Yu. V. Rud', Fiz. Tekh. Poluprovodn. **28**, 132 (1994) [Semiconductors **28**, 748 (1994)].
[11] Yu. V. Rud', Izv. Vyssh. Uchebn. Zaved., Fiz. **29**, 68 (1986).
[12] S. G. Konnikov, V. Yu. Rud', Yu. V. Rud', D. Melebaev, A. Berkeliev, M. Serginov, and S. Tilevov, Jpn. J. Appl. Phys. **32–3**, 515 (1993).
[13] Yu. V. Zhilyaev, N. Nazarov, V. Yu. Rud', Yu. V. Rud', and L. M.

Fedorov, Fiz. Tekh. Poluprovodn. **28**, 1820 (1994) [Semiconductors **28**, 1006 (1994)].
[14] D. Melebaev, V. Yu. Rud', and Yu. V. Rud', Cryst. Res. Technol. **31**, 481 (1981).
[15] G. A. Medvedkin and Yu. V. Rud', Phys. Status Solidi A **67**, 333 (1981).
[16] G. S. Landsberg, *Optics* [in Russian], Moscow, 1976.
[17] R. H. Azzam and N. M. Bashara, *Ellipsometry and Polarized Light*, North-Holland, Amsterdam, 1977.
[18] V. Yu. Rud' and Yu. V. Rud' in *3rd Workshop on Expert Evaluation and Control of Compound Semiconductors*, Freiburg, Germany, 1996, p. 31.
[19] V. Yu. Rud', *Author's Abstract of Candidate's Dissertation*, Physicotechnical Institute of the Russian Academy of Sciences, St. Petersburg, 1995.
[20] *Physicochemical Properties of Semiconductor Materials* [in Russian], Nauka, Moscow, 1978.

Translated by M. E. Alferieff

High-temperature annealing and nuclear-transmutation doping of GaAs bombarded by reactor neutrons

V. N. Brudnyĭ, V. A. Novikov, and V. V. Peshev

V. D. Kuznetsov Siberian Physicotechnical Institute, 634050 Tomsk, Russia

N. G. Kolin and A. I. Noĭfekh

L. Ya. Karpov Affiliate of the Scientific-Research Physicochemical Institute, 249020 Obninsk, Russia
(Submitted January 21, 1996; accepted for publication October 30, 1996)
Fiz. Tekh. Poluprovodn. **31**, 811–815 (July 1997)

The electrical properties and spectrum of deep traps in GaAs under heat treatment, neutron irradiation, and subsequent annealing to $T_{ann}=1100$ °C have been investigated. It is shown that for $T_{ann}>900$ °C thermal acceptors are formed rapidly in GaAs, which degrades the properties of the transmutation-doped material. Estimates are given for the utilization factor of the impurity with transmutation doping of GaAs as a function of T_{ann} and the integrated neutron flux. The parameters of deep traps in the experimental material are presented. © *1997 American Institute of Physics.* [S1063-7826(97)01207-6]

Rapid progress has recently being made in the development of a method of doping by nuclear transmutation for the purpose of obtaining *n*-type gallium arsenide with a high degree of uniformity of the electrical properties in the bulk. The method includes bombardment of the material by reactor neutrons followed by high-temperature annealing and neutron bombardment of the material at high temperatures to eliminate bombardment-induced radiation defects (RDs). Thermal neutrons induce in GaAs the reactions

$$(30.2\%)\ ^{69}\mathrm{Ga}(n,\gamma)^{70}\mathrm{Ga}\rightarrow{}^{70}\mathrm{Ge}+\beta^-,$$

$$(19.8\%)\ ^{71}\mathrm{Ga}(n,\gamma)^{72}\mathrm{Ga}\rightarrow{}^{72}\mathrm{Ge}+\beta^-,$$

$$(50\%)\ ^{75}\mathrm{As}(n,\gamma)^{76}\mathrm{As}\rightarrow{}^{76}\mathrm{Se}+\beta^-,$$

with the parameters, respectively,

$$\sigma=1.68\text{b},\quad T_{1/2}=21\text{ min},$$

$$\sigma=4.7\text{b},\quad T_{1/2}=14.1\text{ h},$$

$$\sigma=4.3\text{b},\quad T_{1/2}=26.4\text{ h},$$

which results in the accumulation of donor-type chemical elements (Ga, Se) in the crystal lattice. Recent investigations of neutron-bombarded GaAs have revealed that annealing of RDs occurs in a wide temperature range from T_{irr} to T_m of the material (T_{irr} and T_m are the irradiation and melting temperatures, respectively); this results in the formation of thermal defects (TD), which degrade the properties of the nuclear-transmutation-doped (NTD) GaAs. For this reason, in transmutation doping it is especially important to choose the optimal annealing or irradiation temperature.

We have investigated the CDLTS (capacitance deep-level transient spectroscopy) spectra of growth defects (GD) and TD in the initial GaAs, the systematic features of their transformation during heat treatment up to 1100 °C, and the spectra of RDs in the irradiated GaAs. Measurements of the electrical parameters of GaAs irradiated with reactor fluxes up to 2×10^{19} neutrons$\cdot$cm^{-2} and annealed in the temperature range 100–1100 °C were performed. The initial material consisted of *n*- and *p*-type GaAs single crystals grown by the Czochralski method: *n*-type GaAs (conductivity $\sigma=10^{-7}$ $\Omega^{-1}\cdot\mathrm{cm}^{-1}$, sample 1), *p*-type GaAs ($\sigma=10^{1}$ $\Omega^{-1}\cdot\mathrm{cm}^{-1}$, sample 2; $\sigma=10^{-1}$ $\Omega^{-1}\cdot\mathrm{cm}^{-1}$, sample 3; $\sigma=10^{-5}$ $\Omega^{-1}\cdot\mathrm{cm}^{-1}$, sample 4), and *n*-type GaAs ($\sigma=10^{-2}$ $\Omega^{-1}\cdot\mathrm{cm}^{-1}$, sample 5). Bombardment with the total neutron spectrum was performed in a VVR-Ts reactor (Obninsk) at temperatures of about 70 and 850 °C, thermal neutron flux densities $D_{tn}=10^{13}-5\times10^{13}$ cm$^{-2}\cdot$s^{-1} and cadmium number 10. Isochronous annealing of the material was performed for 20 min in vacuum ($T_{ann}<500$ °C) or under equilibrium As vapor pressures ($T_{ann}=600-1100$ °C). To eliminate surface effects, the samples were ground after irradiation on each side to 50 μm and to 200 μm after annealing.

It is well known that neutron bombardment of GaAs results in pinning of the Fermi level near $E_v+0.6$ eV (Ref. 1) and an increase in the resistivity of the material to ρ_{max} of about $(3-5)\times10^8$ $\Omega\cdot$cm (at 300 K) as a result of the trapping of free charge carriers by ''deep'' RDs.[2,3] The resistivity was found to decrease (compared with ρ_{max}) under prolonged irradiation; this is attributed to charge transfer along local states in the band gap, which are located near the Fermi level (such ''over-irradiated'' samples are *p*-type).

To eliminate the RDs and to activate the chemical impurity with transmutation doping, the GaAs must be heat-treated. The NTD parameters of GaAs after high-temperature heat treatment at 900 and 1100 °C are presented in Table I. The change in the conductivity σ as a result of isochronous annealing of the irradiated materials is shown in Fig. 1. For the over-irradiated samples 1 and 2 (Table I) a continuous change is observed in the electrical properties of GaAs from the main stages of annealing near the temperature intervals 200–300, 400–600, and 700–900 and above 1000 °C. In addition, the conductivity σ decreases to $10^{-6}-10^{-8}$ $\Omega^{-1}\cdot\mathrm{cm}^{-1}$ at $T_{ann}<500$ °C due to the decrease in the contribution of the hopping conductivity to the total charge transport because of the decrease in the density of local states in the band gap.[2,3] Similar dependences $\sigma(T_{ann})$ also were observed for over-irradiated samples 3 and 4 (Table I). At

TABLE I. Parameters of transmutation-doped GaAs after isochronous ($t=20$ min) annealing at 900 and 1100 °C. The measurement temperature $T_{meas}=300$ K.

Sample No.	D, 10^{15} cm^{-2}	Irradiation temperature T_{irr}, °C: 900 n, cm^{-3}	900 μ, cm^2/(V·s)	1100 n, cm^{-3}	1100 μ, cm^2/(V·s)
1	200	1.6×10^{18}	1490	1.7×10^{18}	1840
2	90	9.2×10^{17}	2170	1.0×10^{18}	2030
3	90	9.5×10^{17}	2300	9.2×10^{17}	2310
4	90	9.8×10^{17}	2230	9.0×10^{17}	2280
5	5	8.0×10^{16}	4140	4.8×10^{16}	3650

$T_{ann}>500$ °C σ was found to increase, and at $T_{ann}>550$ °C a p–n conversion due to doping with Se and Ge impurities was found to occur in the samples 1–4.

In crystals irradiated at $T=900$ °C with weak neutron fluxes (sample 5, Table I), the restoration of the conductivity σ occurs mainly at $T_{ann}=100-200$ °C, which corresponds to annealing of point defects in GaAs and is supposedly due to the accumulation of such defects due to ''self-irradiation'' of the crystals with β^- particles from the radioactive decay of ^{72}Ge and ^{76}As during storage of the irradiated material.[4]

The degree of compensation of the material, calculated from measurements of the mobility of free electrons at 77 and 300 K, lies in the range 0.3–0.4 at $T_{ann}=900$ °C and 0.3–0.5 at $T_{ann}=1100$ °C. It follows from the data in Table I that upon annealing in the temperature interval 900–1100 °C the mobility μ of the free electrons decreases in samples irradiated with weak neutron fluxes (sample 5). For intermediate doping levels (samples 2–4) we have

$$\mu(T_{ann}=900\ ^\circ\mathrm{C})\simeq\mu(T_{ann}=1100\ ^\circ\mathrm{C}),$$

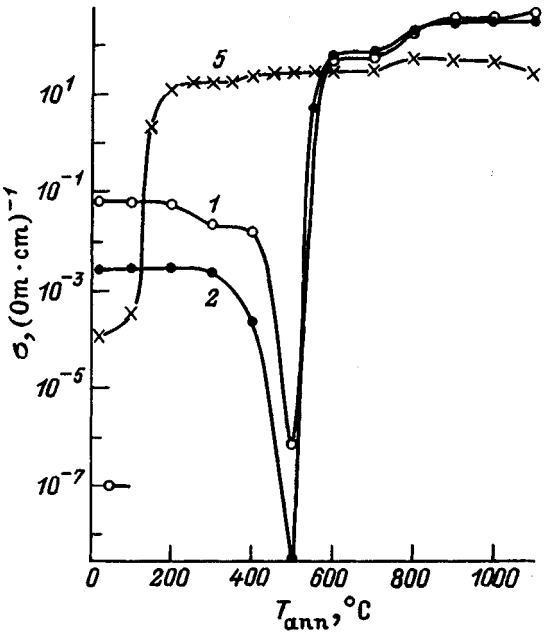

FIG. 1. Variation of the conductivity σ in transmutation-doped GaAs with isochronous (20 min) annealing. The numbers on the curves correspond to the sample numbers in Table I.

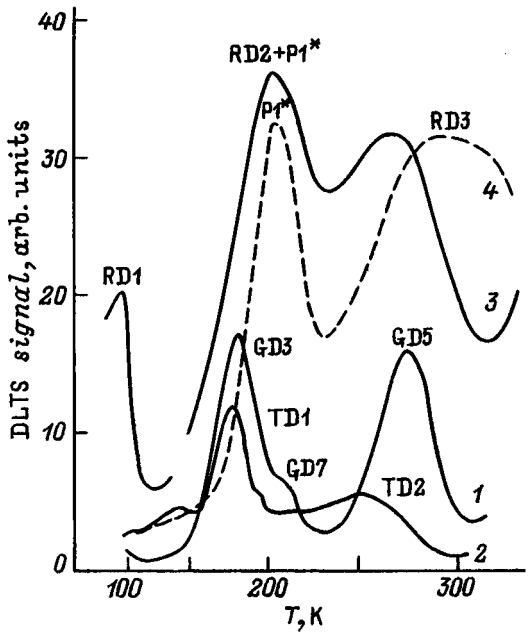

FIG. 2. CDLTS spectra for samples: *1* — Initial GaAs (sample 6), *2* — after annealing up to 1000 °C, *3* — after irradiation with a neutron flux $D=3\times10^{15}$ cm^{-2}, *4* — after irradiation with a flux $D=10^{16}$ cm^{-2} and annealing at 450 °C. Conditions of measurement of the spectra: $t_p=20$ μs, $\tau=5\times10^{-3}$ s; for the E2 peak $\tau=10^{-4}$ s. The designations of the types of defects are the same as in Table II.

and in strongly irradiated material (sample 1) the value of μ continues to increase, remaining less than the corresponding values of μ in samples 2–5.

Measurements of the CDLTS spectra of samples bombarded by fast neutrons with fluxes $D_{fn}=10^{14}-10^{17}$ cm^{-2} were performed to determine the traps responsible for the observed changes in the properties of GaAs. The measurements were performed on Schottky barriers (Pd/n-GaAs) in a material irradiated with neutrons with energy $E>0.1$ MeV and neutron flux density of about $4\times10^9-10^{12}$ cm$^{-2}\cdot$s^{-1}, $T_{irr}<70$ °C, and a cadmium screen ($d=1$ mm). For these measurements, weakly doped ''solar'' n-type GaAs ($n=5\times10^{16}$ cm^{-3}, $\sigma=30$ $\Omega^{-1}\cdot$cm^{-1}, sample 6) was used as the initial material. For $D_{fn}\leqslant10^{15}$ cm^{-2} finished structures were irradiated, and for $D_{fn}>10^{15}$ cm^{-2} Schottky barriers were prepared on samples which were partially annealed after irradiation and were suitable for measuring the CDLTS spectra. The most characteristic CDLTS spectra of the initial, heat-treated and irradiated samples are shown in Fig. 2. The parameters of the traps which were revealed are given in Table II. The identification of the spectra was made by comparing the measured parameters of the initial traps (growth defects GDs), thermal traps (TDs), and radiation traps (RDs), revealed in the experimental material, with the characteristics of known[5–9] traps in GaAs.

More than six traps were observed in the initial material.

The GD1 trap ($E_c-0.12$ eV) in the initial material lies close in energy to the growth defect N_2, which is often observed in the bulk of GaAs according to measurements of the Hall effect and is attributed to the complex ⟨intrinsic lattice defect V_{Ga} or As_I⟩–⟨shallow donor, possibly Si⟩, formed by

TABLE II. Parameters of electronic traps observed in *n*-type GaAs before (growth defects GDs) and after neutron irradiation (radiation defects RDs) and after heat treatment (thermal defects TDs).

Experiment			Published data[4–9]		
Trap type	E, eV	σ_n, cm^2	Trap type	E, eV	σ_n, cm^2
GD1	0.12	1.2×10^{-15}	N_2	0.15	
GD2	0.21	1.4×10^{-15}	EL14?	0.21	5×10^{-15}
GD3	0.30	6.7×10^{-15}	EL7(EL6?)	0.30	7.2×10^{-15}
GD4	0.40	6×10^{-16}	E11	0.43	7.3×10^{-16}
GD5	0.58	3×10^{-14}	EL3	0.57	1.7×10^{-13}
GD6	0.75	2.9×10^{-14}	EL2	0.75–0.82	
GD7	Low-intensity peak, not investigated in detail				
TD1	0.32	3.3×10^{-14}	Appears with annealing above 900 °C		
TD2	0.44	1.2×10^{-14}	Appears with annealing above 900 °C		
RD1	0.18	3×10^{-13}	E2	0.14	1.2×10^{-13}
RD2	0.3	56.6×10^{-15}	E3	0.30	6.2×10^{-15}
RD3			U band		
P1*	0.35	10^{-14}	P1	0.38	6.9×10^{-15}
P2*	0.52	3×10^{-14}	P2	0.50	1.4×10^{-15}
P3*	0.63	2.9×10^{-12}	P3	0.72	1.4×10^{-13}

Note: The P1*–P3* centers were observed after the irradiated samples were annealed.

cooling of the melt.[6] The density of GD1 traps fluctuates in the range $N=(0.5-1)\times10^{13}$ cm^{-3}.

The parameters of the GD2 trap ($E_c-0.21$ eV, density $N\simeq5\times10^{13}$ cm^{-3}) are close to those of the growth defect EL14 observed in bulk GaAs. Sometimes, in the Hall effect measurements the growth traps GD1 and GD2 are not ''resolved'' and a defect with a level near $E_c-(0.13–0.20)$ eV, which presumably controls the electrical properties of GaAs crystals which were not specially doped and which were grown by the Czochralski or the Bridgman method,[8] is reported.

The parameters of the GD3 trap ($E_c-0.30$ eV, density $N\simeq(2-15)\times10^{14}$ cm^{-3}) are close to those of an EL7(EL6?) center in bulk GaAs. With heat treatment of the material at temperatures $T_{\rm ann}>600$ °C the intensity of the corresponding peak in the CDLTS spectra of the initial GaAs decreases (Fig. 3).

The GD4 trap ($E_c-0.4$ eV with density $N\simeq(0.5–5)\times10^{14}$ cm^{-3}) is observed in some initial and annealed samples. Its characteristic feature are low values of the electron trapping cross section, approximately 6×10^{-16} cm^2. Upon heating to 900 °C this trap practically vanishes.

The GD5 trap ($E_c-0.58$ eV) is present in the initial crystals in densities of $(1–2)\times10^{15}$ cm^{-2} and its parameters are close to those of the EL3 center.[7] The character of the variation of its density on annealing from 100 to 1100 °C is illustrated in Fig. 3.

The density of the main trap GD8, which corresponds to the well-known center EL2 (As_{Ga}–X), in the initial material — the trap present with the highest density ($N\simeq10^{16}$ cm^{-3}) — did not change much with annealing right up to 1100 °C (Fig. 3). Furthermore, other peaks of little interest, for example, the peak GD7 in Fig. 2, which have not been studied in detail, were also observed in the CDLTS spectra of the initial samples.

We call attention to the correlation between the annealing of growth traps (GD), the formation of thermal defects (TDs) during heat treatment, and the change in the electrical parameters of the initial material. For example, decreasing the density of GD3 and GD5 centers increases the free-electron density at $T_{\rm ann}\lesssim900$ °C, and the generation of thermal defects TD1 and TD2 at $T_{\rm ann}>900$ °C decreases it (Fig. 3). In addition, the overall decrease in the density of growth traps for electrons equals about 3×10^{15} cm^{-3} with the free-carrier density varying up to 2×10^{16} cm^{-3} for $T_{\rm ann}<900$ °C. This shows that in other acceptor-type growth defects, whose levels lie in the bottom half of the band gap, below the level of the EL2 defect, also vanish in this temperature interval.

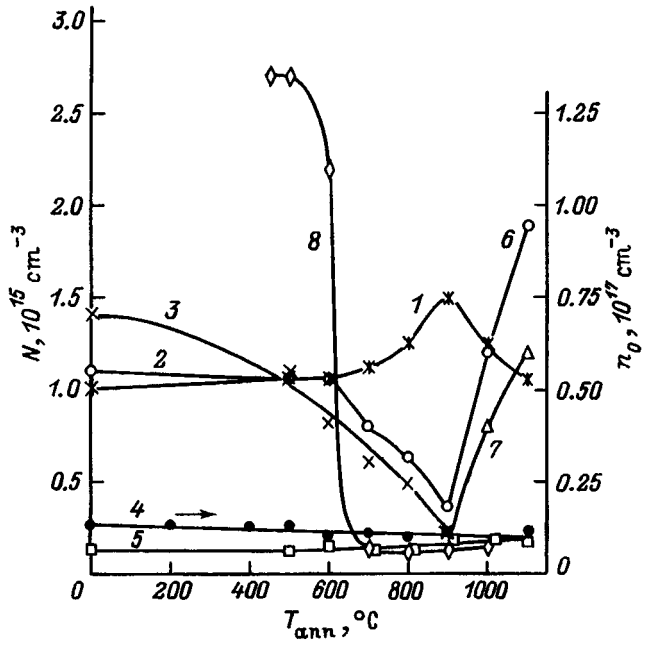

FIG. 3. Variation of the free electron density (1) and density of growth traps (2)–(8) in the initial *n*-type GaAs (sample 6) with isochronous (10 min) annealing. Types of defects: *2* — GD3, *3* — GD5, *4* — GD6, *5* — GD7, *6* — TD1, *7* — TD2, *8* — P1*. The annealing curve of the P1* center was obtained for the sample irradiated with a neutron flux $D=10^{16}$ cm^{-2}.

The CDLTS spectra of the neutron-irradiated *n*-GaAs samples revealed a number of deep electronic traps (RD1, RD2), which can be attributed to the known centers E2 and E3, possibly the point defects in the As sublattice,[8] and a wide band (RD3) in the temperature range 230–320 K (so-called *U* band), which is presumably associated with the presence of cluster-type defects, since it is observed only with neutron and ion irradiation.[9] A characteristic feature of the *U* band is that it appears in the CDLTS spectra of GaAs only with some threshold neutron fluxes, as previously noted in Ref. 10 in an investigation of GaAs obtained by gas-phase epitaxy. At low neutron fluxes, at first, the intensity of the EL3 peak increases and this band is observed to appear in the CDLTS spectra only with fluxes $D_{fn}>3\times10^{15}$ cm^{-2}.

When the samples are heated to 300 °C, the E2 and E3 centers vanish and a P1* center, whose parameters are close to those of the R1 center in the electron-irradiated and annealed (up to 300 °C) *n*-GaAs (Table II), is observed in the CDLTS spectra instead of the peak E3. The intensity of the *U* band decreases (at $T_{\text{ann}}>450$ °C), a displacement of the band to higher temperatures is observed, and the *U* band ''resolves'' into two peaks — P2* and P3* (Table II). Peaks of the type P* are thought to be associated with complex defects, which form as a result of neutron bombardment and, possibly, partially during subsequent annealing. They anneal in the temperature range 500–600 °C (for example, the P1 * peak in Fig. 3). In the samples irradiated with neutron fluxes up to 10^{17} cm^2, there are no ''traces'' of RDs in the CDLTS spectra for $T_{\text{ann}}>700$ °C, but the incomplete restoration of the electrical properties of strongly irradiated material indicates the presence of a group of RDs with high thermal stability, which are not observed in the CDLTS measurements.

Our studies have shown that as a result of the vanishing of at least three groups of radiation defects, annealing of NTD GaAs occurs in a wide temperature interval in three stages:

— annealing of *E*-type traps at 100–300 °C-probably point defects characteristic of GaAs, irradiated with γ rays, electrons, and H^+ ions;

— annealing of P1*–P3* centers at 400–600 °C, which is accompanied by restoration of the lattice period and the density of neutron-irradiated material to values characteristic of unirradiated material[11] and which is attributed to the decay of cluster-type defects; and

— stage of annealing near 700–900 °C, which is associated with the decay of an unknown group of defects in strongly irradiated GaAs.

Annealing of the growth defects GD3 and GD5 in GaAs is virtually complete at temperatures of about 900 °C. This increases the free-electron density in the initial material (Fig. 3). This annealing temperature is critical, since at $T_{\text{ann}}>900$ °C intense formation of acceptor-type defects occurs in GaAs, which decreases the electron mobility and the impurity utilization factor K_{imp} (see below) and increases the degree of compensation of the material (sample 5, Table I, Fig. 3). This limits the choice of maximum heat-treatment temperatures in transmutation doping of GaAs. At the same time, in samples irradiated with strong neutron fluxes ($D=2\times10^{19}$ cm^{-2}), the values of **n** and μ at $T_{ann}=900$–1100 °C continue to increase as a result of the incomplete annealing of RDs even at $T_{\text{ann}}>1100$ °C (Table I). The lower quality of the NTD GaAs with high levels of transmutation doping and heat-treatment temperatures is due to incomplete annealing of RDs and dissemination of thermal acceptors in the material.

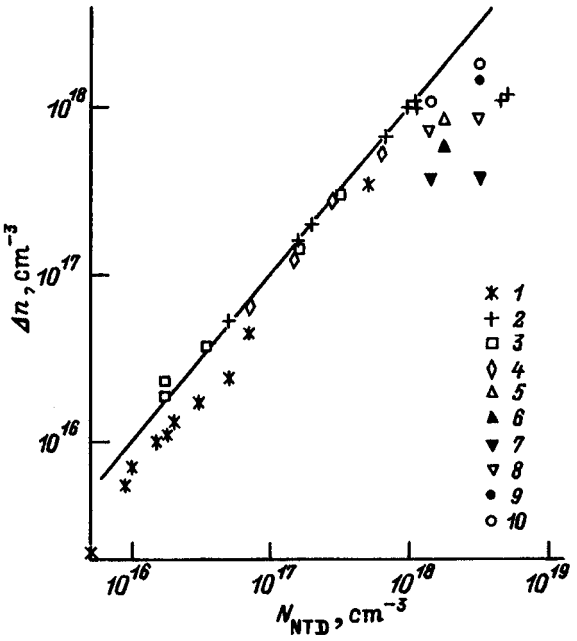

FIG. 4. Values of the impurity utilization factor $K_{\text{imp}}=\Delta n/N_{NTD}$ in transmutation-doped GaAs for different irradiation conditions and annealing temperatures. The solid curve corresponds to $\Delta n/N_{NTD}=1$; *1–6* — published data: *1* — Ref. 12, *2* — Refs. 4 and 13, *3* — Ref. 15, *4* – Ref. 14, *5, 6*, — Ref. 16; *7–10* — our data. Annealing temperature, T_{ann}, °C: *1* — 870; *2, 5, 9* — 900; *3, 8* — 800; *4* — 830; *6* — 750; *7* — 700; *10* — 1100.

In closing, we present data on the impurity utilization factor $K_{\text{imp}}=\Delta n/N_{NTD}$ in NTD GaAs under different doping conditions (integrated thermal neutron fluxes and temperatures of subsequent annealing), obtained on the basis of our investigations and existing data in the literature (Fig. 4).[4,13–16] In Fig. 4 $\Delta n=n-n_0$, where n_0 and n are the free-electron density in the initial and NTD GaAs, respectively; $N_{NTD}=N_{\text{Se}}+N_{\text{Ge}}$ is the impurity density (^{70}Ge, ^{72}Ge, ^{76}Se) in NTD GaAs. The quantity N_{NTD} was estimated from the relation $N_{NTD}=K_{NTD}\cdot D_{tn}$, where $N_{NTD}=0.16$ cm^{-1}. This quantity was obtained in Ref. 3 experimentally by means of measurements performed by the method of chemical macroanalysis of the concentration of impurities introduced by nuclear transmutations and is close to the theoretical estimates of K_{NTD} in GaAs.[15]

It follows from Fig. 4 that for transmutation doping of GaAs the annealing temperature at any irradiation fluxes should not be less than 800–900 °C in order to reach values $K_{\text{imp}}\approx1$ and should not exceed 900 °C in order to prevent generation of thermal acceptors in the material.

In published articles the isochronous annealing time t_{ann} varied over wide limits — from 3 min[16] to 12.5 h.[15] As follows from the data in Fig. 4, short annealing times t_{ann} are inadequate for achieving $\Delta n\approx N_{NTD}$ and long annealing

times t_{ann} result in the appearance of thermal acceptors in the material. For this reason, the times $t_{ann} \approx 20-30$ min are ordinarily used.

In weakly irradiated samples ($N_{NTD} < 10^{17}$ cm^{-3}) values $K_{imp} > 1$ are sometimes observed at annealing temperatures near 900 °C. This is apparently due to the ''decompensation'' process in the initial material, and at high transmutation doping levels ($N_{NTD} > 10^{18}$ cm^{-3}) K_{imp} is always less than 1, which is due to the incomplete annealing of RDs even with long heat-treatment times and possibly the self-compensation effect in the material as a result of the amphoteric nature of Ge when it is present in gallium arsenide at high concentrations.

This work was supported, in part, by grants from the State Committee of Higher Education of the Russian Federation ''Universities of Russia'' and ''Fundamental research in the field of nuclear technology and the physics of beams of ionizing radiations.''

[1] V. N. Brudnyi, S. N. Grinyev, and V. E. Stepanov, Physica B, Cond. Matter. **212**, 429 (1995).
[2] R. Coates and E. W. J. Mitchell, Adv. Phys. **24**, 594 (1975).
[3] N. G. Kolin, L. V. Kulikova, V. B. Osvenskiĭ, S. P. Solov'ev, and V. A. Kharchenko, Fiz. Tekh. Poluprovodn. **18**, 2187 (1984) [Sov. Phys. Semicond. **18**, 1364 (1984)].
[4] N. G. Kolin, L. V. Kulikova, and V. B. Osvenskiĭ, Fiz. Tekh. Poluprovodn. **22**, 1025 (1988) [Sov. Phys. Semicond. **22**, 646 (1988)].
[5] A. V. Kartavykh, S. P. Grishina, M. G. Mil'vidskiĭ, N. S. Rytova, I. V. Stepanova, and E. S. Yurova, Fiz. Tekh. Poluprovodn. **22**, 1004 (1988) [Sov. Phys. Semicond. **22**, 633 (1988)].
[6] G. M. Martin, A. Mitonneau, and A. Mircea, Electron. Lett. **13**, 191 (1977).
[7] D. C. Look, D. C. Walters, and J. R. Meyer, Solid State Commun. **42**, 745 (1982).
[8] D. Pons, A. Mircea, A. Mitonneau, and G. M. Martin, in *Defects and Radiative Effects in Semiconductors*, edited by J. H. Albany, London, 1978 [Inst. Phys. Conf. Ser. N 46, 352 (1979)].
[9] G. M. Martin, E. Esteve, P. Langiade, and S. Makram-Ebeid, J. Appl. Phys. **56**, 2655 (1984).
[10] V. N. Brudnyĭ, N. G. Kolin, and A. I. Potapov, Fiz. Tekh. Poluprovodn. **27**, 264 (1993) [Semiconductors **27**, 145 (1993)].
[11] N. G. Kolin, V. T. Bublik, V. B. Osvenskiĭ, and N. I. Yarmolyuk, Fiz. Khim. Obrab. Materialov **3**, 28 (1987).
[12] R. Rentzsch, K. J. Friedland, A. N. Ionov, M. N. Matveev, I. S. Shlimak, C. Gladun, and H. Vinzeiberg, Phys. Status Solidi A **137**, 691 (1986).
[13] L. I. Kolesnik, N. G. Kolin, A. M. Loshinskiĭ, V. B. Osvenskiĭ, V. V. Tokarevskiĭ, and V. A. Kharchenko, Fiz. Tekh. Poluprovodn. **19**, 1211 (1985) [Sov. Phys. Semicond. **19**, 742 (1985)].
[14] M. H. Young, A. T. Hunter, R. Baron, O. J. Marsh, and H. V. Winston, in *Neutron Transmutation Doping of Semiconductors Material*, edited by R. D. Larrabee, Plenum Press, N. Y., 1984, Vol. XIV, p. 1.
[15] M. A. Vesaghi, Phys. Rev. B **25**, 5436 (1982).
[16] P. D. Greene, Solid State Commun. **32**, 325 (1979).

Translated by M. E. Alferieff

Characteristic structural features of amorphous hydrated silicon films deposited by direct-currect decomposition of silane in a magnetic field

O. A. Golikova, A. N. Kuznetsov, V. Kh. Kudoyarova, and M. M. Kazanin

A. F. Ioffe Physicotechnical Institute, Russian Academy of Sciences, 194021 St. Petersburg, Russia
(Submitted October 25, 1996; accepted for publication October 31, 1996)
Fiz. Tekh. Poluprovodn. **31**, 816–819 (July 1997)

Data on the hydrogen content and different forms of hydrogen bonds with silicon in *a*-Si:H films deposited by direct-current decomposition of silane in a magnetic field (MASD) as a function of the deposition conditions are presented: temperature, pressure of the mixture 25%SiH_4 + 75%Ar, pumping rate, and insertion of a grid into the discharge chamber. The correlations between the photoconductivity and the structural features of the films are established. © *1997 American Institute of Physics.* [S1063-7826(97)01307-0]

1. INTRODUCTION

In our preceding study[1] we showed for the first time that device-quality, amorphous, hydrated silicon *a*-Si:H can be obtained at high film-deposition temperatures (T_s =300–400 °C) by direct-current decomposition of silane in a magnetic field (MASD). The construction of the apparatus for obtaining the films was described in detail in Ref. 1. In this paper we report the results of a detailed investigation of the structure of *a*-Si:H films deposited by this method as a function of T_s with directed variations of the other conditions of deposition: pressure and pumping rate of the gas mixture 25% SiH_4 + 75%Ar and insertion of a grid into the discharge chamber. Data on the photoconductivity of the films as a function of their structure are also presented.

2. EXPERIMENT: METHODS, RESULTS, AND DISCUSSION

The hydrogen density distribution over the thickness of the film was determined by the recoil proton method (ERD). This method yields information about the total content of the hydrogen bound with Si and the hydrogen that is not bound with Si. To determine the content of bound hydrogen, we analyzed the infrared (IR) absorption band at 630 cm^{-1}.

The microstructural parameter was found as

$$R=\frac{I_{2090}}{I_{2000}+I_{2090}},$$

where I_{2000} and I_{2090} are the intensities of the absorption bands at 2000 and 2090 cm^{-1}. As is well known, these frequencies correspond to monohydride (Si–H) and dihydride ($Si–H_2$) complexes, respectively. To identify the form of the dihydride complexes SiH_2 or $(SiH_2)_n$, the IR spectra near 875 cm^{-1} were analyzed, since the absorption band at this frequency corresponds to SiH_2 and the doublet (840, 890 cm^{-1}) corresponds to $(SiH_2)_n$, i.e., the chain structure of dihydrides. The photoconductivity σ_{ph} of the films was measured at room temperature, $h\nu=2$ eV, and generation rate $G=10^{19}$ $cm^{-3}\cdot s^{-1}$; in addition, σ_{ph} was determined as a function of the position of the Fermi level E_F in the mobility gap. The gap E_c-E_F (E_c is the conduction band edge) was found, as usual, from the relation $E_c-E_F=kT\ln\sigma_0/\sigma_d$, where $T=300$ K, σ_d is the dark conductivity at this temperature, and $\sigma_0=150$ $\Omega^{-1}\cdot cm^{-1}$. Investigations of the absorption coefficient near the fundamental absorption edge were performed for a number of films by the constant photocurrent method (CPM). The defect density and Urbach parameter were determined.

The typical hydrogen density distribution over the thickness for the experimental films is shown in Fig. 1: The hydrogen distribution is uniform. We note that C_H determined by ERD and IR spectroscopy methods are the same to within 2–3 at.%.

Figure 2 shows data on the hydrogen content in films as a function of their deposition temperature. In all experiments the anode voltage was equal to 500 V and the applied magnetic field was equal to 500 G. The pressure of the gas mixture was varied in the range $P=(2.5–7.5)\times10^{-3}$ Torr and the gas pump rate $r=1-3$ standard cubic centimeters per minute (s.c.c.m.). A number of experiments were performed with a grid inserted into the discharge chamber; the potential on the grid was equal to that of the substrate holder. The grid was placed 15 mm from the holder, and the target–grid distance was equal to 35 mm.[1] The data displayed in Fig. 2 show that at $T_s=$ const the values of C_H can vary over a substantial range.

The minimum hydrogen content in the *a*-Si:H films deposited by the MASD method at $T_s=300-400$ °C is the same as in the films deposited by the glow-discharge method in standard reactors ($f=13.56$ MHz) using undiluted silane,[2–4] as well as by the method of catalytic decomposition of silane on a hot tungsten filament.[5] At the same time, the *a*-Si:H films deposited by the glow-discharge method in a high-frequency reactor ($f=70$ MHz) and the same values of T_s contain approximately two times more hydrogen.[6] This same picture is observed with diluted silane–argon or silane–helium mixtures in the glow-discharge method of film deposition.[3,4] A high hydrogen content is also observed in *a*-Si:H films deposited by the remote silane–hydrogen plasma method.[7] In contrast to what we have said above, the use of a strongly diluted silane–argon mixture does not increase C_H in films deposited by the MASD method. This undoubtedly should be regarded as an advantage of this method from both the ecological and economic standpoints. Indeed, minimization of C_H, which is important from the standpoint of increasing the stability of *a*-Si:H against exter-

 1063-7826/97/070691-04$10.00

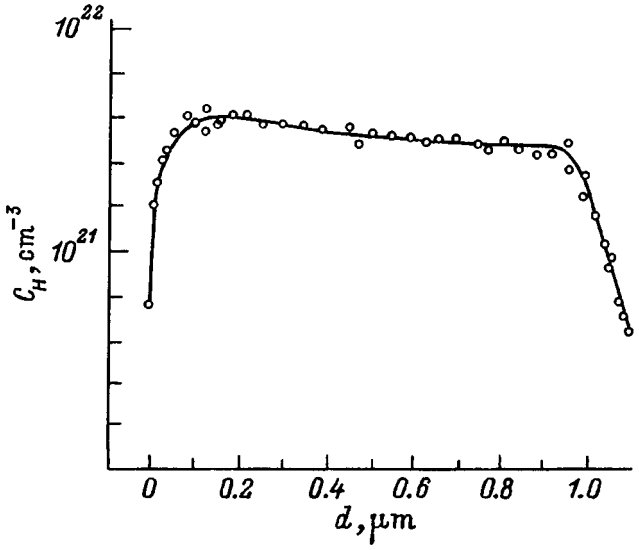

FIG. 1. Hydrogen distribution over the thickness d of the film.

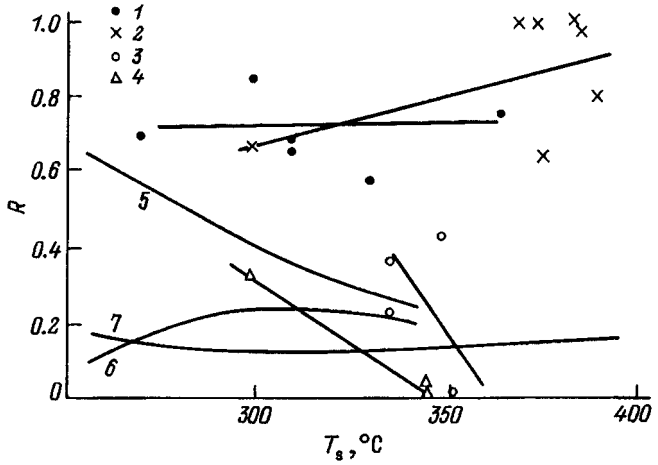

FIG. 3. Microstructure parameter as a function of the film deposition temperature: *1–4* — same as in Fig. 2; *5*, *6* — data from Ref. 3; undiluted SiH_4 and the mixture 40%SiH_4 + 60%He, respectively, were used; *7* — data from Ref. 16.

nal actions, is achieved with a comparatively small amount of expensive, toxic, and explosive silane.

Figure 3 shows how the film deposition conditions influence the microstructure parameter R. At maximum pressure of the gas mixture $R=0.7$ in the entire range of variation of the deposition temperature; i.e., the fraction of SiH_2 complexes is high (curve 1). Doublets (840, 890 cm^{-1}) are observed in the IR spectra; i.e., $(SiH_2)_n$ chains are characteristic of the structure.

At the minimum pressure of the gas mixture R increases with T_s, reaching a value of several units (curve 2). For such films, it is not legitimate to speak about the presence of chain structure $(SiH_2)_n$: An absorption band is observed in the IR spectra at 2100 cm^{-1} with no absorption band in the region 800–900 cm^{-1}. This could be due to a number of factors: presence of impurities (oxygen, nitrogen, and carbon), which, having a higher electronegativity than silicon, can shift the absorption band at 2000 cm^{-1} into the region of large wave numbers or by the presence of hydrogen bonds with silicon, which cover the surface of voids or grains. Increasing the pumping rate of the gas mixture and introducing a grid into the discharge chamber give rise to a further variation of the microstructure parameter (curves 3 and 4). In the process, the dihydride complexes, if they are present in the film, are in the form SiH_2.

Thus, at $T_s=$ const the quantity R can vary in a directed manner over wide limits. This picture is not observed for deposition of *a*-Si:H films by other methods at high temperatures. As examples, Fig. 3 shows data from Refs. 3 and 6: at $T_s=300$–400 °C R approaches zero.

Figure 4 shows the microstructure parameter R as a function of the hydrogen content in the *a*-Si:H films according to data from this study and from a number of other studies. We see that according to the data of Refs. 3 and 6–9,

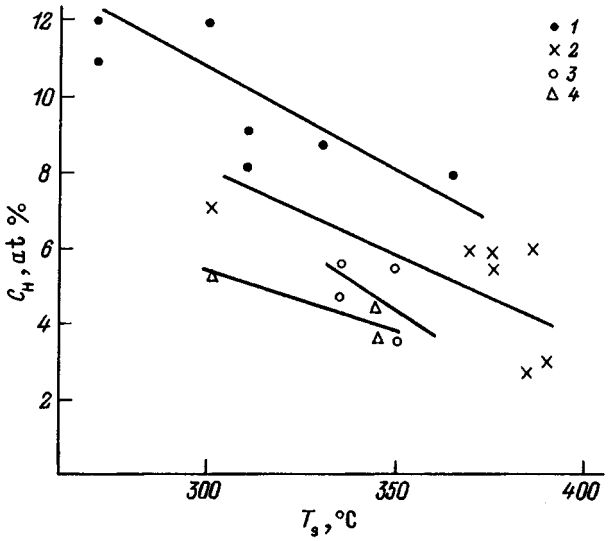

FIG. 2. Hydrogen content versus film deposition temperature: *1* — $P=(7-8)\times10^{-3}$ Torr, $r=1$ s.c.c.m.; *2* — $P=(2.5-3.5)\times10^{-3}$ Torr, $r=1$ s.c.c.m.; *3* — $P=3\times10^{-3}$ Torr, $r=3$ s.c.c.m.; *4* — grid inserted into the chamber $P=7\times10^{-3}$ Torr, $r=1$ s.c.c.m.

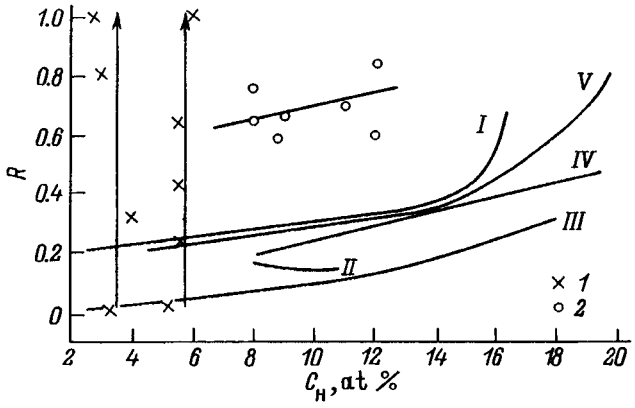

FIG. 4. Microstructure parameter versus hydrogen content in the film. The dots represent our data for films containing the complexes SiH + SiH_2 (1) and $(SiH_2)_n$ chains (2); arrows mark their variations with $C_H=$ const. Curves from different studies: *I* — Ref. 3, *II* — Ref. 6, *III* — Ref. 5, *IV* — Ref. 8, *V* — Ref. 9.

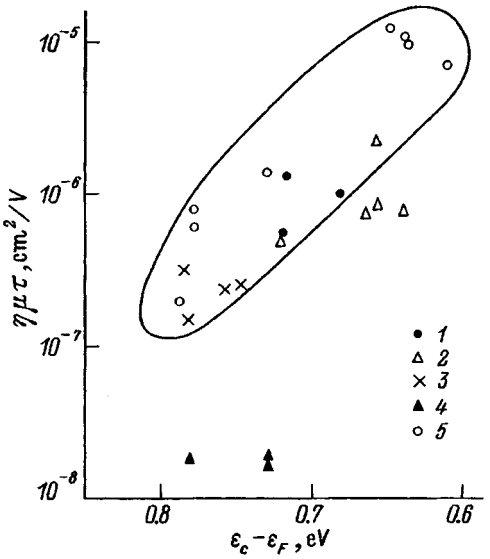

FIG. 5. $\eta\mu\tau$ versus the position of the Fermi level in the mobility gap. Data of this work for films containing: *1* — SiH ($R=0$); *2* — SiH + SiH_2 ($R=0.3-0.8$); *3* — $(SiH_2)_n$ ($R=0.6-0.8$); *4* — for films with $I=1$; *5* — data from the European Science Centers.

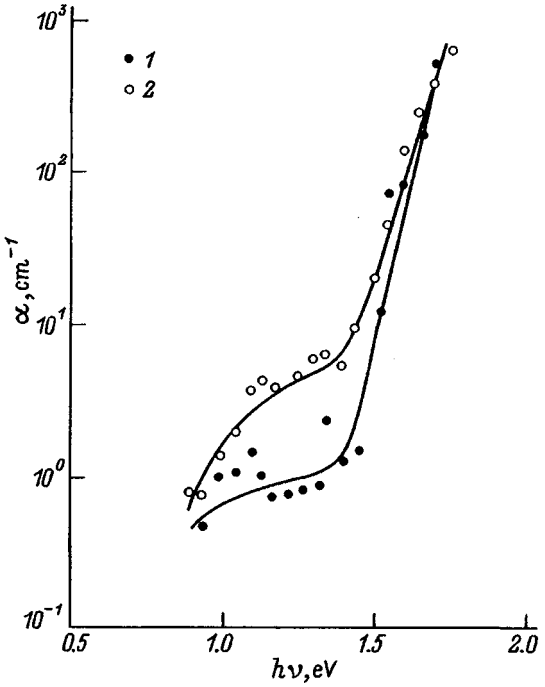

FIG. 6. Spectral dependences of the absorption coefficient for films deposited by the MASD method: *1* — *a*-Si:H itself, *2* — pseudodoped *a*-Si:H.

R increases simultaneously with the hydrogen content. The highest values of R (up to 0.8) are observed for *a*-Si:H films deposited by the glow-discharge method at $T_s=260$ °C using silane–helium mixtures[3] and by the magnetron sputtering method at $T_s=260$ °C and variations of the hydrogen partial pressure in the mixture of hydrogen with argon.[9] It should be noted that in Refs. 3 and 9 the film deposition rates reached 1.5 nm/s. In contradistinction to what we have said above, the MASD method can yield *a*-Si:H films with a low hydrogen content which have high values of R and contain dihydride complexes in the form of both SiH_2 and $(SiH_2)_n$ (Fig. 4). Furthermore, these films are deposited at rates no higher than 0.2 nm/s. Therefore, the deposition process and structure of the *a*-Si:H films studied have a certain uniqueness.

It was of interest to investigate how the characteristic structural features of the films obtained by the MASD method influence the electronic properties of the films, primarily, the photoconductivity. Data on the value of the product $\eta\mu\tau$, obtained from $\sigma_{\rm ph}$ as a function of E_c-E_F (η is the quantum yield, μ is the electron mobility, and τ is the electron lifetime) are presented in Fig. 5. The different symbols show the data for films containing $(SiH_2)_n$ films, SiH + SiH_2 complexes, and also only SiH complexes. The results of investigations of *a*-Si:H obtained in a number of European centers are also presented in Fig. 5 — Philips University (Germany, Ecole Polytechnique (France), BARI (Italy), and PATRAS (Greece).[10] The films were deposited by the glow-discharge method but under different conditions (reactor construction, temperature, composition of the gas mixture, and others). According to Ref. 10, the curve in Fig. 5 shows the limit of the region corresponding to device-quality *a*-Si:H. Let us see how well the data for films deposited by MASD method at $T_s=300-400$ °C correspond to it. Irrespective of their structure (SiH or $((SiH_2)_n)$, the *a*-Si:H films with $E_c-E_F=0.7-0.78$ eV ''fall'' into this region, with the exception of the films for which $I=1$ (Fig. 5): A strong decrease in $\eta\mu\tau$ for them is apparently due to the high impurity content (nitrogen, oxygen). We underscore that E_c-E_F in such *a*-Si:H is close to the ''intrinsic'' value.[11] Some films of ''pseudodoped'' *a*-Si:H, where $E_c-E_F<0.7$ eV, fall out of this region slightly.

Figure 6 shows the spectral curves of the absorption coefficient measured by the constant photocurrent method (CPM) for films of intrinsic and pseudodoped *a*-Si:H deposited by the MASD method. The defect density N_D was determined from these data by the method proposed in Ref. 12, as was also the Urbach parameter ε_u. For intrinsic and pseudodoped *a*-Si:H $N_D=8\times10^{15}$ cm^{-1} and 5×10^{16} cm^{-3} and $\varepsilon_u=50$ and 60 meV. It should be noted that N_D and ε_u for intrinsic *a*-Si:H correspond to the analogous quantities known for films deposited by the glow-discharge method. In the case of pseudodoped *a*-Si:H, for $E_c-E_F=$ const these parameters for the MASD films are high, which explains the small decrease in the value of $\eta\mu\tau$ (Fig. 5). It is significant that the films studied by us have high values $R=0.7-0.8$ and that the dihydride complexes in them are present in the form SiH_2. We also note that in Ref. 8 correlations were established between the microstructure parameter R and the Urbach parameter ε_u for *a*-Si:H films deposited by the glow-discharge method, and that the data for the MASD films correspond to the results of Ref. 8.

3. CONCLUSIONS

The method of direct-current decomposition of silane in a magnetic field (MASD) possesses a number of attractive features from the standpoint of the technology and the physics of amorphous silicon hydride, since it makes it possible to do the following:

— obtain *a*-Si:H films at T_s=300–400 °C with a low hydrogen content, using a strongly diluted silane–argon mixture;

— vary the hydrogen content in films with T= const and vary in a directed fashion the other conditions of deposition;

— vary the microstructure parameter R over wide limits with low hydrogen content, which cannot be done in other methods; and

— obtain at T_s= const (T_s=300–400 °C) films containing dihydride complexes in the form SiH_2 or $(SiH_2)_n$.

On this basis we considered these films as new objects for investigating the relationship between the structure and electronic properties of *a*-Si:H and we determined a correlation between the quantity $\eta\mu\tau$ and different forms of the hydrogen bond in a film. It was shown that a film of intrinsic *a*-Si:H can contain only SiH complexes and only $(SiH_2)_n$ complexes.

This work was supported by a grant INTAS N 931916.

We wish to thank W. Fuhs, the coordinator of the program, for providing the data on the parameters of *a*-Si:H films obtained in a number of European centers. We also thank A. I. Kosarev's group (IP2) for a fruitful collaboration.

[1] O. A. Golikova, A. N. Kuznetsov, V. Kh. Kudoyarova, and M. M. Kazanin, Fiz. Tekh. Poluprovodn. **30**, 1879 (1996) [Semiconductors **30**, 983 (1996)].
[2] G. Ganguly and A. Matsuda, Phys. Rev. B, **47**, 3661 (1993).
[3] P. Morin and Roca i Cabarrocas, MRS Proc. **336**, 281 (1994).
[4] O. A. Golikova, M. M. Kazanin, O. I. Kon'kov, V. Kh. Kudoyarova, and E. I. Terukov, Fiz. Tekh. Poluprovodn. **30**, 405 (1996) [Semiconductors **30**, 226 (1996)].
[5] A. H. Mahan, J. Carapella, B. P. Nelson, and R. S. Crandall, J. Appl. Phys. **69**, 6728 (1991).
[6] U. Kroll, J. Meier, M. Goetz, A. Howling, J.-L. Dorier, J. Dutla, A. Shah, and Ch. Hllenstein, J. Non-Cryst. Sol. **164–166**, 59 (1993).
[7] N. M. Johnson, P. V. Santos, C. E. Nebel, W. B. Jackson, R. A. Street, K. S. Stevens, and J. Walker, J. Non-Cryst. Sol. **137/138**, 235 (1991).
[8] D. Caputo, G. de Cesare, F. Irrera, F. Palma, M. C. Rossi, G. Conte, G. Nolile, and G. Fameli, J. Non-Cryst. Sol. **170**, 278 (1994).
[9] N. Beldi, J. Non-Cryst. Sol. **164–166**, 309 (1993).
[10] W. Fuhs (private communication).
[11] O. A. Golikova and V. Kh. Kudoyarova, Fiz. Tekh. Poluprovodn. **29**, 1128 (1995) [Semiconductors **29**, 584 (1995)].
[12] K. Pierz, W. Fuhs, and H. Mell, Philos. Mag. B **63**, 123 (1991).

Translated by M. E. Alferieff

Effect of laser irradiation on the photoconductivity and noise in n-$Cd_x Hg_{1-x}Te$ single crystals

A. I. Vlasenko, V. A. Gnatyuk, E. P. Kopishinskaya, and P. E. Mozol'

Institute of Semiconductor Physics, Ukrainian National Academy of Sciences, 252650 Kiev, Ukraine
(Submitted September 24, 1996; accepted for publication November 11, 1996)
Fiz. Tekh. Poluprovodn. **31**, 820–822 (July 1997)

The effect of nanosecond laser radiation on the photoconductivity and $1/f$ noise in $Cd_xHg_{1-x}Te$ crystals has been investigated. It is shown that laser irradiation decreases the photosensitivity of the samples and produces a short-wavelength shift of the maximum and the long-wavelength edge of the photoconductivity spectrum. The intensification of $1/f$ noise and the increase in its frequency are due to a laser-induced increase in the defect density in the material. © *1997 American Institute of Physics.* [S1063-7826(97)01407-5]

The electrical properties of narrow-gap semiconductor solid solutions $Cd_xHg_{1-x}Te$ are largely determined by the interaction of point and extended structural defects. The low plasticity threshold has the effect that under different actions (including laser irradiation), to which crystals are subjected in the process of fabrication of IR photoelectronics devices, substantial changes are observed in the defect structure.[1–4]

In this paper we report the results of an experimental study of the photoconductivity (PC) spectra and $1/f$-noise spectra in n-$Cd_xHg_{1-x}Te$ ($x=0.2$) single crystals irradiated by ruby laser ($\lambda=0.694$ μm) pulses with duration $t=20$ ns. The linear dimensions of the samples after polishing and chemical etching were 3×75 mm and the thickness was equal to 30 μm. Contacts were obtained by electrochemical deposition of indium on a freshly etched surface. The electron density determined from Hall measurements in a weak magnetic field $(\mu_H\cdot B)^2\ll1$ was $n=2.5\times10^{14}$ cm^{-3} and the Hall mobility was $\mu_H=1.5\times10^5$ cm^2/(V·s).

The PC spectra were measured at $T=77$ K at a fixed modulation frequency of 400 Hz with an IKS-21 infrared spectrometer. The intensification and conversion of the PC signal were performed with a preamplifier and a synchronous detector. The data processing was performed with a computer, taking into account the corrections for the spectral distribution of the globar. The PC spectra were converted to one photon of the incident radiation, displayed on a monitor screen, and printed out.

The excess noise was measured by the standard three- and four-probe method at $T=85$ K in the frequency range 1–20 kHz with a digital spectrum analyzer, which employs a fast Fourier transform algorithm. The spectral noise density $S_V(f)$ (where V is the constant voltage on the sample), after the generation–recombination component was subtracted out, was a quadratic function of the current and in the frequency range studied it varied as $1/f^{\gamma}$. The values of γ for different samples fell into the range 0.78–1.02.

The PC spectra before (1) and after (2, 3) laser treatment are shown in Fig. 1. The initial spectrum (1) was traced after chemical-dynamic treatment of the samples[1] and storage of the samples in air for one month. The sharp long-wavelength boundary of the spectrum shows that the crystals were uniform. After the samples were irradiated with ruby laser radiation with energy density 0.05 J/cm^2, the short-wavelength wing of the PC spectrum decreased, which indicated a decrease in the surface recombination rate (Fig. 1, curve *2*). Increasing the energy density of the pulses to 0.12 J/cm^2 decreases the PC signal and the short-wavelength shift of the maximum and the long-wavelength limit of the spectrum.

No changes are observed in the frequency spectra of $1/f$ noise with pulse energy density 0.5 J/cm^2. Increasing the irradiation energy density up to 0.12 J/cm^2 intensifies the $1/f$ noise (Fig. 2, curve *3*).

For the interpretation of the results we shall rely on the following facts.

1. Interband Auger recombination predominates in the initial experimental samples. The density of nonequilibrium charge carriers (NCCs) and their lifetime equal, respectively, $\Delta n=\Delta p$ and $\tau_n=\tau_p=\tau=3\times10^{-6}$ s. The NCC lifetime was calculated from the photocurrent relaxation curves with excitation by Nd laser radiation pulses ($\lambda=1.06$ μm, $t=20$ ns) in a linear regime.

2. The chemical-dynamic analysis of the surface does not produce deep damaged layers, and the effective rate of surface recombination, estimated from the short-wavelength drop of the PC signal, was equal to $s\ll10^3$ cm^3/s. After the samples were allowed to stand in air for one month, the surface was oxidized and the surface recombination rate increased to $s=3\times10^4$ cm/s (Fig. 1, curve *1*). The lifetime in the surface layer is lower than in the volume $\tau_s<\tau$. This makes it possible to characterize the interface with an effective parameter s_{eff}, which is not related to the classical quantity s.

3. The damaged regions are effective sinks for NCCs. In $Cd_xHg_{1-x}Te$ extended growth defects — finely dispersed inclusions of a second phase, large-scale fluctuations of the composition, vacancy clusters (voids), impurity and dislocation clusters, networks of small-angle boundaries, and others[5] — can act as sinks. Laser treatment decreases the intensity of the PC signal and produces a short-wavelength shift of the maximum of the PC spectrum (Fig. 1, curve *3*). Such a dependence of the PC is also observed under uniaxial compression of the crystal, when the stresses do not exceed the threshold for plastic deformation.[2] The composition of the crystal changes in the region of local plastic deformation.

 1063-7826/97/070695-03$10.00

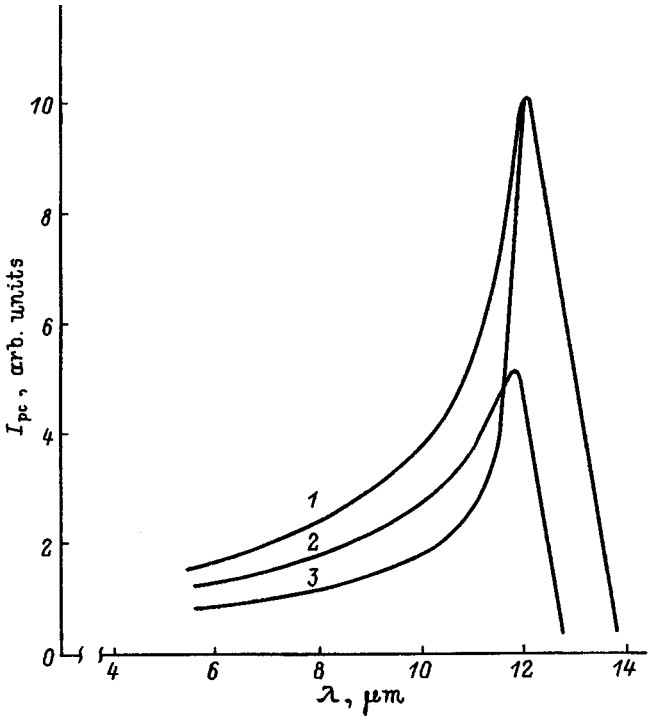

FIG. 1. Photoconductivity spectra of a n-$Cd_xHg_{1-x}Te$ crystal ($x=0.2$) and 77 K before (*1*) and after irradiation with ruby laser pulses with energy density (J/cm^2): *2* — 0.05, *3* — 0.12.

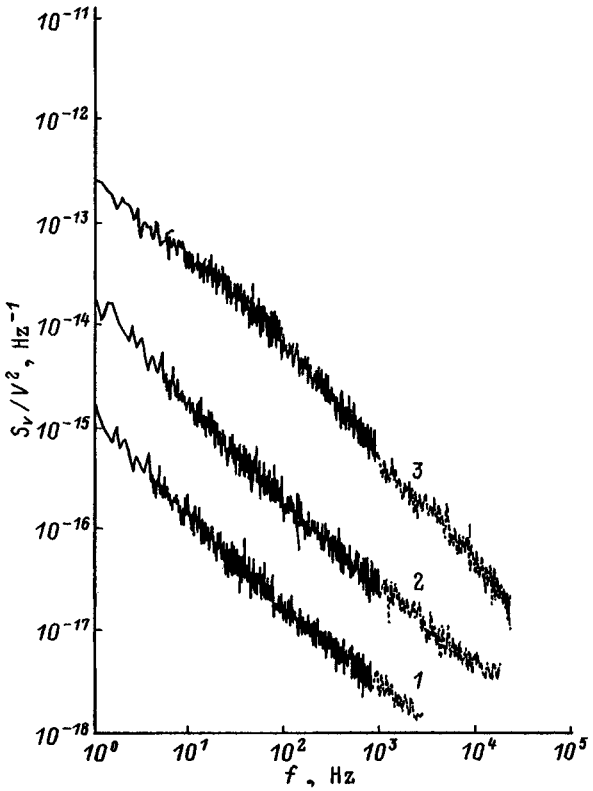

FIG. 2. Excess $1/f$-noise spectra with the generation-recombination component subtracted out: after chemical-dynamical treatment (1), after storage in air for a month (2), and after irradiation with laser radiation pulses with energy density 0.12 J/cm^2 (3).

An excess of mercury, with respect to its content in the matrix, forms around the imperfections.[4] The mercury-enrichment of the deformed region forms a semimetallic shell with a minimum value of τ. On the one hand, this region plays the role of internal short-circuits during current flow and, on the other, when the density of the short circuits is sufficiently high in the volume, they decrease the photosensitivity of the material.[6]

4. The increase in E_g in the state of uniaxial deformation of the crystal matrix is due to the positive pressure coefficient dE_g/dP.

Laser treatment leads to two ''technological'' effects in the surface layer — removal of the oxide film, which decreases the rate of surface recombination (Fig. 1, curve *2*), and evaporation of interstitial mercury with formation of a depleted, with respect to the majority carriers, inverted layer.[3] At high irradiation energy densities the composition of the solid solution changes in the direction of depletion with respect to mercury and compaction of the layers adjoining the surface by the shock wave which is produced. In both cases E_g increases; this can be judged from the short-wavelength shift of the maximum of the PC spectrum (Fig. 1, curve *3*).

5. The degradation of the material has the greatest effect on the photosensitivity of the material. In n-$Cd_xHg_{1-x}Te$ crystals allowed to stand for one year under natural conditions, the PC signal (especially in the region of fundamental absorption) and τ of the NCCs decreased by more than an order of magnitude.[5] Accordingly, the spectral characteristics of the noise density are shifted into the region of higher frequencies.

The model, which has been proposed thus far, for the aging mechanism of $Cd_xHg_{1-x}Te$ crystals reduces to diffusion of mercury atoms from the volume toward the surface and subsequent evaporation or oxidation of these atoms at the interface (at the surface). The rate of this process is determined by the intensity of the mercury flux at the surface, which depends strongly on the extent to which the material is defective.[5]

The measurements of the $1/f$-noise spectra established that the $1/f$-noise intensity increases with increasing irradiation energy. This result agrees with Ref. 7, where it is shown that defects (traps, localized states, scattering centers) are responsible for $1/f$-noise in $Cd_xHg_{1-x}Te$; i.e., a large number of defects corresponds to a higher noise level. Therefore, laser radiation generates in $Cd_xHg_{1-x}Te$ crystals defects which decrease the photosensitivity and are responsible for $1/f$-noise.

We thank Yu. N. Shavlyuk for performing the measurements of the spectral dependences of the noise.

[a)]fax: (044) 265-83-42

[1] B. D. Luft, *Physicochemical Methods for Treating Semiconductor Surfaces* [in Russian], Radio i svyaz', Moscow, 1982.
[2] V. V. Dykin, V. V. Koval', A. V. Lyubchenko, E. A. Sal'kov, and V. G. Chalaya, Neorg. Mater. **25**, 1645 (1989).
[3] I. S. Virt, A. V. Lyubchenko, P. E. Mozol', and V. A. Gnatyuk, Fiz. Tekh. Poluprovodn. **23**, 1386 (1989) [Sov. Phys. Semicond. **23**, 862 (1989)].
[4] S. G. Gasan-zade, E. A. Sal'kov, and G. A. Shepel'skiĭ, Fiz. Tekh. Poluprovodn. **17**, 1913 (1983) [Sov. Phys. Semicond. **17**, 1225 (1983)].

[5] A. I. Vlasenko, A. V. Lyubchenko, and E. A. Sal'kov, Ukr. Fiz. Zh. **25**, 434 (1980).
[6] A. I. Vlasenko, V. V. Gorbunov, and A. V. Lyubchenko, Ukr. Fiz. Zh. **29**, 423 (1984).
[7] I. S. Bakshi, V. F. Grin', L. A. Karachevtseva, T. Z. Kodalashvili, E. A. Sal'nikov, and B. I. Khizhnyak, Fiz. Tekh. Poluprovodn. **23**, 571 (1989) [Sov. Phys. Semicond. **23**, 357 (1989)].

Translated by M. E. Alferieff

Photoelasticity and quadratic permittivity of wide-gap semiconductors

S. Yu. Davydov and S. K. Tikhonov

A. F. Ioffe Physicotechnical Institute, Russian Academy of Sciences, 194021 St. Petersburg, Russia
(Submitted November 1, 1996; accepted for publication November 14, 1996)
Fiz. Tekh. Poluprovodn. **31**, 823–824 (July 1997)

Expressions for the photoelastic constants are obtained on the basis of an analogy between the photoelastic and elastic properties of semiconductor crystals. Calculations were performed for wide-gap semiconductors (silicon carbide and boron, aluminum, and gallium nitrides) with sphalerite and wurtzite structures. The quadratic permittivity is also calculated for hexagonal structures. © *1997 American Institute of Physics.* [S1063-7826(97)01507-X]

Despite extensive study of wide-gap semiconductors in recent years,[1] there is very little experimental information about the optical properties of these materials. For this reason, theoretical estimates of the charactertistics (even rough estimates) are certainly of interest. Phillips[2] advanced, on the basis of his dielectric model,[3] the suggestion that the photoelastic properties of semiconductors can be described by analogy with their elastic properties. Using the well-proven Keating empirical model of elasticity[4,5] and assuming a correspondence between the photoelastic (p_{ij}) and elastic (c_{ij}) constants, Phillips analyzed the satisfaction of the relation for cubic crystals

$$2p_{44}(p_{11}+p_{12})=(p_{11}-p_{12})(p_{11}+3p_{12}), \tag{1}$$

which is the exact analog of the expression relating the elastic constants c_{ij}. A check of the relation (1) for diamond showed that it holds within 16%. In the present paper we employ this analogy to estimate p_{ij} for silicon carbide and boron, aluminum, and gallium nitrides.

The following relation was obtained in Refs. 6 and 7:

$$p_{11}+2p_{12}=-\eta(\varepsilon_\infty-1)/\varepsilon_\infty^2, \tag{2}$$

where $\eta=2-6\alpha_p^2$. Here ε_∞ is the high-frequency permittivity, and α_p is the Harrison polarity of a crystal.[8–10] If $(p_{11}+2p_{12})/3$ is compared with the bulk modulus $B=(c_{11}+2c_{12})/3$, $(p_{11}-p_{12})/2$ is compared with the shear modulus $C_s=(c_{11}-c_{12})/2$, p_{44} is compared with c_{44}, and the relations obtained for the elastic constants in the Keating–Harrison model are used,[11] then we find

$$p_{11}=-\frac{1}{3}\eta k\left(1+\frac{8\lambda}{8+\lambda}\right)\frac{\varepsilon_\infty-1}{\varepsilon_\infty^2},$$

$$p_{12}=-\frac{1}{3}\eta k\left(1-\frac{4\lambda}{8+\lambda}\right)\frac{\varepsilon_\infty-1}{\varepsilon_\infty^2},$$

$$p_{44}=-\eta k\frac{33\lambda}{(8+\lambda)(8+3\lambda)}\frac{\varepsilon_\infty-1}{\varepsilon_\infty^2}, \tag{3}$$

where $\lambda=0.85$ is a dimensionless parameter,[8,9] and k is a dimensionless coefficient. In particular, it thus follows immediately that $p_{12}=0.35p_{11}$ and $p_{44}=0.51p_{11}$. According to the data in Ref. 12, for diamond $p_{11}=-0.38$, $p_{12}=-0.09$, and $p_{44}=-0.17$. This leads to the relations $p_{12}/p_{11}=0.23$ and $p_{44}/p_{11}=0.45$. Therefore, the relations (3) can serve as a preliminary estimate of the photoelastic constants. For $k=2$ we obtain from Eqs. (3) $p_{11}=-0.34$, $p_{12}=-0.12$, and $p_{44}=-0.18$, in good agreement with experiment. We note, however, that the experimental data are inconsistent. For example, in Ref. 3 the following data are given for diamond: $p_{11}=-0.31$, $p_{12}=-0.12$, and $p_{44}=0.09$.

The computational results for the photoelastic constants of wide-gap semiconductors with cubic structure are presented in Table I. The polarities α_p were calculated in Ref. 7 and the experimental values of ε_∞ were taken from Refs. 8 and 14. According to Table I, p_{ij} for silicon carbide and boron nitride agree with p_{ij} for diamond with respect to sign and order of magnitude. For compounds with a higher degree of ionicity, i.e., for aluminum and gallium nitrides, the photoelastic constants are an order of magnitude smaller and positive. In general, Keating derived expression (1) for c_{ij} for group-IV semiconductors and its form changes somewhat for heteropolar compounds.[15] This circumstance, however, is disregarded here.

The photoelastic constants for the hexagonal modification (wurtzite structure), which are converted from the constants for the sphalerite structure in accordance with Martin's theory[16] (see the corrections to this theory in Refs. 17 and 18), are presented in Table II. Here we disregard small changes in the high-frequency permittivity (according to the data in Ref. 19 for silicon carbide, the difference in ε_∞ between the wurtzite and sphalerite structures does not exceed 6%). Unfortunately, we know of no experimental data on the photoelasticity of hexagonal compounds.

The quadratic (bilinear) permittivity X_{14} of cubic wide-gap semiconductors was calculated in Ref. 7. Crystals with the wurtzite structure (6 *mm*) possess three independent components of bilinear permittivity: X_{15}, X_{31}, and X_{33}. The transformation which yields a relation between the permit-

TABLE I. Photoelastic constants p_{ij} for semiconductor crystals with sphalerite structure.

Crystal	SiC	BN	AlN	GaN
α_p	0.26	0.34	0.59	0.60
ε_∞	6.5	4.5	4.8	5.8
p_{11}	−24.5	−26.7	1.7	2.7
p_{12}	−8.5	−9.3	0.6	0.9
p_{44}	−12.5	−13.6	0.9	1.4

Note: The values of p_{ij} are increased by a factor of 10^2.

 1063-7826/97/070698-02$10.00

TABLE II. Photoelastic constants p_{ij} for semiconductor crystals with wurtzite structure.

Crystal	SiC	BN	AlN	GaN
p_{11}	−28.9	−31.4	2.0	3.1
p_{33}	−30.5	−33.1	2.2	3.3
p_{12}	−7.2	−7.4	0.5	0.8
p_{13}	−5.5	−6.0	0.4	0.6
p_{44}	−28.1	−30.5	0.7	1.0
p_{66}	−10.4	−11.8	0.7	1.2

Note: The values of p_{ij} are increased by a factor of 10^2.

tivities of cubic and hexagonal structures was obtained in Ref. 20:

$$X_{14}\frac{2}{\sqrt{3}}=X_{33}=-2X_{31}=-2X_{15}.$$

The values of these permittivities are given in Table III. According to the data in Ref. 21, for GaN films deposited on sapphire it is $X_{33}=2.88\times10^{-8}$ CGSE, in good agreement with the theoretical value 3.04×10^{-8} CGSE.

TABLE III. Bilinear permittivity X_{ij}.

Crystal	SiC	BN	AlN	GaN
X_{14}	0.27	0.29	2.31	2.63
X_{33}	0.31	0.33	2.67	3.04
$X_{31}=X_{15}$	−0.16	−0.17	−1.33	−1.52

Note: The values of X_{ij} are given in units of 10^{-8} CGSE.

This work was supported, in part, by the U.S. Department of Defense.

[1] M. G. Spencer *et al.*, [Eds.] *Proceedings of the 5th Conference on Silicon Carbide and Related Materials*, Inst. Phys. Conf. Ser., No. 137, Philadelphia, PA, 1993.
[2] J. C. Phillips, Rev. Mod. Phys. **42**, 317 (1970).
[3] J. C. Phillips, Phys. Lett. A **25**, 727 (1967).
[4] P. N. Keating, Phys. Rev. B **145**, 637 (1966).
[5] P. N. Keating, Phys. Rev. B **149**, 674 (1966).
[6] S. Yu. Davydov and E. I. Leonov, Fiz. Tverd. Tela (Leningrad) **30**, 1326 (1988) [Sov. Phys. Solid State **30**, 768 (1988)].
[7] S. Yu. Davydov and S. K. Tikhonov, Fiz. Tverd. Tela (Leningrad) **37**, 3044 (1995) [Sov. Phys. Solid State **37**, 1677 (1995)].
[8] W. Harrison, *Electronic Structure and Properties of Solids*, W. H. Freeman, San Francisco, 1980 [Russ. trans., Mir, Moscow, 1983, Vol. 1].
[9] W. A. Harrison, Phys. Rev. B **24**, 5835 (1981).
[10] W. A. Harrison, Phys. Rev. B **27**, 3592 (1983).
[11] S. Yu. Davydov and S. K. Tikhonov, Fiz. Tekh. Poluprovodn. **30**, 683 (1996) [Semiconductors **36**, 390 (1996)].
[12] R. S. Leigh and B. Szigeti, Proc. Roy. Soc. (London) A **301**, N 1465, 211 (1967).
[13] Yu. I. Sirotin and M. P. Shaskol'skaya, *The Principles of Crystal Physics* [in Russian], Nauka, Moscow, 1975.
[14] V. I. Gavrilenko, A. M. Grekhov, D. V. Korbutyakh, and V. G. Litovchenko, *Handbook of the Optical Properties of Semiconductors* [in Russian], Naukova dumka, Kiev, 1987.
[15] R. M. Martin, Phys. Rev. B **1**, 4005 (1970).
[16] R. M. Martin, Phys. Rev. B **6**, 4546 (1972).
[17] A. I. Gubanov and S. Yu. Davydov, Fiz. Tverd. Tela (Leningrad) **17**, 1463 (1975) [Sov. Phys. Solid State **17**, 945 (1975)].
[18] S. Yu. Davydov and S. K. Tikhonov, Fiz. Tverd. Tela (St. Petersburg) **37**, 2221 (1995) [Phys. Solid State **37**, 1212 (1995)].
[19] I. S. Grigor'ev and E. Z. Meĭlikhov [Eds.], *Handbook of Physical Quantities* [in Russian], Énergoatomizdat, Moscow, 1991.
[20] F. N. H. Robinson, Phys. Lett. A **26**, 435 (1968).
[21] J. Miragliotta, W. A. Bryden, T. J. Kistenmacher, and D. K. Wickenden, in *Proc. of the 5th Conf. on Silicon Carbide and Related Materials*, edited by M. G. Spencer *et al.*, Inst. Phys. Conf. Ser., N 137, Philadelphia, 1993, p. 537.

Translated by M. E. Alferieff

Role of spatial localization of a particle during tunneling

N. L. Chuprikov

Siberian Physicotechnical Institute at the Tomsk State University, 634050 Tomsk, Russia
(Submitted July 4, 1996; accepted for publication November 14, 1996)
Fiz. Tekh. Poluprovodn. **31**, 825–829 (July 1997)

The transmission coefficient and tunneling time of particles described by Gaussian wave packets of finite width are investigated theoretically. The average particle momenta in the case of transmission and reflection are calculated. It is shown that the tunneling parameters depend strongly on the degree of spatial localization of the particles. © *1997 American Institute of Physics.* [S1063-7826(97)01607-4]

1. INTRODUCTION

The latest investigations have shown that, even in its simplest formulation, the tunneling problem is not as trivial as it seemed initially. Even in the one-dimensional, one-particle model the stumbling block turned out to be the task of determining the temporal characteristics of tunneling.[1,2] At present, the tunneling process is clearly understood only for particles whose momentum is prescribed accurately. It is assumed that such particles are described by wave packets which are wide compared to the barrier structures, in which the tunneling occurs. Most investigations (see the review article in Ref. 1) are in agreement that the particle dynamics in the barrier region is characterized in this case by the ''phase'' transmission time.

The situation is completely different for particles which are described by wave packets of arbitrary width. Here there is no single opinion (see Refs. 1 and 2) either about how to define the tunneling time correctly or even how to interpret correctly some properties of the wave packet dynamics which have been observed in numerical modeling of one-dimensional structures. This includes effects such as the change in the average momentum of the wave packets during scattering and also the ''premature'' (i.e., with ''breakdown'' of causality) appearance of the transmitted packet on the other side of the barrier.

The analysis in Ref. 3 showed that the observed behavior of wave packets appears to be unphysical because of an incorrect interpretation of the quantum-mechanical description of the tunneling process. Ordinarily (explicitly[4,5] or implicitly[2]), in estimating the tunneling times of a particle the positions of the centers of mass (i.e., the average values of the coordinate x) of the transmitted and reflected packets are compared separately with the corresponding characteristic of the incident packet. However, such a procedure makes no sense physically, because all three packets describe different sets of measurements. This question was examined in detail in Ref. 3, where a new definition of tunneling times was proposed for particles described by wave packets of a general form.

In the present paper we essentially continue the work begun earlier.[3] We will investigate numerically the tunneling parameters of a particle (transmission coefficient, average momentum, and the tunneling times determined in Ref. 3), whose initial state is described by the Gaussian wave packet

$$\psi_{\rm inc}(x,t)=\frac{c}{2\pi}\int_{-\infty}^{\infty}A(k)(i(kx-E(k)t/\hbar))dk, \tag{1}$$

where

$$A(k)=\exp(-l_0^2(k-k_0)^2);$$

c is a normalization constant, l_0 is the packet width, k_0 is the average wave number, and $E(k)=\hbar^2k^2/2m$. Following Ref. 3, it is assumed here that the left-hand boundary of the barrier lies far to the right of the coordinate origin, where the maximum of the incident wave packet is located initially.

Let $T(k)$ and $J(k)$ be the transmission coefficient and phase, respectively, which characterize the tunneling of a separate wave with fixed wave number k (see Ref. 6). Then, according to Ref. 3, the transmission time τ_{tr} of a particle through the barrier region is given by

$$\tau_{tr}=\frac{m\langle J'\rangle_{tr}}{\hbar\langle k\rangle_{tr}}. \tag{2}$$

The corresponding reflection time $\tau_{\rm ref}$, if the analysis is restricted to the symmetric barriers, is given by the expression

$$\tau_{\rm ref}=\frac{m\langle J'\rangle_{\rm ref}}{\hbar\langle -k\rangle_{\rm ref}}. \tag{3}$$

Here and below the symbol $\langle\ldots\rangle$ denotes averaging over the transmitted (tr), reflected (ref), or incident (inc) wave packets (see Ref. 3); the prime denotes a derivative with respect to k. The transmission coefficient $\overline{T}$ of a particle is determined (see Ref. 3) according to the formula $\overline{T}=\langle T(k)\rangle_{\rm inc}$.

We performed all calculations for dimensionless quantities. In addition, we chose the width d of the barrier structure as the unit of measurement in the case of aperiodic structures and the width of one period in the case of periodic structures. The formulas relating dimensional and dimensionless (marked with a tilda) quantities are

$$\lambda_0=\tilde{\lambda}_0 d,\quad l_0=\tilde{l}_0 d,\quad V=\frac{\hbar^2}{2md^2}\tilde{V},\quad t=\frac{md^2}{\pi\hbar}\tilde{t},$$

where V is the potential, t is the time, and $\lambda_0=2\pi/k_0$.

2. SQUARE BARRIERS

The main patterns of the variation of the tunneling parameters with increasing degree of particle localization are

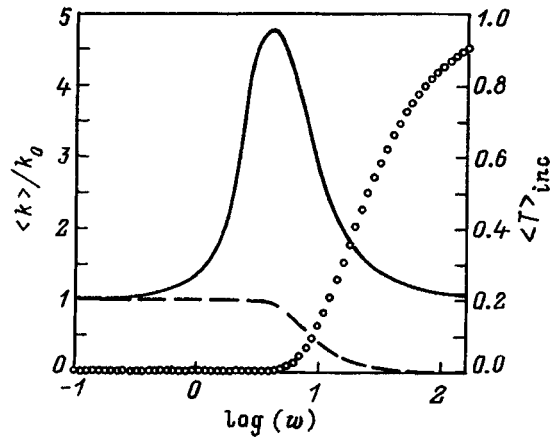

FIG. 1. Transmission coefficient (dots), $\langle k\rangle_{tr}/k_0$ (solid curve), and $\langle k\rangle_{\mathrm{ref}}/k$ (dashed curve) for square barriers of height $\widetilde{V}=30$ and $\widetilde{\lambda}_0=5$.

demonstrated for the example of square barriers with $\widetilde{V}=30$ and $\widetilde{\lambda}=5$. We note first that for any barriers with $w=0$ ($w=1/\widetilde{l}_0$) all particle tunneling parameters are numerically equal to the corresponding parameters for an individual wave. Specifically, the tunneling times (2) and (3) equal the phase times. However, for $w\neq 0$, when the wave packet describing a particle possesses a finite width in x-space, the character of the particle scattering changes substantially. As w increases, the fraction of the harmonics for which the barrier is transparent increases in the spectrum of the wave packet. As a result, the transmission coefficient of the particle increases (Fig. 1). In addition, the most rapid growth is observed in the region $0\leqslant\log(w)\leqslant 2$. For complicated multibarrier structures, when one-wave resonances are present near E_0 ($E_0=E(k_0)$), the behavior of $\overline{T}(w)$ in this region can be nonmononotic. However, in any case, as $w\to\infty$, irrespective of k_0 and the form of the barrier, $\overline{T}\to 1$ for particles which are initially localized at a point and any barrier is transparent.

A characteristic feature of the tunneling of particles described by wave packets of finite width is that the average momenta of the incident, transmitted, and reflected packets are all different. However, as has already been noted (see Fig. 3), this does not at all mean that a particle is accelerated

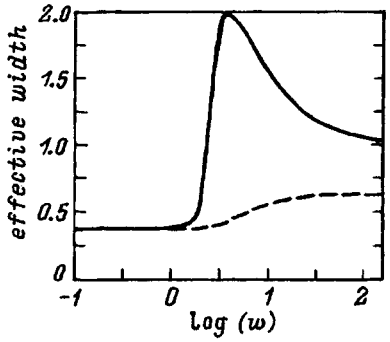

FIG. 2. Effective barrier width ($\widetilde{J}'$) for a transmitted particle (solid curve) and a reflected particle (dashed curve). The parameters of the barrier and of the particle are the same as those in Fig. 1.

or decelerated by a potential barrier (though such an interpretation is possible[2]). Evidently, the particle momentum should not change in the case of scattering by a static potential barrier. In a quantum-mechanical description (which essentially refers to all measurements including the two possible variants of scattering), this property is reflected in the fact that the average values of the momentum over the initial (incident wave packet) and final (transmitted + reflected wave packets) states are identical. Therefore, the fact that the average momenta of the transmitted and reflected wave packets are diffrent indicates only that the average particle momentum in each (of the two) series of measurements is different. In addition, the average particle momentum before and after scattering is the same in each series separately (see Ref. 3). Figure 1 shows for the square barriers investigated the ratio of the average momenta of both packets to the momentum of the incident packet as a function of the parameter w. As one can see from the figure, the average momenta of the incident and transmitted packets are the same for particles whose initial momentum or coordinate is precisely fixed. In the first case this occurs because the incident packet actually consists of one harmonic. In the second case it is due to the fact that the particle passes through the barrier without reflecting (see above). (Here it should be kept in mind that in the first case the form of the wave packet does not change on scattering, whereas in the second case the transmitted packet at sufficiently long times breaks up into a countable set (ensemble) of wave packets with one maximum which move with different velocities.) In the interval $0\leqslant\log(w)\leqslant 2$ we have a situation in which the fractions of the harmonics for which the barrier is transparent and nontransparent are the same in the spectrum of the wave packet. The shape of the wave packet in this case is much more strongly distorted on scattering, and the momentum of the transmitted packet is greater than the momentum of the incident packet by the maximum possible amount. The reflected packet decelerates in this region (see Ref. 3). In general, when resonances are present near E_0, the dependence of the average momenta on w for both packets is more complicated. Specifically, the momentum of the transmitted packet can be less than that of the reflected packet.

Let us now consider the quantities $\langle J'\rangle_{tr}$ and $\langle J'\rangle_{\mathrm{ref}}$ in the expressions (2) and (3) for the particle tunneling times. They can obviously be regarded as effective barrier widths for a particle in the corresponding series of measurements. One can see from Fig. 2 that both quantities are identical if the particle momentum is fixed accurately enough. In all other cases they are different. In the limit $w\to\infty$ the effective barrier width for the transmitted particle (we recall that in this case particle transmission through the barrier eqauls 100%) equals the barrier width d. Particles initially localized at a point pass through the barrier region without ''noticing'' the barrier, since their average energy is infinite.

It is known that the phase tunneling time can be negative. In this case, the corresponding effective barrier width is also negative. For example, this happens for a particle with $\widetilde{\lambda}_0=5$ that passes through a square potential well of depth $\widetilde{V}=-1$ (see Fig. 3). At first glance, this result is unphysical, since the negative times indicate violation of the causality

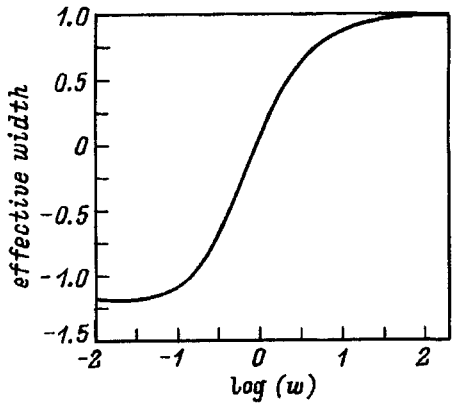

FIG. 3. $\langle \tilde{J} \rangle_{tr}$ for a square well with $\tilde{V}=-1$ and $\tilde{\lambda}_0=5$.

principle (we note immediately that this case of ''violation'' of the causality principle is fundamentally different from the one studied in Ref. 3, which occurs only for packets with $w \neq 0$). However, it should be kept in mind that in this case the well width is much smaller than the width of the wave packet. Under such conditions the tunneling is strongly nonlocal. Furthermore, here it is very important to remember that the formalism proposed in Ref. 3 makes it possible to determine the passage time only for sections (including the barrier region) whose boundaries lie at distances from the barrier that are much greater than the width of the wave packet. The tunneling time of the barrier section is determined in Ref. 3 as the contribution of the barrier region to the total transmission time through these sections. In the case at hand, probes for measuring the tunneling time should be placed at a distance from the barrier that is much greater than the width of the barrier. However, if a particle is initially described by a Gaussian packet, whose width is much less than that of the barrier, then the probes can be placed right up against the edges of the barrier. If the time (3) is negative in this case as well, then there would be grounds for talking about violation of the causality principle. However, the calculations show (see Fig. 3) that as w increases, the effective barrier width for the transmitted particle becomes positive and in the limit $w \to \infty$ it equals d.

3. PERIODIC STRUCTURES

Particle tunneling through bounded and semibounded (super)lattices is of special interest. This question was studied in Refs. 7 and 8 for particles with an accurately defined momentum. It was shown that in this case all resonances for periodic structures lie in the energy regions (transmission regions) which are allowed bands for the corresponding unbounded structures. In Ref. 7, it was shown that, for a sufficiently large number of lattice periods, within each of these regions the plots of the energy dependence of the transmission coefficient and phase transmission time for one period fall between two envelopes. The explicit form of both pairs of envelopes was also found in Ref. 7. In semibounded lattices, when the number of periods is infinite, the energy derivatives of both functions are unbounded almost everywhere in the regions of transmission.

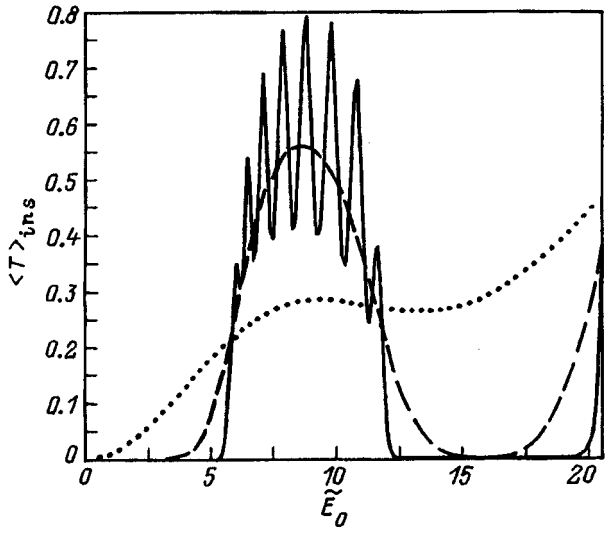

FIG. 4. Transmission coefficient versus the parameter $\tilde{E}_0$ (see text) for a periodic structure consisting of ten square barriers of height 13 and width 0.5, well width — 0.5; $\tilde{l}_0=2$ (solid curve), 0.28 (dashed curve), and 0.07 (dotted curve).

To understand such unusual properties it is important to remember the following. When the problem concerns the tunneling of particles with a well-defined momentum, it is actually assumed that the width of the corresponding Gaussian wave packets in x space is known to be greater than the width of the periodic structure under study. In this case the role of the two boundaries of the structure is important for any arbitrarily large (but finite) number of periods of the structure.

How does tunneling of a particle through a lattice occur if the initial state of the particle is described by a wave packet of arbitrary width? First, here it should be kept in mind that for $w \neq 0$ the solution of the Schrödinger equation no longer satisfies Floquet's theorem in the region of periodicity of the potential. Therefore, particle localization results

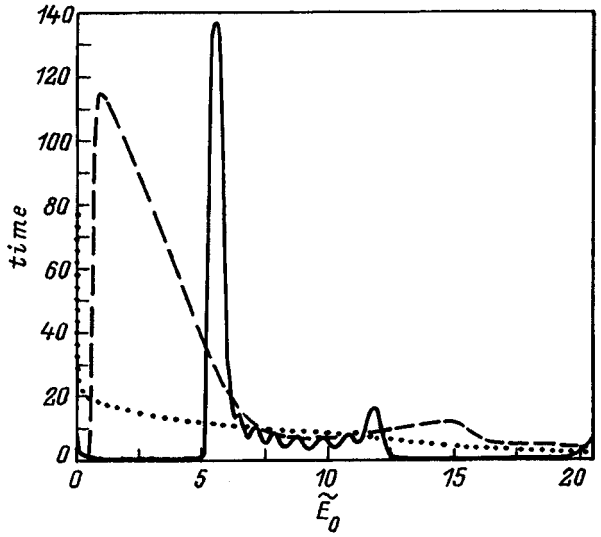

FIG. 5. Tunneling time $\tilde{\tau}_{tr}$ for one period in a periodic structure (see Fig. 4).

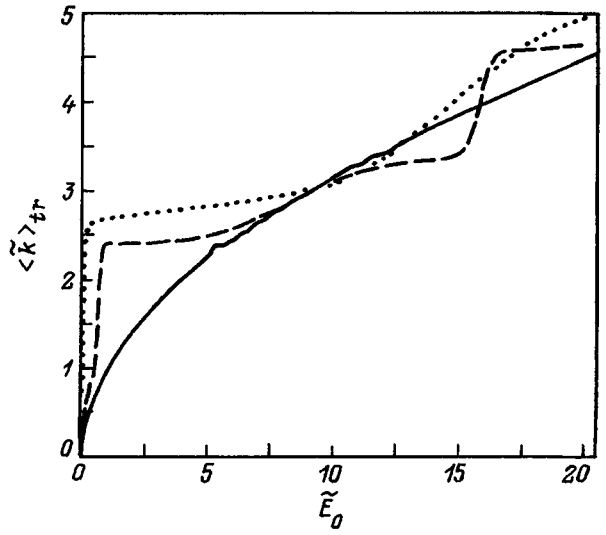

FIG. 6. $\langle \tilde{k} \rangle_{tr}$ for a periodic structure (see Fig. 4).

in destruction of the band character of the energy spectrum (division of the energy scale into regions of transparency and nontransparency). We performed calculations for structures consisting of ten square barriers of width 0.5 (the distance between the barriers obviously also equals 0.5) and height 13. Figures 4 and 5 show the transmission coefficient and transmission time of one period as a function of the parameter $\tilde{E}_0$ for these values of $\tilde{l}_0$: 2, 0.28, and 0.07. The calculations, which were performed for large values of $\tilde{l}_0$ as well, showed that the envelopes of both functions in the transmission regions are most sensitive to a change in $\tilde{E}_0$. As $\tilde{l}_0$ decreases in the interval $N \leqslant \tilde{l}_0 \leqslant 1$ (N is the number of periods), the corresponding pairs of envelopes approach one another and then merge into one curve. As the parameter $\tilde{l}_0$ decreases further, the transmission coefficient is already substantially different from zero in the regions of nontransmission as well. In addition, here the temporal characteristic changes most strongly. If for $\tilde{l}_0 \gg 1$ the transmission time for one period in the region of nontransmission is nearly equal to zero, then for localized particles this characteristic, as one can see from the figure, increases to such an extent that it can even exceed the corresponding tunneling time in the transmission region. The well-known problem of ''superluminal'' propagation of wide (in x space) wave packets through (super)lattices in regions of nontransmission (see, for example, Ref. 2) does not arise for particles for which the uncertainty of the initial position does not exceed one lattice period.

I shall now briefly discuss the dependence of $\langle \tilde{k} \rangle_{tr}$ on $\tilde{E}_0$ (see Fig. 6). As one can see from Fig. 6, an appreciable deviation of this quantity from $\tilde{k}_0$ is observed in the region of nontransmission, when $\tilde{l}_0 < 1$. For $\tilde{l}_0 = 2$, the average momentum of the transmitted (and therefore reflected) particles is virtually identical to that of the incident particles. Small deviations are observed only near the boundaries of the regions of transparency.

In closing, I note the following. It is known that wave packets spread with time. Therefore, it is worth underscoring that in the formalism of Ref. 3 the tunneling parameters depend on the initial width of the packet.

[1] E. H. Hauge and J. A. Stovneng, Rev. Mod. Phys. **61**, 917 (1989).
[2] R. Landauer and Th. Martin, Rev. Mod. Phys. **66**, 217 (1994).
[3] N. L. Chuprikov, Fiz. Tekh. Poluprovodn. **3**, 443 (1996) [Semiconductors **30**, 246 (1996)].
[4] E. H. Hauge, J. P. Falck, and T. A. Fjeldly, Phys. Rev. B **36**, 4203 (1987).
[5] C. R. Leavens and G. C. Aers, Phys. Rev. B **39**, 1202 (1989).
[6] N. L. Chuprikov, Fiz. Tekh. Poluprovodn. **26**, 2040 (1992) [Sov. Phys. Semicond. **26**, 1147 (1992)].
[7] N. L. Chuprikov, Fiz. Tekh. Poluprovodn. **30**, 443 (1996) [Semiconductors **30**, 246 (1996)].
[8] Xue-Wen Liu and A. P. Stamp, Phys. Rev. B **50**, 1588 (1994).

Translated by M. E. Alferieff

Variation of the optical properties of porous silicon as a result of thermal annealing in vacuum

V. A. Kiselev, S. V. Polisadin, and A. V. Postnikov

Institute of Microelectronics, Russian Academy of Sciences, 150007 Yaroslavl', Russia
(Submitted July 4, 1996; accepted for publication November 14, 1996)
Fiz. Tekh. Poluprovodn. **31**, 830–832 (July 1997)

The optical constants of layers of porous silicon in the range 600–800 nm have been determined and the effect of vacuum thermal annealing on them has been investigated. The variation of the complex index of refraction is attributed to the desorption of reagents and products of electricochemical treatment of the silicon. It was determined that the temperature coefficient of the variation of the reflection of a layer of porous silicon on heating up to 600 °C does not exceed 10^{-6} at a wavelength of 633 nm. © *1997 American Institute of Physics.* [S1063-7826(97)01707-9]

There exist two basic models for explaining the luminescence of porous silicon (PS). According to one model, the pumping radiation is absorbed in the volume of the PS and the photoluminescence (PL) is a consequence of radiative recombination at the surface.[1–3] The other model assumes that the luminescence is due to the presence of siloxen-type compounds that arise during anodization of the silicon on the surface of the PS.[4]

The study of the optical properties of PS can yield information about the electronic structure and mechanisms of light absorption and recombination and serve to give a better understanding of the nature of PL. During thermal annealing of samples of PS, products of the electrochemical treatment are desorbed from its surface and its luminescence properties change. To obtain information about the nature of PL in PS, we investigated the change in the optical characteristics of PS during vacuum heat-treatment.

The PS layers were prepared on KDB-1 silicon plates (boron-doped silicon, resistivity 1 $\Omega\cdot$cm) with (100) orientation. The electrolyte consisted of hydrofluoric acid (50% solution) and isopropyl alcohol in a 1:1 ratio. Etching was performed with a current density of 15 mA/cm^2 for 30 min. After anodization the samples were washed in deionized water and dried in air. To remove the film formed during anodization[4,5] and to prepare samples of different thickness, the PS layer was treated in KOH.

The thermal annealing of PS was performed in a vacuum chamber with a residual pressure of 10^{-6} Torr. The temperature of the heater, on which the experimental sample was secured, was raised by steps of 10–20 K and held for 10–15 min at each new temperature. When the plate with the PS layer was heated rapidly, the PS separated from the substrate and cracking occurred along the isothermal lines, indicating the presence of a substantial mechanical stress in the PS layer.[6] The maximum heating temperature was equal to 600 °C. In this manner, PS layers which were heated once and subjected to a heating–cooling cycle several times were prepared. The heat-cycling treatment was repeated until the temperature dependence of the reflection coefficient measured at an angle of incidence of 15° at the wavelength $\lambda = 633$ nm of He–Ne laser radiation repeated. The reflection spectra (in the interval 400–800 nm) and the luminescence and infrared (IR) transmission spectra (500–5000 cm^{-1}) were obtained for the initial samples and for the heat-treated PS layers.

It was established that even after a one-time heating up to 500°C the PS completely loses its ability to luminesce.

Thermal desorption mass spectra were also obtained for the initial PS samples. Figure 1a shows the dependence of the number of desorbed particles on the temperature T for the two most intense components with mass numbers 2 and 18, associated with H_2 and H_2O, respectively. The variations of the reflection coefficient R at wavelength $\lambda = 633$ nm for the first and fifth cycles, in the case where a sample of thickness $h = 8$ μm was heated, are presented in Fig. 1b. Comparing Figs. 1a and 1b one can see that the change in the reflection coefficient can be attributed to the desorption of gases from the surface of the PS. For a sample of thickness $h = 3$ μm, three heat-treatment cycles were required before the results of the measurements of the reflection started to repeat in each cycle (Fig. 1c). We see from Fig. 1c that the effect of the substrate is still felt for a thin sample, since the curve of the variation of the reflection coefficient can be approximated by a straight line which describes the temperature dependence of the reflection coefficient of a clean silicon surface. Therefore, the data from these experiments attest to the fact that sorption–desorption of gases by the PS surface are the mechanisms responsible for the change in the reflection coefficient of PS on heating up to 600 °C.

It is interesting that for sufficiently thick samples, with thickness $h > 5$ μm, the reflection coefficient is temperature-independent.

The reflection spectra before and after annealing are presented in Figs. 2 and 3, respectively. The result of the heat treatment is an increase in the reflection coefficient of the PS surface in the region 400–550 nm (Fig. 3). This can be attributed to the formation of dangling bonds and narrowing of the band gap or to the appearance of additional levels or bands in the band gap due to the hydrogen losses.[7,8]

To calculate the optical constants of the PS layers, the reflection spectra were measured for two states of polarization S and P of the incident light. The fact that for wavelengths of 600–800 nm the imaginary part of the complex index of refraction $\varkappa \ll 1$ and its contribution to the reflection coefficient is very small were taken into account. This made

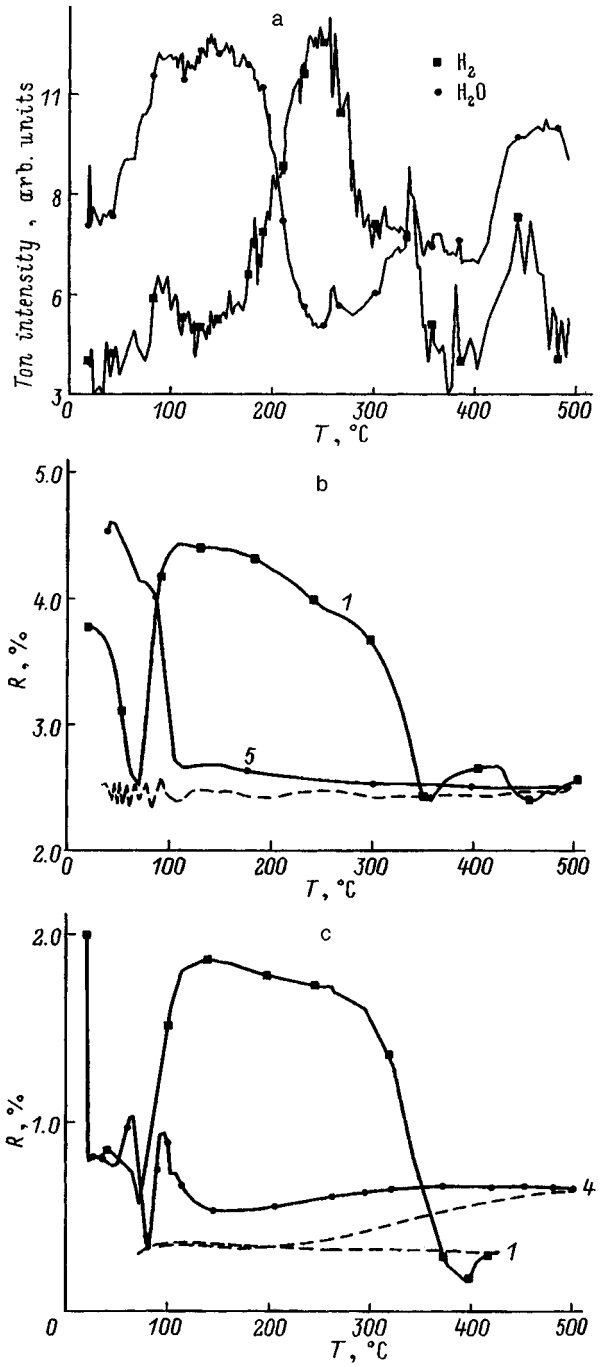

FIG. 1. a — Intensity of thermal desorption of H_2 and H_2O versus temperature T. b — Reflection coefficient R of a PS layer of thickness $h=8$ μm versus temperature T on heating (solid line) and cooling (dashed line) in the first (1) and fifth (5) heat-treatment cycles. c — Reflection coefficient R of a PS layer of thickness $h=3$ μm versus temperature T on heating (solid line) and cooling (dashed line) in the first (1) and fourth (4) heat-treatment cycles.

it possible to calculate by a fitting procedure the complex index of refraction $n+i\varkappa$ and the thickness h of the PS film. A rough estimate of the thickness of the layer was made from microscopic measurements performed on the cleavage face of the sample.

The procedure of fitting the parameters $n, \varkappa$, and h consisted of the following:

1) The dependences of n and $\varkappa$ on λ in the wavelength range 600–800 nm were approximated by straight lines, so that $n=a+b\lambda$ and $\varkappa=c+d\lambda$;

2) assuming that the thickness h is sufficiently large to eliminate interference effects, we chose a and b in such a way that the computed straight line of the reflection coefficient is an average line of the experimentally recorded reflection spectrum;

3) c, d, and h were chosen so that in the computed curve the amplitude of the oscillations of the reflection coefficient corresponded to the experimental amplitude; and

4) the computed curve was phase-matched with the experimental curves by varying h over a small range (tens of nanometers).

The reflection coefficient of the PS layer was calculated using Fresnel's formulas for an absorbing film on an absorbing substrate.[9] The real part of the refractive index of silicon was determined from measurements of the reflection spectra for the initial plate, and the spectral dependence of the imaginary part was taken from the literature.[10] The computational results are given in Table I.

The entire procedure of reconstructing the parameters n, $\varkappa$, and h from measurements of the reflection spectra was tested for a SiO_2 layer on silicon and showed good agree-

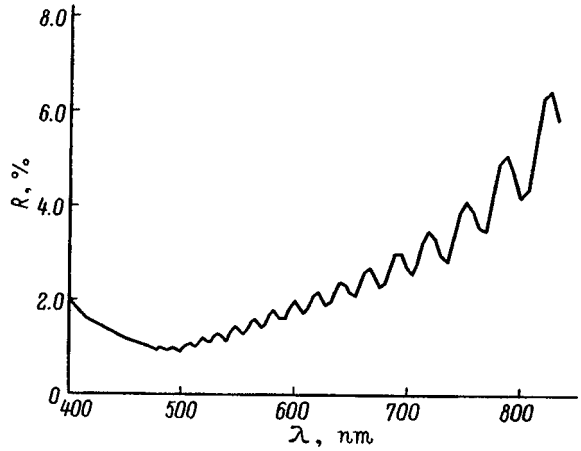

FIG. 2. Reflection spectrum of intial PS sample.

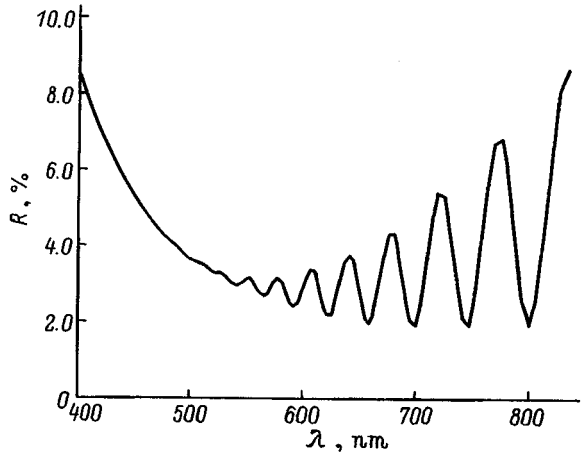

FIG. 3. Reflection spectrum of a heat-treated PS sample.

TABLE I. Optical constants and thickness of initial and annealed layers of PS.

	n		$\varkappa$		h μm	
PS	λ=600 nm	λ=800 nm	λ=600 nm	λ=800 nm	Calculation	Microscopic measurements
Initial sample	1.25	1.58	0.017	0.013	14.475	7.5
Heat-cycled sample	1.3	1.6	0.026	0.015	7.825	7.5

ment between the reconstructed values of n and h and the values obtained from independent measurements.

For PS samples which were not subjected to heat treatment, the computed thickness of the layer was found to be 2–2.5 times greater than the thickness determined from microscopic measurements. For heat-cycled samples the thickness of the layer determined in the fitting procedure was equal to the measurements performed on the cleavage face. From preceding investigations of PS[11,12] it is known that a PS layer is structurally uniform over thickness and the film–substrate interface is sharp. Experiments on oxidation of PS[13] showed that compaction and settling start at temperatures above 1000 °C. On the basis of these data, the difference between the computed and measured film thicknesses can be explained by the substantial optical nonuniformity of the PS layer over depth, i.e., by the fact that chemically adsorbed reagents and products of electrochemical treatment of silicon are present in the voids.

It is evident from Table I that the values of $\varkappa$ for the initial and annealed samples are close, but because the computed thickness of the PS layer is excessive, in order to obtain the same magnitude of damping of the amplitude of the interference maxima and minima in the reflection spectra, the value of $\varkappa$ must be increased by the same factor by which h is overestimated. Because of the optical nonuniformity over the thickness of the initial PS layers, the values of $\varkappa$ found for them are approximate.

In summary, the effect of vacuum thermal annealing on the optical properties of PS has been investigated. It was found that the chemically adsorbed products of electrochemical treatment of silicon substantially alter the electronic states in the layer. This is manifested in the fact that for the initial samples the optical thickness nh of the layer is much greater (2.0–2.5 times) than the optical thickness of the heat-cycled sample. Annealing decreases the imaginary part of the complex refractive index for wavelengths of 600–800 nm. Such changes in the optical constants can affect the probability of surface recombination of carriers and thereby give rise to quenching of luminescence. It was also found that the temperature coefficient of reflection of PS is at least substantially less than for the initial silicon plates and does not exceed 10^{-6}.

[1] G. G. Qin and I. Q. Jia, Solid State Commun. **86**, 559 (1993).
[2] J. Kanemitsu, H. Uto, and J. Masumoto, Phys. Rev. B **48**, 2827 (1993).
[3] F. Koch, V. Petrova-Koch, T. Muschik, A. Nicolov, and V. Gavrilenko, Mater. Res. Soc. Symp. **283**, 197 (1993).
[4] H. D. Fuchs, M. Stutzmann, M. S. Brandt, M. Rosenbauer, J. Weber, A. Breitchwerdt, P. Deak, and M. Cardona, Phys. Rev. B **48**, 8172 (1993).
[5] V. A. Kisilev, A. A. Chrebtugov, and A. B. Churilov, *SPIE Proc. Int. Conf. Microelectronics-92*, Warsaw, Poland, 1992, Vol. 1783, p. 378.
[6] V. Lehmann and U. Gosele, Appl. Phys. Lett. **58**, 856 (1991).
[7] N. Ookubo, H. Ono, Y. Ochial, Y. Mochizuki, and S. Matsui, Appl. Phys. Lett. **61**, 940 (1992).
[8] E. A. Konstantinova, V. Yu. Timoshenko, and P. K. Kashkarov, Poverkhnost', No. 2, 32 (1996).
[9] V. K. Gromov, *Introduction to Ellipsometry* [in Russian], Leningrad State University, Leningrad, 1986.
[10] Zh. Pankov, *Optical Processes in Semiconductors* [in Russian], Nauka, Moscow, 1973.
[11] M. I. J. Beale, J. Crysr. Growth **73**, 622 (1985).
[12] V. A. Labunov, V. P. Bondarenko, L. K. Glinenko, and I. N. Basmanov, Mikroélektronika **12**, 11 (1983).
[13] J. J. Yon, K. Barla, R. Herino, and G. Bomchil, J. Appl. Phys. **62**, 1042 (1987).

Translated by M. E. Alferieff

Electron-hole scattering in *p*-type silicon with a low charge-carrier injection level

T. T. Mnatsakanov and L. I. Pomortseva

V. I. Lenin All-Russia Electrical Engineering Institute, 111250 Moscow, Russia

V. B. Shuman

A. F. Ioffe Physicotechnical Institute, Russian Academy of Sciences, 194021 St. Petersburg, Russia
(Submitted November 11, 1996; accepted for publication November 14, 1996)
Fiz. Tekh. Poluprovodn. **31**, 833–835 (July 1997

A previously proposed method for determining the parameters of electron-hole scattering in indirect-gap semiconductors is used to investigate the properties of *p*-type silicon. Diode n^+–p–p^+ structures were used for the measurements. The results obtained by us indicate that complete dragging of the minority electrons by the majority holes is possible, even at room temperature, in *p*-type material with doping levels $N>10^{18}$ cm^{-3}. © *1997 American Institute of Physics.* [S1063-7826(97)01807-3]

1. A method for investigating the parameters characterizing electron-hole scattering (EHS) in indirect-gap semiconductors with a low charge-carrier injection level was recently proposed in Ref. 1. The first application of this method for investigation of EHS in *n*-type silicon gave interesting results, indicating the possibility for the existence of complete dragging of minority charge carriers by the majority carriers, during which the mobility of the minority charge carriers changes sign and becomes negative, in *n*-type silicon with doping levels $N\geqslant 10^{17}$ cm^{-3} at room temperature. The existence of the complete dragging of minority charge carriers by majority charge carriers was first established experimentally in gallium arsenide quantum wells[2,3] with doping level $N\simeq 10^{17}$ cm^{-3} and temperature $T\simeq 90$ K. A comparative estimate[4] of the effect of the EHS on charge-carrier transport showed that the EHS efficiency in silicon is approximately 50 times higher than in gallium arsenide. The result obtained in Ref. 1 is in agreement with the estimate presented and attests to the fact that the complete dragging of minority charge carriers by the majority charge carriers can appreciably influence the characteristics of silicon structures. According to Refs. 5 and 6, EHS can strongly alter the injection capacity of a p^+–n junction.

Ordinarily, doping levels $N\geqslant 10^{17}$ cm^{-3} are realized in the emitter layers of semiconductor structures. From this standpoint, it is of great interest to investigate this effect in *p*-type silicon, since in most silicon structures, which are ordinarily fabricated on the basis of *n*-type material, the emitter layers are *p*-type. Our objective in the present paper is to investigate the parameters characterizing EHS in *p*-type silicon with a low charge-carrier injection level and to evaluate the possibility of complete dragging of minority charge carriers by the majority charge carriers in this material.

2. The investigation was based on the method proposed and described in detail in Ref. 1. This method involves the measurement of the current-voltage characteristic (IVC) of diode samples in a specially chosen range of current densities and to determine the mobility μ_{np}, determined by the EHS, with the help of the following relations.

In the case where the doping level does not exceed the characteristic value $N_0=10^{17}$ cm^{-3}, i.e., when the bandgap narrowing is small,[7] μ_{np} is given by

$$\mu_{np}=\frac{\mu_n}{A^2-1}, \tag{1}$$

where $A=(j_0)_{\rm cal}/(j_0)_{\rm exp}$, $(j_0)_{\rm cal}=(qn_{i0}^2/N_A)(D_n/\tau_n)^{1/2}$, n_{i0} is the intrinsic charge-carrier density, q is the elementary charge, N_A is the doping level of the base *p*-layer, μ_n and D_n are, respectively, the mobility and diffusion coefficient of the majority electrons, and τ_n is the electron lifetime in the *p*-type base. The experimental saturation current $(j_0)_{\rm exp}$ is determined from the measured IVCs of the diode samples.

For the case of higher doping levels, when bandgap narrowing becomes substantial, the relation for determining μ_{np} becomes

$$\mu_{np}=\frac{\mu_n}{B^2-1}, \tag{2}$$

where $B=(j_0)_{\rm cal}/(j_0)_{\rm exp}$, $(j_0)_{\rm cal}=(qn_{i0}/N_A)(D_n/\tau_n)^{1/2}\times\exp(\Delta E_g/kT)$, ΔE_g is the decrease in the band gap, and all other notation is the same as in the preceding formula.

3. The measurements and calculations were performed in the same sequence as in Ref. 1. The n^+–p–p^+ structures, whose main parameters are given in Table I, were fabricated. The depth of the diffused n^+ layers did not exceed 10 μm.

The IVC was measured for each of these structures by the standard method. The region of current densities, where a low injection level of the nonequilibrium charge carriers was realized in the base layer of the structure, was chosen for the measurements. The experimental dependence of j on V was approximated by an expression of the form

$$j=(j_0)\exp\left(\frac{qV-j\rho_pW_p}{kT}\right), \tag{3}$$

where W_p is the thickness of the *p*-type base, and ρ_p is the resistivity. A least-squares analysis of the experimental points of the IVC made it possible to determine the experimental value of the parameter $(j_0)_{\rm exp}$ for Eq. (1) or Eq. (2). Next, the parameter $(j_0)_{\rm cal}$ was calculated from the formulas presented above. The values of ΔE_g taken from the measure-

 1063-7826/97/070707-03$10.00

TABLE I.

Sample No.	ρ_p, Ω·cm	W_p, μm	S, mm^2	τ_n, μs
1	0.385±0.025	162	19.6	1.5
2	0.100±0.005	240	83.0	0.28±0.04
3	0.100±0.005	270	83.0	0.28±0.04
4	0.040±0.002	146	37.4	0.10±0.02
5	0.043±0.002	165	25.2	0.10±0.02

Note: W_p—thickness of the *p*-type base; ρ_p—resistivity; S—area of the structure, τ_n—lifetime of electrons.

ments in Ref. 7 were used in the calculations, and the dependence of D_n on the doping level was taken into account in accordance with Ref. 8. The electron lifetime τ_n was measured by Lax's method.[9] However, since this method is difficult to apply to strongly doped samples, we also took into consideration the values of τ_n presented in Ref. 10. We shall discuss this in greater detail in a discussion of the results.

4. Figure 1 shows the experimental points corresponding to the samples indicated in Table I. The variance of the points in the figure corresponds to the variance given in the table for the parameters. We note that the data for samples 2 and 3 are combined and are presented in the figure as a single point.

The electron lifetime in the experimental samples merits a separate discussion. The values of τ_n presented in Table I were obtained by Lax's method. The problems in using this method ordinarily arise in strongly doped layers, when the lifetime becomes substantially shorter than 1 μs. For samples 2–5, where the measured lifetime is appreciably shorter than 1 μs, the lifetimes presented in Ref. 10 turn out to be much longer: $\tau_n \simeq 4-6$ μs with $N_A = 5\times10^{17}$ cm^{-3}, corresponding to samples 2 and 3, and $\tau_n \simeq 1-2$ μs with $N_A = 10^{18}$ cm^{-3}, corresponding to samples 4 and 5. Therefore the situation with *p*-type samples is completely different from the *n*-type samples in Ref. 1, since the hole lifetimes measured in *n*-samples fell into the range of values encountered in the literature. The smallness of the lifetime values obtained from measurements in samples 2–5 could be due to the imperfection of the silicon used to fabricate the samples and to the presence of additional recombination levels in the samples as compared with the samples which are employed by other authors for determining τ_n.

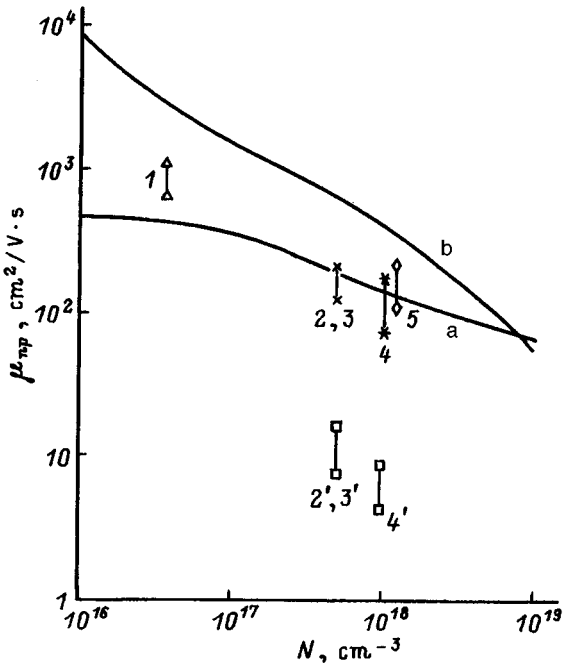

FIG. 1. Mobility μ_{np} versus the density of the majority charge carriers in *p*-silicon. Points: *1*–*5* — our experimental values of μ_{np} for samples 1–5 (see Table I), *2′*, *3′*, *4′* — the values of μ_{np} found for the samples 2, 3, and 4 in calculations using the published values of τ_n.[10] Curves: a — Mobility of the majority charge carriers (holes) according to the data in Ref. 8; b — values obtained for μ_{np} by extrapolating the data in Refs. 11 and 12 using Eq. (4) to the case of a low charge-carrier injection level.

Nonetheless, we determined how the results change when the published lifetime values are used. In Fig. 1 the two lowest values of μ_{np} (the points *2′*, *3′*, and *4′*) correspond to samples 2, 3, and 4, but with lifetimes corresponding to the published values for the corresponding doping level.[10]

Besides the experimental results of the present work, two curves are presented in the figure. Curve *1* represents the dependence of the mobility of the majority charge carriers (holes) μ_p on the doping level. Curve *2* shows the result of extrapolating the μ_{np} data obtained with a high doping level in Refs. 11 and 12 to the case of a low injection level in accordance with the formula proposed in Refs. 13 and 4:

$$\mu_{np} = G/p\left(\frac{1}{p_0} + \frac{1/p_2}{1+(n+p)/2p_1}\right), \tag{4}$$

where $G = 1840$ cm^2/(V·s), $p_0 = 3.2\times10^{17}$ cm^{-3}, $p_1 = 3.5\times10^{16}$ cm^{-3}, and $p_2 = 4.6\times10^{16}$ cm^{-3}.

One can see that the experimental values of μ_{np} are much lower than the values obtained by extrapolation. However, comparing the experimental values of μ_{np} with the mobility of the majority holes (curve *1*) shows that the condition $\mu_{np} \leqslant \mu_p$, determining the possibility of complete dragging of the minority electrons by the majority holes,[5] can be satisfied only for $N_A > 10^{18}$ cm^{-3}. The value obtained for the acceptor density is approximately an order of magnitude higher than the donor density in *n*-samples at which complete dragging of the minority electrons by the majority holes turns out to be possible.[1] Two factors determined the increase in the threshold level for complete dragging of the doping level in *p*-type samples. First, the values found for μ_{np} were found to be somewhat higher but close to the upper values of the mobility μ_{pn} determined in Ref. 1. Second, complete dragging in *n*-type material is determined by the inequality $\mu_{pn} < \mu_n$, and since $\mu_p < \mu_n$, it should be expected at the outset that the appearance of this effect will be impeded in *p*-type silicon.

This work was supported by the Russian Fund for Fundamental Research under projects Nos. 95-02-05767 and 96-02-17902a.

[1] T. T. Mnatsakanov, L. I. Pomortseva, V. B. Shuman, and E. G. Guk, Fiz. Tekh. Poluprovodn. **29**, 1554 (1995) [Semiconductors **29**, 808 (1995)].
[2] R. A. Hopfel, J. Shah, P. A. Wolff, and A. C. Gossard, Phys. Lett. **56**, 2736 (1986).

[3] R. A. Hopfel, J. Shah, P. A. Wolff, and A. C. Gossard, Appl. Phys. Lett. **49**, 572 (1986).
[4] B. N. Gresserov and T. T. Mnatsakanov, Fiz. Tekh. Poluprovodn. **24**, 1668 (1990) [Sov. Phys. Semicond. **24**, 1042 (1990)].
[5] T. T. Mnatsakanov, B. N. Gresserov, and L. I. Pomortseva, Solid–State Electron. **38**, 225 (1995).
[6] B. N. Gresserov and T. T. Mnatsakanov, Zh. Tekh. Fiz. **56**, 1827 (1986) [Sov. Phys. Tech. Phys. **31**, 1090 (1986)].
[7] J. B. Slotboom and H. C. de Graaff, Sol. Electron. **19**, 857 (1976).
[8] N. D. Arora, J. R. Hauser, and D. J. Roulston, IEEE Trans. Electron. Dev. **29**, 292 (1982).
[9] D. Lax and S. T. Neustadter, J. Appl. Phys. **25**, 1148 (1954).
[10] M. S. Tyagi and R. Van Overstraeten, Solid–State Electron. **26**, 577 (1983).
[11] F. Dannhauser, Solid–State Electron. **15**, 1371 (1972).
[12] J. R. Krausse, Solid–State Electron. **15**, 1376 (1972).
[13] V. A. Kuz'min, T. T. Mnatsakanov, and V. B. Shuman, Pis'ma Zh. Tekh. Fiz. **6**, 689 (1980) [Sov. Tech. Phys. Lett. **6**, 299 (1980)].
[14] T. T. Mnatsakanov, I. L. Rostovtsev, and N. I. Philatov, Solid–State Electron. **30**, 579 (1987).

Translated by M. E. Alferieff

Effect of tin impurity on the photoconductivity kinetics of thin amorphous layers of arsenic selenide

M. S. Iovu, E. P. Kolomeĭko, and S. D. Shutov

Institute of Applied Physics, Academy of Sciences of Moldavia, 277028 Kishinev, Moldavia
(Submitted July 1, 1996; accepted for publication November 20, 1996)
Fiz. Tekh. Poluprovodn. **31**, 836–840 (July 1997)

In thermally sputtered As_2Se_3 and As_2Se_3 + 0.1 at. % Sn films the tin impurity strongly influences the photoconductivity kinetics under stepped optical excitation. The tin quenches the ''spike'' on the section of increasing photocurrent, eliminates the dependence of the form of the decrease on the excitation intensity, and leads to a temperature-dependent delay in recombination onset. The effect of the impurity is attributed to an increase in trapping in deep localized states produced by the introduction of tin. © *1997 American Institute of Physics.* [S1063-7826(97)01907-8]

1. INTRODUCTION

It is well known that impurities have only a weak effect on the electrical characteristics of chalcogenide glassy semiconductors (CGSs), if the impurities are introduced during the thermal synthesis of the glass. However, in the case of ''cold'' doping (modification), when the material is not in thermal equilibrium, some impurities, for example, Ni and Fe in As_2Se_3, are electrically active.[1] An impurity in thermally sputtered amorphous films of CGSs, which are characterized by a higher degree of structural disorder than bulk glasses, is of practical interest. For example, modification of arsenic selenide with Bi and Sn impurities has no effect on the position of the Fermi level,[1] whereas in sputtered amorphous films $As_2Se_3Bi_x$ ($x=0.001$, 0.01, and 0.1) substantial changes have been observed in the optical properties and electrical conductivity, indicating that these films have a microheterogeneous cluster structure.[2] Similarly, the photoconductivity in thermally sputtered $As_2Se_3Sn_x$ ($x=0.1-3.5$ at. %) films is much higher than in bulk glass samples of the same composition with a low dark conductivity. The use of As_2Se_3Sn layers in film structures for electrographic recording of optical information increases substantially the photoelectric sensitivity.[3,4] Measurements of the time of flight in As_2Se_3Sn films have recently established[5] that adding tin to As_2Se_3 substantially increases the drift mobility and slows down recombination. Our objective in the present paper is to show that adding tin in small amounts also changes appreciably the parameters of the photoconductivity relaxation process in As_2Se_3 films. The photoconductivity kinetics was investigated with stepped optical excitation, which, together with a drop in photoconductivity, makes it possible to observe an increase in photoconductivity as well.

2. EXPERIMENTAL CONDITIONS

Tin was introduced in an amount of 1 at.% into the charge during thermal synthesis of the initial material for sputtering. Synthesis was conducted by melting the charge in an evacuated quartz cell followed by holding at a temperature of 1100 °C and slow cooling with the furnace switched off. As_2Se_3 and As_2Se_3Sn films of thickness 1.5–10.0 μm were obtained by discrete thermal sputtering in vacuum on glass substrates. The samples had a sandwich configuration with two sputtered electrodes, of which the top electrode was half-transmitting. The photoconductivity was excited by light from a LGN-108 helium-neon laser; a photoshutter with a 10^{-3} s triggering time was used to interrupt the light. The intensity of the light $F_0=10^{15}$ cm$^{-2}\cdot$s^{-1} could be decreased with calibrated light filters. Additional illumination ($\Phi=3\times10^{14}$ cm$^{-2}\cdot$s^{-1}) was produced by light from a KGM-100 incandescent lamp. To obtain uniform optical excitation in the sample, the light was passed through an arsenic selenide film filter. The photoconductivity relaxation curves were recorded with a time constant not exceeding 0.3 s on a ENDIM 622 01 X–Y plotter using an U5-11 electrometric amplifier.

3. EXPERIMENTAL RESULTS

The nonstationary photoconductivity with the excitation switched on and off in As_2Se_3 and As_2Se_3Sn films is shown in Figs. 1a and 1b, respectively, for room temperature and three light intensities. As one can see, the character of the photocurrent relaxation changes appreciably when tin is introduced. In the undoped material the photocurrent on the increasing section passes through a maximum before reaching a stationary state (so-called ''spike''), while in films containing tin the photocurrent increases monotonically up to a stationary value. Substantial differences are also seen in the decay of the photocurrent after the light is switched off. In Fig. 2 the sections of decreasing relaxation in the experimental sample are presented in a double-logarithmic scale. As the intensity of the light increases, the character of the decay in the doped samples (curves *1–3*) remains almost unchanged, whereas in the undoped As_2Se_3 films (curves *4–6*) the photocurrent decreases rapidly, especially in the final part of the dropoff (for $t>2$ s). The tin ''switches off'' the effect of the generation intensity on the decay rate and gives a power-law decay in the entire experimental time interval (Fig. 3). Conversely, in undoped films the relaxation rate, which at first is higher, gradually slows down, approaching the values characteristic of the tin-containing samples and the same variation with time. From Fig. 3 one can also see that the instan-

 1063-7826/97/070710-04$10.00

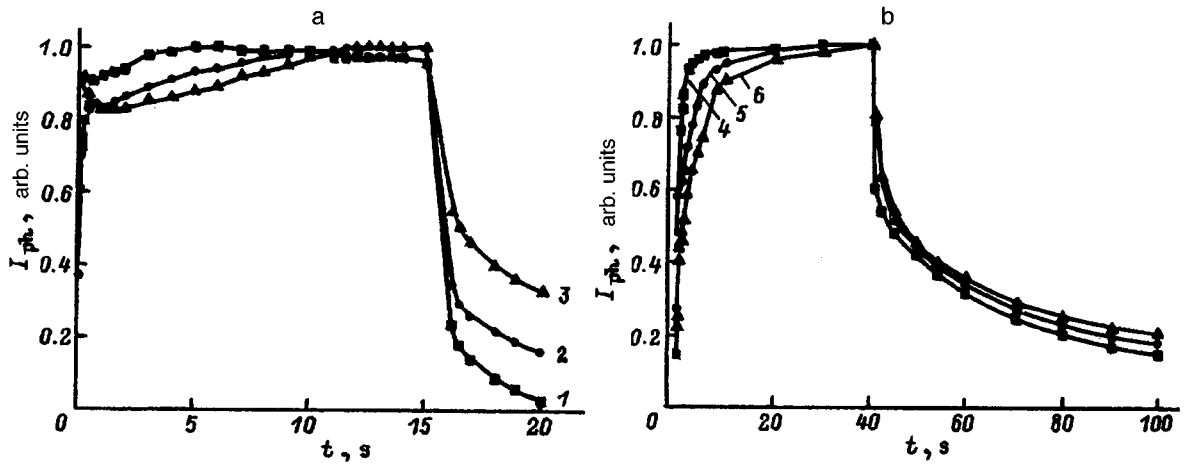

FIG. 1. Photocurrent relaxation in As_2Se_3 (a) and As_2Se_3Sn (b) films ($L=10$ μm) with the light switched on and off . The curves are normalized to the maximum value of the photocurrent. The temperature equals 288 K (a) and 290 K (b). Excitation intensity F, $cm^{-2}\cdot s^{-1}$: *1,4* — 10^{15}; *2,5* — 10^{14}; *3,6* — 10^{13}.

taneous value of the decay time in the tin-containing samples is always higher than in the undoped samples.

A change in temperature has the opposite effect (Fig. 4) from that of a change in the light intensity on the decay kinetics of the photocurrent. An increase in temperature substantially increases the decay rate in the tin-containing films (curves *1–3*) and its effect on the decay in undoped samples is comparatively weak (curves *4–6*). At a sufficiently high temperature ($T=350$ K) the decay rates in undoped and doped films approach one another. Therefore, increasing the temperature of the sample eliminates the relaxation delay due to the introduction of the tin impurity. Constant illumination, acting even after the main excitation is removed, has a similar effect (Fig. 5).

4. DISCUSSION

A satisfactory interpretation of the relaxation of photoconductivity in amorphous As_2Se_3 can be obtained in a model of repeated capture in deep traps, quasicontinuously distributed in energy in the mobility band gap in glassy semiconductors.[6–8] This model also makes it possible to understand other nonequilibrium processes which are specific to CGSs, such as dispersion transport and induced optical absorption. Analysis of these processes leads to an exponential energy distribution of the density of localized states $g(E)=(N_t/kT_0)\exp(-E/kT_0)$, where N_t is the total density of localized states, and T_0 is the distribution parameter. For As_2Se_3, in the energy interval $E=0.2-0.6$ eV above the edge of the conducting states $kT_0=0.05$ eV and $N_t\leqslant 1.4\times 10^{18}$ cm^{-3}.[8] For this reason, we shall adopt this model as the basis for discussing the results on photoconductivity relaxation, under the assumption that it is true for As_2Se_3 films and with the goal of determining the changes that occur upon the introduction of tin impurity.

As we have already mentioned, the most noticeable feature of the section with increasing photocurrent in As_2Se_3 (Fig. 1) is the unusual ''spike-like'' character, observed under certain conditions, of the relaxation, which does not happen in samples with tin. The spike-like kinetics of the photoconductivity in CGSs has attracted attention many times and has often been attributed to charge redistribution near the electrodes. However, it was shown in Refs. 8–10 that the spike in the increasing section follows naturally from a model of repeated capture with sufficiently high generation levels, when bimolecular recombination (BMR) becomes the determining mechanism. The spike is due to time-dependent nonstationary recombination, whose intensity changes with the density of the captured nonequilibrium holes. These model predictions have been confirmed experimentally for arsenic selenide films.[9,10] After excitation is switched on, the relaxation of photocurrent on the increasing section is determined by capture in localized states with an exponential energy distribution and grows monotonically according to a power law $i_{ph}\propto t^{\alpha}$, where α is the so-called dispersion parameter ($\alpha<1$), which depends on the temperature T and the characteristic T_0 of the quasicontinuous distribution of localized states: $\alpha=T/T_0$. A spike appears under conditions of strong recombination (BMR), if the recombination rate is higher than the capture rate, even when traps are not filled.

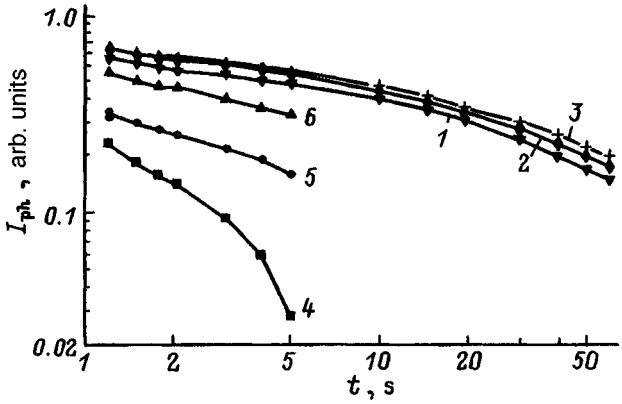

FIG. 2. Photocurrent relaxation in As_2Se_3Sn (1–3) and As_2Se_3 (4–6) samples with light switched off with different excitation intensity F, $cm^{-2}\cdot s^{-1}$: *1,4* — 10^{15}; *2,5* — 10^{14}; *3,6* — 10^{13}. The temperature equals 290 K (1–3) and 288 K (4–6).

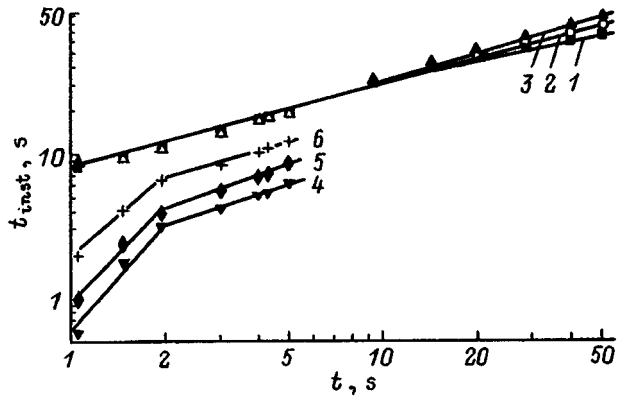

FIG. 3. Variation of the instantaneous relaxation time $\tau_{inst} = -i_{ph}/(di_{ph}/dt)$ as a function of the decay time of the photocurrent in As_2Se_3Sn (1–3) and As_2Se_3 (4–6) samples with different excitation intensity F, $cm^{-2}\cdot s^{-1}$: *1,4* — 10^{15}; *2,5* — 10^{14}; *3,6* — 10^{13}. The temperature equals 290 K (1–3) and 288 K (4–6).

This is confirmed by the fact that the spike vanishes when the excitation intensity decreases as a result of a transition from the bimolecular to a monomolecular recombination (MMR) mechanism. The absence of a spike in the increasing section of the photocurrent in samples with tin indicates that capture is intensified, since the generation of photocurrent carriers under the same excitation intensities is balanced by capture and not recombination.

According to the calculations in Refs. 9 and 10, the time t' at which the recombination starts to predominate over trapping in the photocurrent kinetics is proportional to the total density N_t of localized states

$$t' = \tau_0 (N_t/N_c)(\tau_R/\tau_0)^{1/\alpha}, \tag{1}$$

where τ_0 is the hole lifetime with respect to trapping in all localized states, N_c is the density of delocalized states, and τ_R is the lifetime of nonequilibrium holes with respect to recombination. As one can see from Fig. 1, adding tin increases this time by a factor of 2–8 (on the increasing section).

Analysis of the decay of the photoconductivity from a stationary state after the light is switched off in the repeated-capture model leads to a power-law time dependence of the nonstationary photocurrent, consisting of three sections on which the decay rate increases gradually.[10] In the initial decay section the delocalized-carrier density decreases due to the capture in localized states and $i_{ph} \propto t^{-(1-\alpha)}$. In the intermediate decay section, which is observed with sufficiently high generation intensities, bimolecular recombination predominates and the photocurrent $i_{ph} \propto t^{-1}$. In the final decay section monomolecular recombination dominates and decay accelerates: $i_{ph} \propto t^{-(1+\alpha)}$. The time of the transition from the initial section to the intermediate section corresponds to the onset of bimolecular recombination; i.e., the onset of this mechanism depends strongly on the generation intensity and is comparatively insensitive to the temperature (it is determined by the temperature dependence of the drift mobility[8]). In contrast, the moment of the transition to the final section (MMR) does not depend on the light intensity, it exhibits an activational temperature dependence and is also described by the expression (1).

The features noted above can be seen in the decay kinetics of the photocurrent (Figs. 2–4). Just as in the growth kinetics, tin slows down the relaxation in all cases (except at the highest experimental temperature of 345 K, Fig. 4, curve 3). The relaxation rate is higher in the undoped samples in the entire experimental temperature interval (Fig. 3). This means that earlier stages of relaxation are seen experimentally in undoped As_2Se_3 films than in samples containing tin. In contrast to tin-doped samples, the form of the decay for undoped samples depends strongly on the generation intensity (Fig. 2, curves *1–3*). This shows that the acceleration of the decay in the interval 1–10 s occurs because here recombination predominates over capture (for high intensities — BMR, for low intensities — MMR). This is confirmed by the behavior of the photocurrent on the increasing section (Fig. 1a), where the spike disappears as the generation intensity decreases. The moment of onset of intense recombination can be estimated from the kink in the curve *4* (Fig. 2): ≈ 1 s (for intensity F_0 and $T = 290$ K).

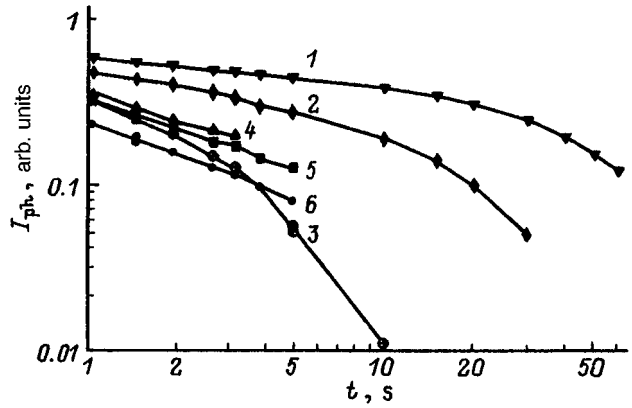

FIG. 4. Photocurrent relaxation on the decay section in As_2Se_3Sn (1–3) and As_2Se_3 (4–6) samples at different temperatures T, K: *1* — 290; *2* — 313; *3* — 345; *4* — 288; *5* — 304; *6* — 341. The excitation intensity $F = 10^{15}$ $cm^{-2}\cdot s^{-1}$.

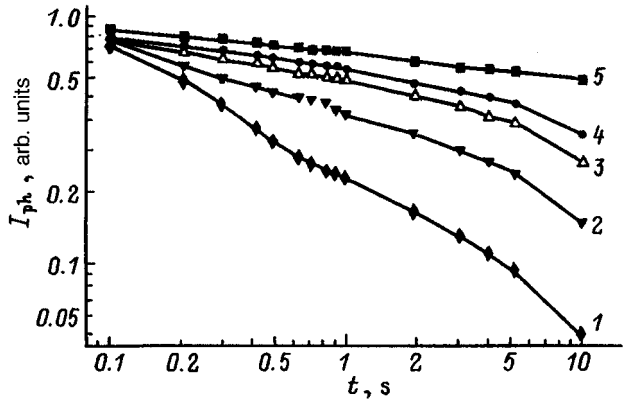

FIG. 5. Photocurrent relaxation on the decay section in As_2Se_3Sn samples under different conditions of constant illumination Φ, $cm^{-2}\cdot s^{-1}$: *1* — 3×10^{14}; *2* — 3×10^{12}; *3* — 2.7×10^{11}; *4* — 9×10^{10}; *5* — 0. Temperature: 290 K.

As noted above, later stages of excitation are seen experimentally in the tin-doped samples. The prolonged hyperbolic decay (Fig. 3, curves *1–3*) and the weak dependence on the generation intensity and quite strong temperature dependence (Fig. 4) show that capture in deep states dominates in tin-doped samples. The demarcation energy, below which these states lie[9,10]

$$E_*(t) = kT \ln[(N_c/N_t)(t/\tau_0)], \quad (2)$$

can be approximately estimated from the kink points on the curves *1–3* (Fig. 4). If it is assumed that the capture time in all traps is $\tau_0 \simeq 10^{-12}$ s, then it follows from Eq. (2) that the demarcation energy lies near the Fermi level (about 0.85 eV) and the density of states is very high $[(N_c/N_t) \simeq 10^2]$.

The kink points correspond to the onset time t' of intense recombination. As one can see, these times in the tin-doped samples are several times longer than in undoped samples ($t' = 25$ s at $E = 290$ K). These times decrease with increasing temperature. The temperature dependence in Eq. (1) includes, in addition to the exponent $1/\alpha$, the temperature dependence of the drift mobility as well.[8] The delay of recombination with the introduction of 1.0 at. % tin in As_2Se_3 was also observed in time-of-flight experiments.[5] Close values were obtained for the times corresponding to the onset of intense recombination (2.3 and 11.8 s for As_2Se_3 and As_2Se_3Sn, respectively).

Additional evidence in support of a delay of recombination in As_2Se_3Sn samples follows from the effect of constant illumination (Fig. 5). Illumination increases the decay rate, which increases with increasing illumination intensity, by accelerating photoionization and recombination of localized nonequilibrium current carriers.

We note that the increase in the role of capture in the characteristics of the drift mobility under nonstationary conditions of dispersion transport has been noted previously for arsenic sulfide films doped with tin up to 0.03 at. %.[11]

The possible nature of the states engendered by tin added to As_2Se_3 can be gleaned from an investigation of tin as an impurity in As_2Se_3 by the Mössbauer spectroscopy method.[12] In the glass As_2Se_3 tin is tetravalent (Sn^{4+}); and all four valence electrons of tin participate in chemical bonds with the matrix atoms and are not manifested in the electrical properties. However, in unannealed films some tin atoms are present in the form of divalent tin (Sn^{2+}). Then only the $5p$ electrons of tin participate in the formation of a chemical bond, and the $5s$ electrons can play the role of deep donors. Another possibility is photoinduced charge exchange on tin impurity centers $Sn^{4+} \Rightarrow Sn^{2+}$ with capture of the electrons on the tin centers.

5. CONCLUSIONS

Tin impurity introduced into CGSs during thermal synthesis has a much stronger effect on the nonstationary characteristics of the photoconductivity than on the equilibrium parameters. This influence is based on the increased role of capture in deep localized states, which apparently appear as a result of the introduction of tin. Intensification of capture, which determines the slow initial relaxation stages which are specific to CGSs, results in a delay of recombination onset in doped samples and increases the lifetime of the photoexcited state after the light is removed. Since the real onset times of intense recombination reach several seconds and several tens of seconds, doping is helpful from the standpoint of increasing the photosensitivity of electrographic devices for recording of optical information based on CGS film structures.

We wish to thank V. I. Arkhipov for interest in this study.

[1] B. T. Kolomiets and V. L. Averyanov, in *Physics of Disordered Materials*, N. Y., 1985, p. 663.
[2] N. P. Kalmykova, T. F. Mazets, É. A. Smorgonskaya, and K. D. Tséndin, Fiz. Tekh. Poluprovodn. **23**, 297 (1989) [Sov. Phys. Semicond. **23**, 184 (1989)].
[3] O. Ya. Korshak, L. M. Panasyuk, V. K. Rotar', and V. I. Fulga, in *Electrography-88* [in Russian], Moscow, 1988, Vol. 2, p. 51.
[4] A. I. Buzdugan, M. S. Iovu, A. A. Popescu, and P. G. Gerbari, Balcan Phys. Lett. **1**, 7 (1993).
[5] M. S. Iovu, S. D. Shutov, and L. Toth, Phys. Status Solidi B **195**, 145 (1996).
[6] V. I. Arkhipov and A. I. Rudenko, Philos. Mag. B **45**, 189 (1982).
[7] A. I. Rudenko and V. I. Arkhipov, Philos. Mag. B **45**, 209 (1982).
[8] J. Crenstein, M. A. Kastner, and V. Vaninov, Philos. Mag. B **46**, 23 (1982).
[9] A. M. Andriesh, V. I. Arkhipov, M. S. Iovu, A. I. Rudenko, and S. D. Shutov, Solid State Commun. **48**, 1041 (1983).
[10] V. I. Arkhipov, M. S. Iovu, A. I. Rudenko, and S. D. Shutov, Fiz. Tekh. Poluprovodn. **19**, 101 (1985) [Sov. Phys. Semicond. **19**, 61 (1985)].
[11] A. M. Andriesh, V. S. Gerasimenko, Yu. N. Ivascheko, M. A. Iovu, M. S. Iovu, A. V. Mironos, V. L. Smirnov, M. R. Chernii, and S. D. Shutov, J. de Physique **42**, Col. C4, 963 (1981).
[12] P. P. Seregin and P. V. Nistiryuk, *Application of the Mössbauer Effect and Photoelectron Spectroscopy in the Physics of Amorphous Semiconductors* [in Russian], Shtiintsa, Kishinev, 1991.

Translated by M. E. Alferieff

Study of submicron deposits in polycrystalline materials using the internal-friction method

Yu. N. Andreev and N. P. Yaroslavtsev

Voronezh State Technical University, 394026 Voronezh, Russia

M. V. Bestaev, D. Ts. Dimitrov, V. A. Moshnikov, and Yu. M. Tairov

St. Petersburg State Electrical Engineering University, 197376 St. Petersburg, Russia
(Submitted November 18, 1996; accepted for publication November 25, 1996)
Fiz. Tekh. Poluprovodn. **31**, 841–843 (July 1997)

An internal friction method is proposed for investigating the kinetics of impurity deposits on grain surfaces in polycrystalline samples. The possibilities of the method have been tested on polycrystalline, gas-sensitive, tellurium-doped layers of tin dioxide. © *1997 American Institute of Physics.* [S1063-7826(97)02007-3]

Polycrystalline semiconductor materials are now being used extensively in microelectronics, optoelectronics, and sensor electronics. Reproducible properties are difficult to obtain in polycrystalline samples because of the effect of structural features associated with intergrain boundaries (IGBs). Depending on the type of IGBs and the character of their interaction with the dopants, the properties of the semiconductors can differ sharply.[1] This is especially strongly manifested in the properties of devices such as gas-sensitive sensors, luminophors, photodetecters, and light emitters. Microsegregation and precipitation of impurities on IGBs make it possible to control the gas sensitivity and selectivity of adsorption semiconductor sensors. The kinetics of segregation and precipitation predetermines the degradation properties.

Different models are used to describe segregation: hard spheres,[2] structural unit,[3] electric,[4] molecular dynamics,[5] and local electronic sheets.[6] The role of the impurity precipitating on a grain boundary in changing the selectivity with respect to an adsorbed gas is studied in Refs. 7 and 8. The experimental investigations of segregation and precipitations of impurities are performed, as a rule, by an electron-probe or other method of surface analysis. Although these methods yield a great deal of information when the probe falls directly on the surface of an IGB, their transverse resolution strongly limits their applicability.[9]

Our objective in the present paper is to evaluate the possibility of using other integral physical methods which are sensitive to precipitation of microinclusions. The objects of investigation were gas-sensitive, doped, tin-dioxide-based layers.[10] The experimental data on the change in the electrical properties, sensitivity, and selectivity of tellurium-doped samples are explained by redistribution of the impurity.

Tin films were deposited on 22KhS ceramic substrates by the method of thermal vacuum sputtering. The substrate temperature was held at 150 °C, which made it possible to avoid the formation of drops of condensate. Two types of charges were used to regulate the tellurium content: pure tin and tin telluride obtained by the iodine method.[11] Traces of iodine make it possible to obtain a more developed granularity of the films. The impurity content was fixed by mixing the compositions of the two initial charges. The uniformity of the phase composition was monitored by an x-ray diffraction method using the technique described in detail in Ref. 12. Tin dioxide was obtained by oxidation in two stages. The low-temperature annealing stage corresponded to 210 °C and lasted for 6 h. The high-temperature stage varied in duration from 6 to 30 h and was conducted at a temperature of

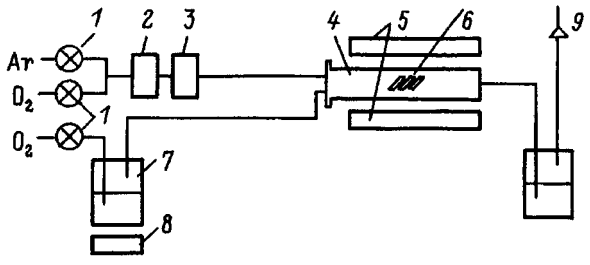

FIG. 1. Diagram of the oxidation setup. *1* — Precision regulation valve *2; 3* — bubblers; *4* — quartz tube; *5* — furnace; *6* — substrate; *7* — bubbler with deionized water; *8* — furnace; *9* — output neutralizing bubbler.

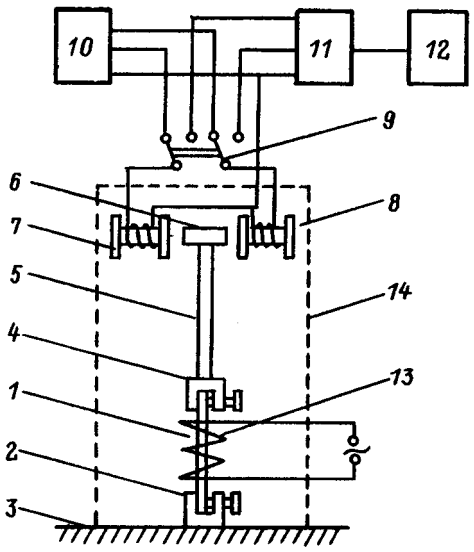

FIG. 2. Diagram of the setup for measuring the temperature dependence of the IF by the inverted-pendulum method. Explanations are given in the text.

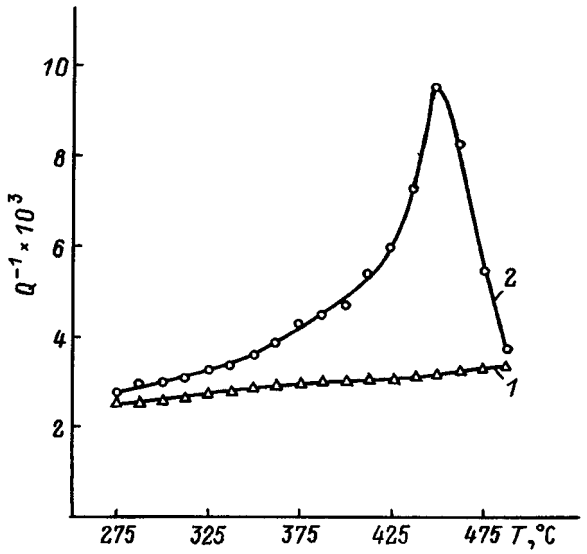

FIG. 3. Temperature dependence of the IF in tellurium-doped tin polycrystalline films on ceramic substrates. *1* — Before annealing; *2* — after annealing for 30 h at 450 °C.

450 °C. Oxidation was conducted in a controlled atmosphere. The arrangement of the apparatus is shown in Fig. 1. The oxygen partial pressure was varied from 0.1 to 0.2 atm.

As a physical method for investigating the redistribution of tellurium between the volume and the grain boundaries, we employed the internal-friction (IF) method, which was previously successfully used to study inclusions of a second phase in semiconductors.[13–15] The method involves measuring the temperature dependence of the IF by the inverted-pendulum method. The arrangement of the apparatus is illustrated in Fig. 2. The experimental sample is secured at one end to base *3* by a collet *2*. A collet *4* with the pendulum *5* is secured to the other end of the sample *1*. A ring 6 of ferromagnetic material is placed on the top of the pendulum. Coils *7* and *8*, which are connected via the switches *9* either to a low-frequency generator *2* or to an amplitude discriminator *11*, whose output is connected to the electronic counter *12*, are arranged symmetrically near the ring *6*. In the first case, coils *7* and *8* are used to excite mechanical oscillations of the pendulum *5* by the interaction of the magnetic field of the coils with the ferromagnetic ring *6*; in the second case they are used as a sensor for displacements of the ring *6*. A heater *13* is placed near sample 1. The elements 1,2,4–8,13 are placed in an airtight container *14*, from which air is pumped out in order to decrease the damping of the oscillations of the pendulum *5*.

Internal friction measurements were performed on samples obtained in a single technological cycle at the stage of deposition of the tin layer and low-temperature oxidation. It was found that in the tellurium-doped samples, in contrast to the samples obtained from pure tin, in the process of high-temperature oxidation an IF peak appears at temperatures close to the melting point of tellurium. The intensity of the peak increases by a factor of 12 as the annealing time increases from 6 to 30 h.

These results can be interpreted as a change in the tellurium distribution in the polycrystalline samples. The absence of an IF peak (Fig. 3) in the case of a short treatment time attests to the presence of tellurium bonds characteristic of SnTe (melting point 805 °C). As the annealing time increases, the tellurium diffuses to the grain surfaces, where it precipitates in the form of a second phase. Figure 3 also shows the temperature dependence of the IF for a sample annealed for 30 h. It should be noted that in a number of samples the maximum of the peak was displaced to lower temperatures.

In summary, the IF-based method can be used to analyze the kinetics of microsegregations and precipitates in polycrystalline samples. Compared with the electron-probe method, this method can be used to determine submicron precipitates in the entire polycrystalline layer formed.

[1] G. Harbeke [Ed.], *Polycrystalline Semiconduction. Physical Properties and Application. Proc. Int. School of Materials Sci. and Technol. at the Etore Majorana Centre*, Erice, Italy, July 1–15, 1984, Springer Verlag, N. Y., 1985 [Russian transl., Mir, Moscow,1989].
[2] H. J. Grost and F. Spaepen, J. Physique **43**, 73 (1982).
[3] V. Vitek, A. P. Sutton, D. A. Smith, and R. C. Pond, *Grain Boundary Structure and Kinetics*, A. S. M., Metal Park, 1980.
[4] R. W. Balutti, P. D. Bristowe, and C. P. Sun, J. Amer. Soc. **64**, 29 (1981).
[5] V. Pontikis, J. Physique **43**, 65 (1982).
[6] C. L. Briant and R. D. Mesmer, J. Physique **43**, 255 (1982).
[7] R. S. Morrison, Sensor and Actuators **12**, 425 (1987).
[8] L. Horer, *Polprgzewodnikowe materialy ceramiczhe z aktywnymi granicami zranicami ziaru*, Warszawa, PWN, 1990.
[9] L. C. Feldman and J. W. Mayer, *Fundamentals of Surface and Thin Film Analysis*, North Holland, N. Y., 1986 [Russian transl., Mir, Moscow, 1989].
[10] M. V. Bestaev, D. Tr. Dimitrov, V. A. Moshnikov, and Yu. M. Tairov, in *SnO_2 Based Gas Sensitive Sensor. Abstracts E-MRS 1996 Spring Meeting*, Strasburg, France, June 4–7, 1996, B-1.
[11] R. Assenov, V. A. Moshnikov, and D. A. Yaskov, Cryst. Res. Technol. **21**, 1553 (1986).
[12] N. I. Dolotov, A. B. Zil'berman, Yu. A. Il'in, A. V. Mokhin, V. A. Moshnikov, and D. A. Yas'kov, Neorg. Mater. **30**, No. 1, 83 (1994).
[13] V. I. Mitrokhin, N. P. Yaroslavtsev, S. I. Rebeza, G. S. Pesotskiĭ, and N. V. Izmaĭlov, Inventor's Certificate, 105/42 SSSR G01N11/16 (1985).
[14] N. V. Izmaĭlov, Yu. L, Il'in, V. A. Moshnikov, V. V. Tomaev, N. P. Yaroslavtsev, and D. A. Yas'kov, Zh. Fiz. Khim. **12**, 1370 (1988).
[15] B. M. Darinskiĭ and N. P. Yaroslavtsev, Vysokochistye Veshchestva, No. 3, 80 (1990).

Translated by M. E. Alferieff

Mechanism of electroluminescence of porous silicon in electrolytes

D. N. Goryachev, O. M. Sreseli, and L. V. Belyakov

A. F. Ioffe Physicotechnical Institute, Russian Academy of Sciences, 194021 St. Petersburg, Russia
(Submitted November 19, 1996; accepted for publication November 25, 1996)
Fiz. Tekh. Poluprovodn. **31**, 844–847 (July 1997)

A generalized model for the appearance of visible- and infrared-range electroluminescence of porous silicon in contact with an oxidizing electrolyte is proposed. According to the model, visible-range electroluminescence arises as a result of bipolar injection of electrons and holes from the electrolyte into electrically insulated quantum-well silicon microcrystallites, while infrared-range electroluminescence is due to monopolar injection of holes from the electrolyte into macrocrystals. A mechanism of electron injection from the electrolyte is proposed. It is concluded that the character of the electroluminescence should not depend on the magnitude and even the type of conductivity of the silicon substrate. © *1997 American Institute of Physics.* [S1063-7826(97)02107-8]

1. INTRODUCTION

Porous silicon (PS) is attracting the attention of many investigators largely because of hopes for producing PS-based solid-state electroluminescence structures operating in the visible region of the spectrum. However, the results obtained in this direction remain very modest. Much better results have been obtained in PS–electrolyte systems.[1,2] The investigation of processes occurring at the PS–electrolyte interphase boundary makes it possible, in our opinion, not only to increase the intensity of the electroluminescence (EL) in such systems, but also to clarify the nature of limitations on the EL intensity in solid-state structures.

Light emission from a number of *n*-type semiconductors with a smooth surface, for example, GaP and GaAs, which are employed as the cathode in an electrolytic cell has been studied in detail.[3] It arises as a result of radiative recombination of conduction band electrons which enter the semiconductor from the external current source, with holes injected in the valence band of the semiconductor from the electrolyte side. An energetic oxidizer, for example, calcium persulfate or hydrogen peroxide, was therefore introduced into the electrolyte. During the passage of a current, the oxidizer ions (molecules) trap electrons from the conduction band of the semiconductor and are converted into short-lived ion radicals, which possess strong acceptor properties and are capable of extracting electrons even from the valence band of the semiconductor or, in other words, inject holes into it.

This point of view is also valid for PS.[4] However, at present, the construction of the model of EL in a PS–electrolyte system is incomplete and it contains many unclear elements. The main one is the mechanism of current passage in the system. The PS microcrystallites do not exceed several nanometers in size.[5] As a result of the quantum-size widening of the band gap, these microcrystallites are high-resistance formations. According to experimental estimates,[6] the resistance of PS microcrystallites can be six to eight orders of magnitude higher than that of bulk silicon (substrate). Filling the voids in the PS, an electrolyte with a resistivity of about 10 $\Omega\cdot$cm should nearly completely shunt the high-resistance formations. Furthermore, it is very likely that many PS fragments have no electric coupling with the substrate at all and are separated from it by layers of silicon oxide. One would think that no electroluminescence should be observed at all under such conditions, which is at variance with the actually observed EL quantum efficiency, equal to 10^{-2}–10^{-3}.

In the present paper we construct a generalized model of current passage and EL in the system under study. The proposed model explains the entire spectrum of phenomena observed at the PS–⟨oxidizing electrolyte⟩ boundary. The high EL efficiency in such a system as well as the nature of the differences in the EL obtained with a liquid or solid contact to the PS become understandable.

2. EXPERIMENTAL DATA

In constructing the model we relied on previously published results and new data. The main experimental facts are as follows.

1. Electroluminescence of porous silicon, on *n*-type substrates, in contact with an oxidizing electrolyte and with a cathode bias (minus on silicon) is characterized by a wide emission band in the physical region of the spectrum, similar to a photoluminescence band.[1,2,4]

2. We performed a series of experiments with PS samples grown on *p*-type silicon substrates. It was found that in this case, in electrolytes containing persulfate, visible-range cathodic EL is observed at virtually the same currents as in the case of *n*-type silicon but with higher values of the electrode potential.

3. Together with visible-range luminescence, radiation is present in the near-infrared (IR) region of the spectrum. The position of the maximum of this band corresponds to the position of the peak of the electroluminescence of the ⟨bulk silicon⟩–electrolyte interface, but the band itself is wider and more intense.[7]

4. In the investigation of the kinetics of visible-range EL in the system under study a substantial delay was observed between the start of the current pulse and the appearance of EL. This suggested that some current bypasses the microc-

rystallites through the substrate (so-called bypass current).[8] Further investigations of the kinetics of the IR band of EL showed that the delay times of the IR pulses are shorter than those of the visible-EL pulses. In both bands the delay times decrease with increasing current density.

5. Cathodic polarization curves (dependence of the current density on the cathode potential) in the system PS–⟨persulfate electrolyte⟩ are characterized by the presence of regions of flattening, indicating that besides the cathodic reduction of persulfate ions, there is an additional chemical reaction. [4,9] An example of such a reaction is the discharging of hydrogen ions, which are always present in the electrolyte because of the dissociation of water molecules. Hydrogen gas release starts at the cathode and visible-range EL appears at the same time,[9] a point which is especially important.

6. The electric resistance of the PS–water electrolyte contact is high. The introduction of organic solvents, which improve the wetting of the PS surface, into the electrolyte decreases this resistance by more than a factor of 20, and the resistance approaches that of the contact of a water electrolyte with a smooth silicon surface. Furthermore, under these conditions EL arises with much lower cathode potentials. In a number of cases EL was observed only in the presence of organic additives in the electrolyte.[9]

3. DISCUSSION

Summarizing these results, we can imagine the mechanism of charge transport and the appearance of EL in porous silicon at the boundary with a persulfate electrolyte as a series of successive processes.

1. Because of the current present in the system, ion radicals are produced at the surface of the silicon substrate and at macrocrystals without a quantum well, which are electrically coupled with it, according to the reaction

$$(S_2O_8)^{2-} + e^- \rightarrow (SO_4)^{\bullet -} + (SO_4)^{2-}, \quad (1)$$

where $(SO_4)^{\bullet -}$ are the ion-radicals formed. In accordance with Ref. 4, the ion radicals inject holes into the silicon according to the reaction

$$(SO_4)^{\bullet -} \rightarrow (SO_4)^{2-} + h^+. \quad (2)$$

In the process an IR-range EL band arises as a result of the radiative recombination of holes with conduction-band electrons in the substrate and macrocrystals. The higher intensity of this EL, as compared with the EL of bulk silicon, is explained mainly by the strongly extended surface of the macrocrystals.

2. When the negative potential of the electrode is sufficiently high, reduction of hydrogen ions starts and, in addition to ion radicals, hydrogen atoms are formed according to the reaction

$$H^+ + e^- \rightarrow H^\circ, \quad (3)$$

where H^o is a neutral hydrogen atom. Subsequently, some hydrogen atoms combine to form molecules, and hydrogen gas release is observed at the electrode.

3. Other hydrogen atoms, which diffuse in the electrolyte, are adsorbed on the surface of electrically neutral quantum-well microcrystallites. Comparing the standard electrochemical potential of atomic hydrogen (-2.1 V relative to the standard hydrogen electrode (SHE))[10] with the position of the Fermi level in silicon shows that with respect to silicon and PS atomic hydrogen is an exceptionally active donor and therefore it can inject electrons directly into the conduction band of PS:

$$H^\circ \rightarrow H^+ + e^-. \quad (4)$$

4. The ion radicals $(SO_4)^{\bullet -}$ are also capable of diffusing in the electrolyte. Reaching the surface of quantum-well microcrystallites, they inject holes into the valence band of these formations according to the reaction (2). The microcrystallites remain electrically neutral and bipolar carrier injection into the microcrystallites via the reactions (2) and (4) gives rise to visible-range EL.

The use of lower-viscosity and more hydrophilic electrolytes (for example, introducing acetone into the electrolyte) gives the best wettability of PS and contact between the electrolyte and a larger number of microcrystallites and therefore improves the conditions for the appearance of visible-range EL.

It is obvious that the visible-range EL should not depend on the resistance of the microcrystallites. Furthermore, it should not depend on the resistivity or the type of conductivity of the silicon substrate on which the porous silicon was grown. This is confirmed by experiments with samples of PS on *p*-type substrates.

The fact that current-carrier transport to PS particles is of an ionic, rather than electronic, character explains the long delay times observed for luminescence relative to the current pulse.[8] The appearance of EL is associated with the accumulation of a sufficient number of ion radicals and hydrogen atoms, as well as with their diffusion time from the electrode to the microcrystallites. The drift velocities and diffusion rates of ions in the electrolyte are several orders of magnitude lower than the carrier drift velocities in solids.

In the case of IR luminescence, the preliminary production of atomic hydrogen is not required and the EL delay times are shorter. Increasing the current density in the system accelerates the production of the required components and decreases the delay times.

One would think that in an electrolyte a direct charge-exchange reaction can occur between hydrogen atoms and ion-radicals, eliminating potential charge carriers to PS particles:

$$H^\circ + (SO_4)^{\bullet -} \xrightarrow{e^-} (SO_4)^{2-} + H^+. \quad (5)$$

However, by virtue of the Franck–Condon principle,[11] the probability of such a direct reaction in an electrolyte is much smaller than the probability of a reaction between the same particles adsorbed on the surface of an electrically neutral solid.[12] The energy stored earlier in these particles is released in the form of radiation and heat.

In summary, the proposed model presumes that charge-carrier transport to PS particles is ionic in nature and that there are two mechanisms of current-carrier injection from

the electrolyte into the PS — monopolar and bipolar. Monopolar injection (only holes) gives IR-range EL while bipolar injection gives visible-range EL.

4. CONCLUSIONS

In this paper we proposed the first generalized model for the appearance of visible- and infrared-range electroluminescence in a ⟨porous silicon⟩–⟨oxidizing electrolyte⟩ system. The model explains the mechanisms for current flow in the complex porous-silicon system containing simultaneously low-resistance macrocrystals and high-resistance quantum-well microcrystallites. While infrared-range EL appears in such a system as a result of monopolar injection of holes from the electrolyte into the low-resistance macrocrystals, visible-range EL is possible only with simultaneous injection of charge carriers of both signs into quantum-well microcrystallites. A mechanism of electron injection directly from the electrolyte was proposed. It was determined that the discharge of hydrogen ions occurring in the volume of the PS is important for electron injection and the appearance of visible-range EL. It was concluded that the character of the EL of porous silicon is virtually independent of the resistivity and even of the conductivity of the silicon substrate on which the porous silicon was grown.

These results make it possible to understand the reason for the main difficulties arising in the production of solid-state luminescence structures on porous silicon. In most known solid-state structures of the Schottky-diode type, which are produced on the basis of porous silicon, current passage does not provide sufficient injection of carriers of both signs in high-resistance or insulated (from the substrate) microcrystallites. The current is mainly of a tunneling or breakdown nature, which results in rapid degradation of the structures. The use of materials that penetrate into the voids (metals, polymers) also lacks the main advantage of having an electrolyte – the production of injecting components, and it results only in shunting of fragments of the microporous silicon.

This work was supported, in part, by the Russian Fund for Fundamental Research under grant No. 96-02-17903, by INTAS under grant No. 93-3325-ext, and under the program ''Physics of solid-state of nanostructures'' of the Ministry of Science (project No. 1-079/4).

[1] P. M. M. C. Bressers, J. W. J. Knapen, E. A. Meulenkamp, and J. J. Kelly, Appl. Phys. Lett. **61**, 108 (1992).
[2] L. V. Belyakov, D. N. Goryachev, O. M. Sreseli, and I. D. Yaroshchetskiĭ, Fiz. Tekh. Poluprovodn. **27**, 1815 (1993) [Semiconductors **27**, 999 (1993)].
[3] B. Pettinger, H.-R. Schoeppel, and H. Gerischer, Ber. Bunsen Ges. **80**, 849 (1976).
[4] A. Bsiesy, F. Muller, M. Ligeon, F. Gaspard, R. Herino, R. Romestain, and J. C. Vial, Phys. Rev. Lett. **71**, 637 (1993).
[5] M. W. Cole, J. F. Harvey, R. A. Lux, and D. W. Eckart, Appl. Phys. Lett. **60**, 2800 (1992).
[6] R. C. Anderson, R. S. Muller, and C. W. Tobias, J. Electrochem. Soc. **138**, 3406 (1991).
[7] L. V. Belyakov, D. N. Goryachev, D. I. Kovalev, F. Koch, V. Petrova-Koch, O. M. Sreseli, and I. D. Yaroshchetskiĭ, Fiz. Tekh. Poluprovodn. **29**, 1288 (1995) [Semiconductors **29**, 667 (1995)]; O. Sreseli, V. Petrova-Koch, D. Kovalev, T. Muschik, S. Hofreiter, and F. Koch, in *Proc. of the 22th Int. Conf. on the Physics of Semiconductors*, Vancouver, Canada, World Scientific, 1994, vol. 3, p. 2117.
[8] O. M. Sreseli, G. Polisski, D. Kovalev, D. N. Goryachev, L. V. Belyakov, and F. Koch, in *Proc. of the 188th ECS Meeting ''Advanced Luminescent Materials,''* ed. by D. J. Lockwood, P. M. Fauchet, N. Koshida, and S. R. J. Brueck (1995). PV 95-25, p. 24 [Electrochem. Soc. Proc. Ser. (Pennington, N.J., 1997).
[9] D. N. Goryachev, O. M. Sreseli, and L. V. Belyakov, Pis'ma Zh. Tekh. Fiz. **22**(3), 14 (1996) [Tech. Phys. Lett. **22**, 97 (1996)].
[10] D. Dobos, *Electrochemical Data*, Academiai, Budapest, 1977 [Russian trans., Mir, Moscow, 1980, p. 226].
[11] S. R. Morrison. *The Chemical Physics of Surfaces*, Plenum Press, N. Y., 1977 [Russian trans., Mir, Moscow, 1980].
[12] F. F. Vol'kenshteĭn, *Electronic Processes on Semiconductor Surfaces During Chemisorption* [in Russian], Nauka, Moscow, 1987.

Translated by M. E. Alferieff

Excitonic effects in the photoconductivity of quantum-well $Ga_xIn_{1-x}As/InP$ structures

M. F. Panov and A. N. Pikhtin

St. Petersburg State Electrical Engineering University, 197376 St. Petersburg, Russia
(Submitted November 20, 1996; accepted for publication November 25, 1996)
Fiz. Tekh. Poluprovodn. **31**, 848–850 (July 1997)

The photoconductivity spectra of quantum-well structures consisting of 50 alternating 7 to 12-mm-thick $Ga_xIn_{1-x}As$ ($x=0.47$) layers forming quantum wells and 10 to 15-nm-thick InP barriers have been investigated. Characteristic excitonic peaks $11H$, $11L$, $13H$, $22H$, and $22L$ were observed in the high-quality structures. A strong temperature dependence was found for the $11H$ exciton, while no such dependence was observed for any of the other excitons. This is explained by the fact that the $11H$ state of an exciton falls in the range of energies which are forbidden for free carriers, while the remaining states are resonance states and overlap with the continuous spectrum. The thermal activation energy of photoconductivity was found to be 150 ± 30 meV, much greater than the exciton binding energy and close to the depth of the potential well for electrons. This shows that the photosensitivity is due to above-barrier charge-carrier transfer and that the tunneling transfer between the wells is negligible.
 [S1063-7826(97)02207-2]

The lattice parameters of the solid solution $Ga_xIn_{1-x}As$ with $x=0.47$ are close to those of InP. Because of this circumstance, the composite quantum-well structures based on them are of great value for modern electronics and optoelectronics and they are of great interest as model objects for investigations.[1]

The structures investigated by us were obtained by molecular-beam epitaxy and are a classical example of a composite undoped superlattice with weakly coupled quantum wells (so-called MQW structures). The $Ga_xIn_{1-x}As$ layers forming the wells were 7–12 nm thick and the InP barriers were 10–15 nm thick. The number of layers was equal to approximately 50. The period and quality of the structure were checked by x-ray methods.

Since the quantum-well structures were obtained on a semi-insulating InP substrate, the photoelectric measurements were performed with the contacts arranged parallel to the layers. Contacts of the alloyed type, prepared with a pulse ruby laser, were used.[2] The spectra were measured by the synchronous detection method.

The photoconductivity (PC) spectra in the absorption region in quantum-well layers for one of the high-quality barriers are shown in Fig. 1. The room-temperature PC spectrum (curve *1*) contains all features observed previously in the absorption spectra.[1] The appearance of intersubband transitions in the form of maxima shows that they are of an excitonic nature. The low-temperature PC spectrum (curve *2*) differs from the absorption spectrum primarily by the fact that the long-wavelength peak vanishes.

To identify the types of excitonic transitions, calculations of the size-quantization levels and the interlevel gaps were performed in the square-well approximation similarly to Ref. 3. The difference in the energies for the $11H$ and $11L$ excitons was found to be very close to that of the size-quantization levels for heavy ($1H$) and light ($1L$) holes. Comparing the experimental quantity $E_{11}=(11H-11L)=12.5$ meV with the computed values made it possible to determine the well width, which was found to be 11.3 nm, close to the technological value. This value corresponded to the excitonic band gap $E_{gx}=0.747$ eV at 300 K for the three-dimensional (3D) solid solution $Ga_xIn_{1-x}As$, which is lattice-matched to InP.[4,5] The computed energies for the corresponding excitonic transitions are marked by arrows in Fig. 1. They agree well with the experimentally observed values. We note that in addition to the transitions 11 and 22, which are allowed by the selection rules, there is a weak transition 13, which was also observed in Refs. 1 in the absorption spectra at 20 K.

The fact that at low temperature the lower excitonic state does not appear in the photoconductivity spectra is understandable in principle: Thermal dissociation of the exciton does not occur and free charge carriers are not produced. However, detailed investigations of the temperature depen-

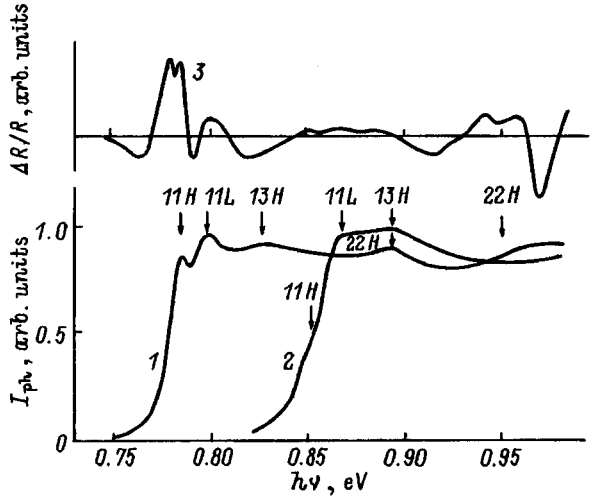

FIG. 1. Photoconductivity spectra I_{ph} at 293 (*1*) and 85 K (*2*) and the photoreflection spectrum $\Delta R/R$ (3) of a multilayer quantum-well structure in the system $Ga_{0.47}In_{0.53}As/InP$. The energies of the following excitonic transitions are shown: $11H(1e-1hh)$; $11L(1e-1eh)$; $22H(2e-2hh)$; $22L(2e-2eh)$; $13H(1e-3hh)$.

 1063-7826/97/070719-03$10.00

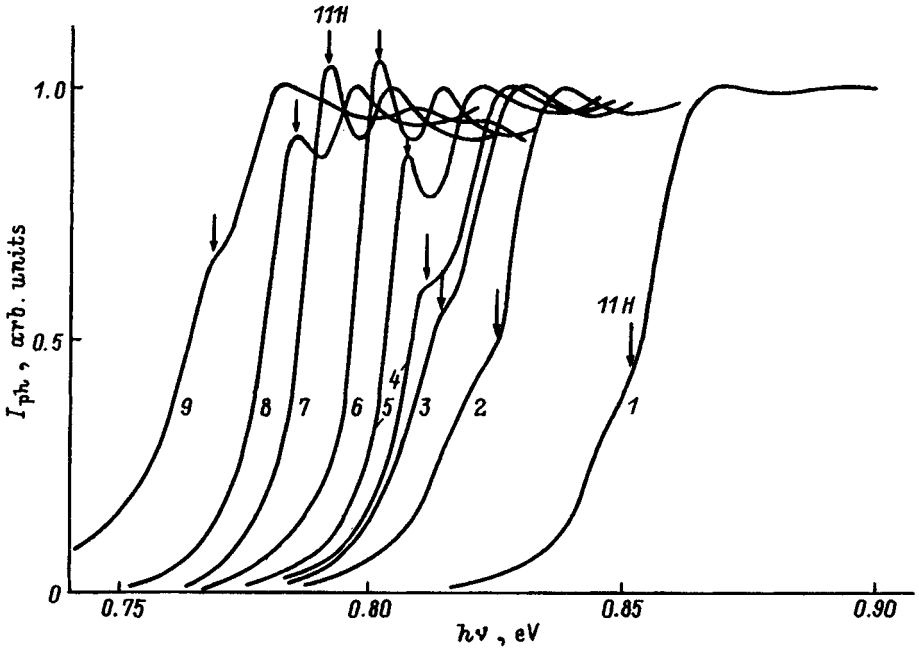

FIG. 2. Temperature dependences of the normalized photoconductivity spectra I_{ph} in the region of the excitonic transitions in quantum wells. Temperature, T, K: *1* — 85, *2* — 162, *3* — 191, *4* — 200, *5* — 219, *6* — 243, *7* — 277, *8* — 300, *9* — 352. The arrows indicate the transitions in the 11H state.

dence of the PC spectra yielded interesting and unexpected results. A strong temperature dependence was observed only for the 11H exciton, as one can see in Fig. 2. The main changes appear in a narrow temperature interval from 140 to 200 K, where rapid growth of the intensity of the 11H peak is observed, while the temperature variations are manifested in the remaining extrema in their energy shift. The relative intensities of the peaks do not change in this case (in Fig. 2 all spectra are normalized to the photoconductivity in the region of the 11L maximum).

The form and intensity of the characteristic spectral features corresponding to transitions into excitonic states and their temperature dependence are determined by the position of the ground states of the excitons relative to the continuum of the allowed energies. For all other excitons the 1S state lies either in or close to (11L exciton) the continuum of allowed free-carrier energies. Such states are resonance states. The lifetime of the excitons in them is short, and no expenditure of energy is required to dissociate an exciton. For this reason, these states exhibit a large broadening.

The thermal activation energy of an exciton was found from the temperature dependence of the photoconductivity near the (11H) excitonic ground state. It was found to be unexpectedly high and equal to 150 ± 30 meV. This is more than an order of magnitude greater than the binding energy of the 11H exciton ($\sim$8 meV) and shows the complicated character of the formation of the PC signal. Indeed, the value of the activation energy is close to the offset of the bands in a lattice-matched heterojunction, which according to data obtained by different authors varies from 0.13 to 0.51 eV for both electrons and holes. This suggests that at least one carrier (probably, an electron) must be ejected from a well in order for the photoconduction process to be activated. This above-barrier carrier is picked up by the tranverse electric field present near the surface of the structure and enters either other wells or the high-resistance InP layer, changing their conductivity. Since photogenerated charge carriers of opposite sign are spatially separated, their lifetime is long and they can make a substantial contribution to the photoelectric effect.

To check the presence of a transverse electric field, the photoreflection of the same structure on which the photoconductivity spectra were measured was measured by the method of Ref. 6. These data are presented in Fig. 1 (curve 3). The presence of a strong signal in the region of the electronic (excitonic) transitions in quantum wells and the fact that the characteristic features of the photoreflection and photoconductivity spectra occur at the same energies indicate the presence of a transverse electric field in the experimental structure. The field intensity, estimated similarly to that in Ref. 7, was found to be of the order of 10^4 V/cm, which confirms the assumptions advanced above about the mechanism of the formation of the photoconductivity signal in the experimental structure.

The relative arrangement of the excitonic and itinerant

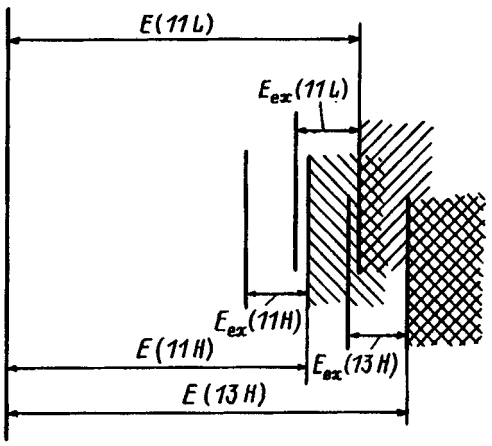

FIG. 3. Relative arrangement of the excitonic (E_{ex}) and itinerant (E) states in the experimental structure.

states in the structure is shown schematically in Fig. 3.

The character of the spectra and their temperature dependences for other similar structures are similar to those presented above, but in a number of cases their broadening is much greater, especially for strained $Ga_xIn_{1-x}As/InP$ structures.

[1] M. S. Skolnic, L. L. Taylor, S. J. Bass, A. D. Pitt, D. J. Towbray, A. G. Cullis, and N. G. Chew, Appl. Phys. Lett. **51**, 24 (1987).

[2] A. N. Pikhtin, V. A. Popov, and D. A. Yas'kov, Fiz. Tekh. Poluprovodn. **3**, 1646 (1969) [Sov. Phys. Semicond. **3**, 1383 (1969)]; Prib. Tekh. Éksp. No. 2, 238 (1970).

[3] J. P. Laurenti, J. Camassel, B. Reynes, D. Grützmacher, K. Wolter, and H. Kurz, Semicond. Sci. Technol. **5**, 222 (1990).

[4] D. K. Gaskill, N. Bottka, L. Aina, and M. Mattingly, Appl. Phys. Lett. **56**, 1269 (1990).

[5] T. W. Nee and A. K. Green, J. Appl. Phys. **68**, 5314 (1990).

[6] M. V. Konyayev and A. N. Pikhtin, in *Abstracts of Int. Symp. on Nanostructures: Physics and Technology* [in Russian], St. Petersburg, Russia, 1994, p. 74.

[7] A. N. Pikhtin and M. T. Todorov, Fiz. Tekh. Poluprovodn. **27**, 1139 (1993) [Semiconductors **27**, 628 (1993)].

Translated by M. E. Alferieff

Lateral association of vertically coupled quantum dots

A. F. Tsatsul'nikov, A. Yu. Egorov, A. E. Zhukov, A. R. Kovsh, V. M. Ustinov, N. N. Ledentsov, M. V. Maksimov, B. V. Volovik, A. A. Suvorova, N. A. Bert, and P. S. Kop'ev

A. F. Ioffe Physicotechnical Institute, Russian Academy of Sciences, 194021 St. Petersburg, Russia
(Submitted November 20, 1996; accepted for publication November 25, 1996)
Fiz. Tekh. Poluprovodn. **31**, 851–854 (July 1997)

The modification produced in the structural and optical properties of vertically coupled $In_{0.5}Ga_{0.5}As$ quantum dots in a GaAs matrix by increasing the number of deposited layers of quantum dots has been investigated. It was shown that the deposition of a sequence of $In_{0.5}Ga_{0.5}As$ quantum-dot planes separated by narrow (of the order of the height of the quantum dots) GaAs layers gives rise to an interaction between neighboring vertically coupled quantum dots. This interaction shifts the photoluminescence line due to the recombination of nonequilibrium carriers via states of the quantum dots into the region of lower photon energies.
 [S1063-7826(97)02307-7]

In the last few years there has been great deal of interest in objects which are bounded in three spatial dimensions — quantum dots (QDs). This stems from a development of a method for obtaining QDs based on the spontaneous transformation of a thin layer of a single material, deposited on the surface of a different material with a different lattice constant, into islands.[1,2] Quantum dots formed by depositing a (In, Ga)As layer on a GaAs (100) surface have been investigated extensively. These QDs are characterized by the absence of mismatch dislocations and by a high photoluminescence (PL) efficiency. Injection semiconductor lasers with a high characteristic temperature and a low threshold current density have been produced on the basis of arrays of (In, Ga)As QDs.[3,4]

The working characteristics of lasers can be substantially improved by using as the active region an array of vertically coupled QDs (VCQD), i.e., sequences of QD planes separated by narrow layers of a wide-gap material. As shown in Refs. 5 and 6, the QDs in each successive row are formed above the QDs of the preceding row. The interaction of the electronic levels of the QDs in neighboring rows increases the localization energy and correspondingly decreases the probability of thermal transfer of carriers from the ground state of the QDs to higher-lying states. Furthermore, the multiplication of the QDs increases the overlapping of the light wave with the active region and therefore increases the gain accompanying a population inversion. Using an array of vertically coupled QDs as an active region made it possible to increase the temperature stability of injection lasers (reach a characteristic temperature $T_0 \approx 400$ K in the temperature range 80–170 K) and decrease the threshold current density ($J_{th} \approx 100$ A/cm^2 at 300 K).[7]

As shown in Ref. 8, in the case of vertical alignment of several QD layers separated by narrow (of the order of the height of a QD) GaAs layers, the lateral dimensions of the QDs in the top rows increases and therefore the distance between individual QDs in the plane of the structure decreases. This can give rise ultimately to lateral interaction of neighboring VCQD and therefore increase the carrier localization energy. As noted above, increasing the localization energy is one way to improve the characteristics of semiconductor lasers and makes it possible to shift the lasing wavelength into the spectral region near ~ 1.3 μm, important from the standpoint of practical applications. In our study we examined the change produced in the structural and optical properties of vertically coupled $In_{0.5}Ga_{0.5}As$ QDs in a GaAs matrix by increaseing the number of deposited layers of QDs.

The samples were grown by molecular-beam epitaxy, performed in the RIBER-32 system, on GaAs (100) substrates. The effective thickness of a $In_{0.5}Ga_{0.5}As$ layer in each deposition cycle was equal to 12 Å and the GaAs layers were 50 Å wide. The formation of QDs was monitored according to the HEED pattern. The number of repeating $In_{0.5}Ga_{0.5}As$ layers varied from sample to sample in the range $N = 1-20$. The PL was excited with a Ar^+ laser with photon energy ~ 2.54 eV and excitation density ~ 100 V/cm^2 and they were recorded with a Ge photodetector.

Figure 1 shows transmission electron microscopy (TEM) images of QDs in a structure with $N = 20$ planes of InGaAs QDs. The lateral dimensions of the QDs equal ~ 300 Å and, as one can see, formation of extended conglomerates of overlapping QDs, which we call lateral association of VCQD, occurs. Moreover, as one can see from the transverse-section images (Fig. 1c), at $N = 10$ the interaction between the closest QDs has the effect that deviations are observed from the strict vertical alignment for QDs located in the upper layers. Both factors decrease the distance between the closest VCQDs and result in overlapping of neighboring VCQDs.

The PL spectra at $T = 77$ K of structures containing a different number of planes of InGaAs QDs are shown in Fig. 2. A single line (QD), resulting from recombination of nonequilibrium carriers via the ground state of the VCQD, can be seen in the spectra of the samples containing 1, 3, and 6 layers of QDs. Increasing the deposition cycles to 10 results in the appearance of a new PL band (CQD) in the spectrum. The new band is shifted relative to the line QD in the long-wavelength direction (Fig. 3), indicating an increase in the characteristic size of the VCQD. As the number of QD planes is increased to 20, a relative drop occurs in the inten-

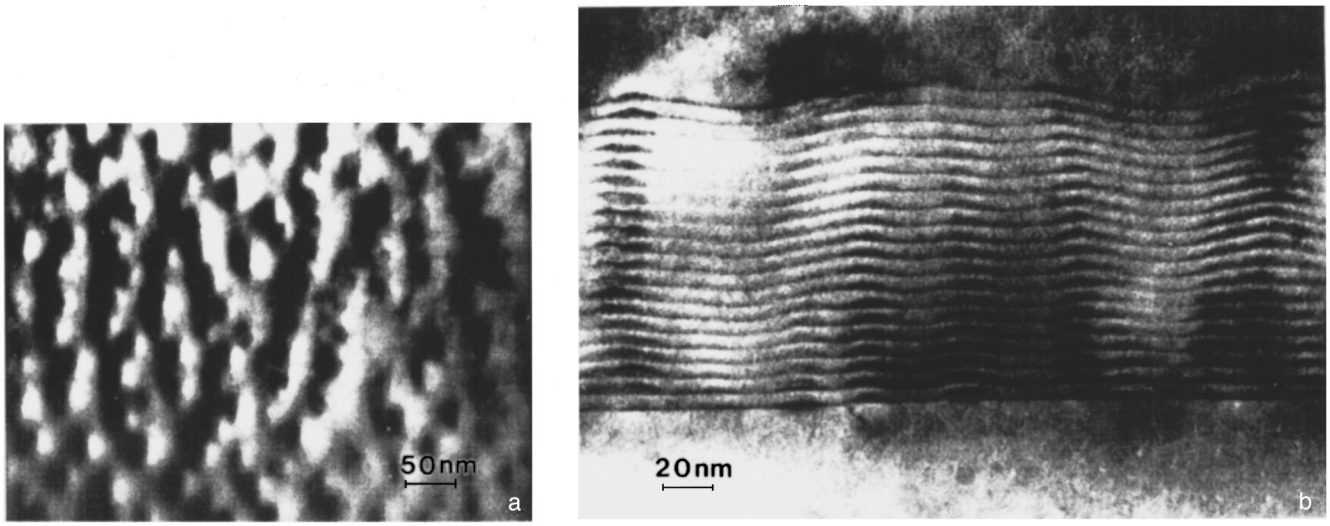

FIG. 1. Thermal-field image of a structure with twenty QD layers in a planar geometry (a) and light-field image (b) in a transverse section ($g=200$).

sity of the band QD and the line CQD dominates the PL spectrum.

This behavior of the PL agrees with the TEM data, which likewise show that increasing the number of $In_{0.5}Ga_{0.5}As$ layer deposition cycles results in a lateral overlapping of the closest VCQD. The combined effect of a decrease in the height and width of the potential barrier between neighboring VCQD is to decrease the quantum-well energy and shift the optical transition energy to lower values (Fig. 4). Recombination via the states of the interacting QDs leads to the appearance of the CQD line in the PL spectrum.

The shift of the QD band with increasing number of $In_{0.5}Ga_{0.5}As$ planes can be described on the basis of perturbation theory, assuming that the interaction between the carriers localized in the aligned QDs is weak.[9,10] Assuming that the only interaction is between the energy states of the neighboring QD layers, the shift $\Delta E_{\max}(N)=E_1-E_N$ in the maximum (E_n) of the PL line in a sample with N QD planes with respect to the position of the maximum (E_1) of the line in the spectrum of a structure with one QD layer can be obtained by equating the following determinant to zero:

$$\begin{vmatrix} E_1-E_n & \Delta & 0 & 0 \\ \Delta & E_1-E_N & \Delta & 0 \\ 0 & \Delta & E_1-E_N & \Delta \\ 0 & 0 & \Delta & E_1-E_N \\ \cdot & \cdot & \cdot & \cdot \end{vmatrix} = 0,$$

where $\Delta=\Delta_c+\Delta_h$, and $\Delta_c(\Delta_h)$ is the matrix element describing the interaction of electrons (holes) localized in neighboring aligned QDs. The approximation of the experimental curve $E_{\max}(N)$ by the curve calculated with $\Delta=45$ meV is shown in Fig. 3. For $N>10$ a discrepancy is observed between the experimental and theoretical curves. This is apparently due to the appearance of lateral overlapping of neighboring VCQD.

Figure 5 shows the PL spectra measured at different temperatures for structures with 20 planes of QDs. At $T\approx 10$ K, the dominant line in the spectrum is the QD line. The intensity of this line decreases with increasing temperature and the line practically vanishes at temperatures above ~ 80 K. Figure 6a shows the temperature dependences of the ratio of the integrated intensities of the QD and CQD lines for samples with a different number of planes of QDs. As one can see from this figure, for a structure with ten layers of QDs the QD band dominates at low temperatures ($T<\sim 170$ K), whereas in the spectrum of the sample with twenty layers of QDs the CQD line dominates in the entire temperature range. As the temperature increases, the intensity of the QD line decreases strongly relative to the intensity of the CQD band. These facts show that increasing the num-

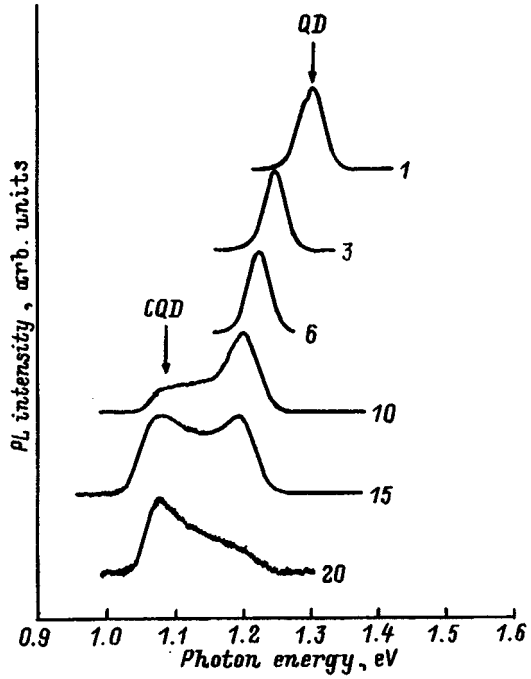

FIG. 2. PL spectra of the experimental structures at $T=77$ K. The numbers on the curves represent the number of QD planes in the structure.

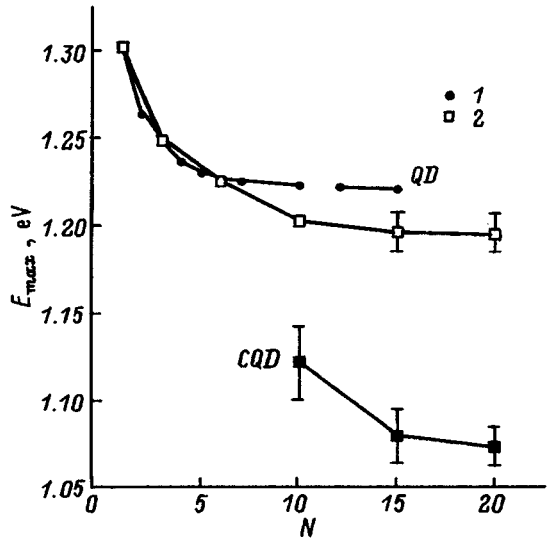

FIG. 3. Position of the maximum of the QD and CQD lines versus the number of deposited QD planes. *1* — Theory; *2* — experiment.

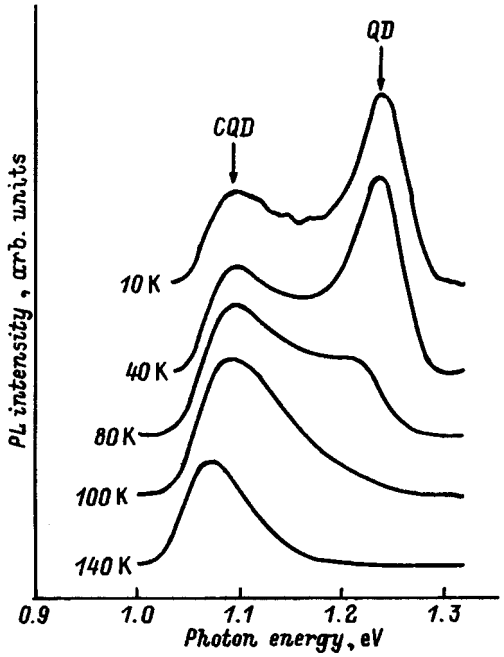

FIG. 5. PL spectra of a structure with twenty QD layers at different temperatures.

ber of $In_{0.5}Ga_{0.5}As$ deposition cycles increases the number of overlapping VCQD (Fig. 1b). At a low temperature, the electron and hole transitions between VCQD are impeded and the form of the PL band is determined by the energy distribution of the density of states of the VCQD array. As the temperature is raised, the probability of carrier transport and relaxation in states with a high localization energy increases. This gives rise to a substantial, compared with the change in the band gap, shift of the minimum of the CQD line in the long-wavelength direction and a decrease in the width of the line with increasing temperature (Figs. 6b and 6c).

As the number of deposited QD layers increases, the decrease in the intensity of the QD band starts at lower values of the temperature (Fig. 6d). This shows that the activation energy of the process, which gives rise to the decrease in the intensity of the QD band with increasing temperature, decreases as the number of $In_{0.5}Ga_{0.5}As$ deposition cycles increases. At the same time, the carrier localization energy in a state with which the PL line QD is associated increases with the number of deposited QD layers, as follows from the long-wavelength shift of the QD band with increasing number N. This confirms the assumption made above that the probability of nonequilibrium-carrier transport between QDs and relaxation of the carriers into a state with a lower quantum-well energy, which are due to lateral association of the VCQD, increases. The activation energy of this process

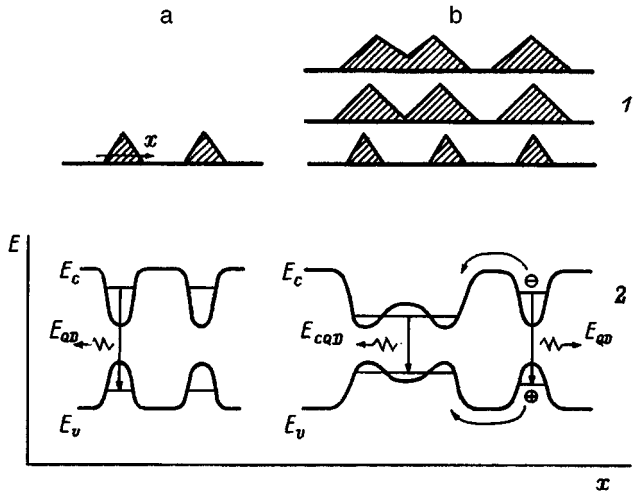

FIG. 4. Schematic diagram of the transverse section (1) and band diagram (2) of structures with nonoverlapping (a) and overlapping (b) VCQD.

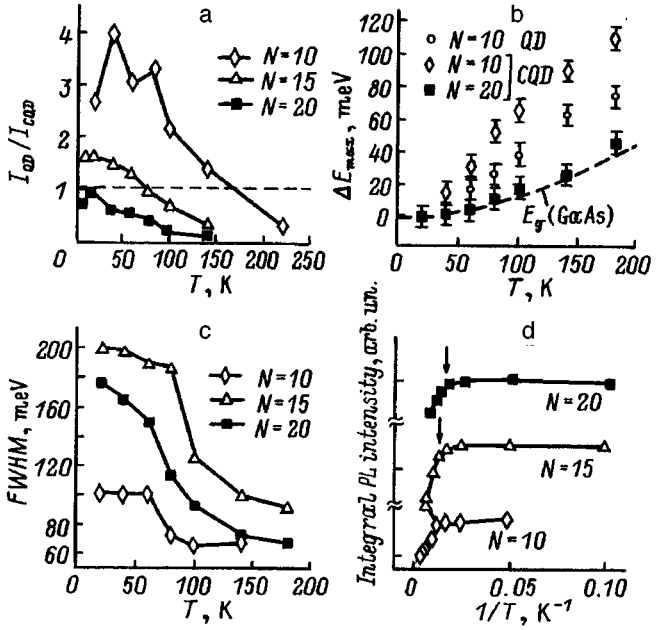

FIG. 6. Temperature dependences: a — Ratios of the QD and CQD line intensities; b — shifts of the maximum of the QD and CQD lines $\Delta E_{max}(T)=(E_{max}(T=0)-E_{max}(T))$; c — CQD band width at half-maximum; d — integral intensity of the QD line.

can be estimated from the experimental curves obtained by us (Fig. 6d): 13 ± 5, 17 ± 5, and 20 ± 5 meV for structures with $N=20$, 15 and 10, respectively.

In summary, our investigations showed that the deposition of a sequence of $In_{0.5}Ga_{0.5}As$ QD planes separated by narrow (of the order of the height of a QD) GaAs interlayers leads to the appearance of an interaction between neighboring VCQD. This interaction shifts the PL line, due to the recombination of nonequilibrium carriers via the states of the QDS, to lower photon energies. The lateral association of VCQD gives an additional possibility of controlling the electronic spectrum and the wavelength of the radiation of structures with QDs.

This work was supported by the Russian Fund for Fundamental Research under Grant No. 96-02-17824, the Volkswagen Foundation, and INTAS under Grant INTAS-94-1028.

[1] L. Goldstein, F. Glass, J. Y. Marzin, M. N. Charasse, and G. Le. Roux, Appl. Phys. Lett. **47**, 1099 (1985).
[2] P. M. Petroff and S. P. Den Baars, Superlat. Microstruct. **15**, 15 (1994).
[3] Zh. I. Alferov, N. A. Bert, A. Yu. Egorov, A. E. Zhukov, P. S. Kop'ev, A. O. Kosogov, I. L. Krestnikov, N. N. Ledentsov, A. V. Lunev, M. V. Maksimov, A. V. Sakharov, V. M. Ustinov, A. F. Tsatsul'nikov, Yu. M. Shernyakov, and D. Bimberg, Fiz. Tekh. Poluprovodn. **30**, 351 (1996) [Semiconductors **30**, 194 (1996)].
[4] Zh. I. Alferov, N. Yu. Gordeev, S. V. Zaĭtsev, P. S. Kop'ev, I. V. Kochnev, V. V. Komin, I. L. Krestnikov, N. N. Ledentsov, A. V. Lunev, M. V. Maksimov, S. S. Ruvimov, A. V. Sakharov, A. F. Tsatsul'nikov, Yu. M. Shernyakov, and D. Bimberg, Fiz. Tekh. Poluprovodn. **30**, 357 (1996) [Semiconductors **30**, 197 (1996)].
[5] Q. Xie, A. Madhukar, P. Chen, and N. Kobayashi, Phys. Rev. Lett. **75**, 2542 (1995).
[6] A. Yu. Egorov, A. E. Zhukov, P. S. Kop'ev, N. N. Ledentsov, M. V. Maksimov, V. M. Ustinov, A. F. Tsatsul'nikov, N. A. Bert, A. O. Kosogov, and D. Bimberg, Fiz. Tekh. Poluprovodn. **30**, 1682 (1996) [Semiconductors **30**, 879 (1996)].
[7] N. N. Ledentsov, in *23rd Int. Conf. on the Physics of Semiconductors*, edited by M. Scheffler and R. Zimmermann, World Scientific, Singapore, 1996, p. 19.
[8] N. N. Ledentsov, M. Grundmann, N. Kirstaedter, O. Schmidt, R. Heitz, J. Bohrer, D. Bimberg, V. M. Ustinov, V. A. Shchukin, P. S. Kop'ev, Zh. I. Alferov, S. S. Ruvimov, A. O. Kosogov, P. Werner, U. Richter, U. Gosele, and J. Heydenreich, in *7th Int. Conf. on Modulated Semiconductor Structures*, Madrid, Spain 1995 [Solid–State Electron. **40**, 785 (1996)].
[9] A. F. Tsatsul'nikov, N. N. Ledentsov, M. V. Maksimov, A. Yu. Egorov, A. E. Zhukov, V. M. Ustinov, B. V. Volovik, I. L. Krestnikov, A. R. Kovsh, A. V. Sakharov, N. A. Bert, P. S. Kop'ev, D. Bimberg, and Zh. I. Alferov, Fiz. Tekh. Poluprovodn. **30**, 1822 (1996) [Semiconductors **30**, 953 (1996)].
[10] L. D. Landau and E. M. Lifshitz, *Quantum Mechanics*, Pergamon Press, N. Y. [Russian original, p. 167].

Translated by M. E. Alferieff

Characteristic features of silicon multijunction solar cells with vertical *p–n* junctions

E. G. Guk, T. A. Nalet, M. Z. Shvarts, and V. B. Shuman

A. F. Ioffe Physicotechnical Institute, Russian Academy of Sciences, 194021 St. Petersburg, Russia
(Submitted November 21, 1996; accepted for publication November 25, 1996)
Fiz. Tekh. Poluprovodn. **31**, 855–857 (July 1997)

A relatively simple technology (without photolithography) based on diffusion welding and ion-plasma deposition of an insulating coating has been developed for fabricating multijunction silicon solar cells with vertical *p–n* junctions. The effective collection factor for such structures is independent of the wavelength of the incident light in the wavelength range $\lambda = 340 - 1080$ nm. © *1997 American Institute of Physics.* [S1063-7826(97)02407-1]

The question of how best to arrange the *p–n* junctions with respect to the direction of the incident light — perpendicular or parallel — was discussed in the beginning stage of development of semiconductor solar-power conversion.[1,2] Calculations and experiments have shown that the recombination of the photogenerated charge carriers on the illuminated surface plays a much larger role in the case of a parallel arrangement of a *p–n* junction relative to the incident light than for a perpendicular arrangement. For a long time the solution of the problem of surface passivation encountered insurmountable difficulties, and the efficiency of silicon solar cells (SSCs) with vertical *p–n* junctions was low — 0.8% (Ref. 3) and 8% (Ref. 4). For this reason, the planar construction became the standard. At the same time, it was noted earlier[1,2] that SSCs with vertical *p–n* junctions have a number of substantial advantages over the planar construction:

1) There are no inconsistent requirements on the layer resistance of the emitter, on the spectral sensitivity, on the contact grid area, and so on;

2) since the front and back surfaces of such SSCs contain no metallization, they are transparent to the long-wavelength part of the spectrum beyond the edge of the main absorption band, so that their equilibrium working temperature should be lower than in the case of the planar analog;

3) they are bilateral and can serve as the main part of cascade solar cells (SCs); and

4) in contrast to planar junctions, SSCs with vertical *p–n* junctions generate a high voltage (because the cells are connected in series) and a low current at the same power. As a result, arrays of such cells are more efficient, because the losses due to the production of the high-current cells are lower.

It is obvious that these advantages can be realized only if use is made of the latest achievements of silicon device technology. Our objective was to develop an efficient technology for fabricating multijunction concentrator solar cells with vertical *p–n* junctions. For example, the p^+–p–n^+ structure was produced by diffusion from polymer sources, which have performed well in the fabrication of planar SSCs.[5] Successful surface passivation required eliminating the soft solder in joining the plates, which is used in Refs. 3 and 4, and replacing it by the methods employed in high-power technology and microelectronics (for example, diffusion welding[6]). Surface passivation was achieved by depositing insulator SiO_2 coatings, a method which is now widely used.[7]

We employed plates of *p*-silicon (KDB-12), 40–60 mm in diameter and 300 μm thick, to prepare the SSCs. A p^+–p–n^+ structure was obtained on the plates by successive diffusion of boron and phosphorus from polymer sources.[8] The diffusion layers were 1 μm thick. After phosphorus diffusion the plates were annealed for 15 h at 720 °C to getter impurities from deep levels. This technology gives electron lifetimes (measured by Lax's method[9]) in the range 45–55 μs; i.e., the electron diffusion length was greater than the thickness of the base. After the oxide layers were etched off, aluminum was deposited on the surface of the plate at 350 °C. Diffusion welding was performed by two methods. In the first one, the plates were assembled into a stack; in the second one, the plates were alternated with 30 to 40-μm-thick Silumin layers. Further investigations show that the characteristics of the samples obtained are close, but the ''shading'' was ~1% in the first variant and ~10% in the second variant. Diffusion welding was conducted in vacuum at 550 °C with sufficient pressure to produce the required plastic deformation of aluminum and Silumin. Next, the stack of plates was cut with a circular diamond sawblade into separate $5 \times 1.2 \times 1$-mm elements, shown schematically in Fig. 1. The outer layer, whose crystal structure was destroyed by the cutting, was removed by systematic grinding, mechanical polishing, and etching in acid.

A passivating coating (~100-Å-thick layer of SiO_2) and a two-layer quarter-wave antireflection coating, consisting of Si_3N_4 and SiO_2, were obtained in a triode-type, ion-plasma sputtering system by means of ion-plasma reactive sputtering of a silicon target in an oxygen atmosphere (to form the SiO_2 layer) or a nitrogen atmosphere (to deposit a Si_3N_4 layer) at working pressures of $(5-7) \times 10^{-4}$ Torr. An oil-free heteroion evacuation with a titanium magnetic-discharge pump was used to obtain a high vacuum and produce the working gas medium. These pumps give high-vacuum evacuation and efficiently remove from the working gas medium uncontrollable gaseous oxidizing impurities (water, oxygen). This purification of the gas medium is achieved as a result of the high evacuation efficiency characteristic of pumps of this type. For example, the rate of evacuation of oxygen is approximately 10 times higher than that of nitrogen and almost 100 times higher than that of argon. The technology developed recently makes it possible to obtain

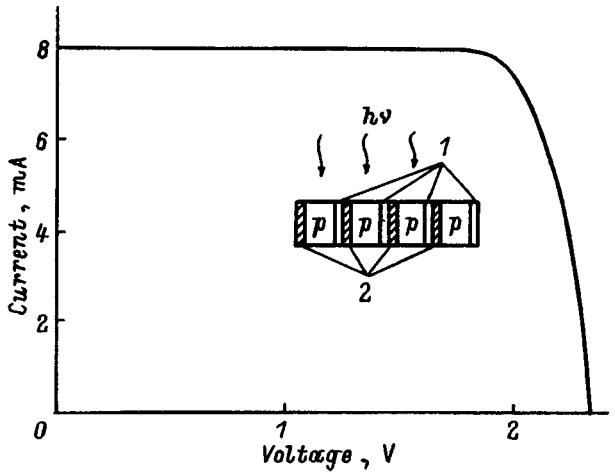

FIG. 1. Load characteristic of SSC containing four serially connected p–n junctions under an illumination intensity of 22 suns. Inset: Structure of SSC: *1* — p^+ layer, *2* — n^+ layer.

Si_3N_4 and SiO_2 layers with refractive indices $n_2 = 1.96 \pm 0.02$ and $n_1 = 1.48 \pm 0.02$, respectively. The layers were deposited on an antireflection surface in one vacuum cycle. Their thickness was determined by the requirement that the antireflection of the surface be optimal in the wavelength range $\lambda \approx 800$ nm. The passivating and antireflection coatings approximately doubled the photocurrent compared with samples with a mechanically polished surface.

The spectral dependence of the reflection coefficient R of one sample is shown in Fig. 2 (curve *3*). A two-layer antireflection coating gives a wider spectral dependence of lower values of the reflection coefficient than a single-layer coating — the value of R in the interval $\lambda = 710-1010$ nm does not exceed 5%. The spectral dependence of the carrier collection factor (Q) for the same sample is represented by curve *2* in Fig. 2 and the effective collection factor $Q(1-R)$ is denoted by curve *1* in the same figure. As one can see from the data presented, multijunction SSCs have a high sensitivity in the infrared (IR) and ultraviolet (UV) regions of the spectrum. In the IR region, the high minority-carrier collection is due to the decrease in the distance (as compared with a planar structure), which the carriers traverse before they are separated by the vertical p–n junctions. High carrier collection is observed in the UV region of the spectrum because the UV radiation is absorbed not in the strongly doped emitter but rather directly in the weakly doped base, which has a large diffusion length and a low surface recombination rate. Therefore, the effective carrier collection factor is virtually independent of the wavelength in a wide range of wavelengths (340–1080 nm). This effect was previously predicted from general considerations.[10]

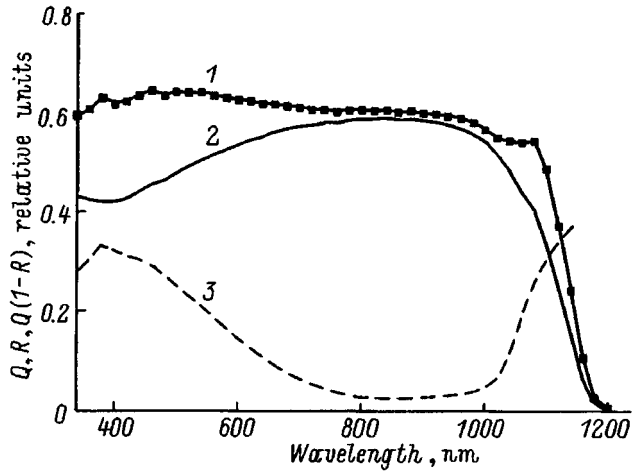

FIG. 2. Spectral characteristics of SSC: *1* — Effective internal collection factor; *2* — external collection factor; *3* — reflection coefficient of the front face.

The absolute current sensitivity of the SSCs was measured with a small solar radiation simulator calibrated to AMO illumination conditions. The short-circuit current I_{sc}, calculated on the photoactive surface of one structure, was in the range 27.5–30 mA/cm^2 (AMO, 25 °C). The load characteristics of SSCs consisting of four serially connected p–n junctions were measured under a pulsed concentrated solar radiation simulator (AMO, 25 °C). The characteristic of one sample with solar radiation concentration $K = 22$ is presented in Fig. 1. The open-circuit voltage U_{oc} on this SSC reached 2350 mV, $I_{sc} = 8$ mA, and the filling factor (FF) was equal to 0.8. The high value of the FF indicates a low serial resistance ($\sim 10^{-2}\ \Omega/\square$) per structure; this was achieved by continuous metallization of strongly doped p^+ and n^+ layers. The radiation conversion efficiency η at 22 suns exceeded 11% (AM 1.5).

In summary, the new technology has made it possible to obtain for the first time satisfactory commercial-silicon-based concentrated solar cells with vertical p–n junctions. As a result of their high UV sensitivity, these structures can be used as sensors in this region of the spectrum.

This work was supported by the Russian Fund for Fundamental Research under Grant No. 96-02-17903.

[1] A. L. Fahrenbruch and R. H. Bube, *Fundamentals of Solar Cells*, Academic Press, N. Y., 1983 [Russian translation, Énergoatomizdat, Moscow, 1987, p. 182].
[2] M. M. Koltun, *Optics and Metrology of Solar Cells* [in Russian], Nauka, Moscow, 1985, p. 30.
[3] A. P. Landsman and D. S. Strebkov, Fiz. Tekh. Poluprovodn. **4**, 1922 (1970) [Sov. Phys. Semicond. **4**, 1647 (1970)].
[4] C. Goradia and M. G. Goradia, in *12th IEEE Photovoltaic Specialists Conference*, Buton Rouge, LA, 1976, p. 789.
[5] E. G. Guk, N. S. Zimogorova, M. Z. Shvarts, V. B. Shuman, and N. A. Tokranova, Pis'ma Zh. Tekh. Fiz. **21**, 40 (1995) [Tech. Phys. Lett. **21**, 35 (1995)].
[6] G. N. Surzhenkov, E. D. Khutoryanskiĭ, and O. M. Korol'kov, in *Technology of High-Power Semiconductor Devices* [in Russian], Tallin, Valgus, 1987, p. 47.
[7] S. Sze [Ed.], *VLSI Technology*, McGraw-Hill, N. Y., 1983 [Russian transl., Mir, Moscow, 1986, Vol. 1, p. 125].
[8] E. G. Guk, A. V. El'tsov, V. B. Shuman, and T. A. Yurre, *Photoresists–Diffusants in Semiconductor Technology* [in Russian], Nauka, Leningrad, 1984, p. 47.
[9] D. Lax and S. F. Neustadter, J. Appl. Phys. **25**, 1148 (1954).
[10] V. M. Andreev, V. A. Grilikhs, and V. D. Rumyantsev, *Photoelectric Conversion of Concentrated Solar Radiation* [in Russian], Nauka, Leningrad, 1989, p. 116.

Translated by M. E. Alferieff

1/*f* noise in strongly doped *n*-type GaAs under band–band illumination conditions

N. V. D'yakonova, M. E. Levinshteĭn, and S. L. Rumyantsev

A. F. Ioffe Physicotechnical Institute, Russian Academy of Sciences, 194021 St. Petersburg, Russia

F. Pascal

Center d'Electronique et de Micro-optoelectronique de Montpellier, CNRS-Universite UMR 5507, Place Bataillon, 34095 U. M. ll, Montpellier

(Submitted November 21, 1996; accepted for publication December 1, 1996)
Fiz. Tekh. Poluprovodn. **31**, 858–863 (July 1997)

The nature of $1/f$ noise, which appears in strongly doped *n*-type GaAs (electron density $n_0 \simeq 10^{17}$ cm^{-3}) under band–band illumination, has been investigated by measuring the low-frequency noise under high geometric magnetoresistance conditions. It is shown that such noise is of a volume nature and is due to carrier number (and not mobility) fluctuations. It is shown experimentally for the first time that surface noise can be distinguished from volume noise by performing measurements under high geometric magnetoresistance conditions. © *1997 American Institute of Physics.* [S1063-7826(97)02507-6]

1. INTRODUCTION

Low-frequency $1/f^{\gamma}$ type noise in strongly doped *n*-type GaAs (electron density $n_0 > 10^{17}$ cm^{-3}) has been investigated extensively (see, for example, Refs. 1–7). Such investigations are of practical interest, because strongly doped GaAs is used for channels in modern field-effect transistors. From the physical standpoint, investigations of low-frequency noise in strongly doped semiconductors make it possible to analyze the relative contribution of the two main mechanisms of fluctuations in solids: carrier number fluctuations, which dominate in weakly doped semiconductors (see the review in Ref. 8), and mobility fluctuations, which dominate in metals.[9]

In Ref. 5, low-frequency noise in *n*-type GaAs with $n_0 \simeq 2 \times 10^{17}$ cm^{-3} was investigated in a wide temperature range (80–560 K) and under band–band illumination conditions. It was shown that at high temperatures ($T > 500$ K) band–band illumination has virtually no effect on low-frequency noise in the entire frequency range 20 Hz–20 kHz.

At low temperatures ($80 < T < 150$ K) extremely weak illumination, corresponding to $\delta\sigma/\sigma_0 < 10^{-3}$ (σ_0 — equilibrium conductivity, $\delta\sigma$ — photoconductivity), increases the noise level by one or two orders of magnitude. As the illumination intensity increases further, the noise level continues to increase at high frequencies; at low frequencies it reaches a maximum and then decreases. For sufficiently strong illumination (corresponding to the level $\delta\sigma/\sigma_0 \leqslant 0.1$) the frequency dependence of the noise at low temperatures ($T \simeq 80$ K) is virtually identical to the frequency dependence of the noise at high temperatures ($T > 500$ K).

At intermediate temperatures $T \simeq 300$ K band–band illumination suppresses noise at low frequencies and increases noise at high frequencies. Once again, under sufficiently strong illumination the frequency-dependence of the spectral noise density $S(f)$ becomes virtually the same as for $T > 500$ K.

The mechanism by which the band–band illumination influences low-frequency noise has been analyzed in detail in the review article[8] on the basis of the model proposed in Ref. 10 for $1/f$ noise in semiconductors. The model assumes that $1/f$ noise is due to population fluctuations in the levels forming the tail of the density of states near the edge of the band gap of the semiconductor. The model proposed in Ref. 10 made it possible to explain an entire series of phenomena associated with $1/f$ noise in Si, GaAs, and SiC.[8] The model explains qualitatively the effect of band–band illumination on low-frequency noise: the character of the change in the noise under illumination, as well as the nonmonotonic dependence of the noise on the illumination intensity. However, in accordance with the model in Ref. 10, under sufficiently strong illumination the spectral noise density at low frequencies should be independent of frequency, and at high frequencies it should drop inversely as the square of the frequency f. At the same time, experiments show[5] that under conditions where the initial noise is suppressed by band–band illumination a new noise mechanism appears. This new noise mechanism is characterized by the fact that its exponent $\gamma = 1$ (flicker noise). Increasing the illumination intensity further has no effect on the noise spectrum, and the noise level is essentially temperature-independent in a very wide temperature interval (80–550 K).

In our study the nature of $1/f$ noise observed in strongly doped GaAs under band–band illumination conditions was investigated by means of measurements of the low-frequency fluctuations under high geometric magnetoresistance conditions.

2. EXPERIMENTAL CONDITIONS

The idea of investigating the nature of noise by performing measurements under high geometric magnetoresistance conditions was proposed in Ref. 11 and later used in Refs. 12–14. High geometric magnetoresistance arises in a magnetic field oriented in a direction transverse to the current under conditions where there is no Hall voltage, i.e. in samples with a small ratio of length L to width d ($L/d \ll 1$)[11,14] or in samples in the form of a Corbino disk.[12]

 1063-7826/97/070728-05$10.00

It is known (see, for example, Ref. 12) that under such conditions the mobility μ in the presence of a magnetic field B is related to the mobility μ_0 at $B=0$ by the relation

$$\mu=\frac{\mu_0}{1+(\mu_0 B)^2}. \tag{1}$$

If it is assumed that the noise is due to mobility fluctuations $\delta\mu_0$, then it is easy to obtain from the expression (1) a relation between the amplitude of the mobility fluctuations $\delta\mu$ in the presence of a magnetic field and the value of $\delta\mu_0$:[11]

$$\left(\frac{\delta\mu}{\mu}\right)^2=\left[\frac{1-(\mu_0 B)^2}{(1+\mu_0 B)^2}\right]^2\left(\frac{\delta\mu_0}{\mu_0}\right)^2. \tag{2}$$

It is obvious from the expression (2) that for $\mu_0 B=1$ the mobility fluctuations μ_0 do not give rise to fluctuations of μ at all. Therefore, by using magnetic fields B corresponding to the condition $\mu_0 B\simeq 1$, the resistance fluctuations due to mobility fluctuations can be distinguished from noise caused by carrier number fluctuations. A strong decrease of the noise for $\mu_0 B\simeq 1$ attests to mobility fluctuations. The absence of a magnetic field dependence of the noise level can be explained in a natural manner on the basis of carrier number fluctuations, which do not depend on the magnetic field.

Furthermore, as noted in Ref. 11, measurements under high geometric magnetoresistance conditions make it possible to distinguish surface from volume noise. Indeed surface noise is usually described by an equivalent circuit in which the ''noisy'' surface resistance R_S is connected in parallel with an ideal (noiseless) volume resistance R_V. In this case $R_S \gg R_V$. The quantity R_S does not depend on the magnetic field. The quantity R_V changes in a transverse magnetic field in accordance with the well-known relation (see, for example, Ref. 16)

$$\frac{\Delta R_V}{R_V}=(\mu_0 B)^2. \tag{3}$$

Therefore, in a magnetic field a relatively larger fraction of the current passes through a noisy surface resistance R_S (the volume resistance R_V shunts the surface resistance to a lesser degree). It is easy to show on the basis of such an equivalent circuit that the relative spectral noise density S_U^B/U^2 in a magnetic field is related to the spectral noise density S_U/U^2 in the absence of a magnetic field by the relation

$$\frac{S_U^B}{U^2}=\frac{S_U}{U^2}[1+(\mu_0 B)^2]^2. \tag{4}$$

In the experiments we employed the epitaxial n-type GaAs samples with electron density $n_0\simeq(1-2)\times10^{17}$ cm^{-3}. The mobility μ_0 at 300 K was in the range $0.33\leqslant\mu_0\leqslant0.5$ m^2/(V·s). The maximum induction B was equal to $B=2$ T. Therefore, the maxmum expected geometric magnetoresistance $\Delta R/R$ was in the range $0.43\leqslant\Delta R/R\leqslant1.08$. In accordance with the expression (2), the maximum expected decrease in the noise in the case of mobility fluctuations would have to be a factor of 6.5 for samples with the minimum mobility. For the maximum mobility $\mu\geqslant0.5$ m^2/(V·s) total noise suppression could be expected. The maximum increase in noise due to carrier number fluctuations and with the surface noise given by the expression (4) could range from 3.1 to 6.7 dB. The accuracy of the noise measurements was equal to ±0.75 dB.

Three types of samples were investigated. Type 1 samples were identical to the samples investigated in Ref. 5. They were GaAs-based Schottky-barrier, field-effect transistors (MOSFET) with gate length $L=1$ μm and gate width $d\simeq200$ μm, i.e., the ratio $L/d=5\times10^{-3}$. The channel thickness $h_0=0.1-0.2$ μm and the electron density $n_0\simeq(1-3)\times10^{17}$ cm^{-3}.

The structures of the types 2 and 3 were commercial field-effect transistors. The type-2 structures were microwave GaAs-based Schottky-barrier, field-effect transistors manufactured by the NEC Company. The gate length $L\simeq1$ μm, the gate width $d\simeq100$ μm, and $L/d\simeq10^{-2}$. The ceramic case of the transistor was transparent to light with wavelength corresponding to a band–band transition in GaAs (the energy $h\nu\simeq1.4$ eV). In the type-3 field-effect transistors the gate length $L\simeq1-2$ μm, the gate width $d=55$ μm, and $L/d\simeq0.02-0.04$.

3. EXPERIMENTAL RESULTS AND DISCUSSION

For all experimental structures $\Delta R/R$ was measured as a function of the magnetic field B for different values of the drain–source current I_{DS}. In all cases the $\Delta R/R - B^2$ dependence was linear. The mobility μ_0 calculated from Eq. (3) depended somewhat on the value of I_{DS}. The dependence $\mu_0(I_{DS})$ was different for different samples. For very low values of I_{DS}, in the case of contacts which were not completely ohmic, the value of μ_0 was relatively low and increased with the drain–source current density. For example, for type-2 samples $\mu_0\simeq0.33$ m^2/(V·s) with a drain–source current on a 1-mm gate $i_{DS}=7.5$ mA and $\mu_0\simeq0.43$ m^2/(V·s) for $i_{DS}=34$ mA. In the case of a complete absence of barrier nonlinearity at the source and sink contacts the mobility μ_0 was maximum even at very low currents I_{DS}. As I_{DS} increased, μ_0 decreased somewhat, apparently reflecting a transition to the saturation regime even for values of I_{DS} corresponding to the apparent linear section of the curve $I_{DS}(U_{DS})$. For example, for type-1 samples $\mu_0\simeq0.4$ m^2/(V·s) for $I_{DS}=3$ mA and $\mu_0\simeq0.35$ m^2/(V·s) for $I_{DS}=25$ mA.

Curves of $\Delta R/R$ versus B^2 for all three types of samples and values of I_{DS} approximately corresponding to the maximum values of μ_0 are shown in Fig. 1. The values of μ_0 calculated from the curves using Eq. (3) are: $\mu_0\simeq0.41$ m^2/(V·s) for type-1 samples, $\mu_0\simeq0.43$ m^2/(V·s) for type-2 samples, and $\mu_0\simeq0.52$ m^2/(V·s) for type-3 samples. The value $\mu_0\simeq0.52$ m^2/(V·s) agrees well with the theoretical estimate of the Hall mobility of electrons in n-type GaAs with electron density $n_0\simeq2\times10^{17}$cm^{-3} and low compensation level.[16] The value $\mu_0\simeq0.42$ m^2/(V·s) in accordance with the estimates of Ref. 16 attests to a compensation level corresponding to the condition $(N_D-N_A)/(N_D+N_A)\simeq0.5$.

For all samples, the frequency- and temperature-dependences of the relative spectral noise density S_I/I^2 were

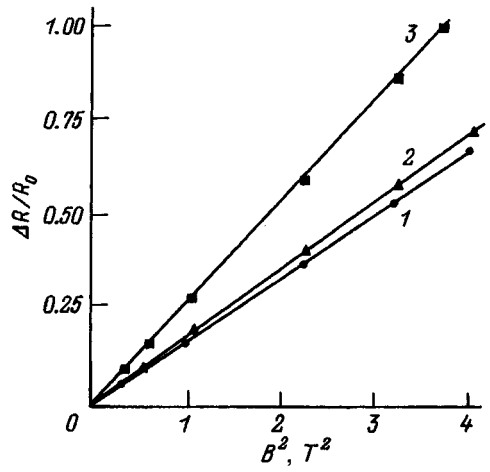

FIG. 1. Relative change in the resistance of the samples ($\Delta R/R_0$) versus the squared magnetic induction. The numbers on the curves indicate the sample type.

obtained before measurements were performed in a magnetic field.

For type-1 samples the observed dependences (Fig. 2) are in complete agreement with the results described in the bried communication.[5] At a high temperature $T=540$ K band–band illumination has no effect on the noise. In accordance with the theory in Ref. 10, this situation arises because of the fact that even in the dark the levels forming the tail of the density of states are emptied at high temperatures because of thermionic emission of electrons into the conduction band. The appearance of holes as a result of band–band illumination does not change the population of the levels in the tail.

At $T=88$ and 239 K (Figs. 2a and 2b) the dark noise has the form $S_I \sim 1/f^{\gamma}$, where $\gamma \simeq 1.5$. The nature of such a frequency $S_I(f)$ was discussed in Ref. 17. Under sufficiently strong illumination (Fig. 2a, curve 3 and Fig. 2b, curve 2) the frequency-dependences of the relative spectral density of the fluctuations are close to the form $S_I \sim 1/f$ (flicker noise). Under maximum illumination the dependences $S_I(f)$ are very close for all three temperatures.

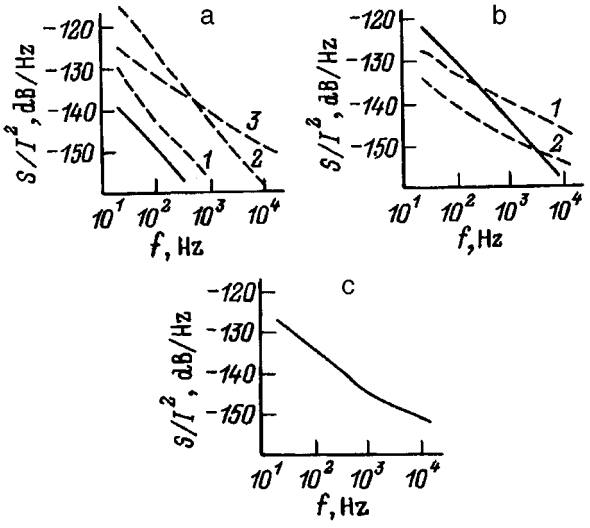

FIG. 2. Frequency dependences of the spectral noise density (S_I/I^2) for type-1 samples at three different temperatures T and under different illumination levels J/J_0. Solid curves — dark noise, dashed curves — noise under band–band illumination conditions. a: $T=88$ K; $J/J_0=5\times10^{-8}$ (*1*), 10^{-4} (*2*), 1 (*3*). b: $T=293$ K; $J/J_0=5\times10^{-3}$ (*1*) and 1 (*2*). c: $T=540$ K; $J_0=5\times10^{18}$ cm$^2\cdot$s^{-1}.

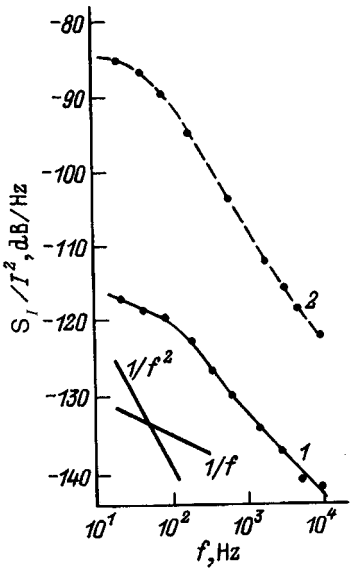

FIG. 3. Frequency dependences of the spectral noise density S_I/I^2 for type-2 samples in the dark (*1*) and under band–band illumination conditions with maximum intensity $J/J_0=1$ (*2*). $T=300$ K. Straight lines — $1/f$ and $1/f^2$.

The effect of the band–band illumination on the spectral noise density in type-2 samples is of a qualitatively different character (Fig. 3). Curve *1* in Fig. 3 follows the dependence $S_I \sim 1/f^{1.5}$ in the frequency range $f \geqslant 150$ Hz. At lower frequencies the dependence $S_I(f)$ is close to $S_I \sim 1/f$. Under illumination the noise level increases monotonically in the entire frequency range. As one can see from Fig. 3, illumination with intensity $J/J_0=1$ increases the noise level by $\sim$30 dB (by a factor of $\sim$1000) at low frequencies ($f \simeq 20$ Hz). At high frequencies ($f \simeq 10$ kHz) the increase is $\sim$20 dB. The character of the function $S_I(f)$ also changes. In the frequency range $f \gtrsim 80$ Hz $S_I \sim 1/f^2$. At lower frequencies a clear tendency to saturation is observed. Therefore, under strong illumination conditions the function $S_I(f)$ corresponds to a classical Lorentzian with characteristic value $\tau = 1/f_0 \simeq 0.012$ s. For $n_0 \simeq 2\times10^{17}$ cm^{-3} and thermal velocity of electrons in GaAs at 300 K $v_t \simeq 4.5\times10^7$ cm/s this value of τ corresponds to an electron capture cross section $\sigma \simeq (n_0 v \tau)^{-1} \simeq 2\times10^{-21}$ cm^2.

We note that a strong increase in noise ($\sim$30 dB) under illumination was observed in Ref. 18 in epitaxial *n*-type GaAs films with doping level $N_D - N_A \simeq 10^{15}$ cm^{-3}. The nature of the observed effect (surface or volume) was not discussed.

Samples exhibiting both types of behavior were found among the type-3 samples. In some samples the band–band illumination at 300 K suppressed noise at low frequencies and converted the noise spectrum of the form $1/f^{1.5}$ into a spectrum of the form $1/f$ similarly to type-1 samples. In other samples the effect of band–band illumination was to

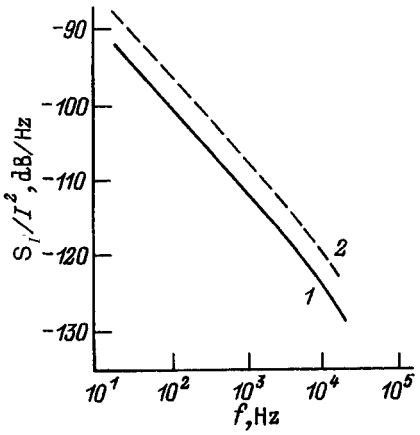

FIG. 4. Frequency dependences of the spectral noise density (S_I/I^2) for type-3 samples in the dark (*1*) and under band–band illumination conditions with maximum intensity $J/J_0=1$ (*2*). $T=300$ K.

increase the noise at all frequencies, similarly to type-2 samples. However, the increase in the noise was not so large (Fig. 4).

The relative spectral noise density in a magnetic field was measured for all samples under high geometric magnetoresistance conditions. The measurements were performed in the dark and under band–band illumination conditions.

The typical dependence for type-1 samples is shown in Fig. 5, where the experimental curve *1* is compared with curve *2* calculated from Eq. (2) for $\mu_0=0.41$ m^2/(V·s). Experiment shows that in the dark and under illumination the relative spectral noise density is independent of the magnetic induction at any frequency in the experimental range 20 Hz –20 kHz. The character of the experimental dependence of the relative noise on the magnetic induction points to carrier number fluctuations as the source of the observed low-frequency noise. On the other hand, no increase is observed in the relative spectral density, which points to a volume nature of the observed noise.

Therefore, the results show that under strong band–band illumination conditions, when the known mechanism of low-frequency noise — fluctuations of the occupancy of levels in the tail of the density of states — is found to be suppressed, the experimentally observed flicker noise is due to carrier number fluctuations in the volume of the sample. The microscopic nature of the carrier number fluctuations observed under such conditions is not clear.

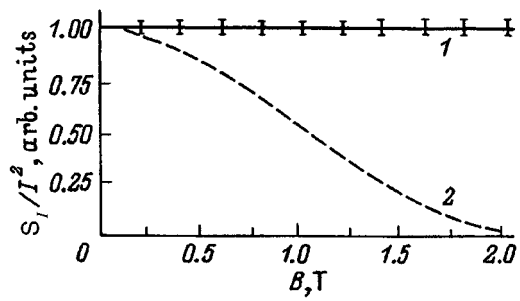

FIG. 5. Relative spectral noise density S_I/I^2 versus magnetic induction B for type-1 samples. *1* — Experimental data, *2* — calculation from Eq. (2) with $\mu_0=0.41$ m^2/(V·s).

As noted above, for type-2 samples the band–band illumination does not suppress noise. In contrast, it increases the noise in the entire experimental frequency range.

For type-2 samples in the dark a magnetic field $B=2$ T increased the relative spectral noise density by the amount $\Delta S_I \simeq 1.5$ dB at all frequencies in the experimental range. The observed increase is appreciably smaller than expected in a magnetic field in the case of a purely surface nature of the noise. It is easy to establish from Eq. (4) that for $\mu_0=0.43$ m^2/(V·s), noise in a field $B=2$ T should increase by $\Delta S_I \simeq 4.8$ dB.

The observed discrepancy can be explained either by the fact that surface and volume noise make approximately equal contributions to the dark noise or the condition $R_V \ll R_S$ does not hold in these structures.

Under band–band illumination conditions a magnetic field has no effect on relative spectral density of the noise in type-2 samples. Therefore, it must be assumed that the very strong increase in the noise under the influence of light is due to a decrease in the occupancy of the deep volume levels. It is completely obvious that the intensity of the source of band–band light available to us was too low to deplete completely the levels responsible for the observed low-frequency noise. A further increase in the band–band illumination intensity should result in noise suppression and possibly reveal the same mechanism of flicker noise which predominates in type-1 samples under strong illumination.

In type-3 samples the effect of a magnetic field on the noise varies, depending on the response of the noise to band–band illumination. In samples where noise suppression by illumination was observed (similarly to type-1 samples), a magnetic field had no effect on the relative spectral density of the noise.

In the samples where illumination increased the noise (Fig. 4), a substantial (up to 5 dB) increase of the relative spectral density of the noise in a magnetic field was observed.

Figure 6 shows the frequency dependences of the spectral noise density in the dark (solid lines) and under band illumination conditions (dashed lines) with no magnetic field (curves *1* and *2*) and in a transverse magnetic field $B=2$ T (curves *1′* and *2′*). One can see that in the dark and under illumination a magnetic field increases the noise at all frequencies in the experimental range. The noise increases by ~ 2.5 dB in the dark and by ~ 5 dB under band–band illumination conditions. For $\mu_0=0.52$ m^2/(V·s) the increase in noise expected in a magnetic field $B=2$ T in accordance with Eq. (4) should be ~ 6.3 dB. On the basis of the results shown in Fig. 6, it can be concluded that in the dark the contributions of surface and volume components to the overall noise are comparable. Under band–band illumination conditions the surface component of the noise dominates.

4. CONCLUSIONS

The investigations, performed under high geometric magnetoresistance conditions, of type $1/f$ noise arising when

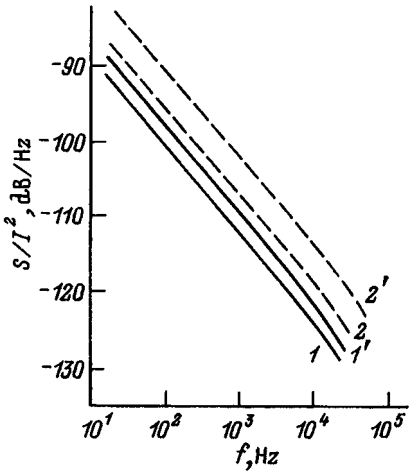

FIG. 6. Frequency dependences of the spectral noise density for type-3 samples in the dark (solid curves) and under band–band illumination conditions (dashed curves). B, T: *1*, *2* — 0; *1′*, *2′* — 2. $T=300$ K.

the ordinarily observed low-frequency noise is suppressed by band–band illumination, show that this noise is of a volume character and is due to carrier number fluctuations in the sample. The nature of these fluctuations is unclear at present.

In a number of samples an increase rather than suppression of noise is observed under band–band illumination conditions.

The very substantial (up to 30 dB) increase in the low-frequency noise in strongly doped ($n_0 \simeq 2\times 10^{17}$ cm^{-3}) n-type GaAs is the first such observation.

The noise observed under illumination conditions is volume noise. The nature of the observed effect is apparently similar to that of the increase in noise under illumination conditions, observed previously in Ref. 18 for weakly doped ($n_0 \simeq 10^{15}$ cm^{-3}) n-type GaAs.

In some samples band–band illumination gives rise to a relatively small (~ 5 dB) increase in the noise, the same at all frequencies in the experimental range 20 Hz–20 kHz. In these samples the noise observed under illumination is of a purely surface nature.

We note that, as is clear from the results presented here, measurements in a magnetic field under band–band illumination conditions make it possible to distinguish surface from volume noise quite reliably. It is important that this method is nondestructive and that it can be used for a wide class of semiconductor devices, since for most modern devices the condition $L/d \ll 1$ holds very well.

We thank I. A. Khrebtov for assisting in this work.

This work is supported by the Russian Fund for Fundamental Research under Grant 96-02-18563.

[1] J. Graffeuil and J. Caminade, Electron. Lett. **10**, 266 (1974).
[2] C. H. Suh, A. van der Ziel, and R. P. Jindal, Solid–State Electron. **24**, 217 (1981).
[3] J. R. Hellum and L. M. Rucker, Solid–State Electron. **28**, 549 (1985).
[4] M. Pouysegur, J. Graffeuil, and J. L. Cazoux, IEEE Trans. Electron. Dev. **34**, 2178 (1987).
[5] M. E. Levinshteĭn and S. L. Rumyantsev, Pis'ma Zh. Tekh. Fiz. **19**, 55 (1993) [Tech.Phys. Lett. **19**, 91 (1993)].
[6] M. Takano, IEEE Trans. Electron. Dev. **40**, 2060 (1993).
[7] M. Chertouk and A. Chovet, IEEE Trans. Electron. Dev. **43**, 123 (1996).
[8] N. V. D'yakonova, M. E. Levinshteĭn, and S. L. Rumyanstev, Fiz. Tekh. Poluprovodn. **25**, 2065 (1991) [Sov. Phys. Semicond. **25**, 1241 (1991)].
[9] Sh. Kogan, *Electronics noise and Fluctations in Solids*, Cambridge Univ. Press, N. Y., 1996, p. 354.
[10] N. V. D'yakonova and M. E. Levinshteĭn, Fiz. Tekh. Poluprovodn. **23**, 283 (1989) [Sov. Phys. Semicond. **23**, 175 (1989)].
[11] M. E. Levinshteĭn and S. L. Rumyanstev, Fiz. Tekh. Poluprovodn. **17**, 1830 (1983) [Sov. Phys. Semicond. **17**, 1167 (1983)].
[12] M. H. Song and H. S. Min, J. Appl. Phys. **58**, 4221 (1985).
[13] T. G. M. Kleinpenning and P. P. J. Huinen, in *Abstracts of 9th Int. Conf. on Noise in Phys. Systems*, Montreal, Canada, 1987, p. 136.
[14] M. H. Song, A. N. Burdas, A. van der Ziel, and A. D. van Rheenen, J. Appl. Phys. **64**, 727 (1988).
[15] T. R. Jervis and E. F. Jonson, Solid–State Electron. **13**, 181 (1970).
[16] D. L. Rode, in *Semiconductors and Semimetals*, edited by R. K. Willardson and A. C. Beer, Academic Press, N. Y., 1975.
[17] N. V. Dyakonova, M. E. Levinshtein, J. W. Palmour, and S. L. Rumyantsev, Semicond. Sci. Technol. **10**, 1126 (1995).
[18] J. Copeland, IEEE Trans. Electron. Dev. **18**, 50 (1971).

Translated by M. E. Alferieff

Longitudinal photoeffect in $In_{0.53}Ga_{0.47}As$ $p-n$ junctions

S. V. Slobodchikov, Kh. M. Salikhov, and E. V. Russu

A. F. Ioffe Physicotechnical Institute, Russian Academy of Sciences, 194021 St. Petersburg, Russia
(Submitted November 22, 1995; accepted for publication December 27, 1996)
Fiz. Tekh. Poluprovodn. **31**, 864–865 (July 1997)

A longitudinal photoeffect in $In_{0.53}Ga_{0.47}As$ $p-n$ junctions was investigated: the dependence of the longitudinal photoemf $V_{ph\,1}$ on the coordinates of the light spot, the temperature, and the magnetic field. The dependences on the coordinates of the light spot were found to be linear; the theoretical values of $V_{ph\,1}$ agree with the experimental values. The temperature variation of $V_{ph\,1}$ in the interval 100–300 K is explained by the variation of the current-carrier mobility as a result of thermal scattering by the lattice. In a magnetic field, $V_{ph\,1}$is observed to increase as a result of the photomagnetic effect. © *1997 American Institute of Physics.* [S1063-7826(97)02607-0]

For a number of years a great deal of attention has been directed to investigations of the photoelectric properties of different types of diode structures ($p-n$ junctions, $p-i-n$ diodes, heterojunctions, and others) based on the solid solutions InGaAs. This interest is due mainly to the production of highly sensitive, fast photodetectors operating in the near-infrared (IR) region of the spectrum $\lambda = 1.0-1.7$ μm. The main, potentially important, application of these devices is in fiber-optic communication systems. A further expansion of the functional possibilities of diode structures was achieved by experimental investigations of these devices as IR radiation and gas (hydrogen) detectors.[1,2]

In this paper we report some results of an experimental study of the longitudinal photoeffect in $In_{0.53}Ga_{0.47}As$ $p-n$ junctions.

The samples were produced by the gas-phase epitaxy method. A 2-μ-m thick layer of n-$In_{0.53}Ga_{0.47}As$ with electron density $n = 10^{15}$ cm^{-3} was grown on a n^+-InP substrate; a 1-μm thick p-type layer with hole density $p = 10^{17}$ cm^{-3} was produced by doping with Zn. A continuous ohmic contact on the substrate side was produced with the alloy Ag + Ge + In. Local 1-μm diam ohmic contacts were produced on the p-side by sputtering the alloy Ag + 10% Zn through a mask. Local illumination from the p-side was performed with monochromatic light from a SPM-2 monochromator with a graphite radiator through a mask with a 0.4-mm-wide light strip. The longitudinal photoemf $V_{ph\,1}$ was measured: the inversion characteristic, the temperature dependence, and the change in a magnetic field.

The inversion characteristics of the photoemf of a diode structure (variation of the photoemf as a function of the coordinate x of the light strip occurring with a change in sign) under illumination with monochromatic light with $\lambda = 1.55$ and 0.67 μm are shown in Fig. 1. Both branches of the characteristics are nearly linear, and the absolute magnitude of the longitudinal photoemf $V_{ph\,1}$ under illumination with light with a wavelength near the maximum of the spectral sensitivity ($\lambda = 1.55$ μm) is approximately three orders of magnitude greater than that in the case of short-wavelength irradiation. Estimates show that this difference is due not only to the large difference in the incident radiation flux density in both cases, but also, in part, to recombination losses of generated electrons and holes at the surface and in the volume. The temperature dependence of the longitudinal photoemf in the interval $T = 100-300$ K with an arbitrary position of the light strip is shown in Fig. 2. In a large part of the temperature interval the photoemf decreases with increasing temperature, decreasing by almost a factor of 3 at $T = 300$ K.

To analyze the data obtained by us, we shall employ the results of a theoretical calculation of the longitudinal photoemf, performed in Ref. 3. From this work it follows that

$$V_{ph\,1} = \varphi_p(0) - \varphi_p(l) = \frac{2t\Phi\rho_p \sin h(\alpha l/2)\sin h\alpha(l/2 - x_j)}{w_p \alpha \sin h\alpha l + 2t\alpha \cos h\alpha(l - x_j)\cos h\alpha x_j}, \quad (1)$$

where $2t$ is the width of the light strip, Φ is the incident radiation flux density, $\alpha = \sqrt{g(\rho_p/w_p + \rho_n/w_n)}$, $\rho_{p(n)}$ is the resistivity of the $p(n)$ layer, $w_{p(n)}$ is the effective thickness of

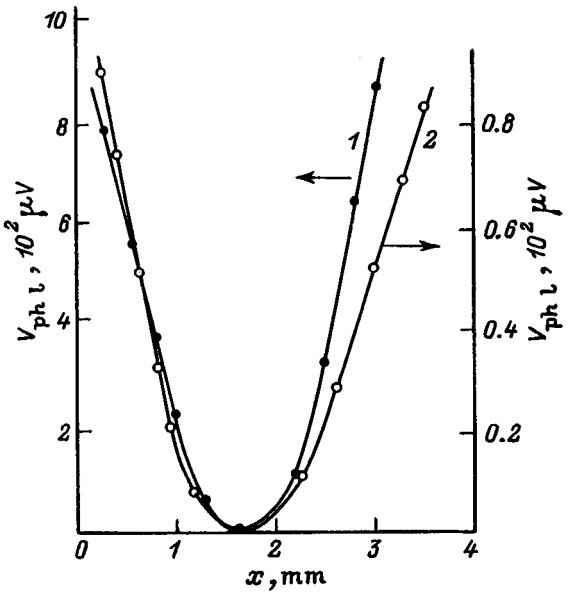

FIG. 1. Inversion characteristics of the longitudinal photoemf in $In_{0.53}Ga_{0.47}As$ $p-n$ junctions under illumination by light with $\lambda = 1.55$ (*1*) and 0.67 (*2*) μm.

 1063-7826/97/070733-02$10.00

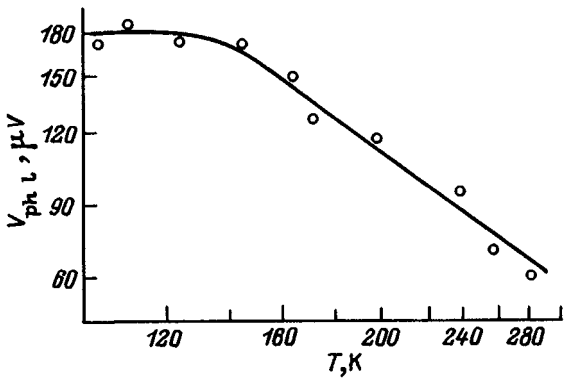

FIG. 2. Temperature dependence of the longitudinal photoemf of $In_{0.53}Ga_{0.47}As$ p–n structures.

the $p(n)$ layer, $g=j_s/nkT$ is the conductivity of the diode, l is the length of the sample, and x is the coordinate of the light strip. The values of $V_{\text{ph}\,1}$ were calculated according to Eq. (1) with electron and hole mobilities $\mu_n \simeq 10^4$ cm^2/(V·s) and $\mu_p \simeq 10^2$ cm^2/(V·s), respectively, $j_s = 6\times 10^{-6}$ A/cm^2 (from the current-voltage characteristic), and $\Phi = 10^{14}$ cm$^2\cdot$s^{-1} corresponds to the experimental value. The inversion characteristic should be linear (for $2t \ll l$) in the limit

$$\lim_{\substack{\text{ph}\,1 \\ \alpha l \to 0}} V\ (x) = \frac{2tlq\Phi\rho_p}{w_p}\left(\frac{1}{2}-\frac{x}{2}\right). \tag{2}$$

In our case $\alpha l = 0.6$. Good agreement was found to exist between the values of $V_{\text{ph}\,1}$ calculated from Eqs. (1) and (2) and the linear characteristic. In general, as follows from Eq. (1), the temperature dependence of $V_{\text{ph}\,1}$ should be determined by the temperature variation of the saturation current j_s and the resistivity ρ_p. Since the relation (2) is applicable in our diodes, $V_{\text{ph}\,1}$ should vary with temperature mainly in accordance with $\rho_p = f(T)$.

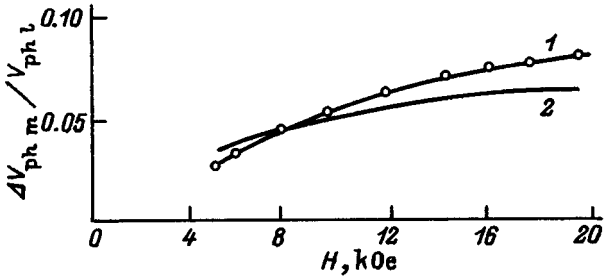

FIG. 3. Variation of the longitudinal photoemf of a $In_{0.53}Ga_{0.47}As$ p–n structure in a magnetic field: *1* — Experimental curve, *2* —computed curve.

The temperature variation of $V_{\text{ph}\,1}$ (Fig. 2) can be represented as $V_{\text{ph}\,1} \sim T^{-\beta}$, where $\beta = 1.4$. Considering the relatively high equilibrium hole density in the p-type layer, its variation in the experimental temperature interval should be small. The temperature dependence of $V_{\text{ph}\,1}$ can then be attributed completely to the temperature variation of the hole mobility, $\mu_p \sim T^{-\beta}$, i.e., to hole scattering by thermal phonons. The weak variation of $V_{\text{ph}\,1}$ observed with decreasing temperature at $T < 140$ K is evidently due to the increasing contribution of scattering by ionized impurities, for which, as is well known, $\mu_p \sim T^{3/2}$. The longitudinal photoemf increases when the diode structure is placed in a magnetic field H directed parallel to the illuminated surface of the p-layer (Fig. 3)

$$V_{\text{ph}\,1}(H) = V_{\text{ph}\,1}(0) + \Delta V_{\text{ph}\,m}. \tag{3}$$

For the maximum magnetic field ($H = 20$ kOe) $\Delta V_{\text{ph}\,m}$ is 7–8%. The curve $\Delta V_{\text{ph}\,m} = f(H)$ in Fig. 3 resembles the corresponding curves of the photomagnetic emf versus the magnetic field in p- or n-type semiconductor crystals.[4] The dependence, expressed analytically by the relation

$$V_{\text{ph}\,m} = A\frac{H/c}{\sqrt{1+(\mu_n H/c)^2}}, \tag{4}$$

corresponds to our experimental curve $\Delta V_{\text{ph}\,m} = f(H)$ (Fig. 3, curve *2*). Equation (4) is valid for a rapid, low-surface recombination rate. The relatively small, experimentally observed, increment $\Delta V_{\text{ph}\,m}$ is largely due to the fact that the generation depth of nonequilibrium current carriers with $\lambda = 1.55$ μm is comparable to the thickness of the p-layer and the gradient of the diffusion current is small. It is obvious that a diode structure can be technologically optimized so as to give the maximum absolute values of the longitudinal photoemf, including those with use of a magnetic field. It will be of practical interest as a longitudinal photocell.

[1] S. V. Slobodchikov, G. G. Kovalevskaya, M. M. Meredov, A. V. Pentsov, E. V. Russu, and Kh. M. Salikhov, Pis'ma Zh. Tekh. Fiz. **17**(5), 1 (1991) [Sov. Tech. Phys. Lett. **5**, 315 (1991)].
[2] S. V. Slobodchikov, E. V. Russu, Kh. M. Salikhov, M. M. Meredov, and A. I. Yazlyeva, Pis'ma Zh. Tekh. Fiz. **21**, 50 (1995) [Tech. Phys. Lett. **21**, 298 (1995)].
[3] U. Nin, T. Matsuda, H. Sadamatzu, and M. Takai, Japan. J. Appl. Phys. **15**, 601 (1976).
[4] Yu. V. Ravich, *Photomagnetic Effect in Semiconductors and Its Applications* [in Russian], Sov. radio, Moscow, Chap. 1, § 3.

Translated by M. E. Alferieff

Deep centers and negative temperature coefficient of the breakdown voltage of SiC $p-n$ structures

A. A. Lebedev

A. F. Ioffe Physicotechnical Institute, Russian Academy of Sciences, 194021 St. Petersburg, Russia

S. Ortoland, C. Raynaud, M. L. Locatelli, D. Planson, and J. P. Chante

CEGELY-INSA–Bat. 401–20, av. A. Einstein–F., 69621 Villerbanne Cedex, France
(Submitted November 28, 1996; accepted for publication December 25, 1996)
Fiz. Tekh. Poluprovodn. **31**, 866–868 (July 1997)

The temperature coefficient of the breakdown voltage of 6H-SiC p–n structures has been investigated. It is shown that the temperature dependence of the breakdown voltage can be explained by charge exchange on deep acceptor levels in the space charge layer. The computational results are in good agreement with the experimental data obtained for boron-doped 6H-SiC p–n structures. © *1997 American Institute of Physics.* [S1063-7826(97)02707-5]

1. INTRODUCTION

It is well known that in 6H-SiC p–n structures, in which the electric field is parallel to the c crystalline axis, the temperature coefficient β_t of the breakdown voltage is, as a rule, negative.[1] This was attributed in a number of studies to the crystalline structure of the hexagonal polytypes of SiC and the presence of a natural superlattice.[2,3] In other studies[4,5] it was assumed that the negative value of β_t could be due to charge exchange on deep centers, as was shown for silicon.[6,7] In our study an attempt was made to attribute the observed temperature dependence of β_t in 6H-SiC p–n structures to deep centers.

2. SAMPLES

We investigated 6H-SiC p–n structures obtained by sublimation epitaxy in an open system.[8] Boron was diffused before the formation of the mesa structures. Diffusion treatment made it possible to solve two technical problems:[9] 1) increase in the breakdown voltage of relatively strongly doped SiC layers as a result of compensation of the base region and 2) decrease of the probability of surface breakdown as a result of the production of weakly doped regions at the periphery of the mesa structures.

The experimental structures possessed a negative temperature coefficient of the breakdown voltage. The room-temperature value of the coefficient was $\sim 2\times 10^{-3}$ K^{-1}. The absolute magnitude of the temperature coefficient of the breakdown voltage also depended on the temperature and decreased approximately by an order of magnitude as the structures were heated to 600 K (Fig. 1).

3. COMPUTATIONAL MODEL

In analyzing the experimental data, following Refs. 4–7 we took into account the influence of deep centers. As shown previously, boron diffusion results in the formation of two acceptor levels in SiC — a shallow boron level and a D-center level. Our model is based on taking into account charge exchange on deep acceptor levels (D centers) by the prebreakdown current in weakly doped p-type layer near the metallurgical boundary of the p–n junction.

Two assumptions were made: 1) A region of avalanche multiplication lies in the weakly doped p-type region near the metallurgical boundary of the p–n junction and 2) the density of deep acceptors in this region is comparable to the density of shallow acceptors. The appearance of such a region could be due to overcompensation of the n-type material because of diffusion of the acceptor impurities (for example, boron). The existence of such a region in the experimental samples was previously shown experimentally in Ref. 9.

The breakdown voltage of an abrupt p–n junction is given by the standard expression

$$U_{\rm br}=\varepsilon_a E_{\rm cr}^2/2qN_i, \tag{1}$$

where $E_{\rm cr}$ is the critical electric field strength, N_i is the impurity density in the base, q is the electron charge, and $\varepsilon_a=\varepsilon_0\varepsilon_s$; here ε_0 is the dielectric constant and ε_s is the relative dielectric constant of the semiconductor.

Let us rewrite the expression (1), taking into account the presence of deep acceptors in a weakly doped p-type base:

$$U_{\rm br}=\varepsilon_a E_{\rm cr}^2/2q(N_s+KM)=U_{\rm br\,0}/(1+KM/N_s), \tag{2}$$

where N_s is the density of shallow acceptors, $K=(M-m)/M$ is the degree of filling of the deep acceptors by electrons, M is the total density of deep acceptors, m is the density of deep acceptors filled with holes, and $U_{\rm br0}$ is the breakdown voltage of the p–n junction in the absence of deep acceptors.

When $U\ll U_{\rm br}$, there is virtually no current flowing through the p–n junction and all deep acceptors in the p-type material are filled with electrons ($K=1$).

When $U\approx U_{\rm br}$, avalanche multiplication starts in the space charge region and the holes which are formed are trapped by deep acceptors. Since the acceptors that trap the holes are neutral, the quantity K decreases and, correspondingly, the electric field decreases. This increases the observed value of $U_{\rm br}$. It should be noted that the degree of filling of

 1063-7826/97/070735-03$10.00

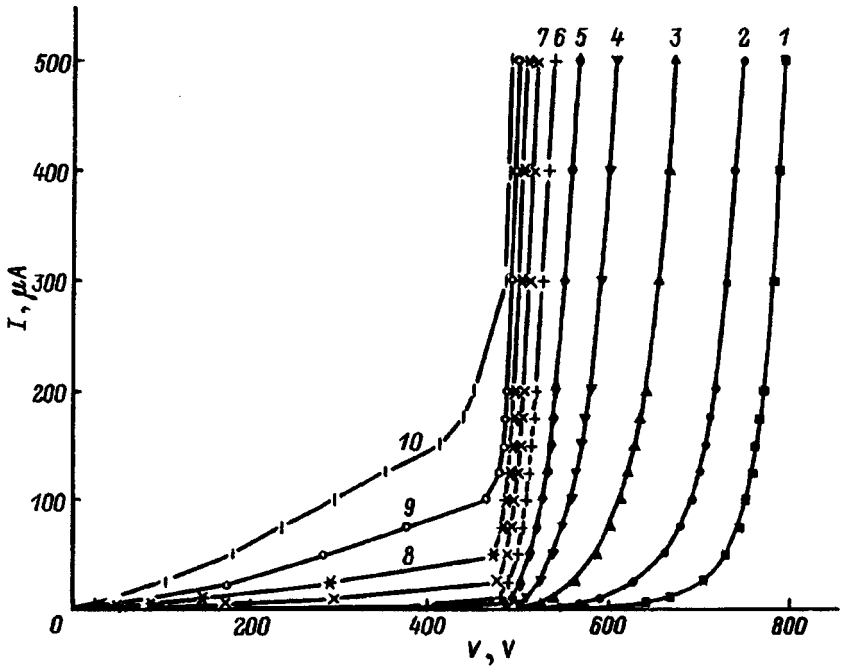

FIG. 1. Temperature dependence of the reverse current-voltage characteristics of p–n structures. T, K: *1* — 298, *2* — 323, *3* — 348, *4* — 373, *5* — 398, *6* — 423, *7* — 448, *8* — 473. *9* — 498, *10* — 523.

the levels (at constant hole density) is temperature-dependent and decreases with heating. For this reason, $U_{\rm br}$ decreases with temperature; i.e., we have a negative temperature coefficient of the breakdown voltage.

On the basis of the Shockley–Read statistics, the rate of charge exchange on deep acceptors can be written in our case as

$$dm/dt=(M-m)\Delta p\,\alpha_p-m\,\alpha_n\Delta n-\alpha_p\beta_i m, \tag{3}$$

where $\Delta n=\Delta p$ is the carrier density in the space charge layer; $\alpha_{n(p)}=\sigma_{n(p)}\nu_t$; $\sigma_{n(p)}$ is the electron (hole) trapping cross section of a center; ν_t is the thermal velocity of the carriers; N_ν is the density of states in the valence band; E_i is the ionization energy of the level; k is Boltzmann's constant; and, T is the absolute temperature.

For the equilibrium case ($dm/dt=0$), since $\alpha_p \gg \alpha_n$, we obtain from Eq. (3) the following expression for K:

$$K=\beta_i(\Delta p+\beta_i)^{-1}. \tag{4}$$

Now, we obtain from Eqs. (4) and (2) the expression for $U_{\rm br}$

$$U_{\rm br}=U_{\rm br0}[1+M\beta_i/N_s(\Delta p+\beta_i)]. \tag{5}$$

Let us now analyze the expression (5) for the region of high and low temperatures.

If $T\to 0$, then $\beta_i\to 0$ and $U_{\rm br}\approx U_{\rm br0}$. If $T\to\infty$, $\beta_i\to 1$ and since $N_\nu \gg \Delta p$, we obtain $U_{\rm br}/U_{\rm br0}-1=M/N_s$.

4. DISCUSSION

In summary, for the p–n structures investigated by us $U_{\rm br0}$ and M/N_s (Fig. 1) were found to $U_{\rm br0}=800$ V and $M/N_s=0.65$. Taking into account these values and the published data for N_ν and the parameters of a D center ($E_\nu+0.58$ eV; $\sigma_n=10^{-20}$ cm^2; $\sigma_p=3\times10^{-16}$ cm^{-2}), we calculated the temperature dependence of $F=\{U_{\rm br0}/U_{\rm br}-1\}$.

The computed and experimental values of F are shown in Fig. 2. As one can see from the figure, the best agreement between calculations and experiment was obtained for values of Δp of the order of 10^{11}–10^{12} cm^{-3}. However, the value of Δp determined from the prebreakdown current as $\Delta p=J/\nu_s q$ (where J is the density of the current flowing through the p–n junction, and ν_s is the saturation velocity), was equal to 10^{10}–10^{11} cm^{-3}. This discrepancy can be explained, from our point of view, by taking into account the fact that breakdown in SiC ordinarily occurs in local regions (microplasma breakdown), whose area is an order of magnitude smaller than the total area of the p–n junction. However, in calculating the density of the current through the p–n junction we employ the value of the entire area of the structure. In other words, the current density is substantially higher and the value of Δp is high in regions where microplasma breakdown occurs, as required by the proposed model.

5. CONCLUSIONS

In summary, the negative value of the temperature coefficient of the breakdown voltage could be attributed to the charge exchange at D centers which form the deepest levels in boron-doped SiC. The calculations of the temperature dependence of β_t performed on the basis of this assumption and the parameters of a D center are in good agreement with experiment.

Since boron diffusion is often used to shield the periphery of SiC-based mesa structures from surface breakdown and since boron (D center) is itself a characteristic background impurity in SiC obtained by different technologies,[10] from our standpoint the question of the sign of β_t can be finally answered only by taking into account or by eliminating the influence of charge exchange at the D centers on the breakdown voltage of SiC p–n structures.

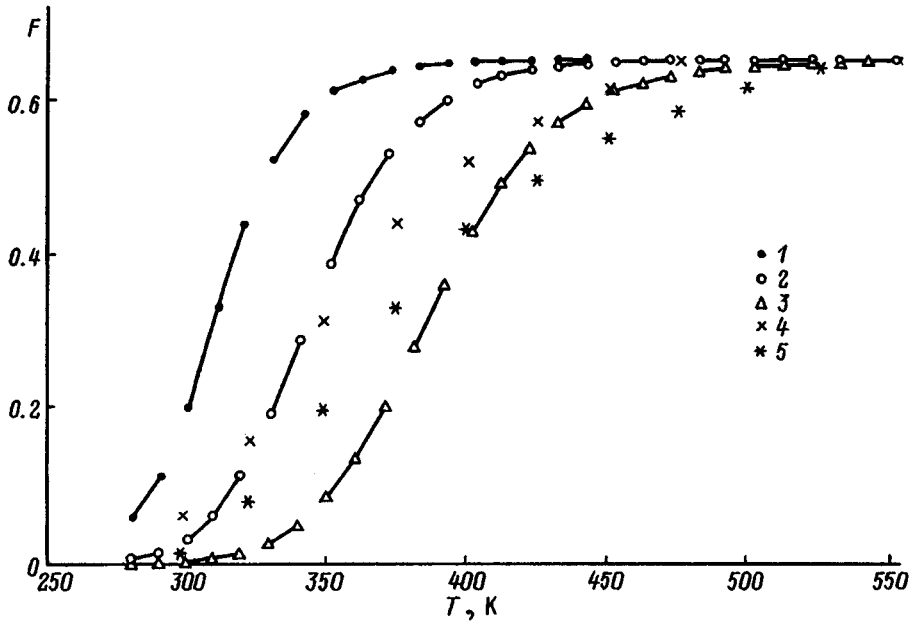

FIG. 2. Temperature dependence of the computed (*1–3*) and experimental (*4–5*) values of F. The computed parameter Δp equals, in cm^{-3}: *1* — 10^{10}, *2* — 10^{11}, *3* — 10^{12}. The experimental values of U_{br} correspond to prebreakdown currents of 100 (*4*) and 500 (*5*) mA.

This work was supported by Arizona University (USA) and the Research Center of Schneider Electric S.A. (France).

[1] A. O. Konstantinov, D. P. Litvin, and V. I. Sankin, Pis'ma Zh. Tekh. Fiz. **7**, 1335 (1981) [Sov. Tech. Phys. Lett. **7**, 572 (1981)].
[2] Yu. A. Vodakov, A. O. Konstantinov, D. P. Litvin, and V. I. Sankin, Pis'ma Zh. Tekh. Fiz. **7**, 705 (1981) [Sov. Tech. Phys. Lett. **7**, 650 (1981)].
[3] A. P. Dmitriev, A. O. Konstantinov, and D. P. Litvin, Fiz. Tekh. Poluprovodn. **17**, 1093 (1983) [Sov. Phys. Semicond. **17**, 686 (1983)].
[4] M. M. Anikin, S. N. Vaĭnshteĭn, M. E. Levinshteĭin, A. M. Strel'chuk, and A. L. Syrkin, Fiz. Tekh. Poluprovodn. **22**, 545 (1988) [Sov. Phys. Semicond. **22**, 390 (1988)].
[5] M. M. Anikin, M. E. Levinshteĭn, I. V. Popov, V. P. Rastegaev, A. M. Strel'chuk, and A. L. Syrkin, Fiz. Tekh. Poluprovodn. **22**, 1574 (1988) [Sov. Phys. Semicond. **22**, 995 (1988)].
[6] A. S. Kyuregyan and P. N. Shlygin, Fiz. Tekh. Poluprovodn. **23**, 1164 (1989) [Sov. Phys. Semicond. **23**, 729 (1989)].
[7] E. V. Astrova, V. M. Volle, V. B. Voronkov, V. A. Kozlov, and A. A. Lebedev, Fiz. Tekh. Poluprovodn. **20**, 2122 (1986) [Sov. Phys. Semicond. **20**, 1308 (1986)].
[8] M. M. Anikin, A. A. Lebedev, S. N. Pyatko, A. M. Strelchuk, and A. L. Syrkin, Mater. Sci. Eng. **11**, 113 (1992).
[9] A. A. Lebedev, A. N. Andreev, A. A. Mal'tsev, M. G. Rastegaeva, N. S. Savkina, and V. E. Chelnokov, Fiz. Tekh. Poluprovodn. **29**, 1635 (1995) [Semiconductors **29**, 850 (1995)].
[10] M. S. Mazzola, S. E. Saddow, P. G. Neudeck, V. K. Lakdawala, and S. We, Appl. Phys. Lett. **64**, 2730 (1994).

Translated by M. E. Alferieff

Photoluminescence of erbium in amorphous hydrogenated phosphorus-doped silicon

E. I. Terukov and A. N. Kuznetsov

A. F. Ioffe Physicotechnical Institute, Russian Academy of Sciences, 194021 St. Petersburg, Russia

E. O. Parshin

Institute of Microelectronics, Russian Academy of Sciences, 150007 Yaroslavl', Russia

G. Weiser and H. Kuehne

Philips-Universitat Marburg, D-35032 Marburg, Germany

(Submitted December 5, 1996; accepted for publication December 25, 1996)
Fiz. Tekh. Poluprovodn. **31**, 869–871 (July 1997)

The photoluminescence of erbium ions in phosphorus-doped *a*-Si:H films has been investigated. The observed increase in the Er photoluminescence with increasing defect density in the samples and the correlation of the temperature variation of the Er photoluminescence and defect-associated photoluminescence intensities are explained on the basis of a model of excitation of Er ions as a result of Auger recombination with defect participation. © *1997 American Institute of Physics.* [S1063-7826(97)02807-X]

Increased attention has been devoted in recent years to the photo- and electroluminescence of rare-earth ions (REIs) in semiconductor materials because of the possibility of electronic pumping of REIs.[1] Erbium-doped silicon is of greatest interest in connection with the potential production of radiators operating at a wavelength of 1.54 μm, which correspond to the absorption minimum of an optical fiber. The drawback of erbium-doped crystalline silicon is the strong temperature quenching of the luminescence due to erbium excitation in this material. Erbium ions are excited during Auger recombination of excitons bound on shallow donor levels with activation energy in the range[2,3] 100–200 meV.

We recently observed efficient room-temperature luminescence of erbium ions in amorphous hydrogenated silicon prepared by magneton-assisted silane decomposition (MASD).[4,5] We explain the efficient erbium luminescence in this material by a different mechanism of excitation, specifically, trapping of matrix electrons in the states of defects at the center of the band gap of *a*-Si:H with energy transferred into the *f*-shell of the erbium ions by the Coulomb interaction (model of Auger recombination with defect participation[6]).

In our study we investigated the photoluminescence of erbium ions in phosphorus-doped *a*-Si:H samples. The introduction of phosphorus changes the initial situation in the *a*-Si:H samples, specifically, it increases the defect density and shifts the Fermi level. The effect of these factors on the erbium photoluminescence is discussed on the basis of a previously proposed model.

Phosphorus-doped *a*-Si:H films were deposited on quartz substrates by decomposition of SiH_4 and PH_3 in a glow-discharge plasma with the following process parameters: substrate temperature $T_s = 250$ °C, working pressure in the chamber $p = 0.1$ mbar, and specific discharge power $P = 50$ mW/cm^2. The experimental samples were 0.1 μm thick. Samples prepared with phosphine PH_3 concentration of 1

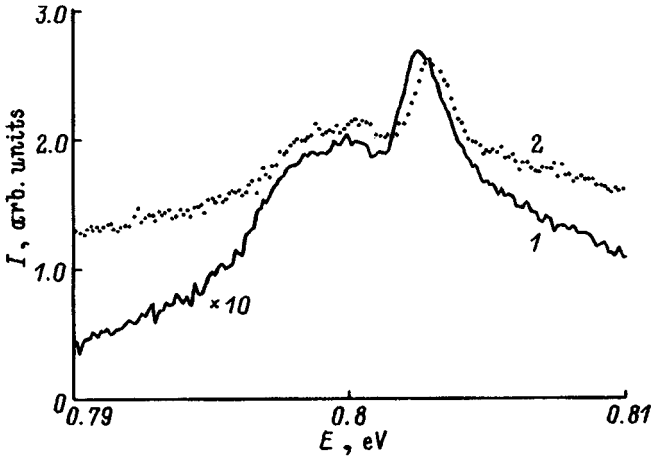

FIG. 1. Room-temperature photoluminescence spectra of Er ions for *a*-Si:H samples with different phosphorus concentrations. Phosphine concentration in the gas phase, ppm: *1* — 1, *2* — 100.

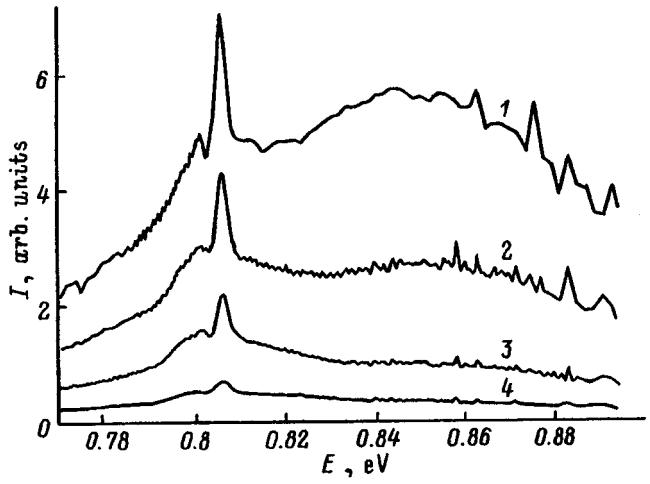

FIG. 2. Photoluminescence spectra of *a*-Si:H⟨Er⟩ samples obtained with a phosphine concentration of 100 ppm in the gas phase. Temperature *T*, K: *1* — 77, *2* — 130, *3* — 200, *4* — 295.

 1063-7826/97/070738-02$10.00

and 100 ppm in the gas phase were investigated. According to electron spin resonance (ESR) data and data from electrical measurements, the Fermi level and the defect density were equal to 0.47 eV and 6×10^{16} cm^{-3} for the first sample and 0.26 eV and 3×10^{17} cm^{-3} for the second sample, respectively. Erbium was introduced by ion implantation with ion energy of 1.2 MeV and a dose of 10^{14} cm^{-2}. The photoluminescence spectra were measured in the temperature range from 77 to 300 K with excitation by argon laser radiation with wavelength $\lambda = 544$ nm. The excitation power was equal to 50 mW in all cases. The photoluminescence was detected with a germanium detector, cooled to liquid-nitrogen temperature with use of a SPEX-1403 double monochromator.

The investigations showed that after implantation the samples exhibited no erbium photoluminescence, consistent with the data of Ref. 7. Photoluminescence appears after the samples are vacuum annealed at 350°C for 2 h.

Figure 1 shows the room-temperature photoluminescence spectra (I) of erbium for two a-Si:H samples with different phosphorus densities. It is interesting that as the phosphorus density in the initial film increases, a small shift of the position of the maximum of photoluminescence of erbium occurs in the direction of higher energies (E). In our opinion, this shift is due to a change in the local environment of the erbium ion. An increase is also observed in the intensity of the photoluminescence of erbium (approximately by an order of magnitude) with increasing phosphorus concentration in the samples.

Figure 2 shows the photoluminescence spectra for a-Si:H⟨Er⟩ samples obtained in a wide spectral range at different temperatures and a phosphine concentration of 100 ppm. These spectra exhibit, together with Er photoluminescence, a clear photoluminescence band near 0.85 eV, which is associated with defects. As the temperature increases, the intensity of the Er photoluminescence decreases and the background of the defect-induced band, where Er photoluminescence is observed, also decreases.

The temperature dependences of the intensities of the characteristic photoluminescence in a-Si:H, the Er photoluminescence, and the photoluminescence due to defects are shown in Fig. 3. It is interesting to note that there is a correlation in the temperature behavior of the photoluminescence due to defects and the Er photoluminescence; this correlation in our view attests to excitation of erbium ions via defects.

Our investigations of the photoluminescence of a-Si:H ⟨Er⟩ samples prepared by the MASD method showed that the pumping of Er photoluminescence occurs as a result of an Auger process. According to these ideas, an electron from the conduction band is trapped by a defect in the D^0 state and a D^- state is produced. As a result of the Coulomb interaction, energy is transferred into the system of f electrons of erbium, where the transition $^4I_{15/2}\rightarrow {}^4I_{13/2}$ occurs.

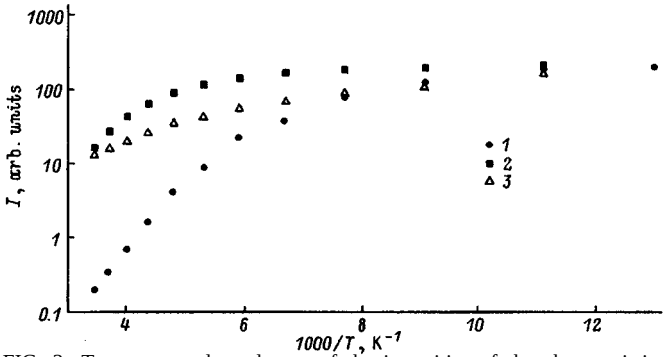

FIG. 3. Temperature dependences of the intensities of the characteristic photoluminescence (*1*), Er photoluminescence (*2*), and defect-induced photoluminescence (*3*) in a phosphorus-doped a-Si:H⟨Er⟩ sample. The phosphine concentration in the gas phase equals 100 ppm.

This is an efficient excitation process because the energies of these electronic transitions are approximately equal.

It is easy to explain on the basis of these ideas the experimental results for Er photoluminescence in phosphorus-doped a-Si:H films. The excitation of an optically active Er atom is possible only if a defect is located next to it. Increasing the density of phosphorus atoms without changing the Er atom density increases the defect density and, hence, the Er photoluminescence because of the higher probability of Auger excitation of the f-electrons in the Er atoms. On the other hand, as the temperature increases, the probability of thermal activation of an electron into the band followed by nonradiative recombination via a defect increases. The experimentally observed correlation between the temperature dependences of the Er and defect-induced photoluminescence (see Fig. 3) confirms this assumption and is consistent with the model of excitation of Er atoms as a result of Auger recombination with participation of defects.

We thank the Ministry of Science of the Russian Federation (Project V.O. UNS), the Russian Fund for Fundamental Research (Grant 9502-04163-a, Grant 96-02-17901-a), and Volkswagen Stiftung (Project No. 1/71 646) for financial support.

[1] G. S. Pomrenke *et al.*, [Eds.], *Rare Earth Doped Semiconductors*, Mater. Res. Soc. Symp. Proc., 1993, vol. 301.
[2] S. Coffa, G. Franzo, F. Priolo, A. Polman, and R. Serna, Phys. Rev. B **49**, 16 313 (1994).
[3] B. Zheng, J. Michel, F. Y. G. Ren, L. C. Kimerling, D. C. Jacobson, and J. M. Poate, Appl. Phys. Lett. **64**, 2842 (1994).
[4] M. S. Bresler, O. B. Gusev, V. Kh. Kudoyarova, A. N. Kuznetsov, P. E. Pak, E. I. Terukov, L. N. Yassievich, B. P. Zakharchenya, W. Fuhs, and A. Sturm, Appl. Phys. Lett. **67**, 3599 (1995).
[5] V. Marakhonov, N. Rogachev, J. Ishkalov, J. Marakhonov, E. Terukov, and V. Chelnokov, J. Non-Cryst. Sol. **137/138**, 817 (1991).
[6] M. S. Bresler, O. B. Gusev, B. P. Zakharchenya, V. Kh. Kudoyarova, A. N. Kuznestova, E. I. Terukov, V. Fus, and I. N. Yassievich, Fiz. Tverd. Tela (St. Petersburg) **38**, 1189 (1996) [Phys. Solid State **38**, 658 (1996)].
[7] Jung H. Shin, R. Serna, G. N. van den Hoven, and A. Pollman, W. G. J. H. M. van Sark, A. M. Vredenberg. Appl. Phys. Lett. **68**, 997 (1996).

Translated by M. E. Alferieff

Photovoltaic effect in an asymmetric GaAs/AlGaAs nanostructure produced as a result of laser excitation

I. V. Kucherenko and L. K. Vodop'yanov

P. N. Lebedev Physics Institute, Russian Academy of Sciences, 117924 Moscow, Russia

V. I. Kadushkin

Scientific-Research Technological Institute, 390011 Ryazan', Russia
(Submitted December 29, 1995; accepted for publication January 15, 1997)
Fiz. Tekh. Poluprovodn. **31**, 872–874 (July 1997)

Photocurrent has been observed in a GaAs/GaAlAs structure with three asymmetric quantum wells in a magnetic field H parallel to the surface of sample irradiated with a quasicontinuous-wave laser with $\lambda = 1.065$ μm. The current flows in the plane of the layers in a direction perpendicular to the magnetic field. The magnitude of the current increases with H, and when the magnetic field is switched, the sign of the photocurrent changes. The effect is explained on the basis of a model with asymmetric electronic wave functions in a magnetic field.
 [S1063-7826(97)02907-4]

The idea that a photovoltaic effect appears in an asymmetric system of quantum wells under illumination in a magnetic field was first advanced in Ref. 1. Photovoltaic effects (PGE) under the action of circularly polarized illumination have been observed in uniform crystals without a center of symmetry center in the absence of a magnetic field.[2] These effects are most often observed in ferroelectric materials. Photoelectric effects have also been observed in semiconductors with complex bands, such as Te, *p*-type Ge, and *p*-type GaAs.[3] In a magnetic field, the well-known Kikoin–Noskov effect arises under nonuniform illumination.[4] The Hall current could also be due to potential barriers, for example, in the metal–heterostructure contact region.

The first results on the experimental observation of PGEs in quantum-well structures excited by light from an incandescent lamp were reported in Ref. 5. The present work is a continuation of the work reported earlier.[5] The following problems were solved: verification of the variation, found in Ref. 5, of the spectral function of the short-circuit current $I_{sc}(\lambda)$ using coherent light sources normalized to a constant energy illumination of the sample at different wavelengths; determination of the dependence of I_{sc} on the magnetic field intensity H in a wider range of H (up to 12 kOe) under illumination with an infrared (IR) laser with subthreshold radiation energy ($\varepsilon_{las} < E_g$). The latter circumstance is of fundamental importance for studying PGEs in semiconductors. The point is that under such excitation carriers of opposite signs (electrons and holes) are not generated and the nonequilibrium distribution function is produced by excitation of carriers of the same sign from impurity states and also as a result of heating of the electron gas. It was of interest in this connection to investigate in greater detail the unusual result obtained in Ref. 5 that the sign of the shift in I_{sc} under excitation with light with $\varepsilon_{las} < E_g$ does not depend on the direction of the magnetic field. It is possible that this effect was associated with the low intensity of excitation in the near-IR region, since the spectral distribution of the radiation power of an incandescent lamp is strongly nonuniform and decays strongly in the region $\lambda > 0.9$ μm.

In the present work we investigated the photovoltage and short-circuit photocurrent in a multiwell structure in magnetic fields up to 12 kOe. The structure consisted of three undoped square GaAs quantum wells of width 70, 60, and 54 Å separated by 30 and 20-Å-wide undoped $Al_{0.25}Ga_{0.75}As$ barriers. This structure is separated from the semi-insulating GaAs substrate by an *i*-GaAs buffer layer and is bounded by barrier layers consisting of undoped $Al_{0.25}Ga_{0.75}As$ (300 Å). The exciting light was directed in a direction normal to the plane of the sample, the magnetic field was applied in the plane of the layers, and the short-circuit photocurrent was measured in the plane of the layers perpendicular to the direction of the magnetic field.

The spectral dependence of the short-circuit photocurrent at $T = 300$ K is shown in Fig. 1. This dependence was measured with the sample under a constant illumination intensity of 0.6 W/cm^2, which was achieved by varying the laser power or the diameter of the excitation radiation spot. The dependence found qualitatively agrees with that obtained in Ref. 5. Therefore, it can be assumed that the maximum of I_{sc} lies at $\lambda = 0.8$ μm, which corresponds to the band gap in GaAs at $T = 300$ K [$E_g = 1.43$ eV (Ref. 6)]. Figure 2 shows the current-voltage characteristics (IVCs) in the case where the structure is illuminated with lasers of wavelengths $\lambda = 6764$ Å and $\lambda = 1.065$ μm and the same illumination intensity of 0.6 W/cm^2. From Fig. 2 we see that the IVCs in the case of illumination by the $\lambda = 1.065$-μm laser is nearly linear; very small deviations from linearity are observed for $U < 0.05$ V. In the case of illumination by the $\lambda = 6764$-Å laser the IVC is strongly nonlinear. When the voltage is switched, the current does not change sign up to $U \leqslant 2$ V (curve 1). This result shows that an electric field appears inside the structure under illumination with light in the fundamental absorption region and no such fields appear under illumination by the $\lambda = 1.065$-μm laser. We performed the investigations in a magnetic field with the sample illuminated by a laser with subthreshold energy $\lambda = 1.065$ μm and

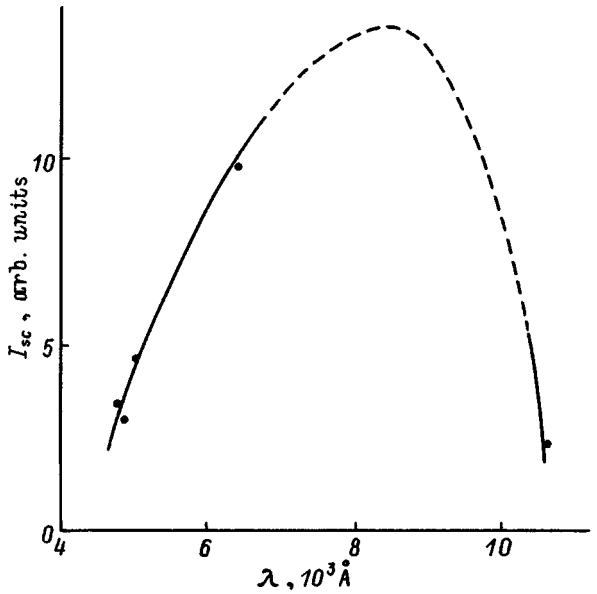

FIG. 1. Spectral dependence of the short-circuit photocurrent I_{sc} at $T=300$ K.

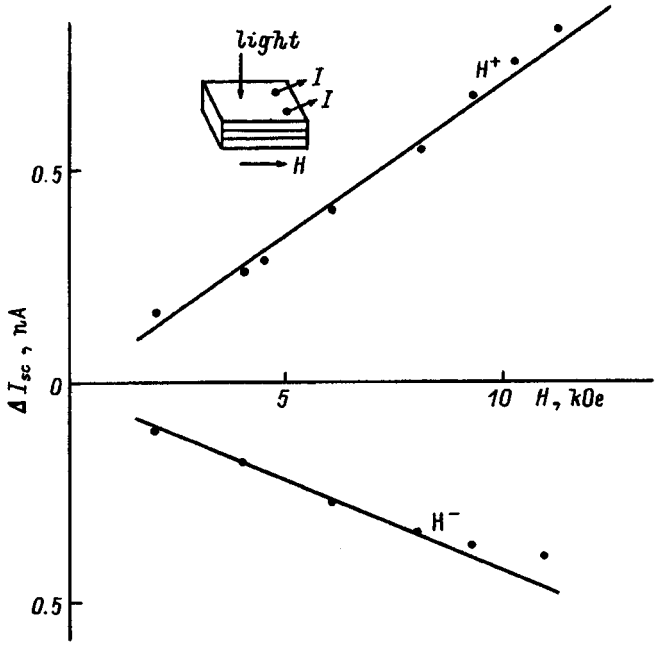

FIG. 3. Photocurrent I_{sc} versus magnetic field intensity H under excitation with a $\lambda=1.065$-μm laser. Inset: Geometry of the experiment.

specific power level 0.6 W/cm^2 (see the inset in Fig. 3). At this wavelength only carriers from the energy states of impurities and defects can be excited; therefore, the photoelectromagnetic effect does not contribute to the photocurrent. As one can see from Fig. 3, the photocurrent increases linearly with the field up to 11 kOe. When the magnetic field is switched, the sign of the photocurrent changes. The values presented here for the photocurrent are $\Delta I_{sc}=I_{sc}(H)-I_{sc}(0)$. When the sample is irradiated with the $\lambda=1.065$-μm laser, the resistance of the sample decreases by two orders of magnitude, evidently as a result of the excitation of carriers from impurities and defects.

In summary, a detailed study of the conductivity in a multiwell asymmetric structure has shown that excitation of the structure in a magnetic field H by coherent light sources produces a photocurrent whose magnitude increases with H. We attribute this photocurrent to the photovoltaic effect, whose nature can be explained on the basis of the model in Ref. 1. According to this model, currents, which induce a toroidal moment, arise in an asymmetric nanostructure in a magnetic field oriented in the plane (x, y) of the heterostructure. According to Ref. 7, the spectrum of the charge carriers in this case becomes asymmetric in the quasimomentum $E(k_y) \neq E(-k_y)$. The total current along the y axis in the case of a nonequilibrium distribution function is different from zero. If the nonequilibrium is caused by optical action, then a photovoltaic effect appears in the system. The current density is $j_{PGE}=\beta T_H$, where the coefficient β is due to the nonequilibrium and T_H is the toroidal moment induced by the magnetic field. In weak magnetic fields $j\sim H$ and in strong magnetic fields $j\sim 1/H$. The decrease in current in strong magnetic fields is due, according to Ref. 1, to an increase in the localization of the wave function, when the electron is increasingly less affected by the presence of the second well. The value of the magnetic field, for which the curve $j=f(H)$ passes through a maximum, can be estimated from the relation $\lambda\sim W$, where λ is the magnetic length, and W is the well width. In our case this maximum should be observed for $H\cong 40-50$ kOe.

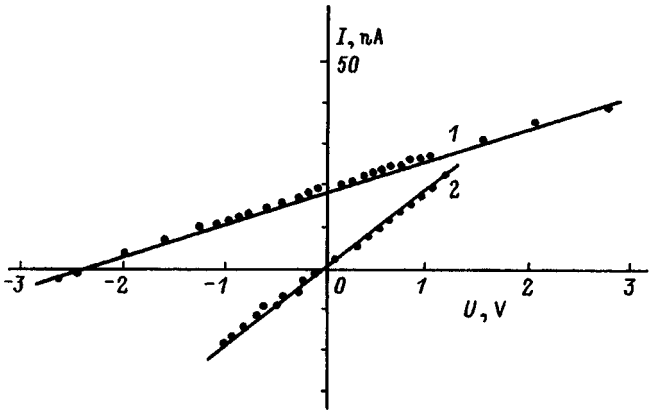

FIG. 2. Current-voltage characteristics of a nanostructure under excitation by lasers with wavelengths $\lambda=676$ Å (*1*) and $\lambda=1.065$ μm (*2*) and $T=300$ K.

We thank Yu. V. Kopaev and A. A. Gorbatsevich for participating in the interpretation of the experimental results.

This work was supported by the Russian Fund for Fundamental Research under Grants Nos. 93-02-2361 and 94-02-04634.

[1] A. A. Gorbatsevich, V. V. Kapaev, and Yu. V. Kopaev, JETP Lett. **57**, 580 (1993).
[2] V. I. Belinicher and B. I. Sturman, Usp. Fiz. Nauk **130**, 415 (1980) [Sov. Phys. Usp. **23**, 199 (1980)].
[3] I. M. Doviak and S. Kothary, in *Proc. 2oth Int. Conf. on the Phys. of Semiconductors*, Stuttgart, 1974, p. 1257.
[4] S. M. Ryvkin, *Photoelectric Phenomena in Semiconductors* [in Russian], Fizmatgiz, Moscow, 1963, p. 371.

[5] Yu. A. Aleshchenko, I. D. Voronova, and S. P. Gripechkina, JETP Lett. **58**, 384 (1993).
[6] V. I. Gavrilenko and A. M. Grekhov, *Optical Properties of Semiconductors* [in Russian], Naukova dumka, Kiev, 1987, p. 208.
[7] Yu. A. Artamonov, A. M. Gorbatsevich, and Yu. V. Kopaev, Zh. Éksp. Teor. Fiz. **101**, 557 (1992) [Sov. Phys. JETP **74**, 296 (1992)].

Translated by M. E. Alferieff

A study of the excitonic characteristics in heterostructures with quantum wells and corrugated surface

I. A. Avrutskiĭ

Institute of General Physics, Russian Academy of Sciences, 117942 Moscow, Russia

V. G. Litovchenko

Institute of Semiconductor Physics, Ukrainian National Academy of Sciences, 252650 Kiev, Ukraine
(Submitted May 12, 1996; accepted for publication May 22, 1996)
Fiz. Tekh. Poluprovodn. **31**, 875–879 (July 1997)

The excitonic characteristics of In_xGaAs_{1-x}–GaAs heterostructures in quantum wells in the presence of a corrugated surface has been investigated. The corrugated surface gives a substantial (up to 20%) polarization of the excitonic spectra even when the exciting light is incident in the direction of the normal. The exciton binding energies are calculated on the basis of data on the phonon repetitions of the photoluminescence spectra and the results agree well with the theoretical calculations. The parameters of the surface microrelief of the experimental layered structures are estimated on the basis of the degree of polarization of the photoluminescence and the magnitudes of the reflection and transmission.
[S1063-7826(97)03007-X]

1. INTRODUCTION

Interest in quantum-well structures with a corrugated surface has increased in the last few years in connection with the possibility of realizing in this manner one- or zero-dimensional quantum-well structures and in connection with the substantial effect of the natural or specially produced microprofile on the optical properties of structures with quantum wells (QWs). A convenient method for investigating the effect of a surface profile is to study the polarization of the photoluminescence (PL), whose magnitude can be substantial even with no change in the energy position and shape of the PL lines. The appearance and investigation of the anomalous polarization of PL under these conditions and the theory of the effect, based on taking into account the anisotropy of the effective masses of the valence band in the case of two-dimensional quantum wells, have been described in detail in several publications[1–5] in application mainly to GaAs-based structures. At the same time, the use of purely optical spectral methods gives additional possibilities from the methodological and physical standpoints. Indeed, the accuracy with which the reflection and transmission signal is recorded in the modulation variant is much higher than in the case of PL. Structures with QWs based on the ternary compounds $In_xGa_{1-x}As$ are of great interest. Such structures make it possible to produce, with comparatively low values of x, heterostructures which are more sensitive to radiation in a longer wavelength region of the spectrum 0.85–1 μm than GaAs-QW-based structures and which can be used for detecting radiation with silicon detectors.

2. EXPERIMENTAL PROCEDURE

This experimental study focused on the excitonic and polarization properties of $In_xGa_{1-x}As$ ($x=0.16-0.32$) structures, grown by gas-phase epitaxy from organometallic compounds on a semi-insulating GaAs substrate with a thin ($\sim$300 Å) GaAs buffer layer and a thin (200–600 Å) protective GaAs layer.[5–7]

The measurements were performed in an automated regime at different temperatures and angles of incidents θ of the light: photoluminescence PL (at 77 K, $\theta=0$), light-modulated transmission $\Delta T/T$ (77 K, $\theta=0$), and light-modulated reflection $\Delta R/R$ ($\theta=45°$, room temperature). Modulation was performed with a He–Ne laser ($\lambda=0.63$ μm), and the magnitude of the signal $\Delta R/R$ and $\Delta T/T$ reached 2×10^{-3}. In the transmission region a signal could be recorded with accuracy up to $\Delta T/T\sim2\times10^{-5}$. The experiments were performed with samples employed for fabricating laser structures. The thickness of the QWs was in the range 73 to 93 Å.

3. EXPERIMENTAL RESULTS

The data on the PL and the light-modulated transmission and reflection in the near-edge region of the spectrum are presented in Fig. 1. The main PL peak lies in the region of the free exciton radiation.[7,8] The small half-width of the lines (7–20 meV) shows that the samples are of high quality. The maxima of the peaks for different thicknesses of the quantum layer lie in the spectral region predicted for the corresponding two-dimensional band gaps E_g with the indicated component composition of the QW.[5,8] Specifically, as the QW decreased in thickness, E_g increased substantially from $\sim$1.2 to $\sim$1.4 eV [with d reaching $d\approx73$ Å (Fig. 2)]. The dependence $E_g(d)$ approximately follows the law $E_g\sim1/d$.

A careful measurement of the long-wavelength wing of the PL spectrum indicates the presence of an additional peak (or step) (Fig. 1a). These features are due to phonon repetition, since the indicated sections are displaced from the main maximum of the PL spectrum by an amount equal to the energy of the longitudinal optical surface phonon $E_{ph}=36\pm2$ meV. From the ratio of the amplitudes of the

 1063-7826/97/070743-04$10.00

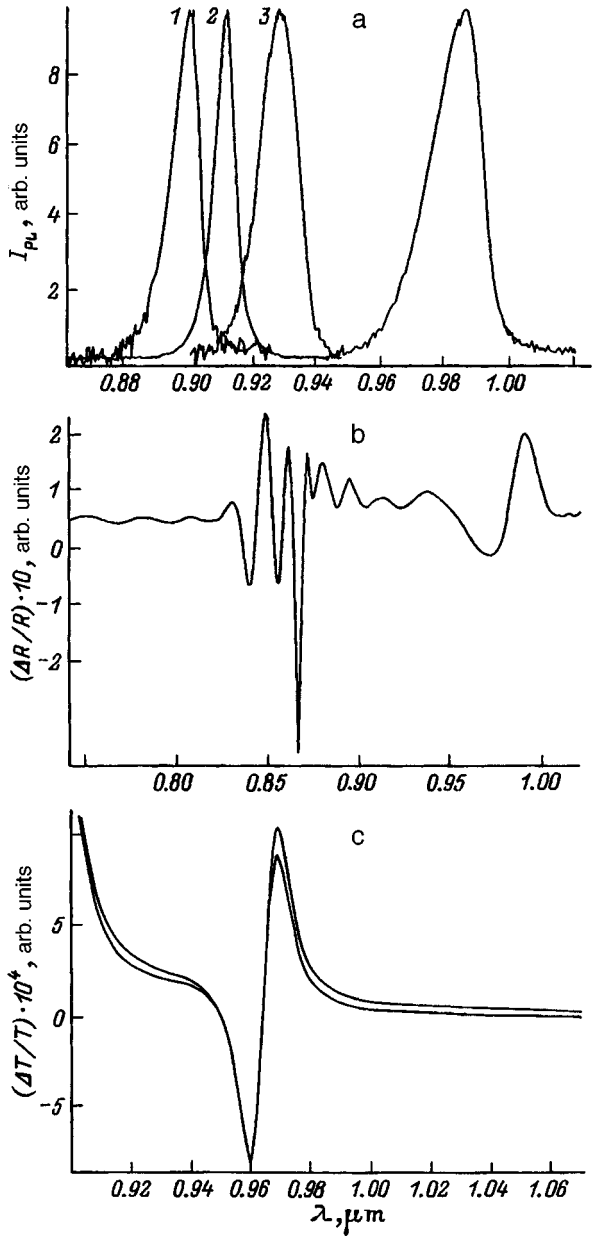

FIG. 1. Experimental spectra obtained for $In_xGa_{1-x}As$–GaAs structures with a single quantum well. a — PL spectra for different values of x: *1* — 0.2, *2* — 0.16, *3* — 0.21, *4* — 0.35. Temperature: 77 K. b — Laser-modulated reflection spectrum (temperature 300 K, $x=0.21, \theta=45°$). c — Photomodulated transmission spectrum for two mutually perpendicular orientations of the plane of the surface relative to the direction of polarization of the incident beam ($\theta=0$; $x=0.02$; 300 K).

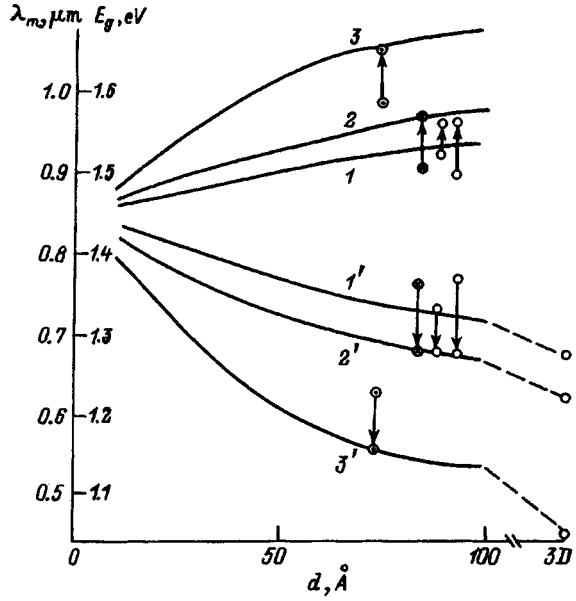

FIG. 2. Maxima λ_m of the PL curves (*1, 2, 3*) and characteristic energies of the excitonic reflection and transmission spectra E_g^* (*1′,2′,3′*) versus quantum layer thickness d for different values $x=0.16$ (*1,1′*), 0.2 (*2,2′*), 0.35 (*3,3′*). Dots — experimental data on PL at 300 K (at the tips of the arrows) and on the optical spectra at 77 K (dots located at the start of the arrows). Solid lines — theory of Ref. 8.

zero-phonon PL peak I_0 and the one-phonon peak I_1, $N=I_1/I_0$, it is possible to calculate the electron–phonon coupling parameter N, which in the adiabatic approximation of a weak electron–phonon interaction makes it possible to calculate, to a high degree of accuracy, the absolute binding energy of the exciton E_{ex}:[11–15]

$$E_{\rm ex}=\left(\frac{\pi}{2}\right)^{1/2}\frac{\varepsilon_\infty}{\Delta\varepsilon}E_{\rm ph}N, \tag{1}$$

where ε_∞ is the the dynamic permittivity, $\Delta\varepsilon=\varepsilon_0-\varepsilon_\infty$, ε_0 is the the static permittivity — all three are known tabulated quantities, and $E_{\rm ph}$ and N are determined from the experiment. In contrast to the standard method, the present method does not require measurements at different temperatures or in electric fields preceding the decay of the exciton. The validity of this approach for two-dimensional GaAs–AlAs quantum systems was confirmed by direct measurements of the exciton energies according to the temperature quenching of the excitonic peak of the PL.[15] In the present work we obtained values of $E_{\rm ex}$ for the heterostructures $In_xGa_{1-x}As$–AlAs with $x_1=0.2$ and $x_2=0.35$. In the calculation, sections characteristic of an excitonic state can be seen in the spectrum. The positions of the excitonic peak, whose magnitude equals, to within the binding energy of an exciton, the band gap E_g, i.e., $E_{\max}=E_g-E_{\rm ex}\approx E_g$, can be calculated from these sections. Figure 2 shows the computed (according to Ref. 8) dependences $\lambda_m(d)$ and $E_g(d)$ on the quantum well thickness d for different values of x. The experimental data obtained for several samples are also presented. The data obtained from the photoluminescence spectra at a temperature of 77 K differ substantially from the room-temperature theoretical curves. The room-temperature data were obtained from the optical transmission and reflection spectra. They follow well the theoretical curves. Values of the temperature coefficients of the variation of E_g and $E_{\rm ex}$ were obtained from the difference in the energies of the peaks at room temperature and at 77 K.

As one can see from Fig. 3, the curve $E_{\rm ex}(d)$ is more complicated (nonmonotonic) than predicted by the simple theory of quantum-well excitons, when $E_{\rm ex}$ is expected to increase as $E_{\rm ex}\sim 1/d$.[16–18] The dependence $E_{\rm ex}(d)$ slowed down substantially with decreasing d for QW thicknesses close to the exciton radius $a_{\rm ex}$ (for the experimental samples $a_{\rm ex}\approx 100$ Å). At $d\approx 0.5a_{\rm ex}$ the dependence reaches a maximum, after which it decreases sharply. As is well known,[10]

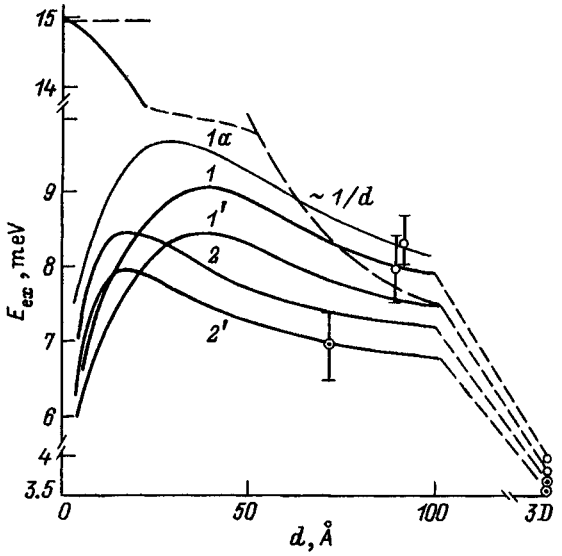

FIG. 3. Exciton binding energy E_{ex} versus quantum layer thickness d for different values of x: *1* — 0.2, *2* — 0.35, *1*, *2* — temperature 77 K; *1′*, *2′* — 300 K. Curve *1a* was obtained for an isolated quantum well,[18] the remaining curves were obtained for heterostructures on the basis of Refs. 8 and 9. The dashed line at the top shows the maximum possible value for the two-dimensional exciton energy $E_{ex}(2D)=4E_{ex}(3D)$.

such a nonmonotonic behavior is due to the tunneling penetration of the electron cloud into the barrier region, i.e. it is due to the delocalization of the electron cloud in the transverse direction. Our values of E_{ex}, computed according to the ''phonon'' method discussed here, agree well with the theoretically predicted values, showing that the proposed method is quite reliable.

As the QW thickness decreases, the interfaces, the characteristics of the boundary barrier, the mismatches of the permittivities, and also the electronic and phonon mixing of the corresponding characteristics of the quantum well and barrier become increasingly more important. An important factor facilitating the appearance of these effects is the formation of small-scale geometric microprofile in the technological process. One consequence of this circumstance is the fact that indirect phonon transitions are no longer forbidden. As a result, nonradiative recombination increases sharply as does the electron-phonon interaction.[2,4] To study the effect of the surface profile, it is of interest to employ polarization effects which are sensitive to the microrelief, comparable in scale to the radius of excitons. This question has been analyzed in detail in Refs. 3 and 4 using the PL spectra. Here we call attention to the possibility of performing measurements with the help of purely optical methods (modulated reflection and transmission spectra). By rotating the sample (oriented in the present case in the [100] plane) around the normal axis by 90° relative to the linearly polarized light, we were able to record the change in the amplitude of the signal I, which in the region of the excitonic resonance reached 20%. The energy position of the peaks (just as in the studies[2–4] of GaAs) remained unchanged (within 1–2 meV). Polarization, calculated according to the standard formula $P=(I_{\parallel}-I_{\perp})/(I_{\parallel}+I_{\perp})$, is present in the region of the main excitonic transition and in the transmission region (Figs. 1b and 4). Moreover, polarization also occurs under normal incidence of the light, although in the latter case polarization should be absent for a flat surface. Therefore, the oriented surface profile is the main mechanism for the appearance of polarization. For the $In_xGa_{1-x}As$ samples, the profile was oriented in the [100] cleavage planes.

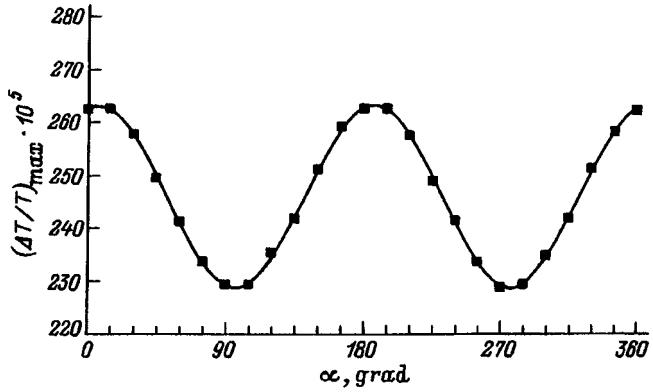

FIG. 4. Modulated transmission $\Delta T/T$ versus the azimuthal angle α for a sample with quantum layer thickness $d=92$ Å ($x=0.2$; 300 K).

The experimental data on the polarization P are presented in Fig. 5. In the figure we see a tendency for P to increase with decreasing thickness d of the quantum well and for the film growth to accelerate. It is also evident that the presence of the additional germanium δ-layer gives rise to a growth of the profile of the heterojunction surface.

To estimate the parameters of the profile, we shall employ the theoretical relations obtained in Refs. 3 and 4. In the

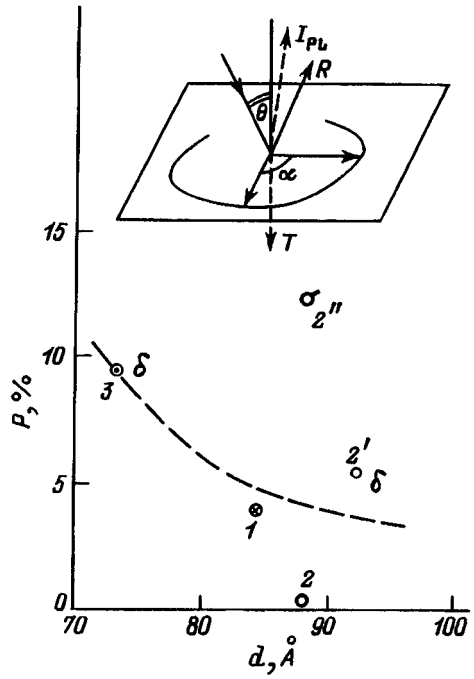

FIG. 5. Polarization of excitonic PL for samples with a quantum layer. Dots — experimental data for samples with different x: *1* — 0.16, *2* — 0.2, *3* — 0.35 and different conditions of film growth [with Ge δ-layer with typical (*2′*) and high (*2″*) growth rates]. Inset: Schematic diagram of the polarization measurement experiment.

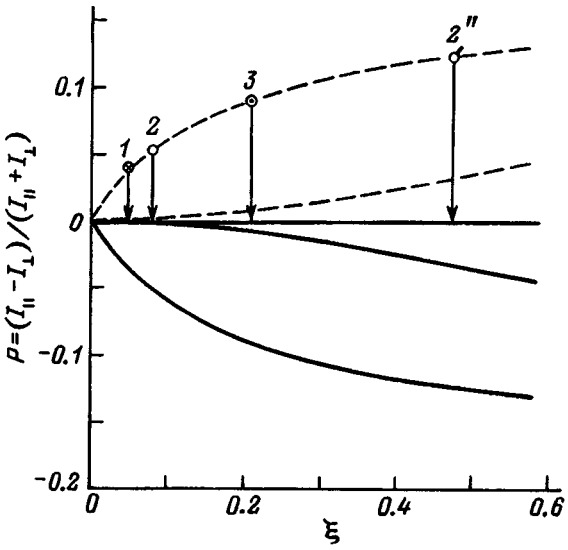

FIG. 6. Comparison of the theoretical curves $P(\xi)$ with the experimental data obtained for structures with quantum layers for different values of x: *1* — 0.16, *2* — 0.2, *3* — 0.35. The dashed lines correspond to a symmetric relief and the solid lines correspond to an asymmetric relief with $l_1/l_2=3$.

calculations of P, optical transitions with participation of the strongly anisotropic, heavy-hole valence band were examined in those studies. The excitonic transitions in a quantum well have an additional specific property which is characterized by the dipole moments P_n, which in the case of a narrow QW are not affected by the distant, symmetric, light-hole band. The dipoles P_n are mutually perpendicular and for this reason the quantity P_n for the flat surface of the sample is direction-independent in the entire quantum region. In the presence of a relief, the modulus of P_n remains unchanged but the direction of the polarization vector P_n changes, following the curvature of the surface. For example, $P_x=P_y=P_z$, where P_z is the dipole which is locally perpendicular to the surface,

$$P_{1,x}=P_1/(1+\xi^2)^{1/2}, \quad P_{1.z}=P_1\xi/(1+\xi^2)^{1/2}, \tag{2}$$

where $\xi=\Delta z/\Delta x\approx h/l$ is the slope of the profile, and h and l are, respectively, the height and length of the profile section. The magnitude of the polarization P depends on the slope ξ of the profile and on its shape. For the most natural shapes (sawtooth or sinusoidal) the functions $P(\xi)$ are similar, but they differ strongly for an asymmetric profile. For sufficiently strong asymmetry, the function $P(\xi)$ is almost identical for profiles of different shapes. The function $P(\xi)$ was calculated for a reasonable real range of profile parameters (Fig. 6). We note that the curves for GaAs and $In_xGa_{1-x}As$ for low values of x are identical, since for them the anisotropy factor $b\approx 0.66$ is approximately the same.

The corresponding experimental data are plotted in Fig. 6. Comparing them with the theoretical curves shows that the profile dimensions lie in the range $h\approx 5-10$ Å and $l\approx 15-50$ Å. We also note that the phonon-repetition peak was most strongly pronounced for the samples with the most prominent profile. .

4. CONCLUSIONS

We analyzed the dependences of the energy of the excitonic peak and the binding energies of the free excitons, as determined from the spectral position of the peaks in luminescence and the reflection and transmission spectra in the excitonic region of the spectrum, on the quantum well thickness for film heterostructures with different compositions $x=0.16-0.35$ for the alloy $In_xGa_{1-x}As$. A method was proposed for calculating the exciton binding energy from the optical spectroscopy data in the presence of phonon repetitions. The effect of the microprofile was found to be substantial for heterostructures with thin quantum wells. The parameters of the profile were estimated on the basis of a theory that takes into account the anisotropic polarization of the heavy-hole band.

This work was performed in collaboration with the Ukrainian National Fund for Scientific and Technical Research, as well as the Soros grant ISSER, SPU No. 062031. The samples for the experiment were provided by B. N. Zvonkov (NIFTI, N. Novgorod).

[1] K. Fujiwaza, N. Tsukada, and T. Nakayame, Solid Status Commun. **69**, 63 (1989).
[2] V. G. Litovchenko, D. Bercha, A. I. Korbutyak, V. Gavrilenko, K. Ploog, and Thin Solid Films **217**, 62 (1992).
[3] D. V. Korbutyak, V. G. Litovchenko, L. A. Troschenko, S. G. Krylyuk, T. Grahn, and K. Ploog, Semicond. Sci. Technol. **10**, 422 (1995).
[4] V. G. Litovchenko, D. V. Korbutyak, Yu. V. Kryuchenko, S. G. Krylyuk, H. T. Grahn, and K. Ploog, J. Phys. Low-Dim. Structur. **10/11**, 187 (1995).
[5] I. A. Avrutskiĭ, Kvant. Élektron. **21**(10) 921 (1994).
[6] I. A. Avrutsky, E. M. Dianov, and V. G. Plotnichenko, Lightwave Commun. **2**, 321 (1992); **3**, 71 (1993).
[7] I. A. Avrutskiĭ, O. P. Osaulenko, V. G. Plotnichenko, and Yu. N. Purkov, Fiz. Tekh. Poluprovodn. **26**, 1907 (1992) [Sov. Phys. Semicond. **26**, 1069 (1992)].
[8] I. A. Avrutskiĭ, V. A. Sychugov, and B. A. Uskevich, Fiz. Tekh. Poluprovodn. **25**, 1787 (1991) [Sov. Phys. Semicond. **26**, 1074 (1991)]
[9] D. S. Chuu and Ying-Chin Lou, Phys. Rev. B **43**, 14 504 (1991).
[10] L. C. Andeani and A. Pasquarello, Phys. Rev. B **42**, 8928 (1990).
[11] J. J. Hopfield, Phys. Chem. Solids **10**, 110 (1959).
[12] V. G. Litovchenko, V. A. Zuev, D. V. Korbutyak, and G. A. Sukach, Jpn. J. Appl. Phys., Suppl. 2, *22*, 421 (1974).
[13] V. A. Zuev, D. V. Korbutyak, and V. G. Litovchenko, Surf. Sci. **50**, 215 (1975).
[14] V. A. Zuev, D. V. Korbutyak, V. G. Litovchenko, and A. V. Drazhan, Fiz. Tverd. Tela (Leningrad) **17**, 3300 (1975) [Sov. Phys. Solid State **17**, 2166 (1975)].
[15] V. G. Litovchenko, D. V. Korbutyak, and S. G. Krylyuk, Phys. Low-Dim. Structur. **4/5**, 123 (1996).
[16] H. Q. Hou, Y. Segawa, Y. Aoyagi, and S. Nambea, Phys. Rev. B **42**, 1284 (1990).
[17] K. I. More, D. G. Duggan, K. Woodbridge, and C. Roberts, Phys. Rev. B **41**, 1090 (1990).
[18] E. P. Pokotilov, S. I. Beril, V. M. Fomin, V. G. Litovchenko, and D. V. Korbutyak, Phys. Status Solidi B **145**, 535 (1988).
[19] V. G. Litovchenko, S. I. Beril, D. V. Korbutyak, E. G. Lashkevich, and E. I. Mikhaĭlovskaya, Dokl. Akad. Nauk Ukrainy, Fiz.-Mat. i Tekhn. Nauki, No. 2, 57 (1988).

Translated by M. E. Alferieff

Faraday rotation of light in a microcavity

M. A. Kaliteevskiĭ, A. V. Kavokin, and P. S. Kop'ev

A. F. Ioffe Physicotechnical Institute, Russian Academy of Sciences, 194021 St. Petersburg, Russia
(Submitted July 11, 1996; accepted for publication November 18, 1996)
Fiz. Tekh. Poluprovodn. **31**, 880–884 (July 1997)

Faraday rotation of light in microcavities is studied theoretically. The reflection and transmission spectra are calculated. It is shown that in the region of the spectrum corresponding to a characteristic mode of the cavity the Faraday rotation is strongly intensified and the polarization of the light changes substantially. © *1997 American Institute of Physics.*
[S1063-7826(97)03107-4]

1. INTRODUCTION

Semiconductor microcavities (MCs) have been under intensive investigation in recent years, both experimentally[1–3] and theoretically.[4–7] This interest stems from the fact that, first, the study of semiconductor microcavities has made it possible to observe a number of new effects (such as Rabi splitting and Rabi oscillations) and, second, microcavities are used to produce lasers with vertical emission of radiation. A typical MC consists of a central semiconductor or dielectric layer (the ''cavity'' of the MC) bounded by two multilayer Bragg reflectors (BRs); the entire structure is grown on a substrate made of a semiconductor material (see Fig. 1). Light modes localized in the central layer can be excited in such a structure. The spectrum of these modes is discrete, and for normal incidence of light it is determined by the relation

$$2nK_0L+f_1+f_2=2\pi N, \tag{1}$$

where K_0 is the modulus of the wave vector of light in vacuum, n is the index of refraction of the cavity, L is the thickness of the cavity, $f_{1(2)}$ is the phase of the amplitude coefficient of the reflection of light from the first (second) BR, and N is an integer. The reflection (transmission) spectra of these structures contain characteristic features in the form of deep, narrow dips (peaks), whose spectral position is the same as that of the characteristic optical modes of the MC.

Our objective in the present work was to study the Faraday rotation of light[8–10] in semiconductor microcavities. It is natural to assume that as a result of multiple rereflection of light from the mirrors forming the cavity, Faraday rotation in the microcavity will be strongly intensified at the frequencies of the characteristic modes.

2. BASIC EQUATIONS

Let light linearly polarized along the x axis be incident on the microcavity in a direction along the normal. A plane wave of unit amplitude propagating along the z axis can be represented in the form

$$\begin{pmatrix}1\\0\end{pmatrix}=\frac{1}{2}\begin{pmatrix}1\\i\end{pmatrix}+\frac{1}{2}\begin{pmatrix}1\\-i\end{pmatrix}, \tag{2}$$

where the components of the column vectors are the x and y components of the electric field **E** of the light wave.

We assume that the external magnetic field is perpendicular to the plane of the layers of the MC. For simplicity, we also assume that the rotation of the polarization plane occurs only in the plane and not in the mirror layers.

The linearly polarized wave in the cavity separates into two circularly polarized waves E_+ and E_-, corresponding to different refractive indices n_+ and n_- (Ref. 8)

$$n_+=n+\delta, \tag{3a}$$

$$n_-=n-\delta, \tag{3b}$$

where for paramagnetic and diamagnetic materials δ is defined as

$$\delta=VH/K_0, \tag{3c}$$

where V is the Verdet constant, and H is the intensity of the magnetic field. Ferromagnetic materials are ordinarily characterized by a specific Faraday rotation F in the state of saturated magnetization.[10] For this case δ is given by the expression

$$\delta=F/K_0. \tag{3d}$$

The values of V and F differ very strongly for different substances and they depend on the temperature and spectral region. For example, for EuS compounds at liquid-helium temperatures F in the wavelength range 0.8–0.9 μm is of the order of 10^3-10^4 rad/cm, which corresponds to $\delta\simeq 0.1$. We note that this wavelength range corresponds to the transmission range of EuS.[10]

The reflected and transmitted light can possess elliptical polarization, which can be written in the form

$$E=\frac{1}{2}A\exp(i\varphi_+)\begin{pmatrix}1\\i\end{pmatrix}+\frac{1}{2}B\exp(i\varphi_-)\begin{pmatrix}1\\-i\end{pmatrix}, \tag{4}$$

where the two coefficients of the column vectors correspond to the complex amplitudes of two different circularly polarized waves. The expression (4) can be put into the form

$$E=\frac{1}{2}(A+B)\exp(i\psi)\begin{pmatrix}\cos\phi\\\sin\phi\end{pmatrix}+\frac{i}{2}(B-A)\exp(i\psi)\begin{pmatrix}\sin\phi\\-\cos\phi\end{pmatrix}, \tag{5}$$

 1063-7826/97/070747-05$10.00

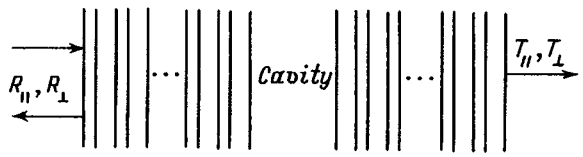

FIG. 1. Diagram of the structure.

where the two terms correspond to two waves polarized linearly along the principal axes of an ellipse, $\psi=\varphi_+ + \varphi_-$, and the rotation angle ϕ of the polarization plane is given by the expression

$$\phi=\varphi_- - \varphi_+ . \tag{6}$$

The degree of linear polarization of light is determined by the expression

$$P_{\text{lin}}=\frac{2AB}{A^2+B^2}, \tag{7}$$

and the degree of circular polarization is given by the formula

$$P_{\text{cir}}=\frac{A^2-B^2}{A^2+B^2}. \tag{8}$$

The amplitude reflection coefficients (r_+, r_-) and transmission coefficients (t_+, t_-) for two different circular polarizations can be calculated by the transfer matrix method.[11] The reflection coefficient for the case in which the reflected light is polarized linearly in the same direction as the incident light will then be given by

$$R_\parallel=\frac{1}{4}|r_+ + r_-|^2, \tag{9}$$

and the reflection coefficient for the case of polarization perpendicular to the polarization of the incident light is given by the expression

$$R_\perp=\frac{1}{4}|r_+ - r_-|^2. \tag{10}$$

The transmission coefficients are found similarly: For polarization in the same direction as the polarization of the incident light

$$T_\parallel=\frac{1}{4}\frac{n_l}{n_0}|t_+ + t_-|^2 \tag{11}$$

and for polarization perpendicular to the polarization of the incident light

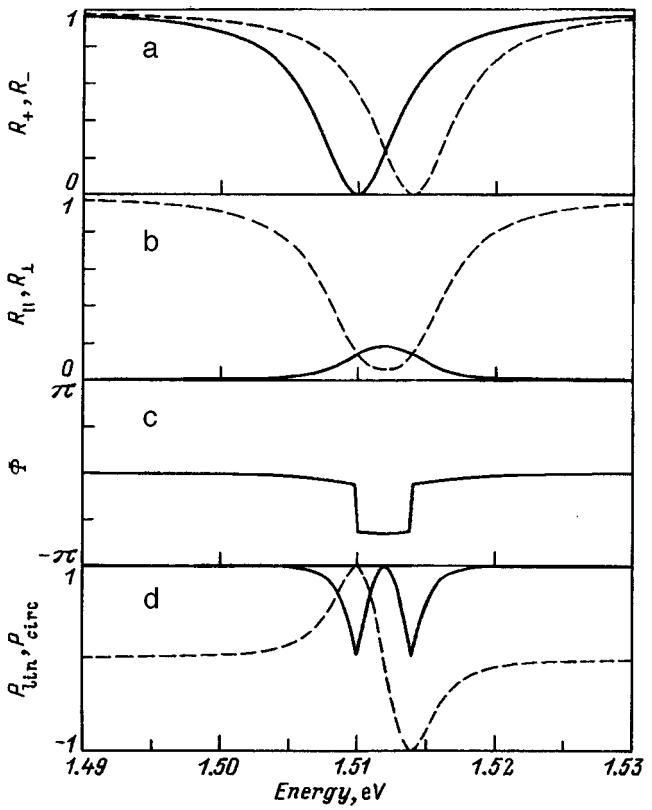

FIG. 2. a — Reflection spectra for two circular polarizations of the light. b — Reflection spectra of light linearly polarized in a direction parallel (dashed line) and perpendicular (solid line) to the polarization of the incident light. c — Spectral dependence of the rotation angle of the polarization plane. d — Spectral dependence of the degree of linear polarization (solid line) and circular polarization (dashed line) of the reflected signal. The reflection coefficients of the mirrors forming the cavity equal 90% and the refractive index mismatch is $\delta=0.03$.

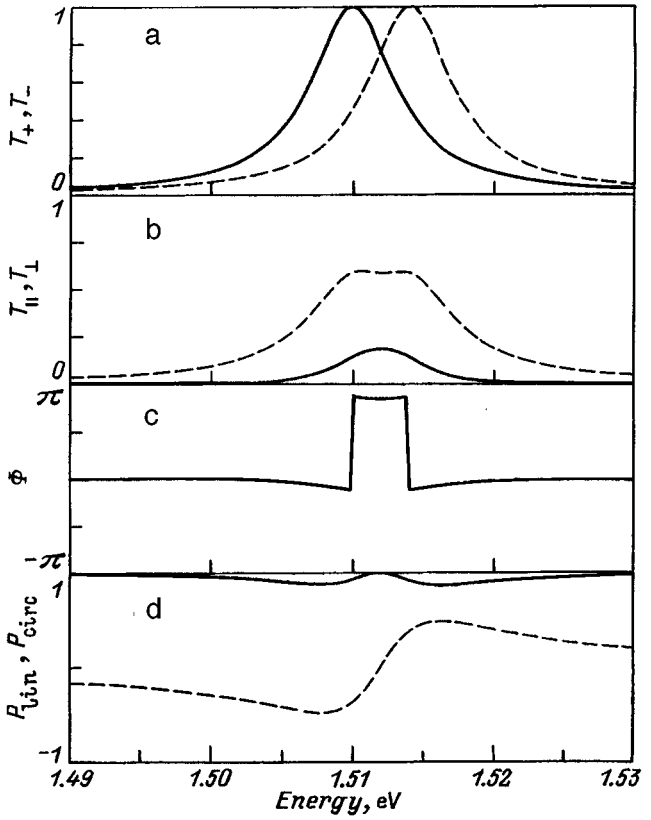

FIG. 3. a — Transmission spectra for two circular polarizations of the light. b — Transmission spectra of light linearly polarized in a direction parallel (dashed line) and perpendicular (solid line) to the polarization of the incident light. c — Spectral dependence of the rotation angle of the polarization plane of the transmitted light. d — Spectral dependence of the degree of linear (solid line) and circular (dashed line) polarization of the transmitted light. The reflection coefficients of the mirrors forming the cavity equal 90% and the refractive index mismatch is $\delta=0.03$.

$$T_{\perp}=\frac{1}{4}\frac{n_l}{n_0}|t_+-t_-|^2, \tag{12}$$

where n_0 and n_l are the refractive indices of the first and last semi-infinite media that bound the structure. We note that this procedure (specifically, the transfer matrix method) is inapplicable for oblique incidence of the light.

3. RESULTS AND DISCUSSION

It is obvious that the optical behavior of the system will be determined by both the Faraday rotation of light in the cavity (i.e., by the parameter δ) and by the reflection coefficients of the mirrors or, more accurately, the cavity Q.

We performed the calculations for three symmetric microcavities with different reflection coefficients of the mirrors. The mirrors consisted of periodic sequences of pairs of layers with refractive indices 3.0 and 3.5 and thicknesses 68.3 and 58.6 nm, respectively. The mirrors in the first MC consisted of eight pairs of layers (the reflection coefficient of the mirrors $R_m=0.9$), the mirror of the second MC consisted of 10 pairs of layers (the reflection coefficient $R_m=0.95$), and the mirror of the third MC consisted of 15 pairs of layers (reflection coefficient $R_m=0.99$). In all three cavities the index of refraction and thickness of the central layer (cavity) were $n=3.5$ and 117.1 nm, respectively; this corresponded to half the wavelength of the light in the cavity at the frequency of the normal mode with $\delta=0$ (so-called $\lambda/2$ cavity). In this case the rotation angle of the polarization plane for light passing through the cavity is related to the value of δ by

$$\phi=\pi\delta. \tag{13}$$

The parameters of the MCs were chosen to be similar to those of the MCs studied experimentally in Refs. 1–3.

The different refractive indices n_+ and n_- for different polarizations give a different spectral position of the normal modes and the corresponding characteristic features in the reflection and transmission spectra of circularly polarized light (Fig. 2a, 3a, 4a, and 5a). For a symmetric microcavity and no absorption in the structure, the positions of the features in the reflection and transmission spectra for light of the same circular polarization coincide, and the reflection and transmission coefficients at the frequencies at the characteristic modes become equal to 0 and 1, respectively.

Let us consider linearly polarized light incident on a microcavity. In the case where the reflection coefficient of the cavity mirrors is small (90%) and the mismatch of the refractive indices is small ($\delta=0.03$) (Figs. 2b and 3b) the degree of modulation of the line corresponding to the characteristic mode is lower and the width of the mode is greater, and a signal appears in the polarization perpendicular to the polarization of the incident light.

The spectral dependence of the rotation angle of the polarization plane of the reflected signal is shown in Fig. 2c. The discontinuities in this dependence correspond to the points where $R_{\perp}$ is of the same magnitude as $R_{\parallel}$. We note that the rotation angle of the polarization plane in the case of light passing through a $\lambda/2$ cavity with $\delta=0.03$ equals 0.1 rad, while the maximum value of the rotation angle ϕ of the polarization plane of the reflected signal in the case at hand exceeds 2 rad.

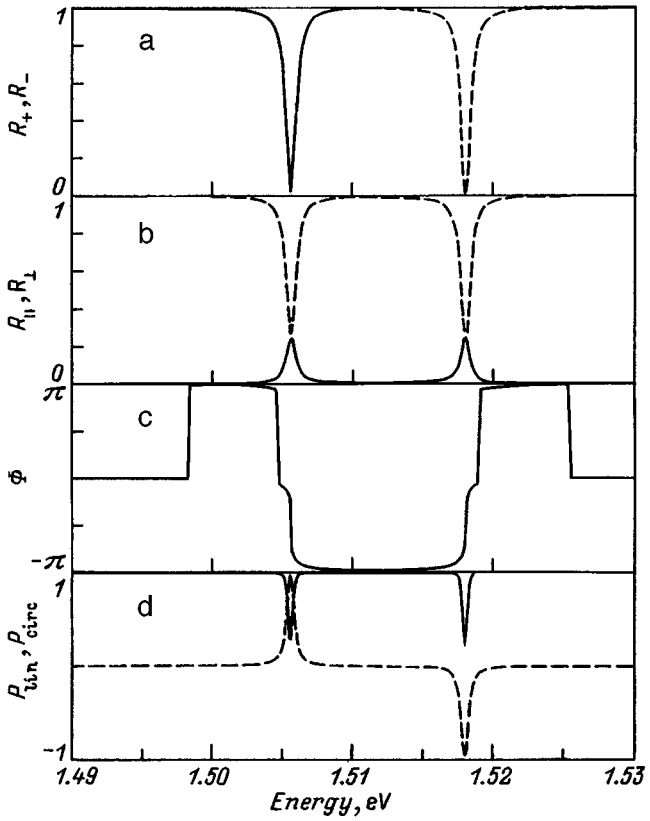

FIG. 4. a — Reflection spectra for two circular polarizations of the light. b — Reflection spectra of light linearly polarized in a direction parallel (dashed line) and perpendicular (solid line) to the polarization of the incident light. c — Spectral dependence of the rotation angle of the polarization plane. d — Spectral dependence of the degree of linear (solid line) and circular (dashed line) polarization of the reflected signal. The reflection coefficients of the mirrors forming the cavity equal 99% and the refractive index mismatch is $\delta=0.1$.

Figure 2d shows the spectral dependences of the degree of linear and circular polarization of the reflected signal. One can see that at frequencies close to the positions of the characteristic modes of the circularly polarized light, the polarization of the incident light is converted from linear to circular.

Figures 3b–3d show similar curves for the transmitted light.

Let us now consider the case of large values of δ for the reflection coefficients of the cavity mirrors. Figures 4 and 5 show the spectral dependences of different characteristics of reflected and transmitted light for the case $R_m=0.99$ and $\delta=0.1$. We see that when the structure is illuminated by linearized light, the reflection and transmission spectra contain two features, each in both linear polarizations, and at the frequencies of the characteristic modes the reflection and transmission coefficients equal 25% for any linear polarization, indicating that the polarization is completely converted from linear to circular.

It should be noted that for the case considered here, a symmetric MC, the reflection and transmission spectra for

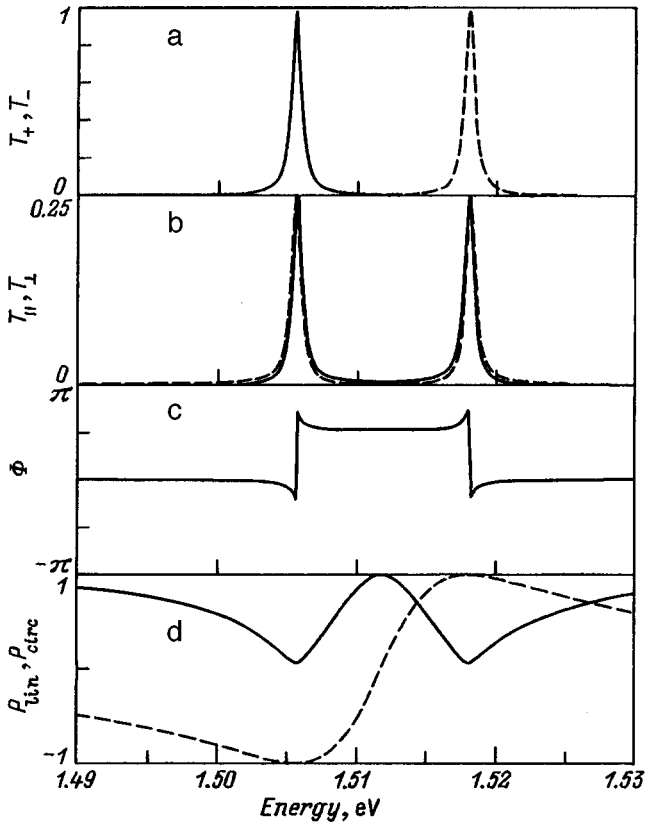

FIG. 5. a — Transmission spectra for two circular polarizations of the light. b — Transmission spectra of light linearly polarized in a direction parallel (dashed line) and perpendicular (solid line) to the polarization of the incident light. c — Spectral dependence of the rotation angle of the polarization plane of the transmitted light. d — Spectral dependence of the degree of linear (solid line) and circular (dashed line) polarization of the transmitted light. The reflection coefficients of the mirrors forming the cavity equal 99% and the refractive index mismatch is $\delta = 0.1$.

light polarized perpendicular to the polarization of the incident light are virtually identical.

Figure 6 shows the position of the features in the transmission spectra for light polarized in a direction perpendicular to the polarization of the incident light, on the value of δ for three MCs with different values of R_m. We see that in the case where R_m is small, for small values of δ, one feature is observed in the spectrum. As δ increases and crosses a critical value, the line splits in two. For large values of R_m two features are present in the spectrum, even for small values of δ; here the positions of these features are virtually identical to the positions of the normal modes of the MC for light with two different circular polarizations.

Figure 7a shows the dependence of the transmission coefficient of light polarized linearly in a direction perpendicular to the polarization of the incident light on the value of δ. This is a saturating dependence: The transmission coefficient approaches 0.25; saturation is reached all the more rapidly, the higher the value of R_m. Saturation corresponds to complete conversion of linearly polarized light into circularly polarized light. For comparison, the figure also shows a plot of the function $\sin^2(\pi\delta)$, which describes the quantity $T_\perp$ in the case where there is no reflection of light from the boundaries of the cavity.

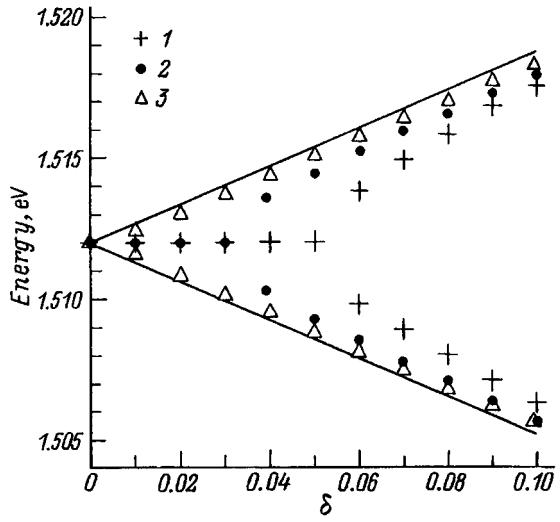

FIG. 6. Positions of the peaks in the reflection and transmission spectra of light linearly polarized in a direction perpendicular to the polarization of the incident light versus the refractive index mismatch δ for three microcavities with reflection coefficients of the mirrors equal to 90% (*1*), 95% (*2*), and 99% (*3*). Solid lines — positions of the characteristic cavity modes for two different circular polarizations of the light.

For possible device applications it is important to know the total power of the signal measured in linear polarization perpendicular to the polarization of the incident light with the MC illuminated with ''white'' light ($P_\perp$):

$$P_\perp = \int I_\perp d\omega. \tag{14}$$

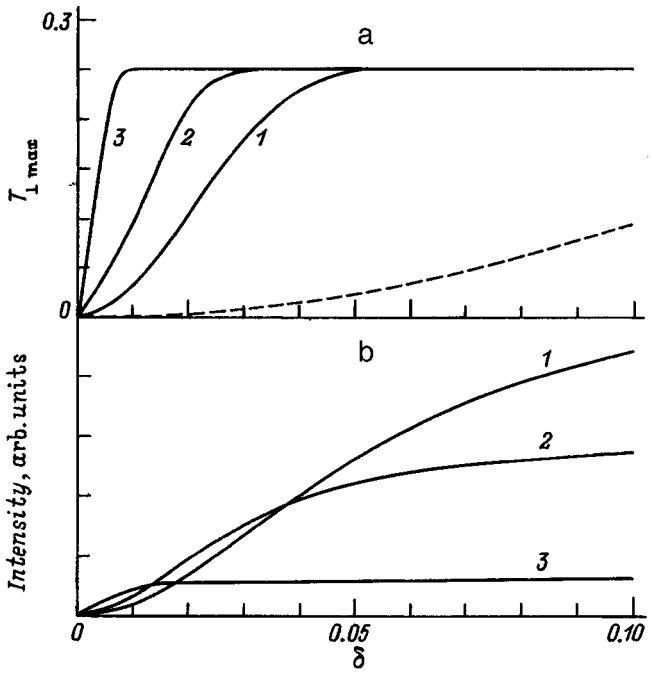

FIG. 7. Maximum value of the transmission coefficient $T_{\perp max}$ (a) and total intensity of the transmitted linearly polarized light (b) with the MC illuminated by ''white'' light versus the refractive index mismatch δ for three symmetric microcavities with reflection coefficients of the mirrors equal to 90% (*1*), 95% (*2*), and 99% (*3*). Dashed line — plot of the function $\sin^2(\pi\delta)$.

The curves of $P_{\perp}$ versus δ are shown in Fig. 7b. We see that these are saturating dependences. It is obvious that saturation is reached at the level $P_{s\perp}$ given by

$$P_{s\perp} = \Delta/2, \tag{15}$$

where Δ is the width of the line corresponding to the normal mode.

The main results of this study are as follows. We investigated the Faraday rotation of light in microcavities. It was determined that the Faraday rotation of light is greatly intensified at the frequencies of the characteristic modes of the cavity and at these frequencies the polarization of the light is substantially transformed. This effect can be used to measure the magnetic field and modulation of light signals with the aid of a magnetic field.

This work was supported by the Russian Fund for Fundamental Research under Grant N 96-0217836-a and the Ministry of Science and Technology Policy under the program ''Physics of Solid-State Nanostructures.''

We are deeply grateful to R. P. Seĭsyan for very useful discussions.

[1] C. Weisbouch, M. Nishioka, A. Ishikava, and Y. Arakawa, Phys. Rev. Lett. **69**, 3314 (1992).
[2] R. Houdre, R. P. Stanley, U. Oesterle, M. Ilgems, and C. Weisbouch, Phys. Rev. B **49**, 16 761 (1994).
[3] J. Tignon, P. Voisin, C. Delande, M. Voos, R. Houdre, U. Oesterle, and R. P. Stanley, Phys. Rev. Lett. **74**, 3967 (1994).
[4] A. V. Kavokin and M. A. Kaliteevski, Sol. St. Commun. **95**, 859 (1995).
[5] E. L. Ivchenko, M. A. Kaliteevski, and A. V. Kavokin *et al.*, J. Amer. Opt. Soc. **13**, N 5 (1996) (in press).
[6] V. Savona, L. C. Andreani, P. Schwendimann, and A. Quatropani, Solid Status Commun. **93**, 733 (1995).
[7] M. A. Kaliteevskiĭ, Fiz. Tekh. Poluprovodn. **30**, 516 (1996) [Semiconductors **30**, 283 (1996)].
[8] M. M. Bredov, V. V. Rumyantsev, and I. P. Toptygin, *Classical Electrodynamics* [in Russian], Nauka, Moscow, 1985, p. 338.
[9] N. I. Kaliteevskiĭ, *Wave Optics* [in Russian], Vyssh. Shkola, Moscow, 1995, p. 160.
[10] I. S. Grigor'eva and E. Z. Meĭlikhova, *Physical Quantities* [in Russian], Énergoatomizdat, Moscow.
[11] M. Born and E. Wolf, *Principles of Optics*, Pergamon Press, N. Y., 4th edition, 1969 [Russian translation, Nauka, Moscow, 1970, p. 77].

Translated by M. E. Alferieff

Effect of radiation on the characteristics of MIS structures containing rare-earth oxides

Ya. G. Fedorenko, L. A. Otavina, E. V. Ledeneva, and A. M. Sverdlova

Saratov State University, 410071 Saratov, Russia
(Submitted March 20, 1996; accepted for publication January 22, 1997)
Fiz. Tekh. Poluprovodn. **31**, 885–888 (July 1997)

The results of experimental studies of the effect of γ-irradiation on the electrical properties of MIS structures containing the rare-earth oxides Y_2O_3, Dy_2O_3, Tb_2O_3, Gd_2O_3, and Lu_2O_3 are reported. The static characteristics (current-voltage, capacitance-voltage) and dynamic characteristics (transient characteristics, diagrams of oscillatory regimes) of the structures before and after irradiation with doses $D=10^4-10^6$ rad are examined. It is found that the irradiation dose $D=10^6$ rad does not produce any substantial degradation of the characteristics of the structures. The radiation-induced changes observed in the experimental samples are consistent with existing data for MIS structures with SiO_2 as the insulator. © *1997 American Institute of Physics.* [S1063-7826(97)03207-9]

In the last few years the effect of radiation on the characteristics of MIS structures has been investigated in a number of studies.[1–13] However, despite the large amount of experimental and theoretical data now available in these studies, it is difficult to pinpoint the process leading to the appearance of radiation-induced volume charge in the insulator and at the oxide–semiconductor interface. This is because the accumulation of radiation-induced charge depends on many factors: the technology for producing the oxide, the irradiation conditions, post-radiation treatment, and the insulator material.[4,5,11,12] Radiation effects arising in MIS structures with silicon dioxide SiO_2 and silicon nitride Si_3N_4 as the insulator have been studied in greatest detail.[2,3,6] The high radiation resistance of the insulators $SiO_2+Si_3N_4$ and $SiO_2+Si_3N_4+SiO_2$ is pointed out in Refs. 3, 7, and 8. Data on the effect of radiation on field structures with rare-earth oxides (REOs) as the insulator are less well known. Investigations of the electrical characteristics of MIS structures with rare-earth oxides have shown that the electric and insulating properties of these oxides are highly stable, the permittivity and chemical stability of the oxides are high, and the band gap is large.[10,14]

Our objective in the present work is to investigate the effect of γ-irradiation on the parameters of MIS structures containing rare-earth oxides. It should be noted that MIS structures prepared on a uniform substrate and on a substrate with a built-in p–n junction were investigated. MIS structures with a nonuniformly doped substrate were chosen because their current-voltage characteristics contain a section of negative differential resistance and the nonequilibrium processes occurring in them can be more sensitive to γ-irradiation.

1. METHOD OF INVESTIGATION

Samples containing the rare-earth oxides (dysprosium oxide Dy_2O_3, terbium oxide Tb_2O_3, lutecium oxide Lu_2O_3, gadolinium oxide Gd_2O_3, and yttrium oxide Y_2O_3) were investigated. The sample ranged in thickness from 100 to 500 Å. An aluminum film served as the field-emission electrode. Three types of substrates were used: uniformly doped n-type Si containing a (n^+-p)-Si junction (OL) and with a buried diffused (n^+-n^--p)-Si layer (BL). The topology of the sample structures is shown in Fig. 1 (inset).

The samples were irradiated with a ^{60}Co source with open electrodes. The irradiation doses varied from 10^2 to 10^6 rad. The measurements were performed on the irradiated samples after the samples were stored for the same length of time following irradiation, equal to 60 h; annealing was not performed.

Measurements of the rf capacitance-voltage characteristics (CVCs), dynamic current-voltage characteristics (IVCs), and transient characteristics before and after irradiation. We measured the duration of the transient process with the depleting voltage pulse switched off, whose amplitude and duration were varied; the durations of the transient process were analyzed as a function of the irradiation dose. Oscillatory states of a RL circuit containing the MIS structure were investigated before and after irradiation. The state diagrams are constructed in the coordinates ''amplitude–⟨frequency of external action⟩.'' The experimental procedure with a nonlinear nonautonomous circuit with a p–n junction and the method for constructing the state diagrams were taken from Refs. 15 and 16.

2. RESULTS AND DISCUSSION

Analysis of the pre- and postirradiation rf CVCs of the structures showed that for all samples the well-known shift of the CVC occurs along the voltage axis, indicating that a positive charge is induced in the insulator and at the interface (Fig. 1). The flat-band voltage assumes values from -1.25 V to -4.5 V for different samples, depending on the preirradiation value of this voltage. The densities of the surface states were found to lie in the range $N_{ss}=(0.7-1.1)\times10^{12}$ $eV^{-1}\cdot cm^{-2}$ for unirradiated samples and $N_{ss}=(2.3-3.7)\times10^{-12}$ $eV^{-1}\cdot cm^{-2}$ for irradiated samples.

Figure 2 shows the IVCs of MIS structures on uniform (*1,1′*) and nonuniform (*2,2′*) substrates. The IVCs of structures on the uniform substrate retain the same form after irradiation. The IVCs of samples with nonuniformly doped (n^+-p)-Si as well as (n^+-n^--p)-Si substrates differ accord-

 1063-7826/97/070752-04$10.00

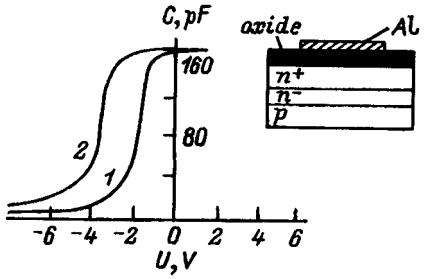

FIG. 1. Pre- (*1*) and post-irradiation (*2*) capacitance versus voltage characteristics of MIS structures containing Lu_2O_3.

ing to the parameter U_s (the voltage switching). These curves have sections of negative differential resistance (NDR). The dependence of U_s on the irradiation dose D is shown in Fig. 3. At low doses $D<10^4$ rad the switching voltage increases to 9–12 V, and as the dose increases above 10^4 rad, U_s decreases to 4–7 V. Evidently, as the dose increases, the degree to which the positive radiation-induced charge in the insulator influences the voltage redistribution between the insulator and the space-charge region (SCR) in the semiconductor changes, leading to the switching effect. At low doses, the introduced positive charge Q_{built} is insufficient for this, and the switching voltage increases. Indeed, the appearance of a positive charge on the insulator–semiconductor interface increases the electron density at the semiconductor surface. Then some of the positive charge of the injected holes and the holes accumulated at the surface compensates for this induced negative charge, and when the hole density required for the switching effect is reached, U_s increases. As the dose D increases to 10^6 rad, the charge Q_{built} increases, which substantially decreases the resistance of the insulator and voltage redistribution starts at a lower bias on the field-emission electrode, i.e., U_s decreases. This result agrees with the data in Ref. 17, in which is noted the role of deep levels in the insulator, which are associated with centers lying near the silicon and the aluminum on which charge accumulation during irradiation results in charging and recharging of the silicon and aluminum with increasing dose.

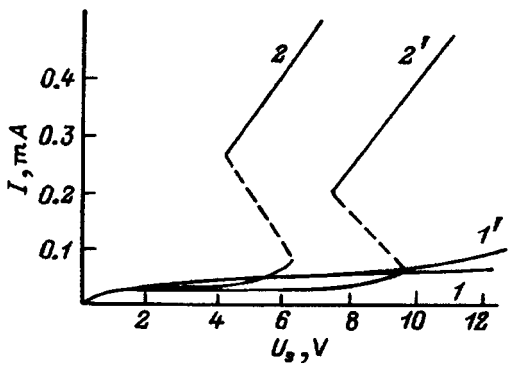

FIG. 2. Pre- (*1, 2*) and postirradiation (*1′,2′*) current versus voltage characteristics of MIS structures containing Lu_2O_3 with a negative voltage on the field-emission electrode with dose $D=10^6$ rad. Type of substrate: *1, 1′* — *n*-Si, *2, 2′*— n–p^+-Si.

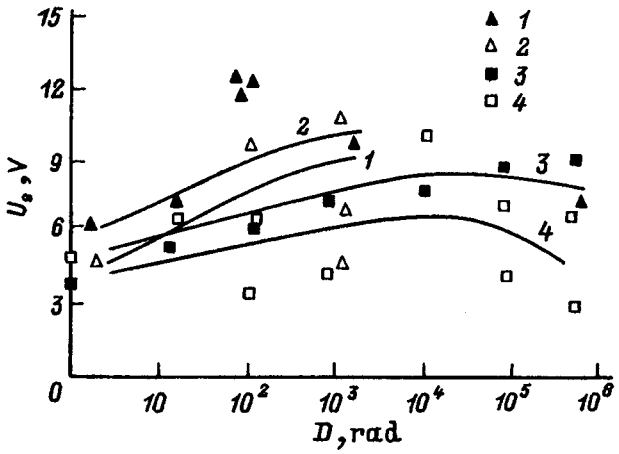

FIG. 3. Switching voltage U_s versus irradiation dose D for MIS structures with insulators: *1* — Dy_2O_3 (BL), *2* — Dy_2O_3 (OL), *3* — Tb_2O_3 (BL), *4* — Tb_2O_3 (OL). Types of substrates in the structures: OL — (n^+—p)-Si, BL — (n^+–n^-–p)-Si.

The dependence of the duration of the transient process on the irradiation dose is presented in Fig. 4. We see that for low ($U_0<10$ V) and high ($U_0>10$ V) amplitudes of the pulse of magnitude U_0 the dose dependences of the duration t_s of the transient process are different. After a pulse with amplitude up to 10 V is switched off, t_s increases, as the irradiation dose increases to 10^4 rad, and then decreases. For a pulse with amplitude greater than 10 V, which transfers the structure into an open state, the duration t_s of the transient process at first decreases with increasing irradiation dose and then increases. Thus, it is clear that for each region of voltages of the bistable state of the system, as the dose increases, the mechanism of relaxation of the nonequilibrium charge carriers changes.

The explanation of the results obtained is based on the following. If the amplitude of the pulse is less than 7–10 V, the structure is in a high-resistance state and the duration of the transient process is determined by the relaxation of the holes accumulated at the insulator–semiconductor boundary with the participation of surface states. When the amplitude

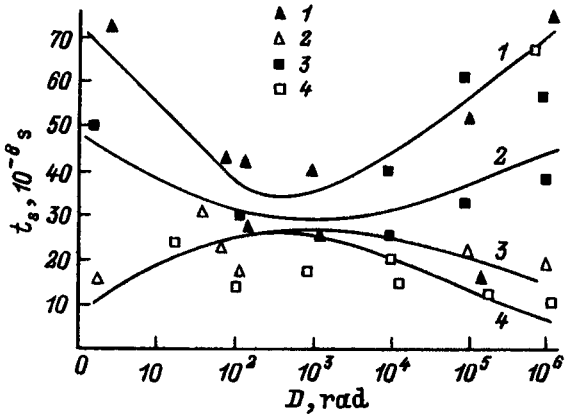

FIG. 4. Duration t_s of the transient process as a function of the irradiation dose. *1, 2* — Pulse amplitude $U_0>10$ V; *3, 4* — $U_0<10$ V. The experimental points 1–4 correspond to the same structures as in Fig. 3.

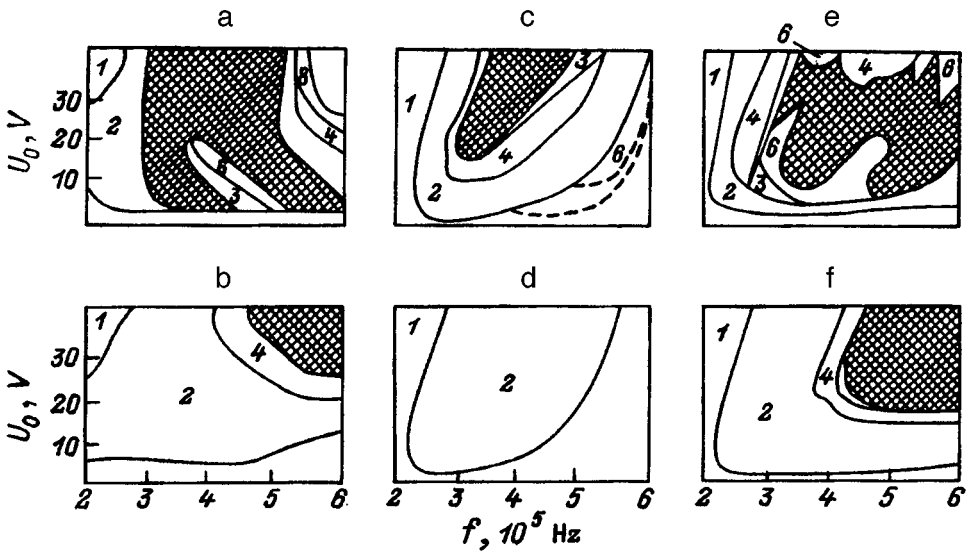

FIG. 5. Pre- (top a, c, e) and postirradiation (bottom — b, d, f) state diagrams of a *RL* circuit containing a MIS structure. Types of substrates in the structures: a, b — *n*-Si, c,d — (n^+-p)-Si, e,f — (n^+-n^--p)-Si. The numbers 1–4, 6, and 8 denote the regions of existence of oscillations with the corresponding period $1T$ — $4T$, $6T$, and $8T$. The dashed lines represent the lines of hysteresis with respect to doping. The hatching indicates regions of chaotic oscillations.

of the pulse is sufficient to switch the structure into a low-resistance state, the duration of the transient process is determined by the passage of carriers through the insulator. At doses $D<10^4$ rad the appearance of radiation-induced charge in the insulator is accompanied by the appearance of a negative charge in the surface region of the semiconductor and an electric field (which remains after the pulse is switched off) which is directed in such a way that the motion of the holes toward the surface is retarded. As a result, the duration of the transient process increases with dose. Increasing the irradiation dose to 10^6 rad decreases the contribution of these factors, decreases the voltage drop across the insulator, and gives rise to unimpeded motion of carriers toward the surface, so that t_s decreases (see Fig. 4, curves *3* and *4*). This argument confirms the dose dependence of the switching voltage presented in Fig. 3. The observed features (maxima) in the curves of t_s and U_s versus the irradiation dose confirm the nonlinearity of the processes studied. As the dose increases, the positive built-in charge increases, but the increase in the built-in charge gives rise not to a constant growth of the parameters t_s or U_s but rather only an increase in these quantities up to a certain value, as a result of the fact that a redistribution of voltage between the SCR and the insulator occurs. This changes the accumulation, relaxation, and motion of the accumulated charge. It is realistic to assume, on the basis of the irradiation dose dependence of t_s with pulse amplitude greater than 10 V (see Fig. 4, curves *1* and *2*), that radiation defects in the insulator influence the passage time of the holes injected by the p–n junction, giving rise to some acceleration of the holes in the range $D=10^2-10^4$ rad and deceleration in the range $D=10^4-10^6$ rad.

The effect of γ-irradiation on the parameters of MIS structures was also observed in studying the oscillatory states of a *RL* circuit containing a MIS structure. It is known[18] that the state diagrams reflect the dynamics of the following processes in the semiconductor sample: carrier accumulation and relaxation with the participation of recombination centers and surface states. Therefore, the changes in the parameters of the surface states, which determine the frequency characteristics of MIS structures, influence the excitation of oscillations in the circuit. When a periodic voltage with a period T was applied, complicated periodic oscillations with different periods — $2T$, $3T$, $4T$, and $6T$ — as well as random oscillations arose in the system.

Figure 5 shows the state diagrams of structures with three types of substrates. Let us examine the state diagram of the circuit containing a MIS structure on a uniform substrate, where a Y_2O_3 film is used as the insulator (Figs. 5a and 5b). As one can see, before irradiation the state diagrams had a complicated structure — regions of period doubling, hysteresis, and chaos. After irradiation the state diagrams simplified: oscillations with periods of $1T$, $2T$, and $4T$ remained, and the area of the region of chaos is smaller.

In the state diagram of a circuit containing a structure on a (n^+-p)-Si substrate (Figs. 5c and 5d) only the doubling region remains after irradiation; none of the other oscillatory states observed before irradiation are observed (Fig. 5d). The preirradiation state diagram of a circuit containing a structure on a (n^+-n^--p) Si substrate (Figs. 5e and 5f) contained regions of periodic, quasiperiodic, and chaotic oscillations. After irradiation, regions of period doubling and chaos were observed in the state diagram, just as in the state diagram of a circuit with a MIS structure on a uniform substrate (see Fig. 5b). It can be assumed that the simplification of the topology of the state diagrams reflects the change in the MIS structure under the action of the irradiation. The number of recombination centers (in the insulator — positively charged centers) increases. As a result, the carrier accumulation time increases and the oscillatory states at a given frequency and amplitude of the external perturbation change.

3. CONCLUSIONS

The results of the investigations of the static (current-voltage, capacitance-voltage) and dynamic (transient process time, oscillatory states) characteristics of MIS structures with uniformly and nonuniformly doped substrates agree with one another and suggest that the observed radiation-induced changes in MIS structures containing rare-earth oxides are

consistent with the standard data for structures with SiO_2 as the insulator.[13] In addition, it was shown that, because of convenience and informativeness, analysis of the oscillatory states can be used to estimate the quality of a silicon–⟨rare-earth oxides⟩ interface.

[1] Vinita Vasudevan and J. Vasin, IEEE Trans. ED **41**, 383 (1994).
[2] G. Q. Lo, A. B. Joshi, and D. L. Kwong, IEEE Trans. ED **40**, 1565 (1993).
[3] Kusi-Shu, Chang Jiao, Jenu-Gwo. IEEE Trans. ED **41**, 612 (1994).
[4] V. A. Gurtov, A. I. Nazarov, and I. V. Travkov, Fiz. Tekh. Poluprovodn. **24**, 969 (1990) [Sov. Phys. Semicond. **24**, 611 (1990)].
[5] V. A. Gurtov and P. A. Raĭkerus, Mikroélektron. **6**, 68 (1987).
[6] Wei Shin Lu, Kuan-Chin. IEEE Trans. ED **40**, 1598 (1993).
[7] O. V. Vovk, V. P. Lelchenko, V. I. Soloshenko, Ya. O. Roĭzman, and V. A. Chkynina, Fiz. Tekh. Poluprovodn. **27**, 1349 (1993) [Semiconductors **27**, 745 (1993)].
[8] P. V. Kuchinskiĭ, Fiz. Tekh. Poluprovodn. **27**, 1354 (1995) [Semiconductors **27**, 747 (1995)].
[9] D. G. Krylov, E. A. Ladygina, and A. P. Galeev, Fiz. Tekh. Poluprovodn. **26**, 1347 (1992) [Sov. Phys. Semicond. **26**, 753 (1992)].
[10] V. A. Rozhkov and A. I. Petrov, in *Abstracts of Reports at the Conference on ''Electrophysics of Layered Structures,''* [in Russian], Tomsk, 1988, No. 5, p. 21.
[11] V. V. Afanas'ev, J. M. M. deNijs, and P. Balk, Appl. Phys. Lett. **66**, 1783 (1995).
[12] N. Sano, M. Sekiya, M. Hara, A. Kohno, and T. Sameshina, Appl. Phys. Lett. **66**, 2107 (1995).
[13] A. M. Emel'yanov and V. V. Golubev, Fiz. Tekh. Poluprovodn. **28**, 2084 (1994) [Semiconductors **28**, 1148 (1994)].
[14] M. Gasgnier, Phys. Status Solidi A **114**, 11 (1989).
[15] J. H. Baxter, M. F. Bocko, and D. H. Douglass, Phys. Rev. A **41**, 619 (1990).
[16] F. Moon, *Chaotic Vibrations: An Introduction for Applied Scientists and Engineers*, Wiley, N. Y., 1987 [Russian transl., Mir, Moscow, 1990].
[17] Kh. K. Al'vares, L. S. Berman, and I. N. Karimov, Fiz. Tekh. Poluprovodn. **28**, 1488 (1994) [Semiconductors **28**, 835 (1994)].
[18] E. Schell, *Self-Organization in Semiconductors* [Russian transl., Mir, Moscow, 1989].

Translated by M. E. Alferieff

Calculation of a hierarchical PbS–C superlattice in a multiwell model

E. Ya. Glushko and V. N. Evteev

State Pedagogic Institute, 324086 Krivoĭ Rog, Russia
(Submitted August 7, 1995; accepted for publication October 25, 1996)
Fiz. Tekh. Poluprovodn. **31**, 889–892 (June 1997)

A multiwell model of hierarchical semiconductor structures, which meets the requirements for stability of the spectrum and orthogonality of the wave functions of the states, is proposed. The energy dispersion, density of states, wave functions, and spectrum of a quasi-Fibonacci semiconductor system are calculated. A classification rule relating the structure of the spectrum to the structure of the system is formulated. The optical manifestations of the hierarchical organization of the spectrum are discussed. © *1997 American Institute of Physics.*
[S1063-7826(97)02806-8]

Experimental studies of hierarchical structures based on semiconductor materials exhibit some interesting electrical and optical properties, which can be utilized for practical purposes.[1–3] They can be important, first of all, for designing materials with an assigned electronic structure and optical characteristics.

Theoretical investigations of the electronic structure of hierarchical systems have been described in the literature mainly within two approaches. The first is based on models of an effective (free) band particle moving in a macroscopic envelope potential of a superlattice.[4–7] Under such an approach each of the layers is described by one flat potential well, and the spectrum is derived directly from the transmission coefficient of the structure.[6,7] The other approach is based on the conception of a model Hamiltonian for a system of one-level quantum wells with ''strong'' and ''weak'' probabilities for the transition of a particle into a neighboring well that alternate according to a hierarchy.[8,9] Because of the nearest-neighbor approximation, the matrix of the Hamiltonian becomes three-diagonal, significantly simplifying the renormalization-group analysis of the structure of the spectrum.

MULTIWELL MODEL

However, there is one more possible physical formulation of the problem of the electronic spectrum of a hierarchical system, which apparently corresponds most closely to optical experiments. In the proposed model[10,11] the atoms or unit cells are represented by quantum wells (QW's) in a hierarchical system that is transverse to the layers, so that each layer of the hierarchical system is described by a system of QW's, and the hierarchical system comprises a superlattice system. The multiwell approach eliminates the serious problem in single-well approximation (where the QW represents a semiconductor layer), viz., the instability of the energy spectrum. For example, doubling the thickness of the layer in the single-well approximation leads to considerable alteration of the miniband pattern, while the real spectrum varies very weakly already for $N \geqslant 10$, where N is the number of unit cells in the transverse direction.

Another aspect of the multiwell model is the explicit consideration of the separation between the longitudinal and transverse motion of an electron in the material. The size quantization is determined by the transverse motion, and such characteristics as the electron affinity U_1 and the work function U_0 are results of the solution of the complete problem. Therefore, in the approximation for the crystal potential developed in Ref. 12, one-dimensional motion across layers is characterized by an electron affinity and a work function that are three times smaller than the bulk equivalents. The area of application of the approximation in Ref. 12 was discussed in Ref. 13 in the example of linear chains of cylindrical potential wells, where its asymptotic accuracy for band states was demonstrated.

With consideration of the foregoing, to calculate a Fibonacci structure of PbS–C layers[3] we approximated the three-dimensional potential of a bulk PbS crystal by a sum of three one-dimensional Kronig–Penney potentials. The potential of the external medium (a vacuum) was taken as 0, and the bottom of the three-dimensional well coincided with the top of the valence band, which was evaluated from the work function for removal of an electron from the material $U_0 = 4.6$ eV. Then, for the depth of the one-dimensional well we have $U_0' = 1.53$ eV. For a constant size of the unit-cell (the well together with the barrier) $a = 5.94$ Å, we varied the barrier height U and the ratio of the barrier width b to the well width a so as to obtain the necessary energy gap, which is equal to $\frac{\Delta}{3}$, where $\Delta = U_0 - U_1$, and $U_1 = 4.2$ eV. The following parameters were obtained after fitting: a well width equal to 5.4 Å, a barrier width equal to 0.54 Å, and $U = U_0'$ (Fig. 1a). The one-dimensional characteristics of the spectrum of PbS are presented in Fig. 1b (smooth line). The carbon film was approximated by a rectangular barrier with a width of 5 Å and a height that is also equal to the depth of the well. Then the structure described in Ref. 3 was constructed. This structure can be described by the formula $VACAACACACAACACAACACACV$[1)], where V is a vacuum barrier, A is a PbS layer consisting of ten unit cells, and C is a monolayer carbon film (Fig. 1a).

According to Refs. 10 and 11, the dispersion relation of the eigenvalue problem has the form

$$(1,\ k_0)\left[\begin{pmatrix}\overline{\mu\nu}\\ \overline{\lambda\mu}\end{pmatrix}\begin{pmatrix}\mu\nu\\ \lambda\mu\end{pmatrix}\begin{pmatrix}\overline{\mu\nu}\\ \overline{\lambda\mu}\end{pmatrix}\right]^{10}\begin{pmatrix}\mu'\nu'\\ \lambda'\mu'\end{pmatrix}\ldots$$

 1063-7826/97/070756-03$10.00

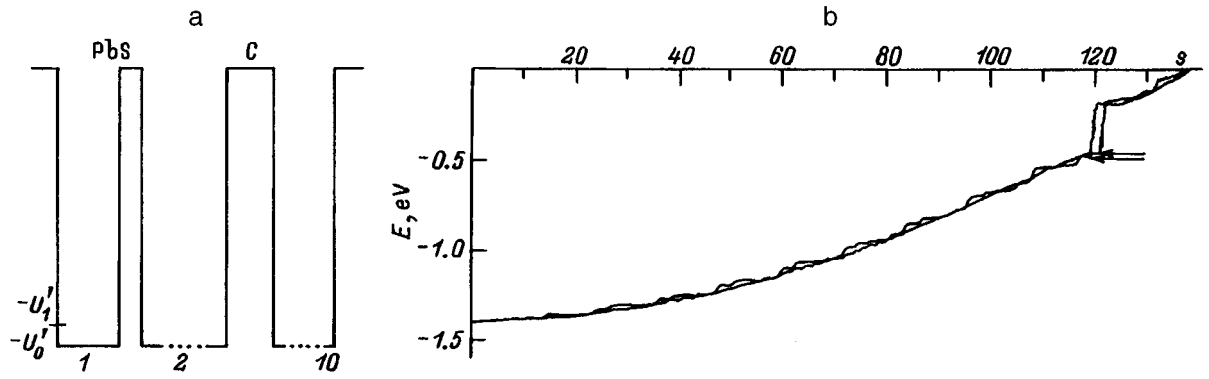

FIG. 1. Multiwell model of a PbS–C hierarchical system. a — Geometry of the one-dimensional potential of the hierarchical system. The total number of wells is 120, there are nine carbon barriers, and the dotted line denotes continuations of the structure. b — Calculated energy dispersion. Here s labels the states (s_{max}=138). Smooth curve – thick PbS layer (120 unit cells). Dashed curve – structure described in Ref. 3.

$$\ldots \begin{pmatrix} \mu' & \nu' \\ \lambda' & \mu' \end{pmatrix} \begin{pmatrix} -1 \\ -k_0 \end{pmatrix} = 0, \tag{1}$$

where $k=\sqrt{\frac{2m(U_0-E)}{\hbar^2}}$ and $k_0=\sqrt{\frac{2mE}{\hbar^2}}$,

$$\mu=-k\cos ka, \quad \lambda=\sin ka, \quad \nu=k^2\sin ka,$$

$$\overline{\mu}=-k_0\cosh k_0\frac{b}{2}, \quad \overline{\lambda}=\sinh k_0\frac{b}{2}, \quad \overline{\nu}=k_0^2\sinh k_0\frac{b}{2},$$

$$\mu'=-k_0\cosh k_0 b', \quad \lambda'=\sinh k_0 b',$$

$$\nu'=k_0^2\sinh k_0 b'. \tag{2}$$

The matrix with the primed elements corresponds to a carbon barrier of thickness b', and the group of three square matrices in the first power corresponds to a half-barrier–well–half-barrier sequence in the PbS crystal potential. The power in (1) corresponds to a ten-well A layer in the formula of the structure. The terminal matrices, i.e., the row and the column, ensure satisfaction of the boundary conditions on the outer surfaces of the hierarchical system. The multiwell model of the PbS–C hierarchical structure described, i.e., the energy spectrum, the wave functions, and the density of states, was calculated using the oscillation theorem, which made it possible to maintain a relative error in the determination of the wave functions no greater than 10^{-8} and to guarantee their orthogonality. One interesting feature of the calculation of the electronic structure of the superlattice and the hierarchical structure is the enormous difference between the accuracies required for the energies of the states and the corresponding wave functions. At the same time, in order for the latter to satisfy the requirements of continuity and orthogonality with respect to the remaining wave functions and to contain the correct number of nodes, the accuracy of the calculation had to be increased by several orders of magnitude. The active computer interface of the model makes it possible to create and approximate hierarchical structures, as well as unordered systems.

CALCULATION RESULTS AND DISCUSSION

The results of a calculation of a hierarchical system containing a total of 120 PbS cells and nine carbon layers are presented in Fig. 1b. It is easily seen that size quantization of the transverse motion in the multiwell model leads to regrouping of the states within the PbS band. The narrowing of the one-dimensional conduction band of the structure by $\approx$0.03 eV in comparison to the PbS band (as indicated by the arrows in Fig. 1b) is a consequence of the insufficient thickness of the PbS layers in the hierarchical structure. A detailed quantitative analysis shows that this effect (see also Ref. 11) is one of the manifestations of the phenomenon of stability of the spectrum of multiperiodic QW systems. There are no carbon levels in the spectrum, since carbon is represented by a simple barrier.

The levels in the conduction band were regrouped into subbands, the maximum gap between the subbands being equal to 0.072 eV. We conclude that such alteration of the spectrum in comparison with the spectrum of pure PbS is unlikely to be detected by nonselective methods, taking into account that the second band gap vanishes when the levels for three measurements are combined. If only the transverse quantum numbers of the problem (s here) participate in the light scattering or absorption processes, the vertical portions of the dispersion curve (Fig. 1b) correspond to horizontal plateaus on the absorption curve, as was observed, in all likelihood, in the experimental study in Ref. 3. Visual inspection of the wave functions of the states showed that they have the form of standing waves and are localized in regions with a double layer of PbS and in regions with a single layer of PbS. A classification analysis of the structure of the spectrum (Fig. 2) reveals a clear-cut relationship between the number of subbands of a lower hierarchy in the band of a higher hierarchy and such factors as the number of single and double PbS layers. The results of the investigations of the states in the wave functions of a given hierarchical system, as well as many other states, leads to a simple classification rule: the higher is the hierarchy of the potential, the more internal is the structural hierarchy of the levels in which it is reflected and vice versa. For example, the two bands of the highest hierarchy (column *1*) are stipulated by the parameters of a single potential well (Fig. 1a), and the six bands of the latest hierarchy (column *4*) are determined by six macrolayers with a single A layer. The smallest unit in the structure is a single PbS well, and this leads to splitting of the spectrum

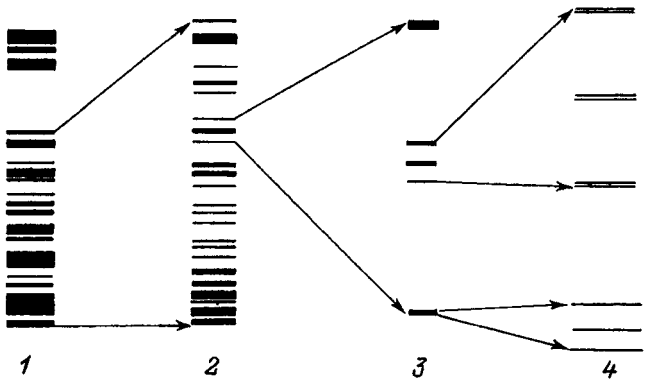

FIG. 2. Energy diagram of a PbS–C hierarchical system. The structures of the spectrum for decreasing hierarchical orders are presented in columns *1–4*; the arrows demarcate the spectral range and indicate the magnification of the scale.

into bands, each of which consists of 120 levels (Fig. 2, column *1*). The upper band is incompletely filled. The next unit determining the hierarchy is a layer of ten PbS wells; therefore, each bands splits into ten bands, each containing twelve levels (Fig. 2, column *2*). Single and double PbS layers are simultaneously responsible for the formation of the next level of the hierarchy. Each band, in turn, splits into three subbands. The upper and lower subgroups consist of three levels, and the middle subgroup consists of six levels (Fig. 2, column *3*). Such splitting is attributed to the fact that the structure has three double layers (each of which supplies two levels to each spectral band) and six single layers. Such an interpretation of the splitting is also supported by the fact that the wave functions of the middle subgroup are localized in single layers, while the wave functions of the upper and lower groups are localized in double PbS layers.

The calculation of the density of states $\rho_s=|E_s-E_{s-1}|^{-1}$ from the dispersion dependence obtained for the hierarchical system revealed the extremely high degree of inhomogeneity of this quantity. The strong inhomogeneity is also conserved on the logarithmic scale (for $\ln\rho_s$).

Placement of the system of wells (Fig. 1a) in an electric field resolved the orderly hierarchy in the spectrum. Erosion of the lower hierarchical orders of the spectrum (column *4*) began already for voltages $\Delta\varphi\approx 0.01$ V. When $\Delta\varphi\approx 0.3$ V, the field completely mixes the structure presented in Fig. 2 without altering the clearly expressed inhomogeneity of the density of states. When $\Delta\varphi\approx 0.4$ V, the gap between the bands in the highest hierarchy vanishes.

CONCLUSIONS

The general conclusions drawn here regarding the electronic structure are also valid for pure Fibonacci structures, as well as for arbitrary hierarchical structures. This can be illustrated by taking a hierarchical system in which ten elementary QW's are reproduced ten times and alternated with inner intervening layers, the structure obtained is again reproduced ten times with thicker intervening layers, and so on. The process is terminated in the highest hierarchical order. The multiwell model gives a clear decimal hierarchy of the spectrum of this structure. In particular, an increase in the thickness of the outermost intervening layers leads to ''sticking'' of the levels in the fine-structure subbands, and the thickness of the inner intervening layers regulates the bands of the highest level in the spectral hierarchy.

The model permits more exact simulation of the one-dimensional crystal potential of the original materials because of the detailing of the shape of the elementary potential well (with steps). It can be made as complicated as one desires, and the number of matrices in the square brackets in Eq. (1) can be increased accordingly.

The grouping of the states in a hierarchical system leads to the appearance of nearly vertical segments on the dispersion curve, which can be the cause (along with the interference effects) of the appearance of the horizontal plateaus in the absorption spectrum of the hierarchical structure, despite the integral nature of the absorption coefficient.

[1)]It should be noted that Fibonacci's recurrence relation did not hold here or in Ref. 3.

[1] *Proceedings of the VIII International Conference on the Electronic Properties of Two-Dimensional Systems*, published in Surf. Sci. **229** (1–3), (1990).
[2] P. S. Kop'ev and I. I. Reshina, Fiz. Tekh. Poluprovodn. **23**, 1316 (1989) [Sov. Phys. Semicond. **23**, 821 (1989)].
[3] S. F. Musikhin, L. G. Bakueva, V. I. Il'in, O. V. Rabizo, and L. V. Sharonova, Fiz. Tekh. Poluprovodn. **29**, 474 (1995) [Semiconductors **29**, 245 (1995)].
[4] B. Sutterland and M. Kohmoto, Phys. Rev. B **36**, 5877 (1987).
[5] L. J. Sham and Y. T. Lu, J. Lumin. **44**, 207 (1989).
[6] Yu. V. Kopaev and S. N. Molotkov, Pis'ma Zh. Éksp. Teor. Fiz. **59**, 770 (1994) [JETP Lett. **59**, 800 (1994)].
[7] A. N. Korol', Ukr. Fiz. Zh. **40**, 749 (1995).
[8] Q. Niu and F. Nori, Phys. Rev. B **42**, 10 329 (1990).
[9] S. D. Gupta and D. S. Ray, Phys. Rev. B **38**, 3628 (1988).
[10] E. Ya. Glushko, Fiz. Tverd. Tela (St. Petersburg) **38**, 323 (1996) [Phys. Solid State **38**, 182 (1996)]; Fiz. Tverd. Tela (St. Petersburg) **38**, 2051 (1996) [Phys. Solid State **38**, 1132 (1996)].
[11] E. Ya. Glushko and V. N. Evteev, Ukr. Fiz. Zh. **40**, 719 (1995); Preprint State Pedagogic Institute, Krivoĭ Rog (1994), p. 56.
[12] V. G. Bar'yakhtar, E. D. Belokolos, and A. N. Korostil', Metallofizika **13** (5), 3 (1991); E. D. Belokolos and A. N. Korostil', Metallofizika **13** (6), 3 (1991).
[13] E. Ya. Glushko, Fiz. Nizk. Temp. **22** (10), (1996).

Translated by P. Shelnitz

Viktor Il'ich Fistul' (On his seventieth birthday)

Fiz. Tekh. Poluprovodn. **31** (July 1997)

[S1063-7826(97)03507-2]

Viktor Il'ich Fistul', Academician of the Russia Academy of Natural Sciences and Professor in the Department of Solid-State Physics and Chemistry at the Moscow Academy of Precision Chemical Technology, celebrated his seventieth birthday on May 1.

V. I. Fistul' is a prominent Russian scientist working in semiconductor materials physics. His scientific authority is acknowledged not only in our country but abroad as well. He has been awarded the honorary title ''Honored Scientist and Technologist of Russia,'' he is a laureate of two state prizes, and he is a member of the Russian Physical Society, the American Physical Society, and the Physical Society of the Hungarian Republic.

At the beginning of his scientific career he had the good fortune of studying under the world-renowned scientist and father of semiconductor physics in Russia, A. F. Ioffe, and his scientific interests were tied firmly and for a long time to semiconductors. Since 1959 he has been studying the state and behavior of impurities in semiconductors. A large part of his scientific works concerns these problems.

The investigations of strongly doped semiconductors which V. I. Fistul' performed together with his students led to the discovery of the phenomenon of polytropy of impurities in semiconductors. These investigations led to his writing the monograph *Strongly Doped Semiconductors* (1965), which has been translated into the English language and published in the USA (1969).

V. I. Fistul' made a large personal contribution to the mastery of the metrics of semiconductors. He was awarded the State Prize in the field of science and technology (1975) for developing a system of procedures for monitoring the quality of gallium arsenide and for his participation in the development of the technology and industrial production of GaAs.

The study of the behavior of impurities in semiconductor heat-treatment processes led to the discovery of a number of characteristic features of the process of decomposition of semiconductor solid solutions and served as a basis for the monograph *Decomposition of Supersaturated Semiconductor Solid Solutions* (1977).

The investigations of transition-metal impurities in IV and III–V semiconductors performed under the direction of V. I. Fistul' yielded unique data and established the basic mechanisms of the behavior of these impurities. These investigations are reflected in another monograph *Transition-Metal Impurities in Semiconductors* (1983), which V. I. Fistul' coauthored with his student É. M. Omel'yanovskiĭ. This book has also been translated into the English language, and it has been published in Great Britain (1986).

The study of the behavior of gasous impurities in semiconductors led to the discovery of a new phenomenon associated with the behavior of hydrogen in germanium and silicon.

V. I. Fistul' and his students made a large contribution to the theories of the behavior of isovalent and amphoteric impurities. V. I. Fistul''s monograph *Amphoteric Impurities in Semiconductors* was published in 1992.

In recent years V. I. Fistul' has been actively generating and developing new ideas concerning the development of nonstandard methods for obtaining new materials. These methods include laser implantation of impurities in semiconductors, the development of polymer–semiconductor compositions, and an entire series of other methods. He is also actively involved in publishing.

Since 1958, V. I. Fistul' has been actively engaged in scientific work and teaching. Since the Department of Semiconductor Materials Technology was formed in 1962 at the M. I. Lomonosov Moscow Institute of Precision Chemical Technology, V. I. Fistul' has been teaching a course on ''Semiconductor Physics'' and in 1977 he became head of the department. In 1984–1985 he was the first one in our country to develop a course on ''Solid-State Physics and Chemistry'' for technical schools of higher learning. In 1986 the Department of Solid-State Physics and Chemistry was created at the Institute through his efforts and headed by him until 1991.

V. I. Fistul' generalized his pedagogical experience in the textbooks *Introduction to Semiconductor Physics* (1975, 1984) and *New Materials* (1995). In 1995 he published his textbook *Solid-State Physics and Chemistry* (two volumes), which is the first effort of its kind, encompassing both aspects of the science of solids, and can be used as a basic textbook for teaching different special solid-state disciplines. This textbook very quickly won wide acclaim from specialists.

V. I. Fistul' has trained six doctors and 45 candidates of science. He is a member of the Scientific Council of the Russian Academy of Sciences, and he has been awarded a ''Badge of Honor'' and medals. He was a member of the editorial board of the journal ''Semiconductors'' from the day the journal was founded and remained on the board for many years.

V. I. Fistul' is a fascinating, well-educated person and at age 70 he is still hale and hearty and actively engaged in his favorite work.

We wish V. I. Fistul' health, optimism, and many years

 1063-7826/97/070759-02$10.00

of fruitful work and success in all his new endeavors.

Instructors and colleagues in the Department of Solid-State Physics and Chemistry and the Department of Semiconductor Materials Technology at the M. I. Lomonosov Moscow Academy of Precision Chemical Technology.

Editorial Board of the journal ''Semiconductors''

Translated by M. E. Alferieff

Electronic Phenomena in Chalcogenide Glassy Semiconductors

Collective monograph edited by K. D. Tséndin, Nauka, St. Petersburg, 1986, 486 pages.

Fiz. Tekh. Poluprovodn. **31** (July 1997)

[S1063-7826(97)03607-7]

This monograph was produced by an international team of authors (Russia, Belgium, Japan, England) whose core are staff members at the A. F. Ioffe Physicotechnical Institute of the Russian Academy of Sciences. The results of wide-ranging experimental and theoretical investigations of the physical properties of chalcogenide glassy semiconductors (CGSs) are described. The development of the physics of CGSs is followed from creation up to the latest achievements. The exceptional role of the electron-phonon interaction, which determines the characteristic features of both the electronic spectrum and the spectrum of defects as well as the specific nature of the electric and optical properties of CGSs, is examined.

The twelve chapters of the book can be divided into several groups according to subject. The first group comprises the chapters devoted to the electric and photoelectric properties as well as the problem of extrinsic conductivity in CGSs. The second group comprises the chapters describing phenomena occurring in strong electric fields. Finally, the third group comprises the chapters concerning nonlinear optical phenomena and metastable photoinduced states.

The book can be recommended to specialists in the field of semiconductor physics and technology, micro- and optoelectronics, materials engineering, and informatics as well as to instructors, graduate students, and students of the corresponding specialities.

This monograph is dedicated to the memory of the discoverer of chalcogenide glassy semiconductors, Boris Timofeevich Kolomiĭts, the anniversary of whose ninetieth birthday will be celebrated in 1998.

This monograph was written and published with the financial assistance of Russian Fund for Fundamental Research.

K. D. Tséndin

Translated by M. E. Alferieff

 1063-7826/97/070761-01$10.00